

**Characterization of TL/OSL phosphors and study of
photo-ionization cross-sections of meta-stable trap
levels- An Experimental and Theoretical approach**

By

Narender Singh Rawat

BHABHA ATOMIC RESEARCH CENTRE, MUMBAI

*A thesis submitted to the
Board of Studies in Physical Sciences
In partial fulfillment of requirements
For the Degree of*

**DOCTOR OF PHILOSOPHY
of
HOMI BHABHA NATIONAL INSTITUTE**



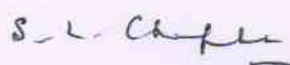
August, 2012

Homi Bhabha National Institute

Recommendations of the Viva Voce Board

As members of the Viva Voce Board, we certify that we have read the dissertation prepared by **Narender Singh Rawat** entitled “**Characterization of TL/OSL phosphors and study of photo-ionization cross-sections of meta-stable trap levels- An Experimental and Theoretical approach**” and recommend that it may be accepted as fulfilling the dissertation requirement for the Degree of Doctor of Philosophy.

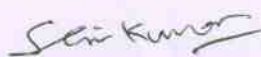
Chairman:



Date: 07/5/2013

(Prof. S. L. Chaplot)

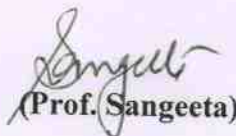
Convenor:



Date: 2/5/13

(Prof. S. K. Gupta)

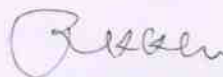
Member 2:



Date: 2/5/13

(Prof. Sangeeta)

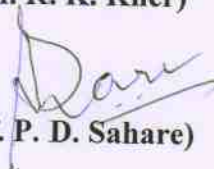
Member 1:



Date: 2/5/13

(Prof. R. K. Kher)

External Examiner:



Date: 02/05/13

(Prof. P. D. Sahare)

Final approval and acceptance of this dissertation is contingent upon the candidate's submission of the final copies of the dissertation to HBNI.

CERTIFICATE

I hereby certify that I have read this dissertation prepared under my direction. All the suggestions made by one of the referees in his evaluation report have been incorporated and the referee has approved these changes. Therefore, I recommend that this dissertation may be accepted as fulfilling the requirement for the Degree of Doctor of Philosophy.

Date:

Dr. S. K. Gupta

Place:

(Convener)

STATEMENT BY AUTHOR

This dissertation has been submitted in partial fulfillment of requirements for an advanced degree at Homi Bhabha National Institute (HBNI) and is deposited in the Library to be made available to borrowers under rules of the HBNI.

Brief quotations from this dissertation are allowable without special permission, provided that accurate acknowledgement of source is made. Requests for permission for extended quotation from or reproduction of this manuscript in whole or in part may be granted by the Competent Authority of HBNI when in his or her judgment the proposed use of the material is in the interests of scholarship. In all other instances, however, permission must be obtained from the author.

Narender Singh Rawat

DECLARATION

I, hereby declare that the investigation presented in the thesis has been carried out by me.
The work is original and has not been submitted earlier as a whole or in part for a degree/diploma at this or any other Institution / University.

Narender Singh Rawat

Dedicated to my Parents and Wife

ACKNOWLEDGEMENTS

I owe a debt of gratitude to many people who made this thesis possible due to their support, suggestions, and encouragements.

I seek great pleasure in expressing my sincere gratitude and indebtedness to my thesis supervisor Prof. S. K. Gupta for his invaluable guidance and constant encouragement to complete this work. I would also like to express my gratitude to the chairman Prof. S. L. Chaplot and members Prof. R. K. Kher and Prof. Sangeeta of my doctoral committee for sitting through long review sessions and coming out with insightful comments and encouragement.

I would like to thank Dr. M. S. Kulkarni, Dr. D. R. Mishra, Dr. B. C. Bhatt, Anuj Soni, Smt. Ratna Pradeep and Lovely Paliwal for their untiring support during the experiments and for many interesting discussions. Their instructions were always constructive and positive. Their assistance opened new doors for my academic pursuits.

I am indebted to Dr. K. P. Muthe for his unconditional support during the course of my work and for carefully going through the chapters during the preparation of the thesis.

I wish to express my sincere gratitude and indebtedness to my parents, parents-in-laws for their blessings, brother and other family members for their love and support to me. Thankfulness in abundance to my wife Renu for her unfailing conviction that I would make it and to our daughter Ojaswini for giving me perspective.

Last but not the least, I would like to thank Dr. D.N Sharma, Director HS&E group for his constant motivation and help throughout this research work.

CONTENTS

	Page No.
<i>SYNOPSIS</i>	VIII-XVIII
<i>LIST OF FIGURES</i>	XIX-XXIII
<i>LIST OF TABLES</i>	XXIV
<i>LIST OF PUBLICATIONS</i>	XXV-XXVI
Chapter 1: Introduction	1-54
1.1. Motivation and background	2
1.2. Luminescence Phenomena	3
1.3. Classification of Luminescence	7
<i>1.3.1. Fluorescence</i>	7
<i>1.3.2. Phosphorescence</i>	7
1.4. Thermally Stimulated Luminescence (TL)	9
<i>1.4.1. Theory of Thermoluminescence</i>	10
<i>1.4.2. Randall-Wilkins Model</i>	11
<i>1.4.3. Garlick-Gibson Model</i>	12
<i>1.4.4. Model for General order kinetics</i>	13
<i>1.4.5. Limitations of TL</i>	13
1.5. Optically Stimulated Luminescence (OSL)	14
<i>1.5.1. Theory of OSL</i>	17
<i>1.5.2. Stimulation Modalities</i>	18
<i>1.5.2.1. Continuous wave OSL (CW-OSL)</i>	19
<i>1.5.2.2. Pulsed OSL (POSL)</i>	22
<i>1.5.2.3. Linearly Modulated OSL (LM-OSL)</i>	23
<i>1.5.2.4. Non-linear OSL (NL-OSL)</i>	27
1.6. Merits of OSL	27
1.7. Key Attributes of a TL/OSL phosphor	30
1.8. Widely practiced Phosphors in TL dosimetry	31
1.9. Phosphors for OSL dosimetry	32

1.10. α -Al ₂ O ₃ as TL/OSL host material	34
1.11. Alternative approaches for preparation of dosimetric Grade α -Al ₂ O ₃ :C	41
<i>1.11.1. Post-Growth Thermal Impurification (PGTI) Technique</i>	42
<i>1.11.2. Electron-gun Method</i>	45
<i>1.11.3. Melt Processing technique for Scaled up Synthesis of α-Al₂O₃:C</i>	46
1.12. Lithium Borate (Li ₂ B ₄ O ₇)	49
1.13. Recent advances in TL and OSL	49
1.14. Summary	51
Chapter 2: Methods of TL/OSL analysis and defect characterization techniques	55 -112
2.1. Introduction	56
2.2. Defects in solids	56
<i>2.2.1. Thermodynamics of defects</i>	57
<i>2.2.2. Color centers</i>	59
2.3. Defects and Diffusion	60
2.4. Defects and Luminescence	63
<i>2.4.1. Selection Rule</i>	64
<i>2.4.2. Quantum efficiency</i>	65
<i>2.4.3. Configurational Coordinate diagram and Thermal Quenching</i>	66
<i>2.4.4. Concentration quenching</i>	69
2.5. Experimental Methods of Determining TL Parameters	72
<i>2.5.1. Initial Rise Method</i>	73
<i>2.5.2. Variable Heating Rate Method</i>	73
<i>2.5.3. Method based on glow curve shape</i>	74
<i>2.5.4. Isothermal Decay Method</i>	74
2.6. Methods for Determination of OSL parameters	75
<i>2.6.1. Optical Stimulation of Trapped Charges</i>	75

Chapter 3: Formulation of Initial Rise method for TL kinetic analysis-Theoretical & Experimental approach	113-125
3.1. Introduction	114
3.2. Theoretical Formulation	114
3.2.1. <i>Determining Kinetic Order</i>	116
3.2.2. <i>Determining Pre-exponential Factor</i>	117
3.2.3. <i>Determining Frequency Factor</i>	117
3.3. Numerical Simulations	119
3.4. Experimental Validation	121
3.5. Results	124
3.6. Conclusion	124
Chapter 4: Characterization & study of temperature dependence of photo-ionization cross-section in Al₂O₃:C	126-172
4.1. Introduction	127
4.2. TL and OSL Characterization of developed α -Al ₂ O ₃ :C	127
4.2.1. <i>TL studies</i>	127
4.2.2. <i>OSL studies</i>	130
4.2.3. <i>Optical Absorption Studies</i>	134
4.2.4. <i>PL studies</i>	136
4.2.5. <i>Conclusion</i>	136
4.3. Dose dependence of photo-ionization cross section in Al ₂ O ₃ :C	137
4.3.1. <i>Experimental</i>	137
4.3.2. <i>Results</i>	137
4.3.3. <i>Model to explain the dose dependence of photo-ionization cross-section</i>	140
4.3.4. <i>Explanation for increase in σ as a function of dose</i>	141
4.4. Temperature dependence of photo-ionization cross section in α -Al ₂ O ₃ :C	142

4.4.1. <i>Theory of Method</i>	142
4.4.2. <i>Analysis under first-order kinetics ($b=1$)</i>	145
4.4.3. <i>Analysis under general-order kinetics ($b\neq 1$)</i>	146
4.4.4. <i>Materials and Method</i>	149
4.4.5. <i>Results</i>	149
4.4.5.1. <i>Generation of Thermally Assisted (TA)-OSL</i>	149
4.4.5.2. <i>Measurements of thermally assisted energy and pre-exponential factor in α-Al₂O₃:C</i>	152
4.4.7. <i>Conclusion</i>	157
4.5. <i>Non-Linear Light Modulation OSL Studies using α-Al₂O₃: C</i>	158
4.5.1. <i>Theory of NL-OSL</i>	159
4.5.2. <i>Specific advantages of NL-OSL over LM-OSL</i>	160
4.5.3. <i>Materials and method</i>	163
4.5.4. <i>Results</i>	163
4.5.4.1. <i>Experimental Generation of NL - Stimulation Profiles</i>	163
4.5.4.2. <i>Measurements of background scattering signal</i>	165
4.5.4.3. <i>Measurements of NL-OSL of α-Al₂O₃:C</i>	168
4.5.4.4. <i>Limitations of NL-OSL technique</i>	169
4.5.5. <i>Conclusion</i>	171
Chapter 5: Application of Al₂O₃: C for OSL based neutron dosimetry	173-208
5.1. <i>Introduction</i>	174
5.2. <i>Neutrons</i>	174
5.2.1. <i>Classification of Neutrons</i>	175
5.2.2. <i>Interaction of Neutrons with Matter</i>	175
5.2.3. <i>Neutron Detection</i>	178
5.2.4. <i>Health hazards and Need for neutron dosimetry</i>	179
5.3. <i>Studies on neutron irradiated pure α-Al₂O₃ single crystals</i>	181
5.3.1. <i>Experimental</i>	182

5.3.2. <i>Results</i>	183
5.3.2.1. <i>OA Studies</i>	183
5.3.2.2. <i>PL Studies</i>	185
5.3.2.3. <i>TL Studies</i>	186
5.3.2.4. <i>CW-OSL Studies</i>	188
5.3.3. <i>Conclusion</i>	189
5.4. Development of Neutron-Sensitive OSL Detectors	190
<hr/>	
5.4.1. <i>Sample preparation</i>	192
5.4.2. <i>Irradiations</i>	192
5.4.3. <i>OSL measurements</i>	197
5.4.4. <i>Data analysis</i>	197
5.4.5. <i>Results</i>	199
5.4.6. <i>Conclusion</i>	205
Chapter 6: TL and OSL Investigations on Lithium Borate Single Crystals	209-244
6.1. Introduction	210
6.2. Investigations on LBO:Cu Single Crystals	212
6.2.1. <i>Experimental</i>	213
6.2.1.1. <i>Crystal growth</i>	213
6.2.1.2. <i>Photoluminescence measurement</i>	214
6.2.1.3. <i>Thermoluminescence measurement</i>	214
6.2.3. <i>Results</i>	215
6.2.3.1. <i>PL Studies</i>	216
6.2.3.2. <i>TL Analysis</i>	217
6.2.3.3. <i>Dose response and Minimum Detectable Dose</i>	223
6.2.3.4. <i>Effect of co-doping Indium in LBO:Cu crystals</i>	224
6.2.4. <i>Conclusion</i>	225
6.3. Investigations on LBO:Cu, Ag single crystals	226
6.3.1. <i>Experimental</i>	226

6.3.2. <i>Results</i>	227
6.3.2.1. <i>Photo-luminescence Studies</i>	227
6.3.2.2. <i>TL Analysis</i>	229
6.3.2.3. <i>OSL Studies</i>	233
6.3.2.3a. <i>Qualitative correlation of OSL & TL</i>	233
6.3.2.3b. <i>Analysis of faster component of CW-OSL</i>	236
6.3.2.3c. <i>Optimization of CW-OSL stimulation time</i>	237
6.3.2.4. <i>OSL readout time versus Residual TL</i>	238
6.3.2.5. <i>Minimum Detectable dose (MDD)</i>	239
6.3.2.6. <i>LM-OSL Studies</i>	240
6.3.2.7. <i>Elevated temperature CW-OSL studies</i>	240
6.3.3. <i>Conclusion</i>	241
Chapter 7: Conclusion	245-252
7.1. Summary of the work	246
7.2. Challenges and scope of future studies	253

**SYNOPSIS OF THE THESIS TO BE SUBMITTED TO THE HOMI BHABHA
NATIONAL INSTITUTE FOR THE DEGREE OF DOCTOR OF PHILOSOPHY IN
PHYSICAL SCIENCES**



Name of the Candidate : Narender Singh Rawat

Name of the Guide : Prof. (Dr.) S. K. Gupta
Physical Sciences, Homi Bhabha National Institute,
Mumbai - 400094, INDIA

Registration Number : PHYS 01200704029

Date of the registration : 1st January, 2008

Title of the thesis : “Characterization of TL/OSL phosphors and study of photo ionization cross-sections of metastable trap levels- An Experimental and Theoretical approach”

Place of the Research Work : Radiation Safety Systems Division, Bhabha Atomic Research Centre, Trombay, Mumbai-400085, India.

Signature of the Candidate :

SYNOPSIS

With the advent of technologically advanced and complex facilities like nuclear reactors, Large Hadron Collider, accelerator driven subcritical systems, and synchrotrons; the impact of radiation associated with these facilities and monitoring of personnel involved in the facilities has become a strenuous and stringent requirement. The practitioners of radiation dosimetry face new and unconventional challenges demanding efficient solutions for monitoring of the personnel working in these facilities. Luminescence dosimetry using **thermoluminescence** (TL) and **optically stimulated luminescence** (OSL) of various phosphors has emerged and proved to be the most viable solution owing to its inherent operational simplicity and cost effectiveness. The luminescence in solids is quite old and highly applied branch of science that covers spectroscopy of atoms / molecules, structural analysis of materials, and lattice defects.

The use of luminescence from solids as a tool to quantify ionizing radiation had gained momentum after the discovery of X-rays by Roentgen (1895) and subsequent discovery of natural radioactivity in uranium salt by Becquerel (1896). However, the possible use of luminescence that stems from the temperature dependent nature of phosphorescence was explored systematically for the first time by Randall and Wilkins [1] in 1945 and is termed as **Thermally Stimulated Luminescence (TSL)** or **Thermoluminescence (TL)**.

The phenomenon of TL is mostly observed in insulators/semiconductors having impurity and defect induced meta-stable trap levels in their forbidden band gap. When exposed to ionizing radiation at normal temperature, the electrons and holes are liberated and migrate throughout the solid and subsequently get trapped at various meta-stable trap levels. The thermal stimulation (at temperatures higher than that of its irradiation) of the trapped charges leads to release of one type of charge carriers (e.g. electrons) to respective de-localized band and their

subsequent recombination with trapped charges of opposite polarity giving rise to luminescence, known as TL. The plot of TL intensity as function of time gives a TL glow curve and the integrated area under this curve is directly proportional to the absorbed dose (in Gray) due to the ionizing radiation to which the TL material has been subjected to. The usefulness of such TL passive dosimeters for environmental and personnel monitoring; archaeological-geological dating and medical dosimetry of ionizing radiation has been established since last four decades.

In recent years, optically stimulated luminescence (OSL) has successfully emerged as an alternative to TL in radiation dosimetry. OSL is the transient luminescence observed during illumination of crystalline insulators or semiconductors that were previously excited, typically by exposure to ionizing radiation. During the OSL process, light stimulates the release of trapped electrons and holes, resulting in electron/hole recombination and excitation of luminescence centers in the crystal. OSL consists of the photons emitted when these excited luminescence centers decay to the ground state. Thus OSL phenomenon is similar to TL: the difference being excitation with light instead of heat.

Technological advances pertaining to stable, nearly monochromatic and intense solid state light sources such as LED and Laser Diodes have led to the development of simple, economical, robust and compact OSL systems for various passive and fiber optics based online dosimetric applications. OSL is a versatile technique with some inherent advantages like fast readout, option of multiple readouts, optical resetting of trapped charges and freedom from thermal quenching resulting in paradigm shift from TL to OSL dosimetry worldwide.

Not all of the numerous known TL and OSL phosphors are suitable for radiation dosimetry. For dosimetric applications, a phosphor should have the attributes like simple glow curve, with

the main dosimetric peak at about ~ 200 °C; high sensitivity, which consists of both high efficiency of light emission and low detection threshold, high resistance against environmental factors as humidity and long term stability of the stored information at room temperature (negligible fading in dark at RT); negligible dependence of the TL/OSL emission on the photon energy; good linearity of the signal in the useful range of radiation dose and **effective atomic number (Z_{eff})** close to that of the biological tissue (tissue equivalence). In addition, for an OSL phosphor the photo-ionization cross-section for stimulation wavelength should be large enough to enable one to extract the luminescence signal in minimum time i.e. the feasibility of fast readout and hence large throughput. Since, only very few materials are found to possess most of the above features, the quest for the highly sensitive and eligible phosphors continues.

In present studies new technique (by incorporating certain modifications initial rise method) for the kinetic analysis of TL glow curve has been developed. Two of the important phosphor materials that match most of the above requirements are anion deficient $\alpha\text{-Al}_2\text{O}_3\text{:C}$ and Cu/Ag doped $\text{Li}_2\text{B}_4\text{O}_7$ (Lithium borate, LBO) have been investigated. $\alpha\text{-Al}_2\text{O}_3\text{:C}$ is one of the most important ultra sensitive OSL material with TL sensitivity of 40-60 times of TLD 100; with effective atomic number ($Z_{\text{eff}} \approx 10.2$) relatively close to that of tissue ($Z_{\text{eff}} \approx 7.4$). LBO is important due to its tissue equivalence with $Z_{\text{eff}} \sim 7.3$ (consequently it has very low photon energy dependence) and dose linearity over a wide dynamic range.

Extensive characterization of $\alpha\text{-Al}_2\text{O}_3\text{:C}$ prepared by two different indigenous techniques (post growth thermal impurification technique [2] and melt processing [3]) developed earlier in our Laboratory and some commercial samples has been carried out. In particular, detailed studies on photo-ionization cross section (a vital and necessary parameter for OSL applications) and its temperature dependence were carried out. Further, investigations on melt processed

polycrystalline α - $\text{Al}_2\text{O}_3:\text{C}$ have been performed to explore its feasibility as an OSL based neutron dosimeter.

Single crystals of $\text{Li}_2\text{B}_4\text{O}_7:\text{Cu}$ and $\text{Li}_2\text{B}_4\text{O}_7:\text{Cu,Ag}$ grown using Czochralski technique, were extensively investigated in OSL domain for the first time. Correlation of OSL and TL response has been carried out. The role of sensitizer and activator in $\text{Li}_2\text{B}_4\text{O}_7:\text{Cu,Ag}$ has been studied in detail using different techniques including Optical Absorption (OA), photoluminescence (PL) and life time measurement. This material system being highly tissue equivalent, offers its suitability for various dosimetric applications, including personnel and clinical.

Entire work has three facets namely: a) Formulation of a novel initial rise technique that enables easy and direct measurement of various TL parameters independent of each other. Normally variable heating rate and condition of maxima of TL peak along with Chen's method have been used for this purpose. The result obtained from variable heating rate method depends on the precision with which temperature of TL maxima is determined and is therefore prone to errors. Similarly, several other techniques require prior information of one or more TL parameters for the assessment of other, thereby leading to the propagation of errors b) Investigations of two important phosphors ($\text{Al}_2\text{O}_3:\text{C}$ and $\text{Li}_2\text{B}_4\text{O}_7$) from dosimetric point of view, in which $\text{Li}_2\text{B}_4\text{O}_7:\text{Cu,Ag}$ has first time been explored for its use as an OSL phosphor and is shown to have promising properties and potential. Comprehensive TL and OSL analysis of $\text{Al}_2\text{O}_3:\text{C}$ was carried out that has given thrust to the indigenous development protocol for large scale synthesis of this material. In addition, the feasibility of using indigenously developed $\text{Al}_2\text{O}_3:\text{C}$ as a neutron dosimeter was demonstrated and c) Determination of temperature and dose dependence of photo-ionization cross-section in $\text{Al}_2\text{O}_3:\text{C}$ that has enhanced the

understanding of defects at microscopic and as well as macroscopic level with several benefits from operational viewpoint.

The research work carried out and compiled here in the form of thesis has been published in peer reviewed journals [Ref.12-20]. An overview of the thesis contents grouped under seven chapters is as follows.

Chapter 1. Introduction

The chapter begins with an introduction of Luminescence phenomenon including details specific to Thermally Stimulated Luminescence (TL) and Optically Stimulated Luminescence (OSL) [4-5]. An overview of popular TL/OSL phosphor materials (viz. fluorides, borates and oxides) used in radiation dosimetry is presented [6]. Two of the materials that are subject of present study i.e. α -Al₂O₃:C and Li₂B₄O₇ have been discussed in detail.

Chapter 2. Methods of TL/OSL analysis and defect characterization techniques

The chapter begins with description of various methods for TL/OSL characterization and kinetic analysis of phosphors that are used in the present work [4-5]. Other techniques used for material characterization and microscopic investigation of defects like optical absorption [7], photoluminescence, electron spin resonance [8], and positron annihilation spectroscopy [9-10] used during the course of this work are also discussed [11-12].

Chapter 3. Formulation of Initial Rise method for TL kinetic analysis – theoretical and experimental approach

This chapter describes the formalism of a novel technique for kinetic analysis of TL phosphors based on incorporation of modifications in already existing initial rise method. Although this method has general applicability, for its experimental validation, it has been tested on CaSO₄:

Dy [13]. Theoretical approach and numerical simulations carried out to devise this technique have been presented. Advantages of the technique along with its limitations are also addressed.

Chapter 4: Characterization and study of temperature dependence of photo-ionization cross section in Al₂O₃:C

TL and OSL characterization of Al₂O₃:C material prepared by a recently post growth thermal impurification (PGTI) technique has been carried out and it has been investigated for dose dependence of photo-ionization cross-section [14]. A model has been proposed to explain measured dose dependence of Photo-ionization cross section. Multiple OSL peaks of Al₂O₃:C have been resolved using a recently reported non-linear light modulation based optically stimulated luminescence (NL-OSL) technique for the first time [15]. Thermal assistance energy associated with photo-ionization cross-section of Al₂O₃:C has been determined by simultaneous stimulation with continuous 470 nm light and linearly increasing temperature (a process termed as Thermally Assisted (TA)-OSL) as well under isothermal conditions. Theoretical modeling has also been carried out for the observed TA-OSL. The value of thermal assistance energy (E_A) and temperature independent pre-exponential factor of photo-ionization cross-section were found to ~ 0.03 eV and ~ 4.24 x 10¹⁸ cm² respectively [16]. Temperature dependence of cross section showed Arrhenius nature.

Chapter 5: Application of Al₂O₃: C for OSL based neutron dosimetry

The chapter illustrates the neutron response of detectors prepared using Al₂O₃:C phosphor. This phosphor mixed with neutron converters was studied in mono-energetic neutron fields. The detector pellets were arranged in two different pairs: Al₂O₃:C + ⁶LiF/Al₂O₃:C + ⁷LiF and Al₂O₃:C + high density polyethylene/Al₂O₃:C + Teflon, for neutron dosimetry using albedo and

recoil proton techniques [17]. The optically stimulated luminescence response of the $\text{Al}_2\text{O}_3:\text{C} + {}^{6,7}\text{LiF}$ dosimeter to radiation from a ${}^{252}\text{Cf}$ source was 0.21, in terms of personal dose equivalent $\text{Hp}(10)$ and relative to radiation from a ${}^{137}\text{Cs}$ source. The results pertaining to $\text{Hp}(10)$ response of the $\text{Al}_2\text{O}_3:\text{C} + {}^{6,7}\text{LiF}$ dosimeters with increasing neutron energy and response of the $\text{Al}_2\text{O}_3:\text{C} +$ high-density polyethylene $\text{Al}_2\text{O}_3:\text{C} +$ Teflon dosimeters are presented. The chapter also discusses the investigations of defects in neutron irradiated pure $\alpha\text{-Al}_2\text{O}_3$ single crystals [18].

Chapter 6: TL and OSL Investigations on Lithium Borate Single Crystals

The LBO being tissue equivalent material is a desirable phosphor that has potential application in various radiation dosimetric applications, particularly in the medical dosimetry. This chapter presents investigations on highly transparent Czochralski grown single crystals of $\text{Li}_2\text{B}_4\text{O}_7$ (LBO) doped with Cu and Cu, Ag [19-20]. The LBO:Cu crystals were studied using photoluminescence, X-ray diffraction (XRD), time resolved fluorescence and thermoluminescence (TL) techniques. These crystals showed a linear TL dose response in the range from 1 mGy to 1 kGy. The TL analysis using variable heating rate method revealed two TL peaks with first order kinetics. The TL sensitivity of these crystals was found to be ~ 4 times that of TLD-100. In addition, Ag and Cu co-doped $\text{Li}_2\text{B}_4\text{O}_7$ crystals were characterized. Three TL peaks with trap depths of 0.77, 1.25 and 1.34 eV and corresponding frequency factors of 1.6×10^9 , 1.3×10^{13} and $6.8 \times 10^{11} \text{s}^{-1}$ were determined. Continuous wave optically stimulated luminescence (CW-OSL) studies of LBO:Cu,Ag were carried out for the first time. The qualitative correlation between TL peaks and CW-OSL response was established.

Chapter 7: Conclusion

Summary of the thesis and scope of future work in the field has been presented in this chapter. Anion deficient $\text{Al}_2\text{O}_3:\text{C}$ and LBO single crystals have been shown to be useful for TL and OSL based luminescence radiation dosimetry. Carbon doped alumina possesses excellent OSL response for ionizing radiations like beta, X-rays, gamma and heavy charged particle. But the lacuna of this material is that it is insensitive towards neutrons that prevent its application in neutron fields. This is because the constituent elements of this material do not have cross-section for neutron interaction. In fact neutron sensitivity of $\text{Al}_2\text{O}_3:\text{C}$ for neutron energies between 0.3 Mev and 6 MeV is zero within the experimental uncertainties. The studies carried out have established the feasibility of indigenously developed $\text{Al}_2\text{O}_3:\text{C}$ mixed with neutron converters for its application in neutron dosimetry. A highlight of the present study is extension of initial rise method that has facilitated the characterization of phosphor materials in TL domain as well as offered enhanced understanding of observed phenomena. It is simple to apply and the essence of this technique lies in the fact that all the TL parameters can be determined independent of each other which in turn reduces the scope of error associated with experimental determination of these parameters. Temperature dependence of photo-ionization cross-section and determination of thermally assisted energy level in OSL has revealed wealth of information as it is now possible to have an estimate of vibrational energy level of defects. Thermally assisted OSL is found to improve signal to noise ratio and thereby reduction in detection threshold of dose. The chapter concludes with some of the aspects of the studied materials that are yet to be answered/explored, setting the tune for the future work.

References

1. J.T. Randall, M.H.F. Wilkins, *Proc. R. Soc. A* 184 (1945) 366
2. M.S. Kulkarnia, D.R. Mishra, K.P. Muthe, Ajay Singh, M. Roy, S.K. Gupta, S. Kannan. *Radiation Measurements* 39 (2005) 277 – 282
3. K.P. Muthe, M.S. Kulkarni, N.S. Rawat, D.R. Mishra, B.C. Bhatt, Ajay Singh, S.K. Gupta. *J. Luminescence* 128 (2008) 445–450
4. S.W.S. McKeever, *Thermoluminescence of Solids*, Cambridge University Press, Cambridge (1985)
5. L. Bøtter-Jensen, S.W.S. McKeever, S.W.S. and A.G. Wintle, *Optically Stimulated Luminescence Dosimetry*, Elsevier, Amsterdam (2003)
6. S.W.S. McKeever, M. Moscovitch, Peter David Townsend, *Thermoluminescence dosimetry materials: properties and uses*, Nuclear Technology Publishing (1995)
7. J. Garcia Sole , Daniel Jaque , L. E. Bausa, *An Introduction to the Optical Spectroscopy of Inorganic Solids*, John Wiley & Sons Ltd. (2005)
8. Colin Banwell, Elaine McCash, *Fundamentals of Molecular Spectroscopy* Tata Mcgraw Hill Education Private Limited (2001)
9. R. Krause-Rehberg, H.S. Leipner, *Positron Annihilation in Semiconductors*, Springer 1998
10. K P Muthe, K Sudarshan, P K Pujari, M S Kulkarni, N S Rawat, B C Bhatt and S K Gupta. *J. Phys. D: Appl. Phys.* **42** (2009) 105405 (5pp)
11. A.K. Bakshi, Bhushan Dhabekar, **N.S. Rawat**, S.G. Singh, V.J. Joshi, Vijay Kumar. *Nuclear Instruments and Methods in Physics Research B* 267 (2009) 548–553
12. E. Alagu Raja, Sanjeev Menon, Bhushan Dhabekar, **N.S. Rawat**, T.K. Gundu Rao. *J. Luminescence* 129 (2009) 829-835

13. **N.S.Rawat**, M.S.Kulkarni, D.R.Mishra, B.C.Bhatt, C.M.Sunta, S.K.Gupta, D.N. Sharma. *Nuclear Instruments and Methods in Physics Research B* 267 (2009) 3475–3479
14. **N S Rawat**, M S Kulkarni, D R Mishra, K P Muthe and S K Gupta. *Proceedings of National Conference on Luminescence and its Applications (NCLA-2010)*
15. D.R. Mishra, M.S . Kulkarni, **N.S. Rawat**, Anuj Soni, B.C. Bhatt, D.N. Sharma. *Radiation Measurements* 46 (2011) 1462-1468
16. D.R. Mishra, Anuj Soni, **N.S. Rawat**, M.S. Kulkarni , B.C. Bhatt, D.N. Sharma. *Radiation Measurements* 46 (2011) 635-642
17. M.S. Kulkarni , M. Luszik-Bhadra, R. Behrens, K.P. Muthe, **N.S. Rawat** , S.K. Gupta, D.N. Sharma. *Nuclear Instruments and Methods in Physics Research B* 269 (2011) 1465–1470
18. M.S. Kulkarni , **N.S. Rawat** , S.V. Thakare , K.C. Jagadeesan, D.R. Mishra, K.P. Muthe, B.C. Bhatt, S.K. Gupta , D.N. Sharma. *Radiation Measurements* 46 (2011) 1704-1707
19. Babita Tiwari, **N.S.Rawat**, D.G.Desai, S.G.Singh, M.Tyagi, Ratna P, S.C.Gadkari, M.S.Kulkarni. *J. Luminescence* 130 (2010) 2076-2083
20. **N.S.Rawat**, M.S.Kulkarni, M. Tyagi, Ratna P, D.R.Mishra, S.G.Singh, B.Tiwari, A. Soni, S.C.Gadkari, S.K.Gupta. *J. Luminescence* 132 (2012) 1969–1975

LIST OF FIGURES

FIGURES	Page No.
1.1. Joblanski diagram to depict a) fluorescence and (b) phosphorescence	8
1.1. Different stages of OSL process	15
1.2. Variation in CW-OSL intensity curve with change in order of kinetics	21
1.3. Variation of LM-OSL intensity under first and general order kinetics	25
1.4. a)Crystal Structure of α -Al ₂ O ₃ b) Schematic representation of the α -Al ₂ O ₃ structure and the model of F ⁺ center	35-36
1.5. The schematic presentation of PGTI process for synthesis of α -Al ₂ O ₃ : C	43
1.6. The vacuum furnace used for PGTI samples	44
1.7. Electron gun evaporation system	46
1.8. Inductively heated vacuum melting system	47
2.1. Diffusion of atoms	61
2.2. Vacancy diffusion	61
2.3. Kirkendall Effect	62
2.4. Configurational coordinate diagram for mechanism of thermal quenching	67
2.5. Quantum efficiency $\eta(T)$ as a function of temperature	69
2.6. The integrated emission intensity of Er ³⁺ ions with increase in concentration	70
2.7. Luminescence concentration quenching mechanism	71
2.8. Possible electronic transitions following the optical stimulation of electrons from an “optically active” trapping center.	76
2.9. Schematic diagrams of a spectrophotometer	82
2.10. A schematic diagram for measuring photoluminescence spectra.	84
2.11. The schematic temporal decay of luminescence	87
2.12. Variation of magnetic field resulting in splitting and divergence of energies of the two spin states of an unpaired electron	89
2.13. Block diagram of a typical EPR spectrometer	92
2.14. Mechanism of PAS	94
2.15. Scheme of the positron lifetime experiment in fast–fast coincidence	95

2.16.	XRD of powder MgAl ₂ O ₄ (as-prepared) and standard XRD pattern	98
2.17.	PL excitation and emission spectrum of MgAl ₂ O ₄ :Tb ³⁺	100
2.18.	TL glow curve of Tb ³⁺ doped MgAl ₂ O ₄	101
2.19.	TL emission spectrum of Tb ³⁺ doped MgAl ₂ O ₄	101
2.20.	(a) CW-OSL curve of MgAl ₂ O ₄ :Tb ³⁺ (b) Exponential fit of OSL decay curve (c) Variation of OSL intensity with annealing temperature for MgAl ₂ O ₄ :Tb ³⁺	102
2.21.	ESR spectra measured at room temperature (a) undoped (b)Tb ³⁺ doped.	104
2.22.	ESR spectra of MgAl ₂ O ₄ after pulse annealing at various temperatures	106
2.23.	Model for 120 and 220 °C TL peak in MgAl ₂ O ₄ :Tb ³⁺	108
3.1.	Numerically simulated TL curves with various input parameters	120
3.2.	Initial rise plots for TL curves in fig. 3.1 for various order of kinetic	121
3.3.	230° C TL glow peak of CaSO ₄ : Dy samples.	122
3.4.	Initial rise plots of 230°C TL peak of CaSO ₄ : Dy.	123
4.1.	TL glow curve of developed α-Al ₂ O ₃ :C phosphor for 20mGy dose.	128
4.2.	TL glow curves of α-Al ₂ O ₃ :C and other popular TL phosphors.	129
4.3.	Effect of Process Temperature on the TL response of α-Al ₂ O ₃ :C.	130
4.4.	Normalized TL response of commercial and processed α-Al ₂ O ₃ :C	130
4.5.	Effect of Process Temperature on the OSL response of α-Al ₂ O ₃ :C.	131
4.6.	CW-OSL response of the Developed and Commercial α-Al ₂ O ₃ : C samples	132
4.7.	Normalized CW-OSL response of Developed and Commercial α-Al ₂ O ₃ : C	132
4.8.	CW-OSL response of α-Al ₂ O ₃ :C sample for ⁹⁰ Sr/ ⁹⁰ Y β dose	132
4.9.	Optical Absorption of developed α-Al ₂ O ₃ :C	134
4.10.	Integrated CW-OSL response of developed α-Al ₂ O ₃ :C for same intensity exposure to 400 nm to 190 nm wavelength of light.	134
4.11.	Photo-Luminescence spectra of F and F ⁺ centers in Al ₂ O ₃ :C.	135
4.12.	Experimentally observed and fitted CW-OSL curves for various doses	139
4.13.	CW-OSL decay time and cross section w.r.t. to absorbed dose in Al ₂ O ₃ :C	140
4.14.	Band gap diagram showing components of cross-section in Al ₂ O ₃ :C	141
4.15.	Configuration coordinate diagram of trap level and conduction band.	143

4.16.	Numerically simulated TA-OSL signal vs. time for various order of kinetic	148
4.17.	Numerically simulated TA-OSL signal vs. time plot for various heating rates	148
4.18.	Numerically simulated TA-OSL signal vs time plot for various CW stimulation intensity	148
4.19.	(A)TA-OSL signal recoded with CW stimulation and linear heating of 3K/s (B) CW-OSL recorded at 52°C with $\phi_0 = 6.2 \text{ mW/cm}^2$	148
4.20.	Experimentally obtained TA-OSL curves for various stimulation intensities	151
4.21.	Experimentally obtained TA-OSL curves for various heating rates	151
4.22.	Log of TA-OSL vs. 1/kT plot	153
4.23.	Optical excitation vs. stimulation flux at room temperature for 470 nm of light slope of above line gives the value of photo-ionization cross-section at RT	154
4.24.	a) The CW-OSL response at various elevated temperature b) Variation of excitation rate for 52mW/cm ² with 1/ kT gives slope as E_A and intercept as σ_0 .	156
4.25.	Numerically simulated TA-OSL curve a) for various CW stimulation intensities and fixed heating b) for various heating rates and fixed CW intensity	156
4.26.	Using experimentally determined value $E_A=0.03 \text{ eV}$, $\sigma_0 = 4.24 \times 10^{-18} \text{ cm}^2$, $E=1.1 \text{ eV}$ and $S= 2.5 \times 10^{11} \text{ s}^{-1}$ numerical simulated curves for $\alpha\text{-Al}_2\text{O}_3\text{: C}$	157
4.27.	Variation of stimulation power at sample position with linear increase in LED forward bias current for various values of TBP(l).	164
4.28.	Comparison of linear LED forward bias current I_{LED} profile with optical stimulation intensity (P) recorded at sample position by the photo diode	165
4.29.	Background count due to Stimulation light detected by PMT for $l=1$	167
4.30.	Variation of scattering background signal recorded in PMT for various l	167
4.31.	Theoretical and experimental signal to noise ratio $A_{\text{LM}} / A_{\text{NL}}$ with various value of “ l ”, for fixed final intensity and fixed time	167
4.32.	NL-OSL curves recorded for various l , but fixed final intensity and time	167
5.1.	OA spectra of irradiated $\alpha\text{-Al}_2\text{O}_3$ crystals for various thermal neutron fluence	184
5.2.	OA for thermal neutron fluence of 10^{18} n/cm^2 with a Gaussian fit	184
5.3.	Emission spectra of F center in $\alpha\text{-Al}_2\text{O}_3$ crystals irradiated to thermal neutron fluence of 10^{18} n/cm^2	185

5.4.	Excitation and emission spectra for F^+ centers in α - Al_2O_3 crystals irradiated to thermal neutron fluence of 10^{18} n/cm ² .	185
5.5.	TL emission spectrum of Al_2O_3 crystals for 10^{18} n/cm ² thermal neutron fluence	187
5.6.	TL glow curves for α - Al_2O_3 crystals irradiated to reactor neutron fluence in the range 10^{14} - 10^{18} n/cm ²	187
5.7.	Comparison of TL glow curves of α - Al_2O_3 single crystals after (a) irradiation to thermal neutron fluence of 10^{17} n/cm ² and (b) gamma dose of 47.5 kGy	187
5.8.	CW-OSL response of α - Al_2O_3 crystals for various thermal neutron fluence	188
5.9.	Normalised OSL response of α - Al_2O_3 crystals for various fluence	188
5.10.	Facilities at PTB Germany and layout of neutron facility	193
5.11.	Experimental Hall	194
5.12.	Integrated OSL signal of $Al_2O_3:C$ mixed with 6LiF , 7LiF , HDPE and Teflon	199
5.13.	CW-OSL signal recorded on α - $Al_2O_3:C$ mixed with 6LiF , 7LiF , HDPE and Teflon and irradiated on an ISO water slab phantom to 24 keV neutrons	200
5.14.	$H_p(10)_{meas,n}$ of α - $Al_2O_3:C$ mixed with $^{6,7}LiF$ and irradiated on an ISO water slab phantom with ^{252}Cf neutrons as a function of the reference personal dose equivalent $H_p(10)_n$	203
5.15.	$H_p(10)_{meas,n}$ of α - $Al_2O_3:C$ mixed with HDPE/Teflon and irradiated on an ISO water slab phantom with ^{252}Cf neutrons as a function of reference personal dose equivalent $H_p(10)_n$	203
5.16.	$H_p(10)$ response (= $H_p(10)_{meas,n} / H_p(10)$) of the $Al_2O_3:C+^{6,7}LiF$ dosimeters for various monoenergetic neutron energies	204
5.17.	Comparison of the $H_p(10)$ response ($H_p(10)_{meas,n} / H_p(10)$) as a function of neutron energy of commercially available (Landauer) and BARC developed α - $Al_2O_3:C$ material mixed with HDPE/Teflon in a 1:0.5 weight ratio irradiated on an ISO water slab phantom	205
5.18.	Comparison of the $H_p(10)$ response (= $H_p(10)_{meas,n} / H_p(10)$) as a function of neutron energy of commercial α - $Al_2O_3:C$ material mixed with HDPE/Teflon in a 1:0.5 weight proportion for free-in-air and on-phantom irradiation	205

6.1.	Czochralski grown single crystals of (a) LBO:Cu, (b) LBO:Cu,Ag	215
6.2.	The XRD pattern recorded for a powdered sample made using $\text{Li}_2\text{B}_4\text{O}_7$:Cu single crystal	216
6.3.	Transmission spectrum recorded for a polished plate of a $\text{Li}_2\text{B}_4\text{O}_7$:Cu crystal	216
6.4.	Excitation and emission spectra of a Cu-doped LBO crystal	217
6.5.	Luminescence decay curve and difference between the fitted and measured data of a Cu-doped LBO crystal	217
6.6.	TL Glow curves recorded on LBO:Cu for various absorbed	218
6.7.	TL emission spectrum of a $\text{Li}_2\text{B}_4\text{O}_7$:Cu single crystal (recorded at 483 K)	218
6.8.	Normalized TL glow peaks of LBO: Cu for an absorbed dose of 100 mGy	220
6.9.	a) TL glow curves of LBO:Cu at different heating rates for an absorbed dose of 100 mGy b) Dose vs. TL response of TL peak 2 of LBO:Cu single crystals	222
6.10.	TL glow curve of LBO:Cu and LBO:Cu, In	224
6.11.	PL spectra of LBO:Cu,Ag	228
6.12.	TL glow curve of LBO: Cu, Ag obtained at a heating rate of 1 K/s, analyzed into its three individual glow peaks deconvoluted using Computerized Curve Deconvolution (CCD) procedure for general order kinetics	230
6.13.	Experimentally obtained TL peak 3 for LBO:Cu,Ag for an absorbed dose of 300 mGy recorded at a heating rate of 1K/s	231
6.14.	CW-OSL curves of LBO: Cu, Ag for an absorbed dose of 1.38 Gy	235
6.15.	CW-OSL curves for different cases (a) Absolute and (b) Normalized	236
6.16.	Integrated CW-OSL signal for various illumination times and the subsequent residual TL(R-TL) signal (obtained after CW-OSL readout) by readout up to 320°C	238
6.17.	Residual TL glow curves obtained after blue light stimulation of 0 to 2000s	239
6.18.	LM-OSL curve for LBO: Cu, Ag for an absorbed dose of 2.2 Gy	241
6.19.	CW-OSL response of LBO: Cu, Ag at various elevated temperatures	241

LIST OF TABLES

TABLE	Page No.
1.1. General Characteristics of Some Commercially Available TLDs	32
1.2. Comparison of LBO based TL phosphors prepared using different methods	48
2.1. Field for resonance for a $g = 2$ sample at various microwave frequencies	90
3.1. Calculated values of E, b and s for different trap occupancies for $b = 1$	118
3.2. Calculated values of E, b, s and s' for different trap occupancies for $b = 1.5$	119
3.3. Calculated values of E, b, s and s' for different trap occupancies for $b = 2$	119
3.4. Experimentally calculated TL parameters for 230°C TL peak of CaSO ₄ : Dy	123
4.1. TL Sensitivity Comparison of different phosphors.	129
4.2. Experimentally determined OSL decay time; and slow, intermediate & fast components of photo-ionization cross-section.	138
5.1. Maximum Fraction of Energy Lost, Q_{\max}/E_n , by neutron in Single Elastic Collision with Various Nuclei.	177
5.2. Main isotopes used as neutron converters in luminescence detectors	178
5.3. Accelerator produced mono-energetic neutrons at PTB, Germany	195
5.4. Types of detector used in the study.	196
5.5. Dose reading due to neutron- and photon-sensitive discs	201
6.1. Kinetic analysis of TL peaks 1 and 2 of LBO: Cu	220
6.2. TL parameters for LBO: Cu using the variable heating rate method	222
6.3. Sensitivity comparison of LBO:Cu with other commercially TL phosphors	223
6.4. Kinetic analysis of TL Peaks 1, 2 and 3 for LBO: Cu, Ag	230
6.5. Kinetic analysis of Peak 3	232
6.6. CW-OSL parameters of LBO: Cu, Ag for different cases	236

LIST OF PUBLICATIONS

Papers in international/refereed Journals (included in thesis)

1. **N. S. Rawat**, M. S. Kulkarni, D. R. Mishra, B. C. Bhatt, C. M. Sunta, S. K. Gupta, D.N. Sharma. Use of Initial Rise Method to analyze a General Order Kinetic Thermoluminescence Glow Curve. *Nuclear Instruments and Methods in Physics Research B* 267 (2009) 3475–3479
2. E. Alagu Raja, Sanjeev Menon, Bhushan Dhabekar, **N.S. Rawat**, T.K. Gundu Rao. Investigation of defect centers responsible for TL/OSL in $\text{MgAl}_2\text{O}_4:\text{Tb}^{3+}$. *J. Luminescence*. 129 (2009) 829-835
3. Babita Tiwari, **N. S. Rawat**, D.G.Desai, S.G.Singh, M.Tyagi, Ratna P, S.C.Gadkari, M.S.Kulkarni. Thermoluminescence Studies on Cu-doped $\text{Li}_2\text{B}_4\text{O}_7$ Single Crystals. *J. Luminescence* 130 (2010) 2076-2083
4. D.R. Mishra, Anuj Soni, **N. S. Rawat**, M.S. Kulkarni, B.C. Bhatt, D.N. Sharma. Method of measuring thermal assistance energy associated with OSL traps in $\alpha\text{-Al}_2\text{O}_3:\text{C}$ phosphor. *Radiation Measurements* 46 (2011) 635-642
5. D.R. Mishra, M.S. Kulkarni, **N.S. Rawat**, Anuj Soni, B.C. Bhatt, D.N. Sharma. Preliminary non-linear light modulation OSL studies using $\alpha\text{-Al}_2\text{O}_3:\text{C}$. *Radiation Measurements* 46 (2011) 1462-1468
6. **N.S. Rawat**, M.S. Kulkarni, D.G. Desai, B. Tiwari, P. Ratna, S. C. Gadkari. Thermoluminescence studies of copper and indium doped $\text{Li}_2\text{B}_4\text{O}_7$ single crystals. *Radiation Protection and Environment*. 34 (2011) 32-33
7. M.S. Kulkarni, M. Luszik-Bhadra, R. Behrens, K.P. Muthe, **N.S. Rawat**, S.K. Gupta, D.N. Sharma. Studies on new neutron-sensitive dosimeters using an optically stimulated luminescence technique. *Nuclear Instruments and Methods in Physics Research B* 269 (2011) 1465–1470+
8. M.S. Kulkarni, **N.S. Rawat**, S.V. Thakare, K.C. Jagadeesan, D.R. Mishra, K.P. Muthe, B.C. Bhatt, S.K. Gupta, D.N. Sharma. TL and OSL studies on neutron irradiated pure $\alpha\text{-Al}_2\text{O}_3$ single crystals. *Radiation Measurements* 46 (2011) 1704-1707

9. **N.S. Rawat**, M.S. Kulkarni, M. Tyagi, Ratna P, D.R.Mishra, S.G.Singh, B.Tiwari, A. Soni, S.C.Gadkari, S.K.Gupta. TL and OSL studies on lithium borate single crystals doped with Cu and Ag. *J. Luminescence* 132 (2012) 1969–1975

Conference papers (included in thesis)

1. **N. S. Rawat**, D R Mishra, Anuj Soni, K P Muthe, M S Kulkarni and S K Gupta. Order of kinetics considerations in NL-OSL phenomena-Theoretical and Experimental approach. *Proceedings of National Conference on Luminescence and its Applications (NCLA-2009)*
2. **N. S. Rawat**, M S Kulkarni, D R Mishra, K P Muthe and S K Gupta. Dose dependence studies of photo-ionisation cross-section for α -Al₂O₃: C single crystals. *Proceedings of National Conference on Luminescence and its Applications (NCLA-2010)*
3. **N.S.Rawat**, D.R.Mishra, G.D.Patra, S.C.Gadkari, S.K.Gupta, M.S.Kulkarni. Elevated temperature Optically stimulated Luminescence Studies on Cu and Ag doped Li₂B₄O₇ Single Crystals. *IARPNC 2012 held at Mangalore University*

Papers in international/refereed Journals (not included in thesis)

1. K. P. Muthe, K. Sudarshan, P. K. Pujari, M.S. Kulkarni, **N. S. Rawat**, B. C. Bhatt and S K Gupta. Positron annihilation and thermoluminescence studies of thermally induced defects in α -Al₂O₃ single crystals. *J. Phys. D: Appl. Phys.* **42** 105405 (2009).
2. K.P. Muthe, M.S. Kulkarni, **N.S. Rawat**, D.R. Mishra, B.C. Bhatt, Ajay Singh and S.K. Gupta. Melt processing of alumina in graphite ambient for dosimetric applications. *Journal of Luminescence. Vol. 128 (2008) 445-450*

Chapter 1 Introduction

1.1. Motivation and Background

The advances in science and technology have led to the development of complex and sophisticated facilities like Large Hadron Collider, Accelerator driven subcritical systems, synchrotrons and nuclear reactors. The threat perception about radiation associated with these facilities in particular nuclear reactors and other radiological installations has necessitated rigorous monitoring of the doses received by personnel involved in such installations. As a result the practitioners of radiation dosimetry constantly face new and unconventional challenges demanding novel dosimetric solutions. Owing to the inherent operational simplicity and cost effectiveness, luminescence dosimetry based on **Thermoluminescence** (TL) and **Optically Stimulated Luminescence** (OSL) of various phosphors has emerged as the most viable option. OSL in particular has demonstrated its exceptional adaptability in terms of its successful application in diverse fields of ionizing radiation viz. personnel, environmental, medical and space which arises from its versatile nature and its ability to retrieve dose information in active as well as passive mode.

These attractive features have fuelled research related to various phosphors that are usable in OSL based dosimeter like feldspar, MgO:Tb^{3+} , $\text{SiO}_2\text{:Cu}$, BaFBr including $\text{Al}_2\text{O}_3\text{:C}$ and $\text{Li}_2\text{B}_4\text{O}_7$. The present study explores $\text{Al}_2\text{O}_3\text{:C}$ (polycrystalline as well as single crystals) and $\text{Li}_2\text{B}_4\text{O}_7$ (single crystals) along with their attributes that make them suitable for their application in dosimetry. Although these materials are being developed for their application in OSL domain, their characterization in terms of defects responsible for OSL signal and stability of this signal with time can be ascertained by means of TL. Therefore in this research work TL is used as a complimentary technique for an in-depth characterization of the developed OSL material. Photo-ionization cross-section being the key parameter to judge the dosimetric

viability of an OSL phosphor, in this work, its dependence on dose and temperature in case of $\text{Al}_2\text{O}_3:\text{C}$ has been extensively investigated. In addition certain novel experimental techniques which have been specifically devised for TL and OSL characterization of a phosphor have been presented and they constitute an important ingredient of this research work.

1.2. Luminescence Phenomena

There are two principal processes causing light emission: 1) Incandescence i.e. heating an object to a high enough temperature so that the atoms become highly agitated leading to the emission of the light from the object. The emission of this light is explained by Planck's Black Body Emission theory. It was for explaining the incandescence that the quantum nature of light was assumed for the first time by Planck. The light from the tungsten filament lamp or a burning piece of coal comes under this category. In this phenomenon only a small percent of the total energy of an object appears as visible light while most of it is dissipated as heat. 2) Relatively cooler mechanism of light emission is luminescence like in fluorescent lamps.

Luminescence is produced by the selective excitation and subsequent radiative de-excitation of the atomic or molecular energy levels. Notwithstanding this simplicity, only few substances are capable of exhibiting luminescence phenomenon, even though the exciting light is falling on them throughout the day. This apparent contradiction is due to the fact that in solids the light energy absorbed is consumed in increasing the rate and amplitude of the atomic vibrations. Increasing the vibrational energy of the system raises its temperature and reduces the available energy for light emission. The specific characteristic which provides an inorganic solid the luminescent property is the presence of defects in terms of atomic centers whose energy levels are protected from the thermal vibrations of the atoms of the bulk matter. For example the rare-earth ions dispersed in calcium salts and in many other crystals and glasses make very efficient

luminescent centres. The transitions of inner 4f electrons in them are well protected by the outer shell electrons. At times the luminescence centers consist of ionic vacancies. A very important example of this class is the negative ion vacancy in the alkali halides which upon trapping an electron is called F centre. This electron has energy levels akin to hydrogen like atoms. Being much less tightly bound than other electrons of the lattice ions, its energy levels fall within the large band gap of the host lattice. This gives rise to absorption bands in the visible range and the corresponding luminescence.

Following description summarizes the variety of luminescence phenomena observed in natural and synthetic materials arising due to different exciting agents.

Photoluminescence(PL): This is the emission produced by excitation of a defect center with the light photons, the intensity and frequency of which can be controlled by using a specific dopant and its concentration. There are a large variety of organic and inorganic phosphors, which are based on PL e.g. displays employed in road and traffic signals, , laundry whiteners. One of the high technology subjects is LASERS which is again a kind of photoluminescence where emission is coherent.

Cathodoluminescence: When excitation is done by electron beams generated at the electrical cathodes, the emission produced is called cathodoluminescence and finds application in CRT's.

Radioluminescence: When the excitation energy is provided by X-rays or nuclear radiations such as α , β and γ rays, the resulting prompt luminescence is called radioluminescence. Luminescence produced by X-rays has also been named as X-ray excited optical fluorescence (XEOF) to differentiate it from X-ray fluorescence (XRF). In both of these the excitation is by X-rays but the emission is in the form of light photons in the former and X-ray photons in the latter. Both these techniques are very useful in trace analysis of elemental impurities. There is a

large variety of inorganic minerals which show strong luminescence under excitation by X-rays and nuclear particles.

Scintillation: This phenomenon is same as radioluminescence. It is given this name, because it is used as a technique to detect individual light pulses generated by the incidence of each X, or gamma ray photon or a nuclear particle. Such light pulses are called scintillations, since like a spark they are very short lived. Thallium activated sodium iodide is a well known scintillation detector used for gamma ray spectrometry. The intensity of the scintillation (light pulse) is directly proportional to the energy of the incident gamma ray photon (when it is totally absorbed). Anthracene and special type of plastics are used for beta ray measurement. ZnS phosphor is used in alpha ray counting. There are liquid scintillators which are used in low energy beta counting like those from carbon-14 and tritium.

Electroluminescence: This luminescence is produced on the application of electric fields. It is believed that steep voltage gradients are formed across the crystalline boundaries or other crystal defects, when electric fields are applied. Electrons reaching these regions get sufficiently accelerated to attain energy enough to ionize the atoms. In practice, alternating voltages are applied across thin layers of the phosphors. There is another type of electroluminescence known as injection luminescence. In this electrons are injected from an external supply across a semiconductor p-n junction. On applying a DC voltage across the junction, such that the electrons flow to the p region, luminescence is produced by the electron-hole recombination in that region. The light emitting diodes (LED) which are now commonly used as display devices in many scientific instruments are based on this principle.

Chemiluminescence: This luminescence is due to chemical reactions e.g. the oxidation of white phosphorous in air. Some molecules which are formed in high energy electronic states

radiate out the energy as light, while the bulk material remains at ambient temperature. Chemiluminescence is, however not a common accompaniment in chemical reactions, because the amount of energy released even in the exothermic reactions is not sufficient to cause electronic excitation, which needs a couple of eV energy. Lyoluminescence which is caused during the dissolution of certain compounds which have been bombarded by X-rays beforehand is a kind of chemiluminescence. A well known example is the case of X-irradiated NaCl which emits a flash of light when quickly dissolved in water. The electrons trapped in the NaCl lattice centres due to the X-ray- bombardment when freed during dissolution are believed to excite the luminescence.

Bioluminescence: Biochemical reactions inside the cells of the living organisms too can produce electronic excited states of the bio-molecules. Fire flies, glow-worms, some bacteria and fungi and many sea creatures (such as planktons), both near surface and at great depths are the striking examples of luminescence in living beings which arises due to enzymic oxidations. For example, the oxidation of luciferin in the presence of enzyme luciferase is in general responsible for the glow of the firefly, sea crustacean and the luminous bacteria.

Triboluminescence: A large number of inorganic and organic materials subjected to mechanical stress, emit light, which is called triboluminescence also named as mechano-luminescence. It has been observed that all piezo-electric crystals exhibit triboluminescence where the excitation is due to electrification of the cleavages and cracks. The discharge in the surrounding gas also adds to the light produced in such crystals under stress.

Thermoluminescence (TL) and Optically Stimulated Luminescence (OSL), owing to their special relevance to the research work reported, are described at length in separate sections of this chapter.

1.3 Classification of Luminescence

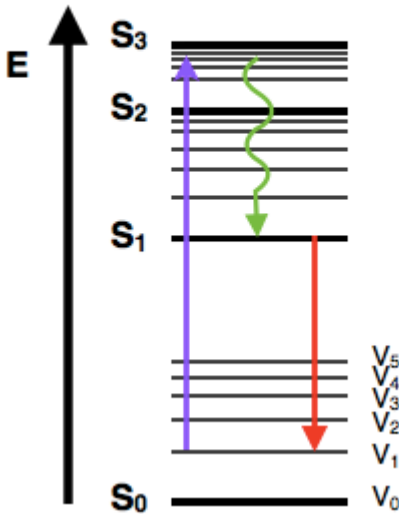
Depending upon the time elapsed between the excitation and light emission, luminescence is termed as fluorescence and phosphorescence.

1.3.1. Fluorescence: It takes place in the time scale of 10^{-9} to 10^{-7} seconds. It is an allowed transition with the electron staying in the same multiplicity. Fluorescence is most often observed between the first excited electron state and the ground state for any particular molecule because at higher energies it is more likely that energy will be dissipated through internal conversion and vibrational relaxation. At the first excited state, fluorescence can compete in regard to timescales with other non-radiative processes. The energy of fluorescent photons is always less than that of the exciting photons. This difference is because energy is lost in internal conversion and vibrational relaxation, where it is transferred away from the electron (refer fig. 1.1(a)). Due to the large number of vibrational levels that can be coupled into the transition between electronic states, measured emission is usually distributed over a range of wavelengths.

1.3.2. Phosphorescence: Another path a molecule may take in the dissipation of energy is called intersystem crossing. In this an electron changes spin multiplicity from an excited singlet state to an excited triplet state. It is indicated by a horizontal, curved arrow from one column to another in fig. 1.1 (b). This is the slowest process in the Jablonski diagram, several orders of magnitude slower than fluorescence. This slow transition is a forbidden transition, that is, should not happen as governed by electronic selection rules. However, by coupling vibrational factors into the selection rules, the transition becomes weakly allowed and able to compete with the time scale of fluorescence. Intersystem crossing leads to several interesting routes back to the ground electronic state. One such direct transition is

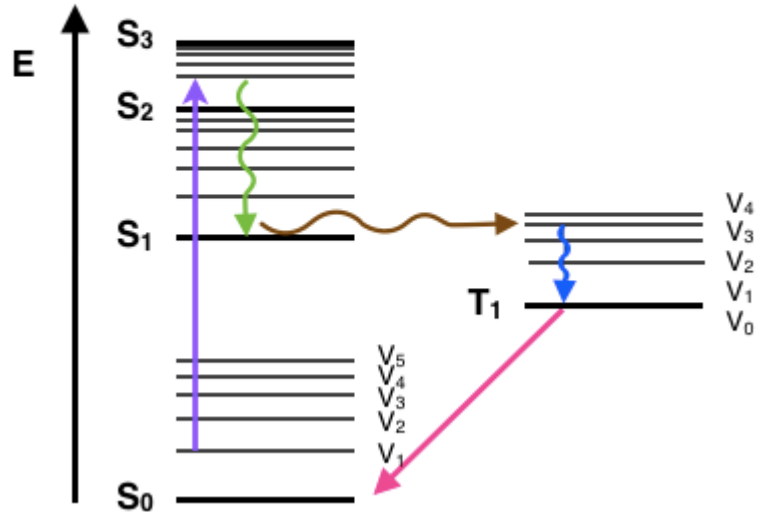
phosphorescence, where a radiative transition from an excited triplet state to a singlet ground state occurs (refer fig. 1.1(b)).

Absorbance, Internal conversion and fluorescence



(a)

A possible phosphorescence pathway: Absorbance, Internal conversion, Intersystem crossing, Vibrational relaxation, Phosphorescence



(b)

Figure 1.1 Joblanski diagram to depict a) Fluorescence and b) Phosphorescence

The delay between excitation and light emission in this type of luminescence can be from minutes to more than 10^{10} years therefore it can be used in solid-state dosimetry for measurement of ionizing radiation. This ability to store the radiation energy is generally ascribed to the presence of activators (i.e. impurity atoms and structural defects) and is central to luminescence based radiation dosimetry which is realized through the phenomena of TL and OSL and described in the following sections.

1.4. Thermally Stimulated Luminescence (TL)

Thermally stimulated luminescence, usually termed thermoluminescence (TL) is the process in which a crystalline insulators or semiconductors previously excited by ionizing radiation emits light while it is being heated. The light emitted is due to the recombination of charges trapped at metastable defect sites within the host lattice, and its intensity is proportional to energy absorbed by the phosphor as a result of its previous exposure to ionizing radiation (ultraviolet, nuclear, cosmic rays). It is as if the excitation energy remains “frozen-in” at a relatively lower temperature in the material until heating stimulates its release in the form of light. As exposure of the material to radiation at room temperature leads to a progressive build-up of trapped electrons proportional to the absorbed dose (holes are trapped in an analogous way) TL material functions as an integrating detector.

The trapping centers facilitate rapid trapping of the electron in the levels between the conduction and valence bands. As long as the energy gap is large enough, the probability that thermal excitation (at room temperature) will excite the electron out of the trap and back into the conduction band is negligible. Normally, charges trapped in the phosphor lattice will remain there for periods ranging from fraction of a second to years or even hundreds of thousands of years at the ambient temperatures. This length of time depends on the stability of the trapped charge in a given defect centre which is a function of sample temperature. Different defect centers have different temperature ranges of stability. However, heating immediately evicts trapped electrons from the deep traps. They promptly undergo recombination, and in doing so emit photons in the visible spectrum. The emitted light can easily be detected by a photomultiplier and associated electronic equipment. In TL, the phosphor material after exposure to ionizing radiation is heated and the corresponding intensity of the emitted light is

recorded as a function of temperature. TL has been used extensively to measure ionizing radiation doses since the early 1950s [1].

1.4.1. Theory of Thermoluminescence

Let us assume that the TL signal is caused by the thermal release of electrons from a single type of trap, at a depth ‘ E ’ from the bottom of the conduction band. The escape probability for a single electron per second is given by

$$p = s \exp(-E / kT) \quad (1.1)$$

where ‘ s ’ is the frequency factor, E trap depth (activation energy), k is the Boltzmann constant and T is the absolute temperature. If the trap is deep enough it will be inactive (stable) at relatively low temperature, but will release electrons at elevated temperatures. As the temperature of the sample is raised the recombination rate increases initially and reaches a maximum as more trapped electrons are released. After reaching the peak temperature it falls down as the trapped carriers (or the recombination centers) are depleted. Thus, the resulting TL curve (light intensity versus temperature) will be a single peak. The peak shape and the temperature T_m at which maxima occurs depend not only on the trap specific parameters such as E and s but also on the heating rate, the radiation dose and the order of kinetics. The exact equations of the process depend on the mechanisms of the recombination. Several types of traps with different activation energies usually result in several TL peaks which may superimpose if they are closely lying. If the sample is kept at a constant temperature and the process of thermal release and recombination of charge carriers are studied at this temperature, the resulting luminescence is called phosphorescence due to isothermal decay of charge carriers. The different models of TL are discussed below

1.4.2. *Randall-Wilkins Model*

Randall-Wilkins [2] in 1945 proposed a one trap one recombination (OTOR) model for thermoluminescence based on the following assumptions: i) once the electron/hole is freed from its trap the probability of its re-trapping is negligible compared to the probability of recombination, ii) the population density of the electrons in the conduction band (n_c) is negligible compared to the number of trapped electrons (n) i.e. that there is no buildup of charge carriers in the conduction band, iii) luminescence intensity at any temperature is directly proportional to the rate of de-trapping of charge carriers. If ' n ' is the concentration of filled traps at time ' t ', then during heating, the intensity of TL with time is proportional to the rate of change of population density of trapped electrons, and can be given by $I(t) \propto -\frac{dn}{dt}$ where,

$$\frac{dn}{dt} = -np = -ns \exp(-E / kT) \quad (1.2)$$

The negative sign indicates that the population density of trapped electrons n decreases with time or temperature. Assuming linear heating rate of $\beta = dT/dt$, and substituting it equation (1.2) and on subsequent integration, we obtain

$$n = n_0 \exp\left[-\frac{s}{\beta} \int_{T_0}^T \exp(-E / kT) dT\right] \quad (1.3)$$

The intensity of thermoluminescence $I(T)$ at the temperature T in Randall-Wilkins model is,

$$I = -\frac{dn}{dt} = n_0 s \exp(-E / kT) \exp\left[-\frac{s}{\beta} \int_{T_0}^T s \exp\left(-\frac{E}{kT}\right) dT\right] \quad (1.4)$$

where, n_0 is the number density of trapped electrons (m^{-3}) which is dependent on the radiation dose, E is the activation energy (eV), s is the frequency factor or attempt to escape factor (s^{-1}), T_0 is the starting temperature, $T(t)$ is temperature at any time t , $\beta = dT/dt$ is the heating rate

(Ks^{-1}) and k is the Boltzman's constant (eV K^{-1}). It is seen that the intensity builds up as T increases, reaches a maximum value at T_m and then falls with further heating of the sample. At $T = T_m$, $dI/dT = 0$, and we obtain the condition of maxima of TL peak as

$$\frac{\beta E}{kT_m^2} = s e^{-E/kT_m} \quad (1.5)$$

Equation (1.5) indicates that a) at constant heating rate β we observe shift in T_m (peak temperature) towards higher temperature as E increases or s decreases, b) for a given trap (ie constant E & s), T_m shift towards higher temperature as β increases.

1.4.3. Garlick-Gibson Model

TL glow curves obtained from the solution of Randall-Wilkins equation are of first order (no retrapping), so the TL glow curve falls relatively faster than in case of retrapping. In Randall-Wilkins model, neglecting the retrapping of the electrons released from the traps is an idealistic assumption as during heating the release of electrons make traps empty and therefore the possibility that retrapping of electrons during TL process may exist. Garlick and Gibson [3] in 1948 proposed a new model, which takes into account the retrapping of conduction band electrons during the TL measurement. For simplicity they assumed the retrapping and recombination probabilities to be equal,

$$I = -\frac{dn}{dt} = \frac{n^2}{N} p = \frac{n^2}{N} s \exp(-E/kT) \quad (1.6)$$

that can be expressed as

$$I = \frac{n_0^2 s \exp(-E/kT)}{N[1 + \frac{n_0 s}{\beta N} \int_{T_0}^T \exp(-E/kT) dT]^2} \quad (1.7)$$

The intensity of TL in Garlick-Gibson model is proportional to n^2 , implying that the order of kinetics is two. It is to be remembered that a second order glow curve arises because of the

increased possibility of retrapping as compared to the first-order case (i.e., the light emission is delayed), then it might reasonably be expected that a second order curve will display more thermoluminescence during the second half of the peak than will a first-order TL curve. Therefore, the TL glow curves obtained in Garlick-Gibson model are symmetric compared to Randall-Wilkins model.

1.4.4. Model for General order kinetics

The situations in which retrapping and recombination probabilities are not equal and the shape factor μ_g can have values different than 0.42 or 0.50 are found to follow general-order kinetics. In such situations, the order of kinetics is neither one nor two but between one and two or greater than two. May and Partridge [4] in 1964 proposed an empirical relation representing general order TSL kinetics for such situations

$$I = n^b s' \exp(-E/kT) \quad (1.8)$$

where 's' has dimensions of $m^{3(b-1)}s^{-1}$ and b is defined as the general order parameter and is not necessarily one or two. However, s' does not have much physical significance and the dimensions of s' change with the kinetic order. A more logical form of the general order kinetics is given by recasting of the general order kinetic equation as proposed by Rasheedy [5]

$$I = -\frac{dn}{dt} = \frac{n^2}{N} p = \left(\frac{n^b}{N^{b-1}}\right) s \exp(-E/kT) \quad (1.9)$$

which clearly reduces to the first and second-order kinetics equations for $b=1$ and $b=2$. The advantage of the Rasheedy's proposal on general-order model of TL is that the difficulty encountered in the interpretation of 's' in May and Partridge model is removed.

1.4.5. Limitations of TL

From the standpoint presented so far, it is evident that TL properties of materials are intimately linked with the defect structure. The emission from a phosphor depends on the activator. The

trapping details, however, are normally decided by defects and impurities of another kind. Control of such defects is an integral part of development of a dosimetry grade phosphor. Further, the collective stability of these defects with respect to temperature decides the reliability of the dose related information and thereby governs its performance as a phosphor. TL efficiency of certain materials exhibits a sharp reduction at elevated temperatures due to the dominance of non-radiative relaxations at elevated temperatures. This reduction in TL efficiency, namely thermal quenching, effectively hinders their application as dosimetric phosphor.

Heating of a sample is intrinsic to the process of TL and hence is inevitable. Moreover, it is essential to frequently subject a TL phosphor to additional heat treatments for its reuse. These heat treatments are specific to a particular material. The heat treatment especially the cooling rate may upset the defect structure and markedly influence the location, size as well as the shape of the peak and thereby the performance of a phosphor. Therefore it is necessary maintain a precise heating profile at each and every stage of TL process. Apart from these complications, the heating of a phosphor, in the long run, compromises the chemical integrity of the phosphor and limits its reusability. These deficiencies call for an appropriate solution in terms of stimulation and next portion of this chapter relates to such a technique which is based on a more convenient mode of stimulation named- *light*.

1.5. Optically Stimulated Luminescence (OSL)

OSL is the light emitted during stimulation of crystalline insulators or semiconductors that were previously excited, typically by exposure to ionizing radiation. The excitation puts the crystal in a meta-stable state, characterized by electrons and holes separately trapped at defects in the crystal lattice. During the OSL process, light stimulates the release of these electrons and

holes from these trapping centers, resulting in electron/hole recombination and excitation of luminescence centers in the crystal. OSL consists of the photons emitted when these excited luminescence centers decay to the ground state [6].

Schematic representation of OSL process is illustrated in fig. 1.2. The three stages involved in the OSL process being: a) **Excitation** in which the OSL phosphor is exposed to ionizing radiation leading to excitations and ionizations and therefore the generation of electron/hole (e/h) pairs across conduction band (CB) and valence band (VB). Subsequently, these e/h pairs have probability of getting trapped at defects in the crystal lattice, the energy levels for which are represented by the short horizontal lines in the band gap, in between the VB and CB (fig. 1.2a).

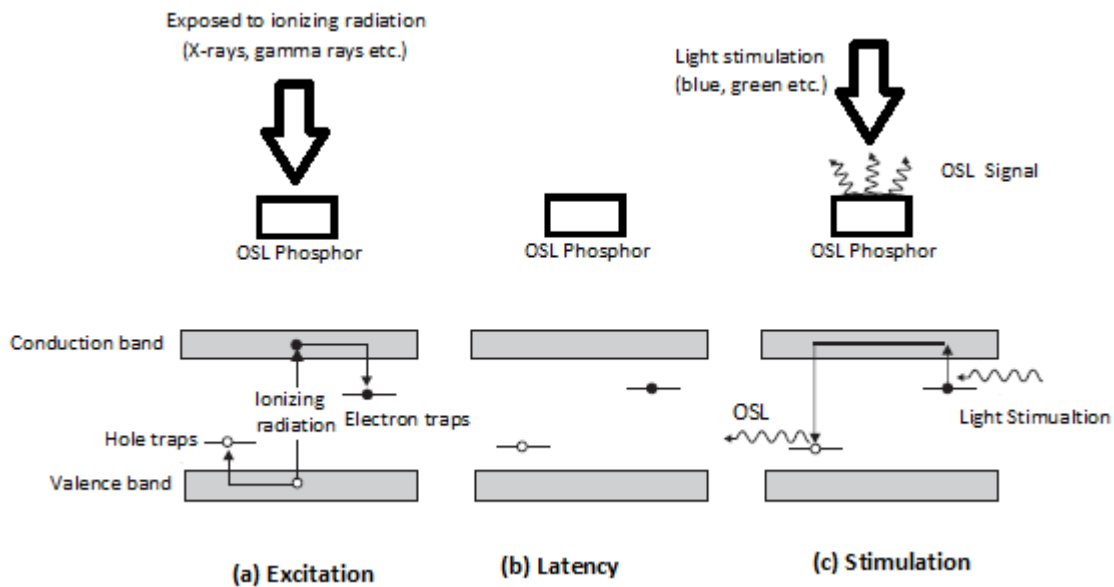


Figure 1.2. Different stages of OSL process: (a) Excitation with ionizing radiation creating free electrons and holes; (b) latency period characterized by a metastable concentration of electrons and holes trapped at defects in the crystal and (c) stimulation of the detector with light [6]

b) **Latency period** characterized by a metastable concentration of trapped electrons and holes (fig. 1.2b). If trap depth/potential wells associated with the trapping centers are sufficiently deep, then the thermally induced escape probability of the trapped charges is negligible at room

temperature. This relatively stable concentration of trapped electrons and holes is related to the energy absorbed by the crystal during the excitation process, that is, to the absorbed dose of radiation; it represents latent information about the radiation field [6].

c) **Stimulation** by light that is eventually used to read information stored in the OSL detector (fig. 1.2c). Here a photon of wavelength λ_{stim} (e.g., green light) stimulates the electron to the conduction band. As the electron is free to move in the delocalized conduction band (but within the confines of the crystal/solid), the electron may reach and recombine with the trapped hole that creates a defect in the excited state, which on radiative relaxation to the ground state emits a photon of wavelength λ_{OSL} (e.g., blue light). Notably, OSL differs from photoluminescence in that the latter involves intra-band transitions rather than ionization of traps [6].

Earlier OSL, was not extensively used when compared to TL in radiation dosimetry due to the lack of good luminescent material having high OSL sensitivity to radiation, low effective atomic number and low post irradiation fading characteristics until the introduction of highly sensitive $\alpha\text{-Al}_2\text{O}_3\text{:C}$ OSL phosphor about twenty years ago. The potential of OSL for radiation dosimetry has been reviewed by Bøtter-Jensen and McKeever [7]. Another mode of stimulation being “Delayed OSL” (DOSL) was also suggested for radiation dosimetry that involves optical stimulation for the transfer of trapped charge carriers from deeper to shallow traps and then monitors the phosphorescence at room temperature [8]. Phosphors such as BeO [9], $\text{CaSO}_4\text{:Dy}$ [10] were used in this mode, but they exhibited weak sensitivity. In a photo-transfer thermoluminescence (PTTL) technique, the irradiated samples are illuminated with suitable light to transfer charges from deeper traps to record the TL [11]. If the shallow traps are filled at the illumination a larger TL peak results than would have obtained without illumination.

1.5.1. Theory of OSL

a) Models and Rate Equations: The transition of charge between energy levels during irradiation and subsequent optical stimulation of phosphor material can be described by a series of non-linear coupled rate equations. Many assumptions are introduced to arrive at the analytical expressions for the evolution of OSL intensity with time during the optical stimulation. Based on this analysis several energy level models have been proposed. Each of these models assumes the transport of electron through the conduction band in order to reach the trapped holes at the radiative recombination site. The system containing one type of electron trap and one type of hole trap is the simplest model. The trapped hole acts as a recombination centre at which recombination of electrons with hole occurs which leads to emission of luminescence. This model is known as one trap/one center model.

b) The One Trap / One Recombination Center Model

Most models for OSL assume transport of the optically excited charge through the delocalized bands in order to reach the recombination site. The simplest model by which OSL can be produced is one trap one recombination center model. The charge neutrality for this system can be written as,

$$n_c + n = m_v + m \quad (1.10)$$

Where n_c and n are the concentrations electrons in the conduction band and electron traps, and m_v and m are the concentrations holes in the valence band and the hole traps respectively. At the end of irradiation if we consider $n_c = m_v = 0$ (at the start of optical stimulation $n_0 = m_0$). The light stimulates trapped electrons into the conduction band at rate f , followed by recombination with trapped holes to produce OSL of intensity I_{OSL} . During optical stimulation the charge neutrality condition demands, $n_c + n = m$, from which the rate equation describing the charge

flow is expressed as

$$\frac{dn_c}{dt} = -\frac{dn}{dt} + \frac{dm}{dt} \quad (1.11)$$

The terms dn/dt and dm/dt can explicitly be written as

$$-\frac{dn}{dt} = np - n_c A(N - n) \quad (1.12)$$

$$-\frac{dm}{dt} = n_c A_m m = \frac{n_c}{\tau} \quad (1.13)$$

With the assumptions of quasi-equilibrium ($dn_c/dt \ll dn/dt$, dm/dt and $n_c \ll n$, m) and negligible retrapping we have

$$I_{OSL} = -\frac{dm}{dt} = -\frac{dn}{dt} = nf \quad (1.14)$$

the solution of which is

$$I_{OSL} = n_0 f \exp(-ft) = I_0 \exp(-t/\tau) \quad (1.15)$$

Here, n_0 is the initial concentration of trapped electrons at time $t = 0$, I_0 is the initial luminescence intensity at $t = 0$, f is excitation rate in s^{-1} and $\tau = 1/f$ is the decay constant. One can observe a straightforward relationship in which the initial intensity is directly proportional to the excitation rate and the decay of the OSL with time is a simple exponential. The excitation rate ' f ' is given by the product of the excitation intensity, ϕ and the photo-ionization cross-section, σ .

1.5.2. Stimulation Modalities

The OSL technique provides precise control over the stimulation intensity obtained from a light source (LED, laser etc.). Optimization of OSL readout involves not only the choice of stimulation wavelength, but also the modulation of intensity and its duration. Therefore, several approaches have been proposed for the OSL readout and are discussed as follows.

1.5.2.1. Continuous wave OSL (CW-OSL)

This is the simplest OSL readout mode in which detector is stimulated with light of constant intensity in time, and is referred as continuous-wave OSL (CW-OSL). Here discrimination between OSL and stimulation light is based only on wavelength separation (as $\lambda_{OSL} \neq \lambda_{stim}$). Therefore, it is essential that the transmission band of the detection filters does not overlap with the spectrum of the stimulation light, which is determined by the light source and optical filters used in front of it. One monitors the intensity of the luminescence as a function of time resulting in a characteristic luminescence-versus-time curve. The integral of the luminescence-versus-time curve is related to the trapped charge concentration, which in turn, is proportional to the absorbed dose of radiation. Owing to its simplicity and satisfactory performance CW-OSL is the most widely practised stimulation mode in radiation dosimetry as well as luminescence dating [6].

Mathematical description of CW- OSL

We assume here once again one-trap/one-center model for mathematical simplification in our further discussion. One can assume quasi-equilibrium condition and the rate of change of electron population in conduction band is negligibly small as compared to the rate of change of optically stimulated depleted trapped electron concentration, i.e.

$$\frac{dn_c}{dt} \ll \frac{dn}{dt}, \frac{dm}{dt} \quad \text{and } n_c \ll n, m$$

Where, n_c and n are the concentrations of electrons in conduction band and OSL active traps respectively, m is the concentration of holes in recombination traps. Therefore, OSL intensity, I_{OSL} is proportional to rate of depleting OSL active electron traps, i.e.

$$I_{OSL} = -\frac{dn}{dt} \tag{1.16}$$

Let us consider that electrons of concentration n are trapped at a localized state until stimulated into the conduction band by absorption of photons (of energy $h\nu_{ex}$). The freed electrons are then able to recombine at trapped holes centers m via conduction band, producing OSL with intensity I_{OSL} . If ' f ' is optical excitation rate (s^{-1}) of optical released charges, under no re-trapping of optically released charge carriers, i.e. first-order kinetics, equation (1.16) can be written

$$I_{OSL} = -\frac{dm}{dt} = -\frac{dn}{dt} = nf \quad (1.17)$$

The f can be expressed in terms of photo-ionization cross-section " $\sigma(\lambda)$ " (cm^2) of trap level and stimulating light flux " $\phi(\lambda)$ " (no. of photons/ cm^2 /sec) as

$$f = \sigma(\lambda)\phi(\lambda) \quad (1.18)$$

For a given stimulation wavelength, $\sigma(\lambda)$ remains constant for the given trap level if we keep stimulation flux constant with respect to time as $\phi(\lambda) = \phi_o(\lambda)$.

Therefore equation (1.18) can be written as

$$f = f_o = \sigma(\lambda)\phi_o(\lambda) \quad (1.19)$$

Incorporating equation (1.19) in equation (1.17), we get

$$I_{OSL} = -\frac{dm}{dt} = -\frac{dn}{dt} = nf_o \quad (1.20)$$

$$\frac{dn}{dt} = -nf_o \Rightarrow n = n_o e^{-f_o t} \quad (1.21)$$

Here n_o is initial number of trapped charges at time $t = 0$. Incorporating equation (1.21) into (1.20) gives following CW-OSL equation

$$I_{OSL} = n_o f_o e^{-f_o t} = I_o e^{-f_o t} \quad (1.22)$$

Where, I_o is initial CW-OSL intensity. The plot of equation (1.22) is a well-known exponential

decay function with decay constant f_o (s^{-1}) as shown in fig 1.3.

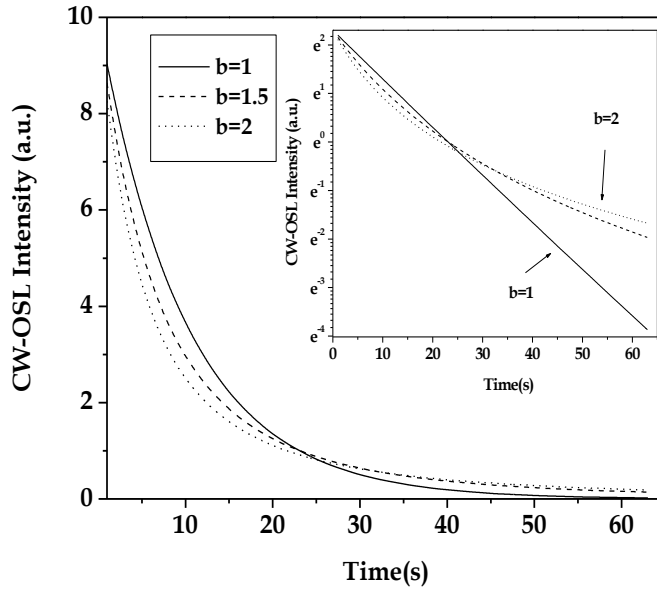


Figure 1.3: Variation in CW-OSL intensity curve with change in order of kinetics.

However, in case of re-trapping of released charge carriers, i.e., general-order kinetic model, for the rate of recombination equation (1.20) gets modified as [12]

$${}^b I_{OSL} = -\frac{dn}{dt} = f_o \frac{n^b}{n_o^{b-1}} \quad (1.23)$$

Where b is kinetic order; it is a dimensionless positive number.

The solution of above equation (1.23) can be derived as

$${}^b I_{OSL} = f_o n_o \left[1 + (b-1) f_o t \right]^{-\frac{b}{b-1}} \quad (1.24)$$

Where, $b > 0$, $b \neq 1$.

The plot of equation (1.24) for change in order of kinetics has been shown in (fig.1.3) for same initial number of trapped charges n_o . The (fig.1.3) highlights the effect of non-first order kinetics on CW-OSL curve. The inset figure shows (natural log scale plot) that the CW-OSL

intensity decay is no longer linear for non 1st order kinetics. Any attempt to fit pure exponential decay function to such non-1st order kinetics, CW-OSL curve will give inaccurate decay constant as well as photo-ionization cross-section. However, the natural log plot of CW-OSL intensity is capable of identifying the non-1st order kinetics associated with OSL process.

1.5.2.2. Pulsed OSL (POSL)

Although CW-OSL is the simplest technique in terms of mode of stimulation, the need to completely eliminate the scattered stimulation light often requires the use of optical filtration that unintentionally ends up in significant reduction of the measured OSL intensity which is undesirable. The problem becomes more critical when the wavelength separation between the stimulation light and the OSL emission band is not much.

For low-dose measurements, it is advantageous to accomplish temporal discrimination between the stimulation light and the OSL emission and thus obviating the need of optical filters. This can be achieved by making use of a pulsed light source and a gated detection system that detects the OSL signal between the stimulation pulses (during off time), when there is no scattered light. If the intensity of the scattered stimulation light is too high, gating PMT may be essential, which involves switching off the PMT voltage during stimulation and restoring it between the stimulation pulses. However, the most practical approach is to make use of the optical filters to reduce the scattered light to an acceptable and safe level, thereby avoiding any damage to PMT while gating. This approach avoids an extreme measure of turning the PMT on and off, and improves stability and durability of the OSL reader. This mode of stimulation is called as pulsed OSL (POSL) [6].

Markey et al, in 1995 [13] were the first to explore the applicability of POSL for dosimetry using $\text{Al}_2\text{O}_3:\text{C}$ detectors and subsequently further investigations were carried by Mckeever and Akselrod [14, 15].

This temporal discrimination essentially depends on the lifetime of the luminescence centers responsible for the OSL signal. If the luminescence lifetime happens to be shorter than the duration of the stimulation, the luminescence centers decay immediately after recombination and, consequently, the OSL emission occurs only during stimulation. This results in the negligible OSL intensity in the periods between laser pulses thereby making POSL technique ineffective. However, on the contrary if luminescence lifetime is significantly longer than the stimulation pulses, a significant fraction of the luminescence signal decays after the culmination of stimulation pulse, producing signal in the period between stimulation pulses [6].

The exploitation of of pulsed OSL presents several opportunities in radiation dosimetry like a) Fast throughput: As millisecond pulses are required to read, OSL signal can be extracted in very short time to assess the radiation dose b) Multiple dose readout: This is feasible since the signal is not depleted in one reading unlike the CW-OSL mode c) Since the emission is not detected while the pulse is on, this arrangement can extend the range of stimulation wavelengths that may be used d) Dose imaging: shorter the excitation pulse greater is the amount of light emitted after the pulse compared with that emitted during the pulse [16]. The high S/N ratio and better spatial resolution allow the use of this method for dose imaging [17].

1.5.2.3. Linearly Modulated OSL (LM-OSL)

In the LM-OSL mode, the stimulating light intensity at the sample position is increased linearly from zero to a maximum as a function of time to obtain the OSL curve. The OSL output is observed to increase steadily as the stimulation power increases linearly and reaches

its maximum peak value (OSL peak), after which the OSL intensity decreases non-linearly to zero due to depletion of charge carriers. This method is useful for distinguishing between OSL originating from different traps. For a material having more than one type of OSL traps, LM-OSL technique yields a series of OSL peaks as a function of read-out time. Each peak corresponds to a different trap, with traps having largest photo-ionization cross-section (σ) emptying first. In LM-OSL, from the knowledge of ramp rate, one can determine the photo-ionization cross-section at the wavelength used in the experiments. This technique has been applied to a variety of materials including quartz and sapphire.

Mathematical description LM-OSL

In LM-OSL method, the OSL output is observed to increase initially linearly as stimulation intensity increases, reaches a maximum value with respect to time, after which the OSL intensity decreases non-linearly to zero [12]. The time at which the luminescence intensity reaches its peak value is dependent on the variation of stimulating intensity ramp rate γ ($\text{W}/\text{cm}^2/\text{s}$) (expressed in terms of photon fluence rate, i.e. $\text{photons}/\text{cm}^2/\text{s}^2$) with respect to time and photo-ionization cross-section σ of the trap. The traps with different photo-ionization cross-sections result in multiple peaks in LM-OSL curve. One can assume quasi-equilibrium condition i.e, the rate of change of electron population in conduction band is negligibly small as compared to the rate of change of optically stimulated depleted trapped electrons concentration. Considering the linear variation of stimulating light flux $\phi(t)$ as

$$\phi(t) = \phi(\lambda, \gamma, t) = \gamma t \tag{1.25}$$

Now re-writing the optical excitation rate in $f(t)$, the LM-OSL case can be written as

$$f(t) = \sigma(\lambda) \phi(t) = \sigma \gamma t \tag{1.26}$$

The LM-OSL intensity can be given as

$$I_{LM} = - \frac{dn}{dt} = f(t) n = \sigma \gamma n t \quad (1.27)$$

Solution of above differential equation will be

$$I_{LM} = \sigma \gamma n_o t e^{-\left(\frac{\sigma \gamma}{2}\right)t^2} \quad (1.28)$$

The above equation gives the LM-OSL intensity under no re-trapping of optically released charges, i.e. 1st order of kinetics. Fig. 1.4 shows the plot of equation (1.28) for 1st order, 2nd order and general order kinetic.

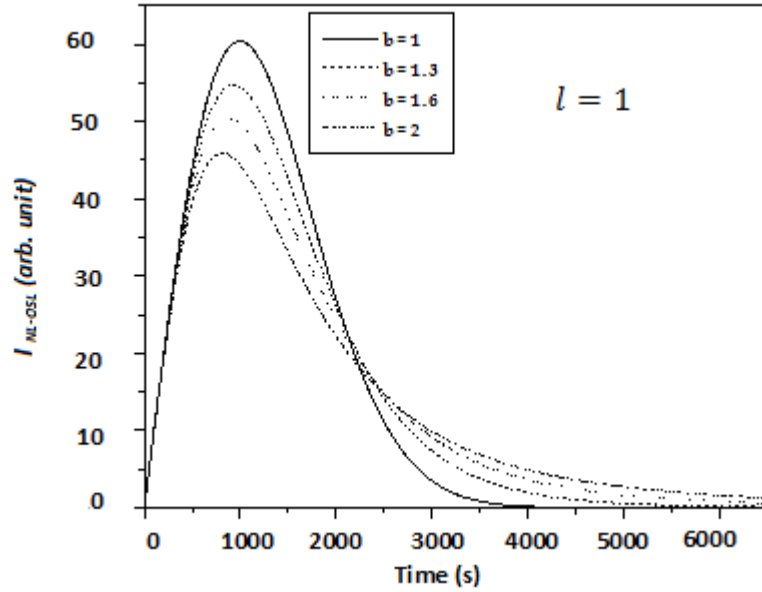


Figure 1.4 Variation of LM-OSL intensity under first and general order kinetics.

The condition for OSL intensity maximum can be obtained by applying the condition of maximum to equation (1.28), we get

$$\left(\frac{dI_{LM}}{dt} \right) \Big|_{t=t_{\max}} = 0$$

$$\Rightarrow t_{\max} = \frac{1}{\sqrt{\sigma \gamma}} \quad (1.29)$$

Where, t_{max} is the time required to reach the maximum in OSL intensity curve. As we can see from equation (1.29) that the photo-ionization cross-section comes in the denominator, for a fixed γ , the different photo-ionization cross-sections associated with various trap levels results in distinct OSL peaks in LM-OSL intensity curve. This is why this technique is extensively used to estimate the possible photo-ionization cross-sections associated with OSL active trap levels in luminescent material.

The value of LM-OSL intensity at t_{max} can be given by incorporating equation (1.29) into (1.28) as

$$I_{LM-max} = n_o \sqrt{\sigma \gamma} e^{-\frac{1}{2}} \quad (1.30)$$

From this equation it can be seen that the value of peak maximum increases with increase in photo-ionization cross-section, as well as with increase in value of intensity ramp rate γ .

In case of re-trapping of optically stimulated charges we have LM-OSL intensity (${}^b I_{LM}$) as

$${}^b I_{LM} = -\frac{dn}{dt} = f \frac{n^b}{n_o^{b-1}} = \sigma \gamma t \frac{n^b}{n_o^{b-1}} \quad (1.31)$$

The solution of above differential equation gives

$$n = n_o \left[1 + (b-1) \frac{\sigma \gamma t^2}{2} \right]^{b/1-b} \quad (1.32)$$

Where, $1 < b \leq 2$.

Incorporating equation (1.32) into (1.31) we get,

$${}^b I_{LM} = \sigma \gamma n_o t \left[1 + (b-1) \frac{\sigma \gamma t^2}{2} \right]^{b/1-b} \quad (1.33)$$

This is the equation representing the LM-OSL intensity under general order kinetics. Re-trapping decreases the value of peak intensity and LM-OSL peak occurs in shorter time but

shows extended tail in time domain due to delay in depopulating the OSL active traps and relatively longer time is taken in recording complete OSL signal with increase in order of kinetics.

The time required to reach peak of LM-OSL intensity ${}^b t_{max}$, can be derived by equating first derivative to be zero i.e.

$$\left(\frac{d {}^b I_{LM}}{dt} \right) \Big|_{t={}^b t_{max}} = 0 \quad \Rightarrow \quad {}^b t_{max} = \left(\frac{2}{\sigma \gamma (b+1)} \right)^{\frac{1}{2}} \quad (1.34)$$

The increase in order of kinetics brings OSL peak in shorter time. The value of peak intensity can also be derived by incorporating equation (1.34) into equation (1.33) as

$${}^b I_{LM-max} = n_0 \sqrt{\frac{2\sigma \gamma}{b+1}} \left(\frac{2b}{b+1} \right)^{\frac{b}{1-b}} \quad (1.35)$$

From equation (1.35), it is evident that increase in order of kinetics decreases the value of peak intensity.

1.5.2.4. *Non-linear OSL (NL-OSL)*

In this technique the intensity is modulated non-linearly to deplete traps with different photo-ionization cross-sections. It is particularly useful for the systems with closely overlapping LM-OSL peaks. This mode of stimulation has been dealt with in detail in Chapter 4 highlighting the results of preliminary investigations on $Al_2O_3:C$ using this technique.

1.6. Merits of OSL

The OSL is comparatively recent technique as an alternative to the TL and has significant advantages over the TL technique for various reasons, which have led to its increasing popularity in radiation dosimetry applications. The physical principles of OSL are closely related to those of TL technique. OSL is normally measured at room temperature,

which simplifies the design of the equipment and thus results in instrumental simplicity. The OSL dosimetry is becoming a serious contender to TL dosimetry due to its operational ease. The OSL readout method is fully optical in nature. For routine OSL readout, heating of the sample is not required unlike the case of TL, where a reliable and reproducible heating profile needs to be maintained for every TL read out (however, some additional advantages may be gained by performing the OSL at slightly elevated temperature for the academic interest). This avoidance of heating eliminates problems due to thermal quenching (i.e. reduction in efficiency of luminescence as the temperature of the sample increases due to non radiative relaxations of charges) of luminescence efficiency of the phosphor and thus a significant increase in sensitivity can be achieved. This non-destructive optical nature of OSL is a potential advantage over TL, particularly in geological dating, in which OSL is measured at room temperature and only the component of the trapped population sensitive to light is measured.

Another important advantage of OSL is that trapped charges in the irradiated phosphor can be emptied by simply exposing it to the daylight for some hours, enabling its reset as well as reuse. This '*All optical*' nature of OSL readout processes has vital consequences. Since the material does not need to be heated during readout, it allows the extension of OSL material to neutron dosimetry through use of "plastic" material as the matrix with which, the neutrons upon interaction produce knock-on protons.

Further, this all optical nature also allows remote measurement of doses which has immediate application in space dosimetry. The expansion of the exploration program of US, Asian and EU Space Agencies is leading to an increased exposure of astronauts to space radiation. The sources of radiation are galactic cosmic rays (high-energy proton and heavy charge particles), solar particles (medium-to high energy protons and electrons.). Thus the

customized monitoring of space radiation has acquired a high priority. In this regard, the change in certain OSL parameters is being actively used to identify and differentiate such particles involved in the space dosimetry. The determination of the radiation dose received during the proposed extended duration space missions would need, '*on-board*' readers that besides being energy efficient must be light weight as well. In several case studies, connected with such space radiation experiments, OSL has been used effectively. Thus the OSL technique offers active as well as passive space dosimetry option which can cater to such advance level radiation monitoring.

The all-optical nature together with high sensitivity of OSL has proved itself beneficial to the medical dosimetry. In the diagnostic applications of radiation, OSL has been used with significant success in dose imaging systems. In the therapeutic usage, due to recent inclination towards use of charged particle beams viz. protons, carbon ions poses different sets of problems in dose determination as compared to those caused via use of high energy photons, the technique of OSL has sought its application and helped medical physicists and Oncologists to work out an irradiation plan which is efficient as well as effective.

The high sensitivity of OSL also leads to the multiple readout of the same sample unlike in TL, which can be read only once, and second or repeated readouts are not possible. In OSL technique, one has a fine control over the degree to which the traps can be emptied by varying the intensity and wavelength of stimulation light. Because, it is not necessary to stimulate all the trapped charges in order to obtain sufficient luminescence signal, with an appropriate choice of stimulation wavelength and power, the dose can be reanalyzed multiple times subject to material sensitivity. The residual information, in the form of trapped charges, can be stimulated later to verify the dose. In dating and retrospective dosimetry, repeated

measurements on the same sample are the basic necessity. In short, the lower detection limits (nGy), convenient optical stimulation, short readout time (~ ms), optical erasing of the dose, high dynamic dose range (7 order), high sensitivity, dose imaging, optical fiber based on-line remote dosimetry are some of the advantages of OSL over TL. However, the OSL technique has associated limitation that it requires dark room facility during the complete readout process.

1.7. Key Attributes of a TL/OSL phosphor

A phosphor for dosimetric use should possess the attributes like: a) High luminescence efficiency; b) long storage stability of trapped charge carriers and hence the stored signal at normal temperature; c) simple glow curve structure, preferably with single glow peak; d) chemical stability and inertness to extreme climatic conditions such as temperature, humidity; e) TL emission spectrum should be suitable for the detector system. Phosphors having their characteristic light emission lying in the high efficiency region (300-500nm) of photomultiplier tube and low infrared emission from the heated phosphor are most suitable for radiation dosimetry; f) preferably near tissue equivalence response; g) linear dose response over a wide range; h) simple annealing procedure for reuse and no loss of sensitivity with reuse and repeated annealing; g) should have a very good shelf life. Its sensitivity should not show any decrease if the phosphor is used after long duration; i) should not be affected by any external agency such as mechanical, electrical or any other type; j) it should be possible to make dosimeter of any form, size and shape from the phosphor without any change in its sensitivity or other dosimetric characteristics; k) convenience of synthesis in terms of instrumentation and economy along with a reliable supply chain; l) most importantly for being an OSL phosphor it should exhibit high photo-ionization cross-section for a given stimulation wavelength.

1.8. Widely practiced Phosphors in TL dosimetry

Table 1.1 enlists important characteristics of certain materials that are frequently encountered in TL dosimetry including $\text{Al}_2\text{O}_3:\text{C}$. The information furnished in this table amply endorses the reputation of TL as a popular mode of readout which stems from its capability of detection of very low levels of radiation which in turn is intimately linked to the presence of defects and arises from the extremely efficient detection of the luminescence signal emitted by these defects by photomultiplier tubes.

However, a typical glow curve does not get precisely replicated in every sample or even in the same sample after its re-use. In practical terms this means it is necessary to calibrate every individual dosimeter. Ever since 1956, these inadequacies had driven researchers to explore materials that would provide dose related information with a much more manageable means of stimulation namely *light*. OSL also known as photo-stimulated luminescence (PSL) operates at room temperature offers a solution to get around these difficulties as it does not alter defect structure and excludes loss of signal due to thermal quenching and prohibits thermal noise. These advantages have inspired many an investigations on various material systems that would serve as an OSL phosphor and what follows next, is a gist of these efforts.

Table 1.1. General Characteristics of Some Commercially Available TLDs

TLD type	Effective atomic no. (Z_{eff})	Main TL peak ($^{\circ}\text{C}$)	Emission max. (nm)	Relative sensitivity	Fading ^b (at 25 $^{\circ}\text{C}$)	Dose range
LiF:Ti,Mg	8.2	200	400	1	5%/year	20 μGy -10Gy
LiF:Mg,Cu,P	8.2	210	400	25	5%/year	0.2 μGy -10 Gy
Li ₂ B ₄ O ₇ :Mn	7.4	220	605	0.20	4%/month	0.1mGy-3Gy
Li ₂ B ₄ O ₇ :Cu	7.4	205	368	2	10%/2months	10 μGy -10 ³ Gy
MgB ₄ O ₇ :Dy	8.4	190	490	10	4%/month	5 μGy -50 Gy
BeO	7.1	190	200-400	0.20	8%/2 months	0.1 mGy-0.5 Gy
Mg ₂ SiO ₄ :Tb	11	200	380-400	40	very slight	10 μGy -1 Gy
CaSO ₄ :Dy	15.3	220	480-570	30	1%/2 months	2 μGy -10 Gy
CaSO ₄ :Tm	15.3	220	452	30	2%/2 months	2 μGy -10 Gy
CaF ₂ :Mn	16.3	260	500	5	16%/2 weeks	10 μGy -10 Gy
Natural CaF ₂	16.3	260	380	23	very slight	10 μGy -50 Gy
CaF ₂ :Dy	16.3	215	480-570	15	8%/2 months	10 μGy -10 Gy
Al ₂ O ₃ :C	10.2	190	420	60 ^c	5%/year	0.1 μGy -10 Gy

^c Heating rate 4 $^{\circ}\text{C}/\text{s}$, ^b Fading in the dark

1.9. Phosphors for OSL dosimetry

Sulfides were one of the earliest material systems to be investigated as a prospective OSL phosphor for dosimetric application [18]. In this attempt, various sulfides after irradiation were stimulated using IR light and the emitted light was used as a guide to monitor the dose

received. The follow-up efforts however were reported almost a decade later which involved many sulfides (MgS, CaS, SrS) and included SrSe doped with rare earth elements like Ce, Sm, Eu [19,20]. Although these materials possessed high sensitivity to radiation, the fact that they could be read even with IR stimulation implied that their dosimetric traps were not deep and as a result these phosphors exhibited a significant fading at room temperature. These phosphors also have a very high effective atomic number causing OSL response to be strongly photon energy dependent thus preventing their use in personnel monitoring.

The first report on Sulfides was immediately followed by a study in which BeO samples exposed to X-rays were stimulated by 410 nm light to cause emission of UV light. This emission was attributed to the presence of doubly occupied electron traps [21]. Although this system possesses an ever needed attributes namely near tissue equivalence, wide separation between emission and excitation wavelengths and low cost, its toxicity has discouraged its large scale application. A variant of the OSL was also attempted on $\text{CaSO}_4\text{:Dy}$ and $\text{CaF}_2\text{:Mn}$ in which optical stimulation was used to transfer the trapped charge carriers from deeper traps to shallow traps and the phosphorescence due to release of these charges from the shallow traps was monitored at room temperature. However, these phosphors suffered from low sensitivity. In the recent past, phosphors like MgO:Tb^{3+} , YAG:Ce^{3+} , Tb^{3+} , C, $\text{SiO}_2\text{:Cu}$, BaFBr:Eu too have been reported to possess high OSL sensitivity. Amongst these, quartz doped with Cu^+ has been reported to be a strong candidate for OSL based radiation dosimetry. But so far none of these phosphors has qualified the criterion of successful commercialization.

In this regard, an opening was provided by TLD-500 i.e. $\alpha\text{-Al}_2\text{O}_3\text{:C}$. Originally this phosphor was developed by Urals Polytechnic Institute, Russia as a TL phosphor. However, the truth that this phosphor needs to be protected from exposure to light during its post-irradiation

storage coupled with a masterly insight that the very vulnerability of dosimetric information to ambient light is going to make it quite amenable to dose readout by optical stimulation, lead a group at Oklahoma State University to reveal that $\text{Al}_2\text{O}_3:\text{C}$ can as well be used as a very sensitive OSL phosphor for radiation dosimetry [22]. This material besides being exceptionally stable in thermal, chemical and mechanical terms also has a large cross-section for a broad band of stimulation wavelength (450 nm to 555 nm). Further, the lifetime of the emission from $\text{Al}_2\text{O}_3:\text{C}$ is 35 ms which is long enough to render it appropriate to optical stimulation in the form of pulses whose widths are typically 100 ns. Since the luminescence can now be monitored between the pulses i.e. immediately after end of each such pulse, the separation between stimulation light and emission light is greatly facilitated. The phosphor $\alpha\text{-Al}_2\text{O}_3:\text{C}$ has been found to be so well suited to OSL applications that currently, more than 1.5 million dosimeter badges based on $\alpha\text{-Al}_2\text{O}_3:\text{C}$ are in routine use for personnel and environmental monitoring.

Notwithstanding its popularity, utility and supremacy of $\text{Al}_2\text{O}_3:\text{C}$ in OSL dosimetry and immediate relevance of this phosphor to quite a few research avenues of high social priority namely healthcare, space and energy, the access to this phosphor was neither easy nor dependable, as only one source had the requisite technology for its manufacture. This led us to revisit the synthesis of $\alpha\text{-Al}_2\text{O}_3:\text{C}$. The following section presents a summary of the exhaustive efforts and various techniques devised for synthesis of dosimetric grade $\text{Al}_2\text{O}_3:\text{C}$.

1.10. $\alpha\text{-Al}_2\text{O}_3$ as TL/OSL host material

Crystal Structure: For dosimetric purposes, only α modification of Al_2O_3 (corundum) is used, either in single or in polycrystalline form. The crystal structure of $\alpha\text{-Al}_2\text{O}_3$ is rhombohedral with the unit cell containing two molecules of Al_2O_3 . The large O^{2-} ions are on a slightly

distorted close-packed hexagonal sub lattice with smaller Al^{3+} ions occupying two out of three sites on layers between the oxygen layers. Each Al atom is bonded to six O in the form of a distorted octahedron and each O is bonded to four Al atoms in the form of a distorted tetrahedron. There are two short Al-O bonds of 1.846 Å and four longer bonds of 1.985 Å (fig. 1.5a). Each O also has twelve second-nearest-neighbor O atoms with distance of separation ranging from 2.524 to 2.869 Å.

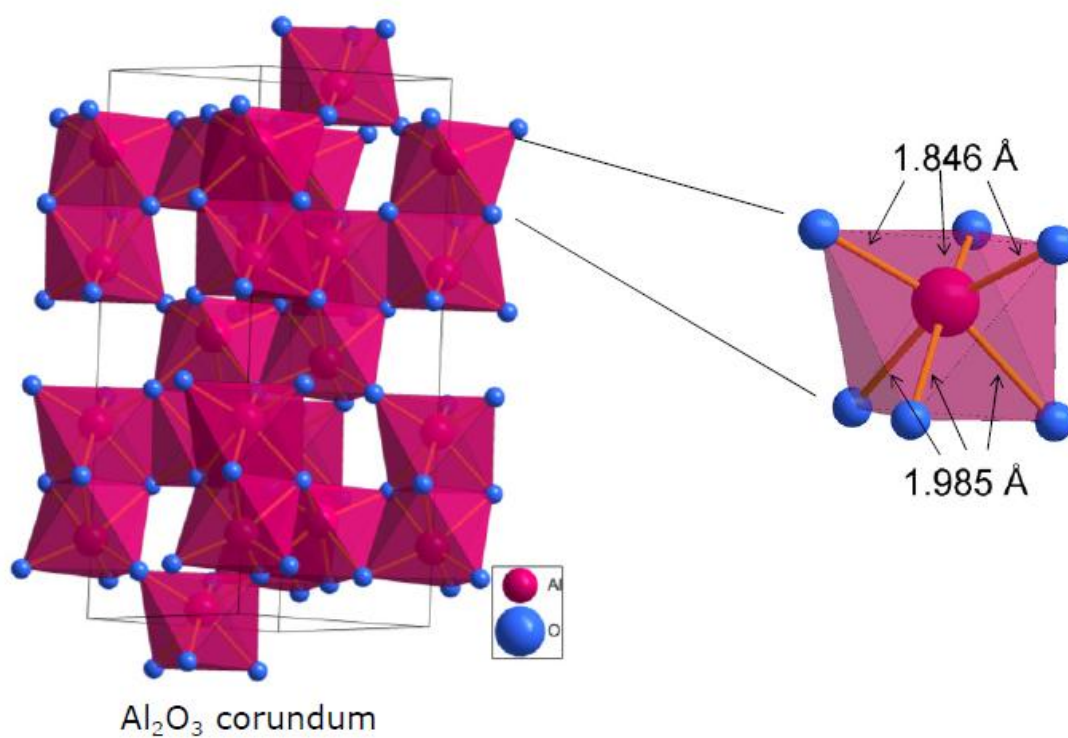
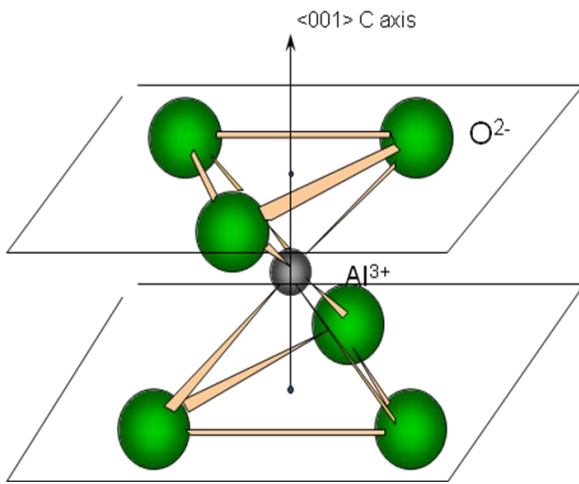
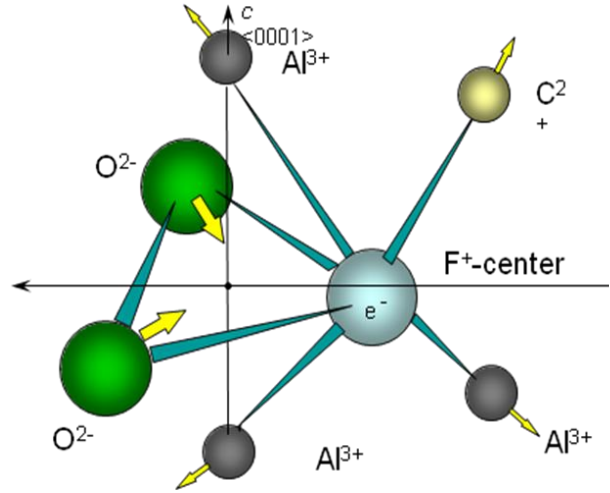


Figure 1.5a. Crystal Structure of $\alpha\text{-Al}_2\text{O}_3$



Aluminum oxide crystal structure



Model of F^+ -center

Figure 1.5b. Schematic representation of $\alpha\text{-Al}_2\text{O}_3$ crystal structure and the Model of F^+ center.

The structure can also be viewed as a stacking of alternate layers of O and Al atoms in the a-b plane of an equivalent hexagonal cell triple the size of the rhombohedral primitive cell. In the cation layer, half of the Al atoms are actually slightly above and the other half slightly below the plane (fig. 1.5b).

Even the highly pure Al_2O_3 crystal contains some impurities, of which the 3d series transition metals (TM) play an important role in the TL phenomenon. The impurity ions such as Cr^{3+} , substitute normally for Al^{3+} ions, not exactly occupying an Al site, but slightly displaced from it. It should also be noted, that there is a considerable proportion of covalent bonding in Al_2O_3 , having an effect even more expressed on the energy levels and wave functions of substitutional TM ions than of the host Al^{3+} ion.

Though the band gap of Aluminum oxide (Al_2O_3), 9.5 eV is not as large as its Fluoride companions, it has a peculiar type of bonding. Its constituent atom Al is unique in the respect that, although technically a metal, it is not located in the left portion of the periodic table where

regular i.e. alkali metals are positioned but rather towards right and borders on being a semimetal. Since its position in the periodic table is closer to oxygen than many of the other metals the difference in their electro-negativities is relatively less and bonds between aluminum and oxygen are not purely ionic but somewhere in between ionic and covalent. Moreover, Al ion has a high charge of +3 and a very small radius and thus a large charge density which makes it a strongly polarizing cation. Hence Al^{3+} ion is able to distort the electron cloud of the oxide ion i.e. it attracts the donated electrons toward itself therefore causes existence of a net effective electron density *between* the aluminum ion and oxygen anion and ensures that these electrons stay shared. This introduces a substantial covalent character in the bonding which further enhances the strength of the bonds. As a result its lattice energy is singularly large i.e. 15916 kJ/mol. Therefore a lot of energy is required to break these bonds causing the melting point of Al_2O_3 to be as high as 2080°C. For the same reason it becomes difficult to create number of oxygen vacancies (essential for it to possess TL/OSL sensitivity) in sufficient concentration in the matrix of the Al_2O_3 unless it is heated to a high enough temperature at which other phases of alumina except alpha alumina are unstable.

Such a large lattice energy of $\alpha\text{-Al}_2\text{O}_3$ together with its large enough band gap and its density which due to a very closely packed crystal structure equals the maximum value admissible theoretically, makes the formation of ionic defects i.e. lattice vacancies and /or interstitial ions as well as that of electronic defects related to oxygen i.e. localized electrons and holes, very difficult [23].

As a desirable consequence, the population of native charge carriers in valence and conduction bands and thus the '*zero dose background*' in this host is kept low very effectively. Further the large differences between lattice energies and melting points of oxides and halides

have a direct implication that the corresponding activation energies and temperatures for movement and thereby diffusion of these defects are appreciably larger in the case of former [24]. All these factors impart alumina an exceptional thermal and chemical stability and the unique ability to accommodate, retain and preserve the defect structures in a much more disciplined manner. Alumina therefore represents a classic opportunity and a model platform to visualize, prototype, implement and thereafter actually evaluate engineering of defects in such a manner that quest for phosphor with a predictable dosimetric performance dispenses its premise.

The initial attempt towards Alumina as a host material which dates back to 1957, did not involve any intentional doping but plain Alumina samples representing various crystal phases, degree of hydration and chemical purity. The magnitude of TL signal in synthetic sapphire which is highly crystalline phase of alumina i.e. α -Al₂O₃ was found to be relatively large but typical sensitivity of these samples was about a tenth of that of TLD 100 [25]. Despite this low sensitivity, Alumina due to its thermal and chemical inertness, acceptably low atomic number, ready availability at a decidedly economical price, was still regarded as a serious contender for radiation measurements and therefore invited attempts that were sporadic but fervent and involved various dopants. In 1967, studies related with effect of Chromium (Cr) on Al₂O₃ revealed TL emission around 400-450 °C in the red region of the visible frequency spectrum [26]. But the thermal noise associated with these temperatures interfered with the signal itself rendering emission spectrum inconvenient for reading. The studies carried out so far were generally confined to samples acquired out of standard commercial alumina based products which were made for purposes other than dosimetry.

First step forward in improving the sensitivity of Al_2O_3 is due to the Indian Scientists who methodically devised dopants Si and Ti using a technique known as flame synthesis which involved heating the mixtures with Oxygen-Burshane (N-Butane 60%, iso- butane 18%, propane 14%) flame. They could achieve a clear fivefold increase in sensitivity over TLD 100 [27]. The next attempt involved use of dopants Mg, Ti in Al_2O_3 and revealed the TL response to be linear between 1 mGy and 10 kGy [28]. In the same year i.e. 1980 it was reported that single crystals of alumina grown in Molybdenum crucible could successfully measure doses as low as 0.1 mGy and the reason to this was ascribed to the presence of impurities Ti and Mo [29]. These attempts were however based on an approach that typically reflected a traditional mindset namely an emphasis on substitutions at cationic site.

The lateral thinking that the connection of anionic deficiencies in oxides with emissive properties too deserves to be investigated, lead Kortov and colleagues at Ural State Technical University Russia to identify the decisive role of oxygen vacancies in shaping up the luminescent properties of Zirconium oxide initially [30] and then about a decade later in Al_2O_3 [31]. The notion that led to the extension of these studies from ZrO_2 to Al_2O_3 was formed on the results of TL and **thermally stimulated exo-electron emission** (TSEE) studies. Both of these processes originate from a phenomenon known as Auger Recombination.

Earlier investigations on α - Al_2O_3 doped with Chromium had revealed that occurrence of TL was synchronous with TSEE and this was not merely accidental but they shared an intimate connection not only with each other but also with the presence of defects i.e. color centers. In TSEE a sample that has been exposed to radiation earlier is heated. The trapped electron thus gets liberated and subsequently gets localized at another trap. This diffusion continues unless and until it recombines with a hole (mostly a trapped one). The energy of

recombination is then imparted to a third electron and may cause to its transition to the states above vacuum level. Thus electron- hole recombination leads to TSEE. Likewise in TL, the first stage i.e. liberation of trapped electron to conduction band is initiated thermally; therefore activation energy of TSEE corresponds to thermal activation energy of traps. Like in TL, this description of process is equally applicable even when trapped charge carrier is a hole.

A variant of this process is also possible in which the energy released during recombination is transferred to an electron localized at an impurity rather than to the one occupying valence/conduction is known as '*two-center Auger emission*'. The probability of occurrence of TSEE and thereby the TL is governed by strength of Auger mechanism which in turn depends on the ratio of concentration of electron (hole) traps and separation between electron trap and the center where Auger recombination happens. The probability of this mode of relaxation increases significantly if the impurity is positioned nearby. Thus in order to increase the TL sensitivity the necessary condition is to ensure simultaneous existence of hole and electron traps in sufficiently large concentration. It is possible to realize such condition in Al_2O_3 by doping with Mg. Here Al^{3+} is substituted by Mg^{2+} which causes formation of hole trap centers and oxygen vacancies which compensate for excess negative charge. In the case of doping Alumina with Mg, vide '*two-center Auger emission*' formalism it was observed that, TSEE was accompanied by F center emission regardless of the polarity of the thermally liberated charge carrier i.e. hole or electron. This provided a valuable insight to Kortov, Akselrod and their colleagues that Oxygen vacancies in the form of F and F^+ centers act as traps as well as emission centers and therefore are of key significance in so far as enhancement of TL sensitivity of alumina is concerned [32].

In a bid to further boost the concentration of oxygen vacancies Akselrod intentionally melt alumina in the ambience of *graphite*. The strongly reducing atmosphere provided by hot graphite ensures a low partial pressure of oxygen through $C + O_2 = CO_2 \uparrow$ and $2 C + O_2 = 2CO \uparrow$

The degree of difficulty in reduction of a particular metal oxide depends on the affinity of that metal for the oxide lattice, a property characterized by the standard free energy of formation for the oxide. The heat of formation of CO_2 is -94 kcal and that of CO is -26 kcal. Therefore, Reaction 1 is favored at temperatures lower than about 650 °C, whereas Reaction 2 is expected to dominate at higher temperatures. Notably, reaction 1 only incurs a small change in volume and therefore the change in entropy is negligibly small. Reaction 2, in contrast, involves an increase in volume and thereby larger change in entropy as well [33]. This implies that carbon can theoretically remove oxygen from any oxide provided the temperatures are high enough.

Next portion of the chapter presents a new process concept for synthesis of $Al_2O_3: C$ which effectively generates dosimetrically relevant defects and that too in a manner which is straightforward and highly economical.

1.11. Alternative approaches for preparation of dosimetric grade $\alpha-Al_2O_3: C$

Conventional method of synthesis of $\alpha-Al_2O_3: C$ uses Czochralski crystal growth. This ‘single crystal’ approach is expected to pose certain difficulties as crystal growth takes place at a specific temperature/growth rate and during the course of crystal growth, vacancies in the aluminum oxide melt have a tendency to drive forward as a result the defect concentration shows an increase along the growth axis and in the part of the crystal that solidifies last, the F center concentration is reported to be maximum. Therefore, in this mode of synthesis it is not possible to manage the extent of incorporation of carbon into lattice and achieve homogeneity

in nature and concentration of defects. As a result dosimetric properties show undesirable variation across different regions of crystal [34]. Further the crystal growth route is time consuming and needs expensive equipment. These factors increase the basic cost of the phosphor as well as overheads. The need to deal with these limitations of such a varied nature has prompted the successful development of a new low- cost ‘polycrystalline’ pathway for synthesis this high performance multifunctional phosphor. Following are the techniques for synthesis of $\text{Al}_2\text{O}_3\text{:C}$ which effectively generates dosimetrically relevant defects and that too in a manner which is straightforward and highly economical.

1.11.1. Post-Growth Thermal Impurification (PGTI) Technique

For the synthesis of $\alpha\text{-Al}_2\text{O}_3\text{:C}$ we proceed by heating a pre-formed pure alumina crystal in graphite environment to the temperatures below its melting point in vacuum rather than in the presence of Argon as was attempted earlier and further examine the TL/OSL dosimetric implications of the defects thus produced. Since this new technique sets out to build the defects in an alumina crystal whose growth has already been carried out by processing it at elevated temperatures in a novel ambience of vacuum in the presence of carbon in the form of graphite, it is referred to as Post-Growth Thermal Impurification Technique (PGTI) described below, presented schematically in fig. 1.6.

This process is based on the concept of a measured incorporation of impurities into solids by means of thermal diffusion whose speed and extent is well defined due to the fact that the temperatures involved are well below the melting point of solid, in particular alumina wherein diffusion is initiated at the surface of crystal and progressively expected to advance to its core. This technique is therefore anticipated to realize a slow and steady generation of defects and therefore is expected to enable the monitoring of thermal evolution of these defects vis-a-vis

TL/OSL properties which is quite relevant in understanding the systematics of the mechanisms responsible to these properties.

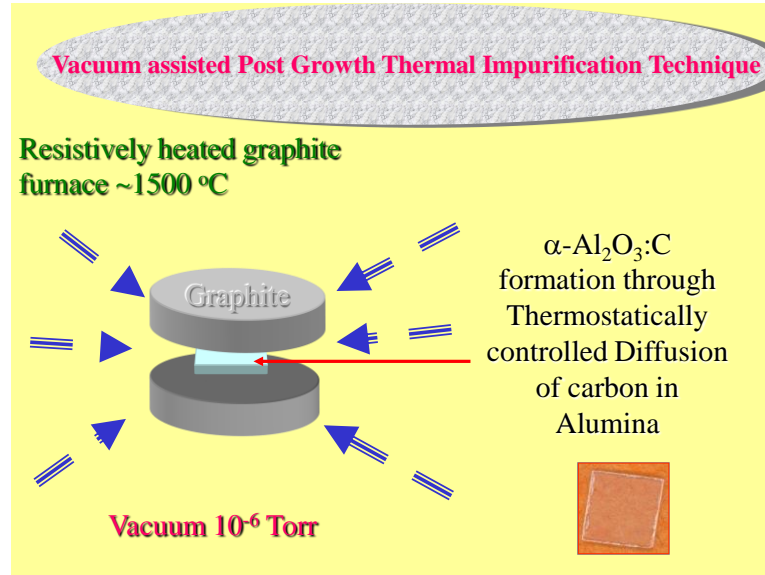


Figure 1.6. The schematic presentation of PGTI process for synthesis of $\alpha\text{-Al}_2\text{O}_3\text{:C}$

Experimental

In PGTI method, commercially available grown plain single-crystal $\alpha\text{-Al}_2\text{O}_3$ (size 10 mm \times 10 mm and thickness 0.4 mm) were heated in a furnace in the presence of graphite at the temperatures ranging from 1100 to 1500°C in the vacuum of $\sim 10^{-6}$ Torr. The vacuum hot furnace consists of two units, one its main vacuum chamber and the other is its control unit as shown in fig. 1.7. The single crystal along with the graphite powder was placed in the graphite crucible which was placed in the vacuum chamber. Now the chamber is subjected to the rotary pump to create the vacuum of (10^{-2} mbar) inside it. Once the rotary vacuum is achieved the chamber is connected to the rotary via diffusion pump to have a vacuum of 10^{-6} mbar. The temperature of the furnace was controlled to within $\pm 1^\circ\text{C}$ using a temperature controller Eurotherm 2416 in which the process parameters such as heating and cooling rate, target

temperature and the duration at that temperature can be set. Samples were processed for different process parameters and subsequently cooled to the room temperature. Uniform heating and cooling rates of 20°C/min were used. The samples were given a post-processing annealing treatment at 900°C for 10 min.



Control



Furnace



Graphite heater

Figure 1.7. The vacuum furnace used for PGTI samples.

The $\alpha\text{-Al}_2\text{O}_3$ crystals processed in vacuum at 1500°C in presence of graphite for 90 minutes were found to possess excellent TL and OSL response. Hence the studies were mostly conducted for $\alpha\text{-Al}_2\text{O}_3$ samples processed at 1500°C for 90 minutes in presence of graphite.

1.11.2. Electron-gun method

In the earlier technique for the synthesis of dosimetry-grade $\alpha\text{-Al}_2\text{O}_3\text{:C}$, in which a pure $\alpha\text{-Al}_2\text{O}_3$ crystal is heated to temperatures of 1500°C in the graphite environment and vacuum [35] allows better control over defect formation. However, the process depends on availability of single crystals of alumina as a necessary prerequisite.

In the conventional process for fabrication of OSL dosimeters, synthesized $\alpha\text{-Al}_2\text{O}_3\text{:C}$ single crystals are crushed to a powder. The TL sensitivity of powdered material has been found to be dependent on the grain size. Interestingly, the sensitivity increases with grain size and nearly saturates when the grain size is 80–100 nm [36]. This indicates that growth of single-crystalline material for dosimetry applications is not necessary and polycrystalline material with sufficient grain size may be an acceptable dosimetry material. Therefore, a process of melting polycrystalline alumina in vacuum in the presence of graphite followed by cooling was envisaged as a possible simple process for preparation of dosimetry-grade $\alpha\text{-Al}_2\text{O}_3\text{:C}$ [37].

To confirm the feasibility of this concept, we have employed the electron gun evaporation system shown in fig. 1.8, which is normally used for vacuum deposition of thin films, to realize temperatures high enough to melt alumina in the presence of graphite. For this purpose, commercially available polycrystalline alumina powder of 99.99% purity (Make: Aldrich) was pressed into pellets of 10 mm diameter and 2 mm thickness at a pressure of 50 kg/cm². The pellets were sintered at 1200°C for 8 h. Subsequently, the pellets were placed in an electron gun crucible of ~20 mm diameter and 11.5 mm height, of an electron gun system

(Hind High Vacuum make Model: EBG-PS-3 K). A graphite liner was used around alumina pellets to provide a reducing environment necessary for the formation of defects suitable for dosimetry. The pellets were slowly heated to melting temperature (in 20 min.) and were maintained in molten state for 10 min. Subsequently, the material was cooled to room temperature in 5 min. The material so obtained was characterized for its crystalline, optical, and dosimetric properties. The material prepared without the use of graphite liner did not show good response in either TL or OSL modes.

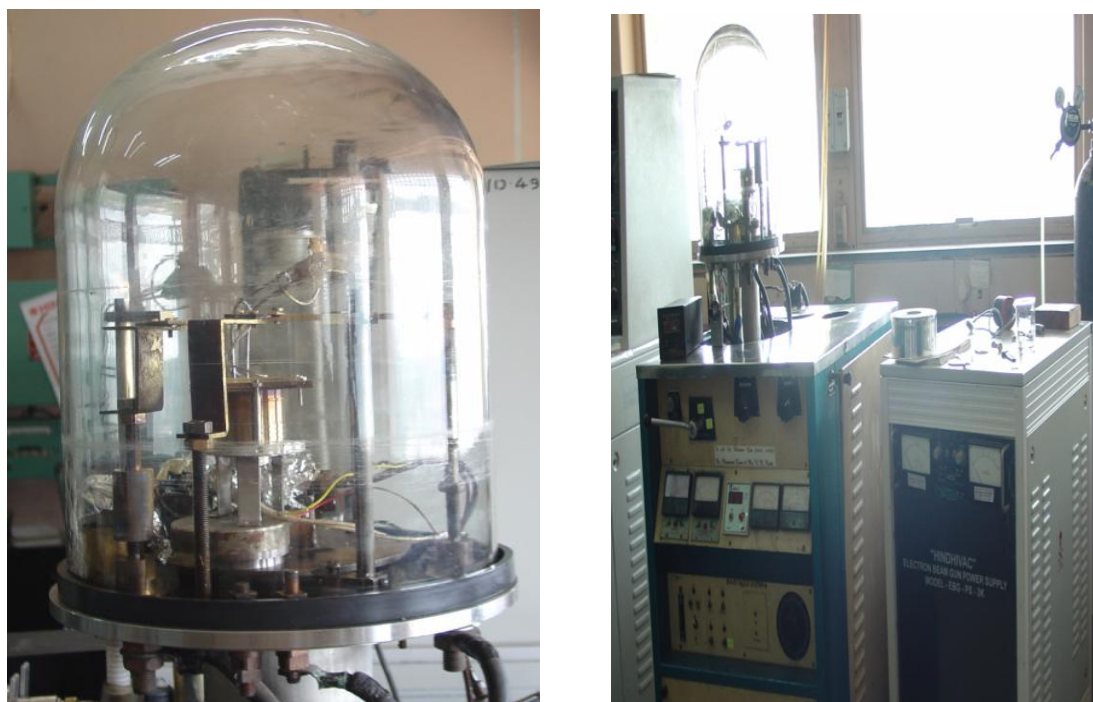


Figure 1.8. Electron gun evaporation system

1.11.3. Melt Processing technique for Scaled up Synthesis of $\alpha\text{-Al}_2\text{O}_3\text{:C}$

In this method, a stack of sintered pallets of polycrystalline alumina powder weighing ~50 gm was placed in a graphite crucible and then was melted in high temperature vacuum induction furnace shown in fig. 1.9 at 2000°C at 10^{-6} Torr vacuum. Subsequently the furnace was cooled down to room temperature (RT). The material formed was then annealed at 850 °C.



Figure 1.9. Inductively heated vacuum melting system

Fifteen batches of polycrystalline $\alpha\text{-Al}_2\text{O}_3$ (99.99% pure, 100 g each) were processed using melt processing technique under reducing atmosphere in the high temperature vacuum induction furnace for large scale production of dosimetric grade $\alpha\text{-Al}_2\text{O}_3\text{:C}$ phosphor. The processed $\alpha\text{-Al}_2\text{O}_3\text{:C}$ phosphor was characterized for its suitability as a viable OSL phosphor for large scale personnel and environmental monitoring applications. The TL and OSL sensitivity variation in all the processed batches of $\alpha\text{-Al}_2\text{O}_3\text{:C}$ is found to be within $\pm 30\%$ and three batches have sensitivities comparable to that of commercially available $\alpha\text{-Al}_2\text{O}_3\text{:C}$ phosphor (from Landauer Inc. USA). The material has shown negligible fading in both TL and OSL domain for a period of 3 months compared to its TL/OSL signal obtained after 24 hours of exposure. The processed material has very good linearity in the range 20 μGy to 10 Gy. The minimum measurable dose (MMD) is found to be 20 μGy (3σ). The application of this material as a neutron dosimeter is discussed in chapter 5.

Table 1.2. Comparison of doped $\text{Li}_2\text{B}_4\text{O}_7$ (LBO) based TL phosphors prepared using different methods

S.N.	Phosphor and Method of Preparation	TL sensitivity w.r.t. LiF:Mg,Ti (TLD-100)	TL emission (nm)	Dose range (Gy)	Remarks
1.	LBO: Mn (0.1 wt. % using Schulman et al. method [38]. Li_2CO_3 and H_3BO_3 as starting materias, are mixed along with appropriate amount of dopant, melted at 950°C and then rapidly cooled to room temperature. The resulting glass material is reheated at 650°C to complete crystallization. Main TL peak $\sim 200^\circ\text{C}$	0.4	600	10^{-4} to 10^3	Emission at 600nm is far from the good response region of most photomultipliers. The phosphor is affected by humidity.
2.	LBO: Mn, Si (0.1, 0.25 wt %), Preparation method is similar to Schulman et al. [38].	~ 0.4	600	10^{-4} to 10^3	Adding silica (0.25% by weight improves moisture resistance. [39]
3.	LBO: Ag (0.1 wt. %) [40]. Preparation method is similar to Schulman et al. [38]	Marginal improvement in the sensitivity and is comparable to LBO: Mn	290	-	-
4.	LBO: Cu, Ag (0.02, 0.02% by weight) Preparation method is similar to Schulman et al. [38]	-	360	-	Reproted to be least attractive for medical dosimetry [41]
5.	LBO: Cu; LBO powder containing the activator compound is heat-treated in air in a platinum boat for about 1h at a temperature of $900\text{-}913^\circ\text{C}$, just below the melting point (917°C) of LBO. TL peak $\sim 205^\circ\text{C}$ at a heating rate of 7°C/s	3 (20 times higher than LBO: Mn)	360	3×10^{-4} to 10^3	Phosphors prepared by stoichiometric matrix composition exhibit greater moisture resistance [42]. Pradhan etal. [43] studies the suitability of various raw materials with regard to the presence of unintentional impurities, for preparation of LBO: Cu.
6.	LBO: Cu (0.1 mol %). Solid state diffusion method. The thoroughly mixed powders were heated at 700°C for several hours and then slowly cooled[44]	4	369	0.27 to 10	-
7.	LBO: Cu single crystals grown by Czochralski method [45]	Sensitivity higher than the powder samples	366	2×10^{-4} to 20	Minimum detectable dose (MDD) is $10\mu\text{Gy}$. Together with higher sensitivity, single crystals are much less hygroscopic.
8.	LBO: Cu sintered pellets. Main TL peak $\sim 210^\circ\text{C}$. [46]	0.5	360	10^{-4} to 3×10^3	MDD is $20\mu\text{Gy}$. During preparation SiO_2 was added for preventing effects of humidity
9.	LBO: Cu, In (0.07, 0.05 Wt. %), sintered ($\sim 850^\circ\text{C}$) pellets. Main TL peak $\sim 210^\circ\text{C}$ [47]	0.7-1.0	360	10^{-4} to 3×10^3	MDD is $10\mu\text{Gy}$. During preparation SiO_2 was added.
10	LBO: Cu, In, Ag (0.07, 0.07, 0.05 wt. %). Main TL peak $\sim 190^\circ\text{C}$ [47]	2.0	360	10^{-4} to 3×10^3	MDD is $10\mu\text{Gy}$
11.	LBO: Cu, Ag, Mg (0.02% by weight each) prepared by the sintering technique [48] Main TL peak $\sim 219^\circ\text{C}$	-	421, 380, 350		Proper concentrations of Ag and Mg can enhance the TL of LBO: Cu. Ag can enhance $\sim 219^\circ\text{C}$ & reduce $\sim 130^\circ\text{C}$ TL peaks [39]

1.12. Lithium Borate ($\text{Li}_2\text{B}_4\text{O}_7$)

So far we have described various materials for radiation dosimetry with a special emphasis on $\text{Al}_2\text{O}_3:\text{C}$ and also discussed the processes to realize its synthesis. Besides its sensitivity, a crucial parameter of a bonafide phosphor material is its tissue equivalence that is its ability to mimic the response of a human tissue. In the light of this, we have also investigated dosimetric behavior of Lithium Borate (LBO) having a Z_{eff} value ~ 7.3 which is remarkably close to that of human tissue viz. 7.42 as compared to $\text{Al}_2\text{O}_3:\text{C}$.

Since material in the single crystal form potentially offers a better sensitivity as compared to polycrystalline material, we have investigated the TL and OSL response of single crystals of LBO. Our studies show that single crystals of this material doped with Cu exhibit significantly high TL sensitivity which on co-doping with Ag shows further improvement in terms of OSL as well. Synthesis details of this material system have been discussed at length in a subsequent chapter. Table 1.2 Shows an overview of LBO based phosphors with various dopants.

1.13. Recent advances in TL and OSL

The recent advances are immense and the field has grown mature in terms of its applications and understanding e.g. the favorable dosimetric characteristics of BeO namely high sensitivity to ionizing radiation, a linear dose response over six orders of magnitude (ranging from $\sim 5 \mu\text{Gy}$ to $\sim 5 \text{Gy}$), a low effective atomic number ($Z_{\text{eff}} = 7.2$), and relatively low cost [49-51] have lead to the development of OSL dosimetry system based on BeO ceramics by Thermalox TM 995, Brush Wellman Inc., USA as an alternative to $\text{Al}_2\text{O}_3:\text{C}$, particularly for personal and medical dosimetry applications.

OSL unlike TL does not require elevated temperatures and therefore it has become possible to extend its application in real-time, optical-fiber based dosimetry that can be used for dose verification in radiotherapy, determination of entrance and exit doses in mammography and estimations of skin dose in interventional radiology. In addition to this, it has also been utilized in the characterization of radio-therapeutic beams by recording one-dimensional dose profiles.

Bio-dosimetry is another latest application of OSL and TL in which hair, nail and dental enamel are used for the estimation of doses received by an individual in an accidental scenario. Fading of signal in biological samples however, is a serious concern and warrants efforts in this direction. OSL technique has also found application in forensics pertaining to nuclear terrorism involving illicit trafficking of radioactive sources. Recently it has also been demonstrated that using OSL it is possible to monitor levels of uranium-235 in enrichment plants. This development has got direct bearing on the implementation of IAEA safeguards.

Use of OSLDs and TLDs in Space-Radiation Fields: Conventional plastic nuclear track detectors (PNTDs) used in space dosimetry typically are sensitive for LETs ~ 5 keV and above. Whereas, the efficiency of OSLDs and TLDs is best for LET range ~ 10 KeV/ μ m and below. Therefore the desirable and appropriate type of personal dosimeter that meets the required criteria (for low and high LET) for current space applications is a PNTD in combination with TLDs and OSLDs.

Another novel application of TL is the development of TL detector foil, of thickness 0.3 mm and diameter 60 mm, containing a mixture of highly sensitive LiF:Mg,Cu,P powder and Ethylene TetraFluoroEthylene (ETFE) polymer the Institute of Nuclear Physics of the Polish Academy of Sciences (IFJ) in Kraków for 2-D dosimetric technique for radiotherapy [52]. Novel thermoluminescence dosimetry (TLD) foils, developed from the hot-pressed mixture of

LiF:Mg,Cu,P (MCP TL) powder and ethylene-tetrafluoroethylene (ETFE) copolymer, have been applied for 2-D dosimetry of radiotherapeutical proton beams at INFN Catania and IFJ Krakow. They have demonstrated the possibility of measuring 2-D dose distributions with point resolution of about $0.5 \times 0.5 \text{ mm}^2$ [53].

1.14. Summary

In this chapter we have presented an introduction of Luminescence phenomenon that includes the details specific to Thermally Stimulated Luminescence and Optically Stimulated Luminescence. Subsequently an overview of popular phosphor materials used in radiation dosimetry is presented. Two of the materials that are subject of present study i.e. $\alpha\text{-Al}_2\text{O}_3\text{:C}$ and $\text{Li}_2\text{B}_4\text{O}_7$ have been discussed in detail. $\alpha\text{-Al}_2\text{O}_3\text{:C}$ developed using different approaches was presented. We have also seen how the defects produced due to dopants can decisively improve sensitivity of a material system. Thus the dosimetric performance of a material critically depends on defect concentration, its nature and distribution throughout the host lattice. Consequently, studies of these defects assume critical importance as they not only offer important insights into the mechanism of their operation but also provide clues about prospective material systems which can be relevant to dosimetric applications. Next chapter deals with techniques that are often used for characterization of such defects and also includes a brief on their classification scheme.

References:

1. F. Daniel, C. A. Boyd, D. F. Sanders, *Science* **117**, 343 (1953).
2. J.T. Randall, M.H.F. Wilkins, *Proc. R. Soc. A* **184** 366 (1945).
3. G.F.J. Garlick, A.F. Gibson, *Proc. Phys. Soc.* **60** 574 (1948).

4. C.E. May, J.A. Partridge, *J. Chem. Soc.* **40** 1401 (1964).
5. M.S. Rasheedy, *J. Phys.: Condens. Matter* **5** 633 (1993).
6. Eduardo G. Yukihara and S. W. S. McKeever, *Optically Stimulated Luminescence: Fundamentals and Applications, A John Wiley and Sons, Ltd., Publication* (2011).
7. L. Botter-Jensen and S. W. S. McKeever, *Radiat. Prot. Dosim.* **65** (1-4), 273 (1996).
8. R. C. Yoder and M. R. Salasky, *Health Phys.*, **72**, S18 (1997).
9. C. R. Rhyner and W. G. Miller, *Health Phys.*, **18**, 681–684 (1970).
10. A. S. Pradhan and R. C. Bhatt, *Phys. Status Solidi A*, **68**, 405–411 (1981).
11. S. D. Miller, G. W. R. Endres, J. C. McDonald, K. L. Swinth, *Radiat. Prot. Dosim.*, **25** 201 (1988).
12. E. Bulur, *Radiat. Meas.*, **26**, 701 (1996).
13. B. G. Markey, L. E. Colyott and S. W. S. McKeever, *Radiat. Meas.*, **24**, 457 (1995).
14. M. S. Akselrod and S. W. S. McKeever, *Radiat. Prot. Dosim.*, **81**, 167 (1999).
15. S. W. S. McKeever and M. S. Akselrod, *Radiat. Prot. Dosim.*, **84**, 317 (1999).
16. S. W. S. McKeever, M. S. Akselrod and B. G. Markey, *Radiat. Prot. Dosim.*, **65**, 267(1996).
17. M. S. Akselrod, N. Agersnap Larsen, and S. W. S. McKeever, *Radiat. Meas.*, **32**, 215(2000).
18. V.V. Antonov –Romanovski, I.F. Keirum-Marcus, M.S. Proshina, Z.A. Trapeznikova, *Conf. of the Acad. Of Sciences of the USSR on the peaceful Uses of Nuclear Energy, Moscow, 1955, USAEC Report AEC-tr-2435 (Pt.1)* 239 (1956).
19. P. Bräunlich, D. Schafer and A. Scharmann, *Proc. International Conf. on Lum. Dosim.* , USAEC P. 57 (1967).
20. E.N. Sanborn and E.L. Beard, *ibid.* P. 183.
21. H.O. Albrecht and C.E. Mandeville, *Phys. Rev.* **101** 1250 (1956).

22. B.G. Markey, L.E. Colyott and S.W.S. McKeever, *Radiat. Meas.* **24** 457 (1995).
23. R. Prescott and M.J. Graham, *Oxid. Met.* **38** 233 (1992).
24. A.I. Popov, E.A. Kotomin, and J. Maier, *Nucl. Instrum. Methods. in Physics Research B* **268** 3084 (2010).
25. J. F. Rieke, F. J. Daniels, *J. Phys. Chem.* **61** 629 (1957).
26. C.R. Philbrick, W.G. Buckman and N. Underwood, *Health. Phys.* 798 (1967).
27. S.K. Mehta and S. Sengupta *Phys. Med. Bio.* **21** 955 (1976).
28. M. Osvey and T. Biro, *Nucl. Instrum. Methods* **175** 60 (1980).
29. J. Kvapil, Z. Vitamvas, B. Perner, Jos. Kvapil, B. Maneck, O. Admatez, and J. Kubelka, *Krist. Tech.* **15** 859 (1980).
30. V.S. Kortov, J.M. Polezhaev, A.I. Gaprindashvily, A.L. Shaljapin, *Izv.. Akd. Nauk. SSSR. Ser. Neorg. Mater.* **11** 257 (1975).
31. V.S. Kortov, *Jpn. J. Appl. Phys.* **24** 65 (1985).
32. V.S. Kortov, T.S. Bessonova, M.S. Akselrod, I.I. Milman, *Phys. Stat. Sol. (a)* **87** 629 (1985).
33. J. Barker, M.Y. Saidi and J.L. Swoyer, *Electrochem. Sol. Stat. Lett.* **6** (2003) 53.
34. T.L. Gimadova, T.S. Bessonova, I.A. Tales, L.A. Avvkumova and S.V. Bodyachevsky, *Radiat. Prot. Dosim.* **33**(1990) 47.
35. M.S. Kulkarni, D.R. Mishra, K.P. Muthe, A. Singh, M. Roy, S.K. Gupta and S. Kannan, *Radiat. Meas.* **29** (2005) 277.
36. M.S. Akselrod, V.S. Kortov and E.A. Gorelova, *Radiat. Prot. Dosim.* **47** (1993) 159.
37. J.H. Schulman, R.D. Kirk, E.J. West. *Luminescence dosimetry CONF- 650637, US At. Energy Comm. Symp. Ser. 8*, p. 113 (1967).

38. K.P. Muthe, M.S. Kulkarni, **N.S. Rawat**, D.R. Mishra, B.C. Bhatt, Ajay Singh and S.K. Gupta, *Journal of Luminescence*. Vol. 128 (2008) 445-450
39. L. Botter-Jensen, P. Christensen, *Acta Radiol. Suppl.* **313** 247 (1972).
40. J.J.ames Thompson, Zeimer, L. Paul, *Health Phys.* **25** 435 (1973).
41. B.F. Wall, C.M.H. Driscoll, J.C. Strong, E.S. Fisher, *Phys. Med. Biol.* **27** 1023 (1982).
42. S.W.S. McKeever, *Thermoluminescence of Solids*, Cambridge University Press, (1985)
43. A.S. Pradhan, R.C. Bhatt, K.G. Vohra, *Radiochem. Radioanal. Lett.* **53** 103 (1982).
44. D.I. Shahare, B.T. Deshmukh, S.V. Moharil, S.M. Dhopte, P.L. Muthal, V.K. Kondawar., *Phys. Status Solidi A* **141** 329 (1994).
45. M. Martini, F. Meinardi, L. Kovacs, K. Polgar, *Radiat. Prot. Dosim.* **65** 343 (1996).
46. C. Furetta, M. Prokic, R. Salamon, V. Prokic, G. Kitis, *Nucl. Instrum. Methods Phys. Res. Sect. A* **456** 411 (2001).
47. M. Prokic, *Radiat. Meas.* **33** 393 (2001).
48. X. Zheng, Ye, T. Qiang, Z.C.hun Xiang, *Sci. China-Phys. Mech. Astron.* **50** 311 (2007).
49. M. Sommer, and J. Henniger, *Radiat. Prot. Dosim.*, **119**, 394–397 (2006).
50. M. Sommer, R. Freudenberg, J. Henniger, *Radiat. Meas.*, **42**, 617–620 (2007).
51. M. Sommer, A. Jahn, J. Henniger, Beryllium oxide as optically stimulated luminescence dosimeter. *Radiat. Meas.*, 43, 353–356 (2008).
52. P. Olko, B. Marczevska, L. Czopyk, *Radiat. Prot. Dosim.*, **118**, 213–218 (2006a).
53. L. Czopyk, M. Klosowski, P. Olko, J. Swakon, M. P. R. Waligorski, T. Kajdrowicz, G. Cuttone, G. A. P. Cirrone and F. Di Rosa, *Radiat. Prot. Dosim.*, pp. 1–5 (2007).

Chapter 2

Methods of TL/OSL analysis and defect characterization techniques

2.1. Introduction

In the previous chapter we have amply discussed Luminescence phenomena, their origins along with the associated material systems. For a typical phosphor material to qualify to the status of a bonafide phosphor, it is necessary to understand its defect structure and establish its correlation with the observed sensitivity and also with the variations in process parameters. Thus the characterization of a phosphor with regards to the nature of defects, their concentration and distribution is an integral part of development of synthesis protocol. Moreover, the study of these defects offers important insights into the TL and OSL mechanism and provides answers to various questions like which dopant in a given host material can improve its sensitivity and dosimetric performance, and in what concentration?

The study of defects and ability to generate them in a controlled manner is central to deliver a dosimetric grade material by various pathways one such being the process of diffusion of a dopant into the host lattice. This chapter addresses such issues related to material synthesis and includes a précis on its TL and OSL kinetic analysis; followed by the description of other spectroscopic techniques like Electron Paramagnetic Resonance, Positron Annihilation Spectroscopy, Photoluminescence, Optical Absorption etc. that can probe the role of defects involved and suggest a possible luminescence mechanism.

2.2. Defects in solids

The crystalline structure of solids forms the basis for understanding their properties. Most real systems, however, are not perfect crystals. To begin with, even in those real solids which come close to the definition of a perfect crystal there are a large number of defects. For instance, in the best quality crystals produced with howsoever great care for high-technology applications,

such as Si wafers used to manufacture electronic devices, the concentration of defects is still there and is rarely below few parts per billion (ppb). These imperfections play an essential role in determining the electronic and mechanical properties of the real crystal [1].

Moreover, there are many solids whose structure has none of the characteristic symmetries of crystals (amorphous solids or glasses) as well as many interesting finite systems whose structure has some resemblance to crystals but they are not of infinite extent [1].

A natural way to classify defects in crystalline structure according to their dimensionality is:

(i) Zero-dimensional or “point” defects consist of single atomic sites, or complexes of very few atomic sites, which are not in the proper crystalline positions; examples of point defects are missing atoms called vacancies, or extra atoms called interstitials. Point defects may also consist of crystalline sites occupied by atoms foreign to the host crystal; these are called substitutional impurities [1].

(ii) One-dimensional defects consist of lines of atomic sites perturbed from their ideal positions; these can extend for distances comparable to the linear dimension of the solid. The linear defects are called dislocations [1].

(iii) Two-dimensional defects consist of a plane of atomic sites where the crystalline lattice is terminated; this is a true surface of a crystal. Alternatively, a two-dimensional defect may correspond to the intersection of two crystallites (grains); these are called grain boundaries and interfaces [1].

2.2.1. Thermodynamics of defects

Of all the defects mentioned above, the point defects are distinctive in the respect that the presence of defects like dislocations always leads to increase in free energy of a material while

the point defects tend to reduce the same. The reason for this can be traced back to second law of thermodynamics,

$$G = H - TS \quad (2.1)$$

Where G is the Gibbs free energy of a given system, H is the heat content or enthalpy and TS is the entropy, or disorder. The enthalpy term in equation (2.1) conveys that it is necessary to provide energy to the atoms for creation of defects. However, due to the portion of the Maxwell-Boltzmann distribution that extends to higher energies, quite a few atoms in the solid may acquire enough thermal energy to get displaced from the equilibrium positions and therefore can produce defects at all temperatures. The production of such defects, leads to increased disorder (ΔS is positive). Correspondingly the term $T\Delta S$, especially in case of crystalline hosts, is large in the initial stage. The contributions of enthalpy and entropy terms being opposite, for a certain (maximum) concentration of defects, the free energy exhibits a minimum suggesting that the formation of point defects is admissible and therefore spontaneous [2]. This concentration of defects is called **thermal equilibrium concentration** and can be controlled by temperature and pressure.

Energy is required to form a defect is endothermic process. Although there is a cost in energy, there is a gain in entropy in the formation of a defect. At equilibrium, the overall change in free energy of the crystal due to the defect formation is zero according to:

$$\Delta G = \Delta H - T\Delta S \quad (2.2)$$

At any temperature, there will always be an equilibrium population of defects. The number of defects (for an MX crystal) is given by:

$$n_s \approx N \exp\left(-\frac{\Delta H_s}{2kT}\right) \quad (2.3)$$

Where n_s is the number of Schottky defects per unit volume, at absolute temperature T, in a crystal with N cation and N anion sites per unit cell volume, and ΔH_s is the enthalpy required to form one defect. The number of Frenkel defects present in a MX crystal is:

$$n_s = (N N_i)^{1/2} \exp\left(-\frac{\Delta H_F}{2kT}\right) \quad (2.4)$$

Where n_f is the number of Frenkel defects per unit volume, N is the number of lattice sites, and N_i the number of interstitial sites available, and ΔH_F is the enthalpy of formation of one Frenkel defect. If ΔH_F is the enthalpy of formation of one mole of Frenkel defects:

$$n_s = (N N_i)^{1/2} \exp\left(-\frac{\Delta H_F}{2RT}\right) \quad (2.5)$$

Knowing the enthalpy of formation for Schottky and Frenkel defects, one can estimate how many defects are present in a crystal

2.2.2. *Color centers*

The charge neutrality requirement makes it possible to enhance concentration of point defects much higher than that admissible to thermal equilibrium through the process of ‘doping’ with an element having a valence which is different than those forming host matrix. Doping of Ca^{++} into NaCl is a typical example of this. Oxides in particular, allow possibility of having defects in the form of mixed valence in cations and deficiency in anions and thus offer opportunity to further tune their properties through variations in either or both of them. The anionic vacancy in a crystal may be filled by one or more electrons, depending on the charge of the missing ion in the crystal. Electrons in such a vacancy tend to absorb light in the visible spectrum. As a result, a material which is transparent otherwise, becomes colored. The greater the number of such defects the more intense is the color of the compound. Therefore this point

defect is called color or F-center. The name F-center originates from the German word Farbzentrum. An F-centre thus can be regarded as a negative ion vacancy and an electron which is equally shared by the positive ions, surrounding the vacant lattice site. Alternatively holes may get trapped at a +ve ion vacancies to give rise to V-centers. In case of Oxides, when the vacancy is occupied by two electrons it is called neutral F centre and when occupied by one electron it is known as F^+ center. An F^+ center has a positive charge with respect to lattice. In case of oxides the neutrality condition requires presence of charge compensators to enable formation of F^+ centers. Aggregate of two F centers is called M centre while clusters of three and four F centers are called R and N centers respectively.

F centers may be produced by neutron irradiation or bombardment of material by heavy charged particles, or by addition of impurities or excess constituents. Another efficient technique to generate such color centers and defects in a given host lattice is the process of diffusion and in the next section we briefly discuss this process and its mechanism.

2.3. Defects and Diffusion

Diffusion of elements is possible because of the presence of defects. For e.g. substitutional diffusion occurs because of exchange of an atom with vacancies. Further, impurities are present at the interstitial positions, which could diffuse to any neighbouring vacant interstitial sites. This is called interstitial diffusion.

a) Diffusion Phenomena

Diffusion is a process of mass transport by atomic movement under the influence of thermal energy and a concentration gradient. Atoms move from higher to lower concentration region

(fig. 2.1.). If this movement is from one element to another e.g. Cu to Ni, then it is termed inter-diffusion. If the movement is within similar atoms as in pure metals, it is termed self-diffusion.

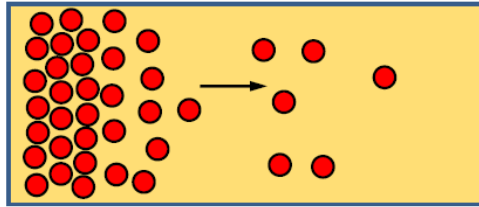


Figure 2.1. Diffusion of atoms

b) Diffusion Mechanism

Diffusion of atoms involves movement in steps from one lattice site to another. An empty adjacent site and breaking of bonds with the neighbor atoms are the two necessary conditions for this.

Vacancy Diffusion: This mechanism involves movement of atoms from a regular lattice site to an adjacent vacancy (fig. 2.2). Since vacancy and atoms exchange position, the vacancy flux is in the opposite direction.

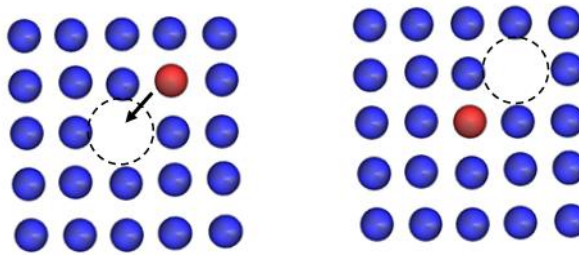


Figure 2.2. Vacancy diffusion

c) Kirkendall Effect

If the diffusion rates of two metals A and B in to each other are different, the boundary between them shifts and moves towards the faster diffusing metal. This is known as Kirkendall effect named after the inventor Ernest Kirkendall. It can be demonstrated experimentally by placing

an inert marker at the interface. This is a direct evidence of the vacancy mechanism of diffusion as the other mechanisms do not permit the flux of diffusing species to be different. Zn diffuses faster into Cu than Cu in Zn. A diffusion couple of Cu and Zn will lead to formation of a growing layer of Cu-Zn alloy (Brass) (fig. 2.3.).

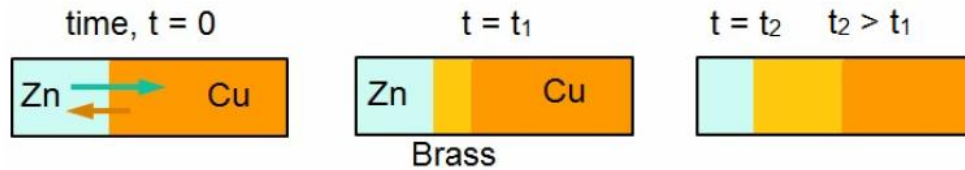


Figure 2.3. Kirkendall Effect

Same will happen in a Cu-Ni couple as Cu diffuses faster in Ni than vice versa. Since this takes place by vacancy mechanism, pores will form in Cu (of the Cu-Ni couple) as the vacancy flux in the opposite direction (towards Cu) will condense to form pores.

d) Fick's Law

i) Fick's First Law (Steady-state diffusion)

Steady-state diffusion is the situation when the diffusion flux is independent of time (e.g. diffusion of a gas through solid medium where concentration/pressure of the gas is kept constant at both the end). Fick's first law describes steady-state diffusion and is given by

$$J = -D \frac{dC}{dx} \quad (2.6)$$

Where, J is the diffusion flux or the mass transported per unit time per unit area and dC/dx is the concentration gradient. D is known as the diffusion coefficient.

ii) Fick's Second Law (Non- Steady state diffusion)

In most practical situations, diffusion is non-steady state i.e. diffusion flux and concentration gradient varies with time. This is described by Fick's second law

$$\frac{\partial C}{\partial t} = D \frac{\partial^2 C}{\partial^2 x} \quad (2.7)$$

A solution to this equation can be obtained for a semi-finite solid with certain boundary conditions.

e) Factors affecting Diffusion

Diffusing species: The magnitude of the diffusion coefficient, D , is an indication of the rate at which atoms diffuse. As the value of D is fixed for a given element in a given material, the extent of diffusion is first decided by the diffusing species itself.

Temperature: Temperature is a major factor which affects diffusion. Temperature dependence of the diffusion coefficient is expressed as

$$D = D_o \exp\left(-\frac{Q}{RT}\right) \quad (2.8)$$

Where, D_o is the pre-exponential factor and the Q is the activation energy for diffusion

2.4. Defects and Luminescence

In dielectric materials the probability of recombination of electron–hole pairs across the band gap (e.g., by exciton formation) is low [3]. In OSL materials, this recombination occurring at defects in the crystal is responsible for luminescence. The defect can first capture a hole and subsequently capture an electron (e.g., released from a trapping center), or vice versa. During the recombination process, the capturing of electron leaves defect in an excited state. Luminescence is the consequence of radiative relaxation of defect from its excited state to the ground state [4].

Important parameters describing the luminescence process are: emission wavelength, lifetime and quantum efficiency of the luminescence. The latter is related to the nature of pathway of relaxation that is whether radiative or non-radiative.

In OSL based luminescence dosimetry knowledge of the OSL emission wavelength is important when choosing the appropriate light detection system and optical filters, which in turn is also an important factor when choosing the stimulation wavelength. To take full advantage of the OSL process the stimulation wavelength should be longer than the emission wavelength to avoid the detection of any photoluminescence signal from other sources [4].

The lifetime of the luminescence center is vital in POSL mode to improve the signal-to-noise ratio or for time-resolved measurements. When a light pulse of short duration releases electrons from trapping centers, they are captured at a recombination center creating say N_e defects in the excited state, the concentration of these centers in an excited state decay exponentially (and eventually relaxes to ground state) w.r.t. time and is expressed as:

$$N_e(t) = N_0(t)\Delta e^{\left(-\frac{t}{\tau_R}\right)} \quad (2.9)$$

(where t is the time since the stimulation pulse and τ_R is the radiative decay time or mean lifetime of the luminescence center. The luminescence intensity is proportional to the rate of decay of centers in the excited state, dN_e/dt , which will also decay exponentially [4].

2.4.1. Selection Rule

The lifetime associated with optical transitions within defects in crystals can range from less than 10^{-9} s to $\sim 10^{-3}$ s [3]. This is determined by the relative probability of such transitions, which depends strongly on quantum mechanical selection rules that determine whether a transition is “allowed” or “forbidden.” First approximation predicts that when the wavelength

of the electromagnetic radiation (light absorbed or emitted) is large compared to the size of an atom or ion (electric dipole approximation), conditions as stipulated by quantum mechanics must be satisfied between the initial and final states for the transition to be allowed [4, 5].

Two selection rules that are valid for single and multi-electron centers are based on parity and spin. The parity (Laporte) selection rule states that only those transitions are allowed for which parity changes. For example, transition between energy levels within the f shell ($l = 3$) are forbidden, because the parity is given by $(-1)^l$ and the wavefunctions of both initial and final states have the same parity (both are odd, i.e., the signal of the wavefunction is changed under reversal of spatial coordinates, e.g., $x \rightarrow -x$, $y \rightarrow -y$, $z \rightarrow -z$). While the spin selection rule states that transitions between initial and final states characterized by different values of total spin angular momentum ($\Delta S \neq 0$) are forbidden. However, in solids these selection rules do not hold strictly and are relaxed as some forbidden transitions are still possible due to influence of the crystalline field or due to high-order term effects (e.g., magnetic dipole and electric quadrupole), which are not considered in the electric dipole approximation. Consequently, “forbidden” transitions can still be observed, although with low probability, that is, they are feeble and have relatively long lifetimes when compared to “allowed” transitions [3, 4, and 6].

2.4.2. *Quantum efficiency*

The quantum efficiency for the luminescence process is associated with number of centers that radiatively relax to the ground state compared to the centers that relax non-radiatively. In the fluorescence process, the quantum efficiency can be defined in terms of number of photons emitted by the center per unit time divided by the number of photons absorbed per unit time. Here the luminescence center is brought to the excited state by electron–hole recombination, but the concept of quantum efficiency defined in of the probability of radiative and non-

radiative transitions still applies. If the probability of radiative transition is $\Gamma_R = \tau_R^{-1}$, where τ_R is the mean radiative lifetime, and the probability of non-radiative transition is $\Gamma_{NR} = \tau_{NR}^{-1}$ where τ_{NR} is the mean lifetime for non-radiative transitions, the luminescence efficiency η can be expressed as [4,8]:

$$\eta = \frac{\Gamma_R}{\Gamma_R + \Gamma_{NR}} = \frac{\tau_R^{-1}}{\tau_R^{-1} + \tau_{NR}^{-1}} \quad (2.10)$$

2.4.3. *Configurational Coordinate diagram and Thermal Quenching*

Configurational coordinate diagram (refer fig. 2.4) helps in understanding several aspects of the luminescence process related to the interaction of the electrons with the vibrating environment. It also explains the possible dependence of the luminescence efficiency with temperature. In this diagram, one assumes the defect separated by a distance R_0 from the neighbouring ions and approximates the ionic vibrations about equilibrium position in the crystal to be harmonic. Therefore the potential energy curve for the ground state is parabolic and the vibrational energy states of the harmonic oscillator are represented by equally spaced horizontal lines within this parabola. The excited state may be represented in the same way, except that it can have an equilibrium position at a distance R'_0 different than R_0 . Electronic transitions are represented by vertical arrows as they occur much faster than the crystal relaxation around the new equilibrium position (Franck–Condon principle) [4,8].

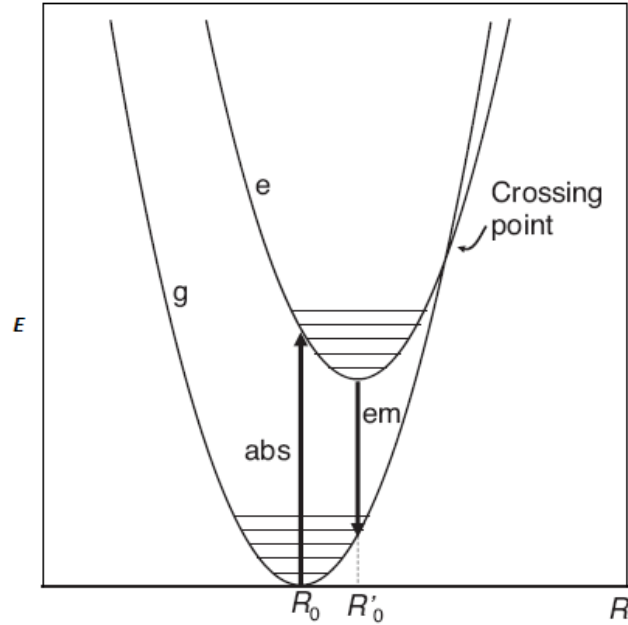


Figure 2.4. Configurational coordinate diagram representing the potential energy curves of the ground state (g) and excited state (e) of a luminescence center as a function of the separation R .

As represented in fig. 2.4, a transition can occur from the lowest vibrational energy level of the ground state to some higher vibrational energy level of the excited state (vertical arrow is labeled “abs” to indicate absorption). The system can then relax to a new equilibrium position in the diagram by phonon emission (lattice vibration), achieving the lowest vibrational energy level of the excited state. Now, from this point/state a radiative transition can occur to a high vibrational energy level of the ground state (vertical arrow labelled as “em” to indicate emission), after which it eventually relaxes again to the bottom of the ground state by phonon emission [4].

The configurational coordinate diagram also explains the difference in energy or wavelength of the absorption bands and emission bands of a luminescence center. As from fig. 2.4 it is evident that emitted photon has lower energy than the absorbed photon that results into the shifting of emission band to longer wavelengths when compared to the absorption band (Stokes shift). The

degree of the Stokes shift is attributed to the interaction (coupling) of electrons with the lattice vibration (phonons). Large Stokes shift is consequence of strong coupling [4].

As temperature increases the probability that the system will gain sufficient energy by phonon interaction to reach vibrational levels where cross-over of two parabolas is experienced also increases. If this happens, the system can relax to the ground state by phonon emission which represents a non-radiative transition. Clearly, the probability of such non-radiative transitions increases with temperature. Considering that the probability of non-radiative transition is $\Gamma_{NR} = \Gamma_0 e^{-E/kT}$, where E is related to the energy required for the system to reach the crossing point in the configurational diagram and Γ_0 is a constant, Equation (2.10) can be re-written as:

$$\eta = \frac{\Gamma_R}{\Gamma_R + \Gamma_0 e^{-E/kT}} = \frac{1}{1 + C e^{-E/kT}} \quad (2.11)$$

where $C = \Gamma_0 / \Gamma_R$ is a constant. Equation (2.11) shows that at low temperatures the quantum efficiency approaches unity, as the available thermal energy is not sufficient to enable the system to reach the crossing point. As the temperature increases and $kT \sim E$, the efficiency is drastically reduced, and approaches zero at high temperatures when $C \gg 1$. This behaviour is illustrated in fig. 2.5 [4].

Another consequence of non-radiative transitions is that the lifetime of the luminescence process becomes shorter than the radiative lifetime as the temperature increases. Since the excited centers will return to the ground state with a total probability given by $\Gamma_0 = \Gamma_R + \Gamma_{NR}$, the lifetime of the luminescence is given by [7]:

$$\frac{1}{\tau} = \frac{1}{\tau_R} + \frac{1}{\tau_{NR}} \quad (2.12)$$

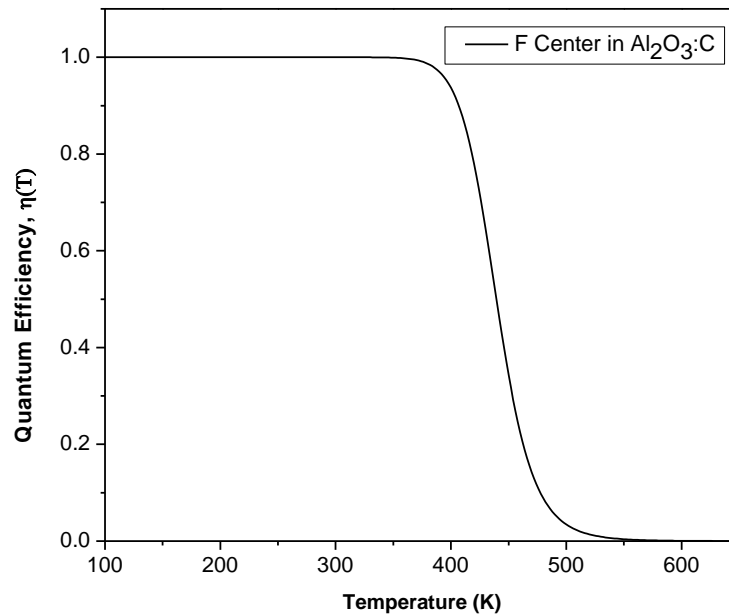


Figure 2.5. Quantum efficiency $\eta(T)$ according to Equation (2.11) for F-centers in $\text{Al}_2\text{O}_3:\text{C}$ ($C = 8.5 \times 10^{11}$ and $E = 1.03$ eV) [9] as a function of temperature.

2.4.4. Concentration quenching

An increase in the concentration of a luminescent center in a given material should result in an increase of emitted light intensity, which is attributed to an increase in the absorption efficiency. However, such behavior occurs only up to a certain critical concentration of the luminescent centers. Above this concentration, the luminescence intensity does not increase rather it decreases. This process is known as *concentration quenching* of luminescence [11].

Fig. 2.6 shows a manifestation of this effect for the infrared luminescence at $\sim 1.5 \mu\text{m}$ due to Er^{3+} ions in CaF_2 layer crystals [10]. In this figure, the luminescence intensity of Er^{3+} ions is shown as a function of the Er concentration at a fixed excitation intensity. The emitted intensity grows monotonously until Er concentration reaches $\sim 35\%$ beyond which the luminescence decreases to an extent that above 50% Er concentration the emission is nil [11].

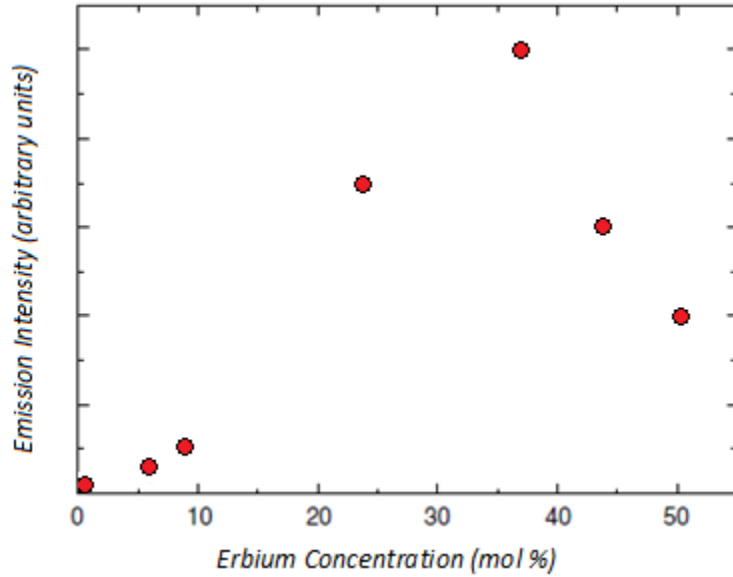


Figure 2.6. The integrated emission intensity of Er^{3+} ions as a function of Er concentration [10].

The onset of quenching occurs at certain concentration, for which there is a sufficient reduction in the average distance between the luminescent centers that favors energy transfer. Thus, the origin of luminescence concentration quenching lies in a very efficient energy transfer among these luminescent centers. Two mechanisms generally invoked to explain the luminescence concentration quenching are as follows:

(i) Due to very efficient energy transfer, the excitation energy can be transferred amongst large number of centers before being emitted. However, even for the crystals of highest purity, there is always a presence of certain defects or trace impurity that can act as acceptors, so that the excitation energy can eventually be transferred to them. Therefore these centres act as an energy sink and can relax to their ground state by multi-phonon emission or by infrared emission and thereby quenching luminescence signal (refer fig. 2.7(a)). These centers are also called as *killers* or *quenching traps* for obvious reasons [11].

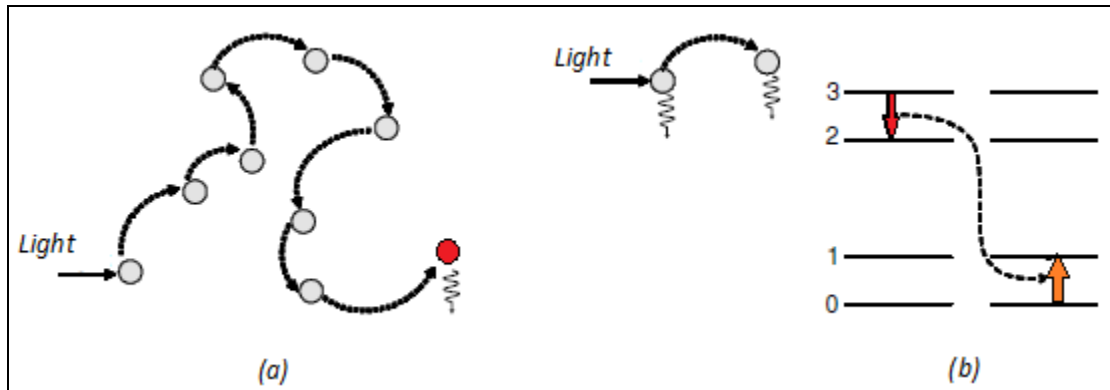


Figure 2.7. Mechanism of Luminescence concentration quenching for: (a) energy migration of the excitation along a chain of donors (circles) and a killer (black circle), acting as non-radiative sink; (b) cross relaxation between pairs of centers. (Sinusoidal arrows indicate non-radiative decay or radiative decay from another excited level [10, 11].

(ii) Concentration quenching can also be produced without actual migration of the excitation energy among the luminescent centers. This occurs when the excitation energy is lost from the emitting state via a *cross-relaxation* mechanism. This kind of relaxation mechanism occurs by resonant energy transfer between two identical adjacent centers, due to the particular energy-level structure of these centers. Fig. 2.7(b) shows a simple possible energy-level scheme involving cross-relaxation [10, 11].

As the concentration quenching results from energy transfer processes, the decay time of the emitting ions is reduced when one concentration quenching mechanism occurs. In general, this decay-time reduction is much easier to measure than the reduction in the quantum efficiency. In fact, the easiest way to detect luminescence concentration quenching is to analyze the lifetime of the excited centers as a function of the concentration. The critical concentration is that for which the lifetime starts to reduce.

Finally, it is important to mention that besides the possibility of energy transfer, a high concentration of centers can lead to new kinds of centers, such as clusters formed by

aggregation or coagulation of individual centers. Thus, these new centers can have a different level scheme to that of the isolated centers, giving rise to new absorption and emission bands. This is, of course, another indirect mechanism of concentration quenching for the luminescence of the isolated centers and is also observed in TL and OSL of materials when doped with a dopant in various concentrations.

During a thermoluminescence experiment, one typically obtains several glow curves under different conditions. For example, a series of TL glow curves may be obtained for a material that was irradiated at several different doses, or was pre-annealed at various temperatures. Usually the main goal of measuring and analyzing these TL glow curves is the extraction of several parameters that can be used to describe the TL process in the material. Examples of these parameters are the activation energy E for the TL traps (also called the trap depth), the frequency factor s , the order of kinetics b of the TL process, the capture cross-sections for the traps and recombination centers, and the concentrations of these traps and centers.

The following section presents various theoretical methods and analytical expressions used to analyze TL glow curves that were used during the course of this work and the subsequent section also discusses briefly the parameters associated with OSL analysis.

2.5. Experimental Methods of Determining TL Parameters

The TL characteristic of any material is labeled by parameters like kinetics obeyed by the TL process, the trap depth, frequency factor, etc. The shape of the TL glow curve can be used to know the order of kinetics using following points: i) The glow peak temperature T_m is independent of radiation dose in first order kinetics whereas in second order kinetics, the glow peak temperature T_m decreases with the increase of dose, ii) The TL glow curves representing

second order kinetics are more symmetric than that of the first order TL glow curves, iii) The shape/geometrical factor μ_g represents first-order kinetics if its value lies in the range 0.38-0.42 whereas the values from 0.48-0.52 represent second order kinetics. The experimental methods for the determination of these parameters are given below.

2.5.1. *Initial Rise Method*

It is the simplest procedure to obtain the trap depth and is independent of the kinetics involved. In the initial rise part of a TL curve (early rising range of temperatures), i.e. $T \ll T_m$, the rate of change of trapped carrier population is negligible, hence intensity I is strictly proportional to $\exp(-E/kT)$, assuming that frequency factor remains same & there is no overlapping of glow peaks, i.e.

$$I(t) = \text{Const.} \times \exp(-E/kT) \quad (2.13)$$

If the plot of $\ln(I)$ vs. $1/T$ is made over this initial region (i.e. $T \ll T_m$), then a straight line of slope $-E/k$ is obtained from which the activation energy E is evaluated. This procedure is commonly termed the 'initial rise' method. The important requirement in this analysis is that ' n ' remains approximately constant. Only upon increase in temperature beyond a critical value, T_c , does this assumption become invalid. It may be noted that the initial rise technique can only be used when the glow peak is well defined and clearly separated from the other peaks.

2.5.2. *Variable Heating Rate Method*

In this method we use two different heating rates β_1 and β_2 , and their corresponding peak temperatures T_{m1} & T_{m2} . Writing equation (1.5) for β_1 and β_2 , on dividing and rearranging the terms, expression for trap depth E is

$$E = \frac{kT_{m1}T_{m2}}{(T_{m1}-T_{m2})} \ln \left[\frac{\beta_1}{\beta_2} \left(\frac{T_{m2}}{T_{m1}} \right)^2 \right] \quad (2.14)$$

The value of E thus obtained can be inserted in to equation (1.5) for either β_1 or β_2 and the value of 's' can be calculated. Hoogenstraaten in 1958 [12] proposed use of several heating rates. From equation (1.5), on rearranging we get

$$\frac{T_m^2}{\beta} = \frac{E}{sk} \exp\left(-\frac{E}{kT_m}\right)$$

Taking logarithm on both sides,

$$\ln(T_m^2 / \beta) = \ln(E / sk) - E / kT_m \quad (2.15)$$

Here $\ln(E / sk)$ is a constant term and plot of $\ln(T_m^2 / \beta)$ vs. $1/T_m$ should yield a straight line with slope of $-E/k$, from which E can readily be evaluated. Extrapolation to $1/T_m \rightarrow 0$ gives the value of $\ln(sk / E)$ from which s can be calculated by the use of E/k found from the slope.

2.5.3. Method based on glow curve shape

The shape of the TL low curve strongly depends on the order of kinetics. In this method, temperatures T_m is the peak temperature and T_1, T_2 are the temperatures on the low and upper sides of T_m corresponding to half peak intensity. The values of T_m, T_1 and T_2 depend on the shape of the glow curve and can be utilized to calculate the E value expression for which is,

$$E = 1.51kT_m T / (T_m - T_1) \text{ Using only ascending part of the glow curve} \quad (2.16)$$

$$E = kT_m^2 / (T_2 - T_1) \text{ Using only descending part of the glow curve} \quad (2.17)$$

2.5.4. Isothermal Decay Method

Isothermal decay is a general technique for determining E & s. The pre-excited TL phosphor is quickly heated to a particular constant temperature and the light emission (phosphorescence), which decays exponentially as a function of time, in the case of first-order kinetics is monitored. The slope m of the linear plot between $\ln(I_t/I_0)$ and t will be equal to $s \exp(-E/kT)$.

The decay is observed at several temperatures and their respective slopes m are calculated. The slope of the linear plot $\ln(m)$ vs. $1/T$ will be E/k from which the activation energy E can be evaluated. The value of $\ln(s)$ can be easily found from the intercept of line with Y-axis, and thus the value of frequency factor s is immediately known. Area measurement method and curve-fitting method are some other methods suggested for calculating the TL parameters.

2.6. Methods for Determination of OSL parameters

The determination of OSL parameters is bit different than TL. As the mode of stimulation being optical the most important parameter in the OSL process is the measurement of photo-ionization cross-section of electron traps which are OSL sensitive for a given wavelength of stimulation. However determination of optical trap depth is still big challenge due to complex dependence of photo-ionization cross-section on optical trap depth or optical energy threshold. The assessment of degree of re-trapping is also very important parameter as it has great influence on the shape of OSL curve in any method of stimulation. In most of the cases the re-trapping gives rise to stretched tail in OSL curve in time domain.

2.6.1. *Optical Stimulation of Trapped Charges*

Optical transitions can occur between localized defect levels and the delocalized conduction and valence bands as illustrated in Fig. 2.8, where the possibility of the charge being recaptured by other trapping centers have also been included. Charges captured by shallow traps can escape to the conduction band by thermal stimulation [4].

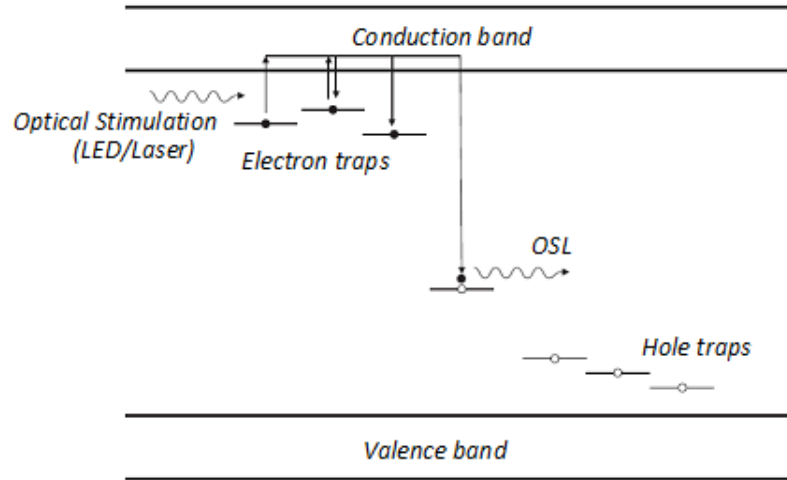


Figure 2.8. Possible electronic transitions following the optical stimulation of electrons from an “optically active” trapping center [4].

An important aspect is the interaction of the defects with the optical radiation field, particularly the effect of the stimulation wavelength and intensity on the transition probability p given by,

$$\frac{dn}{dt} = -np \quad (2.18)$$

The probability of optical transition, p can also be expressed in terms of a photo-ionization cross-section σ by:

$$p = \sigma\phi \quad (2.19)$$

2.6.2. Photo-ionization cross section

Photo-ionization is the probability of interaction of trapped electrons at meta-stable (defect levels) states with stimulating photons. Stronger the interaction higher is the probability of de-trapping (ionization to delocalized bands) of trapped electrons on stimulation with photons. Equation (2.19) shows that the transition probability is proportional to the incident photon flux $\phi(\lambda)$ and, therefore, the higher the photon flux (or light intensity), the higher the rate of release of trapped charges. Here it is important to note that for certain materials (e.g. quartz, $\text{Al}_2\text{O}_3:\text{C}$

and BeO) the detrapping probability varies linearly with stimulation intensity and for others (e.g. NaCl), a non-linear behavior is observed [13, 14].

The photo-ionization cross-section σ has a threshold energy E_I below which its value is zero (i.e., the photon energy is smaller than the energy required for the optical transition). This threshold may not be well-defined in experimental measurements due to the possibility of a two-step process in which the charge is optically stimulated to an excited state and then thermally stimulated to the conduction band [14]. Above this threshold energy, the photo-ionization cross-section is expected to increase due to the contribution of transitions to the quasi-continuum density of states of the delocalized band, and then decrease as the photon energy becomes larger than the energy corresponding to the possible optical transitions [4].

The theoretical framework for the calculation of the photo-ionization cross-section σ of deep impurity centers is extremely unsatisfactory, basically due to the problem of defining the initial and final wave functions for the quantum mechanical calculation of the transition probability [14]. The various assumptions and resultant expressions for the photo-ionization cross-section were discussed by Bøtter-Jensen, McKeever and Wintle (2003) [15]. The expressions used to express the wavelength dependence of the photo-ionization cross-section in OSL materials by Lukovsky (1965) [16] is given by:

$$\sigma(h\nu) \propto \frac{(h\nu - E_I)^{3/2}}{(h\nu)^3} \quad (2.20)$$

and that by Grimmeiss and Ledebø (1975a, b) [17,18] is expressed as:

$$\sigma(h\nu) \propto \frac{(h\nu - E_I)^{3/2}}{h\nu[h\nu + E_I(m_0/m^* - 1)]^2} \quad (2.21)$$

Where m_0 is the free electron mass and m^* is effective mass in the band. These expressions have been used usually in a descriptive manner, given the general lack of knowledge on specific defects responsible for the trapping centers and the current status of the theoretical framework [4].

2.6.3. Determination of photo-ionization cross-section

The measurement of this parameter is possible if one accurately knows the stimulating light flux incident on the sample position. In CW-OSL under 1st order kinetics well known exponential decay can be fitted to OSL curve and from which excitation rate ' f_0 ' can be determined using equation (1.22). However, if the CW-OSL curve deviates from 1st order kinetics then determination of photo-ionization cross-section (σ) leads to inaccuracy due to non-exponential decay nature under condition of re-trapping in the mode of CW-OSL readout. In case of multiple photo-ionization cross-sections the 2nd or 3rd order decay curve has to be fitted to resolve them. Under non-first order kinetic process, determination of photo-ionization cross-section requires prior knowledge of order of kinetics. Thus measurement of photo-ionization cross-section in such a situation is fraught with inaccuracies. Therefore new initiation is needed in this field to suggest some better method of measuring OSL parameters.

We have seen the experimental techniques for TL and OSL kinetic analysis. However, to understand the luminescence mechanism we have to resort to other spectroscopic techniques for identifying defects in the phosphor material. Next section describes some of these techniques.

2.7. Spectroscopic Techniques for defect characterization

2.7.1. Optical Absorption Spectroscopy

2.7.1.1. The Absorption Coefficient

A light beam is attenuated after passing through a material. Experiments show that the beam intensity attenuation dI after traversing a differential thickness dx can be written as

$$dI = -\alpha I dx \quad (2.22)$$

where I is the light intensity at a distance x into the medium and α accounts for the amount of reduction due to the constitution of the material. In the case of negligible scattering, α is called the *absorption coefficient* of the material. Upon integration of equation (2.22) we obtain

$$I = I_0 e^{-\alpha x} \quad (2.23)$$

which gives an exponential attenuation law relating the incoming light intensity I_0 (the incident intensity minus the reflection losses at the surface) to the thickness x . This law is known as the *Lambert–Beer law*.

2.7.1.2. The Absorption Probability

The absorption probability of a two-level center is given by

$$P_{if} = \frac{\pi}{3n\varepsilon_0 c_0 \hbar^2} I |\mu_{if}|^2 \delta(\Delta\omega) \quad (2.24)$$

where $I = \frac{1}{2} n c_0 \varepsilon_0 E_0^2$ is the intensity of the incident radiation (assuming an incident plane wave), c_0 is the speed of light in a vacuum, n is the refractive index of the absorbing medium, ε_0 is the permittivity in a vacuum, and μ_{if} is the so-called *matrix element of the electric dipole moment* [11]. Expression (2.24) shows that the absorption probability depends on both the incoming light intensity and the matrix element μ_{if} . It is important to note that $|\mu_{if}| = |\mu_{fi}| = |\mu|$

and so we can conclude that the absorption probability between two defined energy levels i and f is equal to the stimulated emission probability between levels f and i :

$$P_{if} = P_{fi} = P \quad (2.25)$$

2.7.1.3. *Oscillator Strength: Smakula's Formula*

We can relate $|\mu|^2$, or the transition probability given in equation (2.24), with experimental measurements, such as the absorption spectrum.

Considering our single two energy level center, it is easy to understand that the area under the absorption spectrum, $\int \alpha(\omega) d\omega$, must be proportional to both $|\mu|^2$ and the density of absorbing centers, N . In order to build up this proportionality relationship, it is very common to use a dimensionless quantity, called the ***oscillator strength, f*** expression for which is given by:

$$f = \frac{2m\omega_0}{3\hbar e^2} \times |\mu|^2 \quad (2.26)$$

where m is the electronic mass and ω_0 is the frequency at the absorption peak. Classically, the oscillator strength f represents the number of electric dipole oscillators that can be stimulated by the radiation field (in the dielectric dipole approximation) and has a value close to one for strongly allowed transitions. The oscillator strength f is directly correlated with the spontaneous emission probability A by

$$A = \frac{1}{4\pi\epsilon_0} \frac{2\omega_0^2 e^2}{mc_0^3} \left[\left(\frac{E_{loc}}{E} \right)^2 n \right] \times f \quad (2.27)$$

Where in dense media such as crystals, a suitable correction must be introduced to take into account the actual local electric field \mathbf{E}_{loc} acting on the valence electrons of our absorbing center due to the electromagnetic incoming wave [11].

Area under the absorption spectrum is related to f and density of absorbing centers, N , by

$$\int \alpha(\omega) d\omega = \frac{1}{4\pi\epsilon_0} \frac{2\pi^2 e^2}{mc_0} \left[\left(\frac{E_{loc}}{E} \right)^2 \frac{1}{n} \right] \times f \times N \quad (2.28)$$

For ions in crystals of high symmetry, as in the case of octahedral AB_6 center, the correction factor is $\mathbf{E}_{loc}/\mathbf{E}_0 = (n^2 + 2)/3$ [19], where n is the refractive index of the medium. Although this correction factor is not strictly valid for centers of low symmetry, it is often used even for these centers. Thus, assuming this local field correction and inserting numerical values for the different physical constants, equation (2.28) becomes

$$N(cm^{-3})f = 54.1 \frac{n}{(n^2 + 2)^2} \int \alpha(\omega)(cm^{-1})d\omega \quad (2.29)$$

which is known as *Smakula's formula* for electric dipole absorption processes. This relation is very useful in experimentally determining the oscillator strength (or $|\mu|^2$) from the absorption spectrum of a given system, if the density of absorbing centers is known. Smakula's formula can also be used to determine the density of absorbing centers from the absorption spectrum if the oscillator strength is known [11].

2.7.1.4. The Measurement of Absorption Spectra: Spectrophotometer

Absorption spectra are usually registered by instrument known as *spectrophotometer*, schematic diagram of which is shown in fig. 2.9 (a). The main elements of the simplest spectrophotometer (*a single-beam spectrophotometer*) are: (i) a light source (usually a deuterium lamp for the UV spectral range and a tungsten lamp for the VIS and IR spectral ranges) that is focused on the entrance to (ii) a monochromator, which is used to select a single frequency (wavelength) from all of those provided by the lamp source and to scan over a desired frequency range; (iii) a sample holder, followed by (iv) a light detector (usually a

photomultiplier for the UV–VIS range and a SPb cell for the IR range) to measure the intensity of each monochromatic beam after traversing the sample [11].

Optical spectrophotometers work in different modes to measure *optical density, absorbance, or transmittance*.

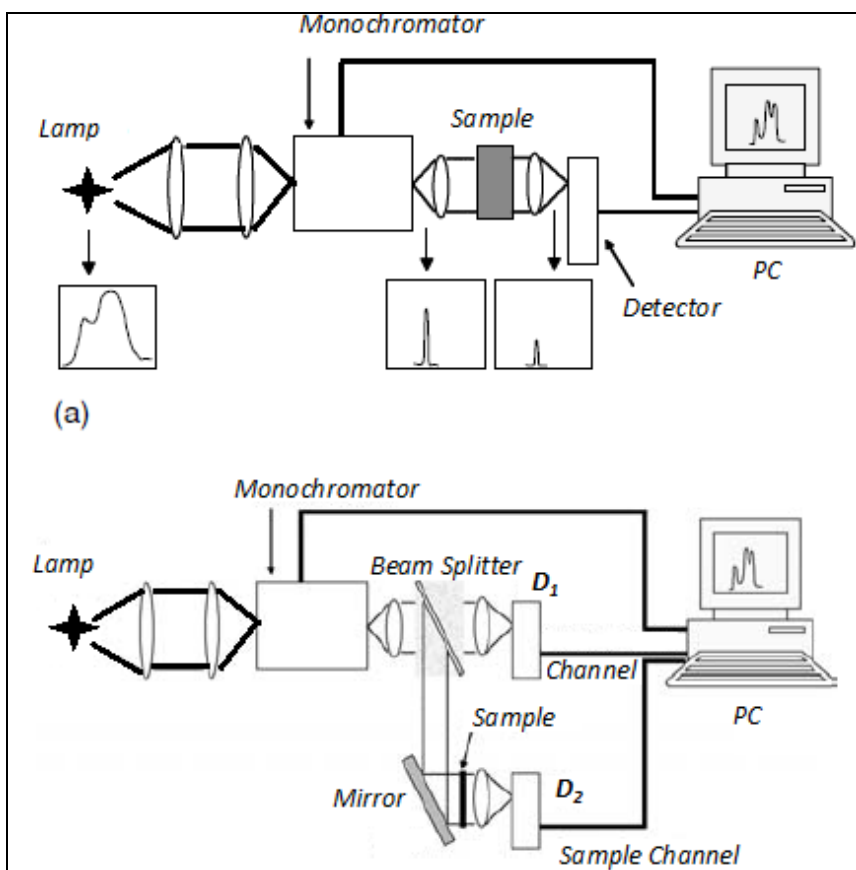


Figure 2.9. Schematic diagrams of (a) a single-beam spectrophotometer and (b) a double-beam spectrophotometer [11].

The *optical density* is defined as $OD = \log(I_0/I)$, so that according to Equation (2.23) the absorption coefficient is determined by

$$\alpha = \frac{OD}{x \log e} = \frac{2.303(OD)}{x} \tag{2.30}$$

That is, by measuring the optical density and the sample thickness, the absorption coefficient can be determined. The optical density can be easily related to other well-known optical magnitudes that are also directly measurable by spectrophotometers, such as the *transmittance*, $T = I/I_0$, and the *absorbance*, $A = 1 - I/I_0$:

$$T = 10^{-OD}; \quad A = 1 - 10^{-OD} \quad (2.31)$$

Nevertheless, it is important to emphasize here the advantage of measuring optical density spectra over transmittance or absorbance spectra. Optical density spectra are more sensitive, as they provide a higher contrast than absorbance or transmittance spectra. In fact, for low optical densities, expression (1.11) gives $A \approx 1 - (1 - OD) = OD$, so that the absorbance spectrum (A versus λ , or $1 - T$ versus λ) displays the same shape as the optical density. However, for high optical densities, typically higher than 0.2, the absorbance spectrum gives a quite different shape to that of the actual absorption (α versus λ or OD versus λ) spectrum.

2.7.2. *Photoluminescence*

Photoluminescence is the emission of light which is caused by the irradiation of a substance with other light. The term embraces both fluorescence and phosphorescence, which differ in the time after irradiation over which the luminescence occurs.

Photoluminescence is often used in the context of semiconductor devices (e.g. semiconductor lasers or amplifiers, solar cells, or saturable absorbers). Here, photoluminescence is excited by illumination of the device with light which has photon energy above the bandgap energy. The photoluminescence then occurs for wavelengths around the bandgap wavelength. The optical spectrum of the photoluminescence (*PL spectrum*) and also the dependence of its intensity on the irradiation intensity and device temperature can deliver important information for device characterization. In particular, PL spectra and their intensity dependencies can allow one

- to determine the bandgap energy and/or the wavelength of maximum gain
- to determine the composition of ternary or quaternary layers
- to determine impurity levels
- to investigate recombination mechanisms

PL mappers can spatially resolve the photoluminescence, e.g. from epitaxially grown wafers.

PL maps can reveal, e.g., a radial dependency of layer thickness or material composition.

2.7.2.1. The Measurement of Photoluminescence: the Spectrofluorimeter

Photoluminescence spectra are also often measured using compact commercial equipment called *spectrofluorimeters*. Their main elements are shown in fig. 2.10.

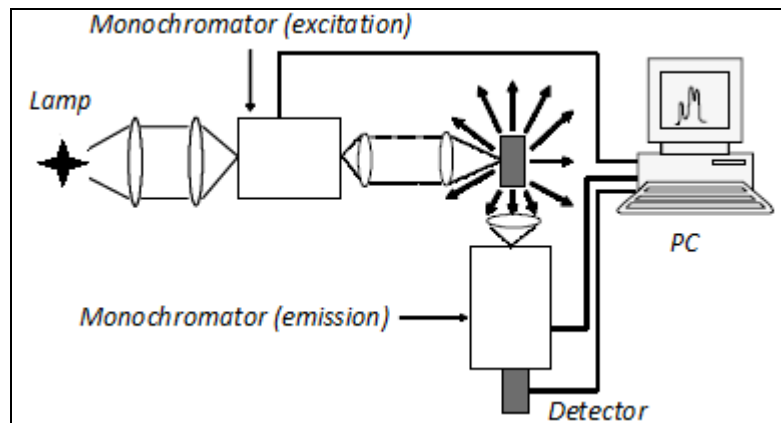


Figure 2.10. A schematic diagram showing the main elements for measuring photoluminescence spectra. The excitation can also be produced using a laser instead of both a lamp and an excitation monochromator.

The sample is excited with a lamp, which is followed by a monochromator (the excitation monochromator) or a laser beam. The emitted light is collected by a focusing lens and analyzed by means of a second monochromator (the emission monochromator), followed by a suitable

detector connected to a computer. Two kinds of spectra, (i) *emission spectra* and (ii) *excitation spectra*, can be registered [11]:

(i) In *emission spectra*, the excitation wavelength is fixed and the emitted light intensity is measured at different wavelengths by scanning the emission monochromator.

(ii) In *excitation spectra*, the emission monochromator is fixed at any emission wavelength while the excitation wavelength is scanned in a certain spectral range.

It is important to note that excitation/emission spectra allow us to obtain information on the energy-level scheme of the studied phosphor. For instance, it can give us information on the transition probability, which is not accessible by optical absorption as the population of ground state is negligible.

2.7.3. *Time-Resolved Luminescence*

Under pulsed wave excitation, non stationary density of centres N , are promoted to the excited states. Subsequently these excited centres can decay (relax) to the ground state by either radiative mode or non-radiative mode or combination of both, giving a decay time signal intensity. The temporal evolution of the population of these excited states is given by [11]:

$$\frac{dN(t)}{dT} = -A_T N(t) \quad (2.32)$$

where A_T is the total decay rate (or total decay probability), and is given by:

$$A_T = A_r + A_{nr} \quad (2.33)$$

A_r and A_{nr} correspond to the *radiative and non-radiative rates* respectively. The solution of the differential equation (2.32) gives the density of excited centers at any arbitrary time t :

$$N(t) = N_0 e^{-A_T t} \quad (2.34)$$

where N_0 is the density of excited centers at $t = 0$; that is, immediately after the absorption of light pulse.

The de-excitation process can be experimentally observed by analyzing the temporal decay of the emitted light. In fact, the emitted light intensity at a given time t , $I_{em}(t)$, is proportional to the density of centers de-excited per unit time, $(dN/dt)_{\text{radiative}} = A_r N(t)$, so that it can be written as

$$I_{em}(t) = C \times A_r N(t) = I_0 e^{-A_r t} \quad (2.35)$$

where C is a proportionality constant and so $I_0 = C \times A_r N_0$ is the intensity at $t = 0$.

Equation (2.35) corresponds to an exponential decay law for the emitted intensity, with a *lifetime* given by $\tau = 1/A_r$. This lifetime represents the time in which the emitted intensity decays to I_0/e and it can be obtained from the slope of the linear plot, $\log I$ versus t . As τ is measured from a pulsed luminescence experiment, it is called the *fluorescence or luminescence lifetime*. It is important to stress that this lifetime value gives the total decay rate (radiative plus non-radiative rates). Consequently Equation (2.33) is usually written as

$$\frac{1}{\tau} = \frac{1}{\tau_0} + A_{nr} \quad (2.36)$$

where $\tau_0 = 1/A_r$, called the *radiative lifetime*, would be the luminescence decay time measured for a purely radiative process ($A_{nr} = 0$). The quantum efficiency η can be expressed in terms of the radiative τ_0 and luminescence τ lifetimes as:

$$\eta = \frac{A_r}{A_r + A_{nr}} = \frac{\tau}{\tau_0} \quad (2.37)$$

The previous formula indicates that the radiative lifetime τ_0 (and hence the radiative rate A_r) can be determined from luminescence decay-time measurements if the quantum efficiency η is measured by an independent experiment.

The experimental setup used for luminescence decay-time measurements is similar to PL setup although the light source must be pulsed (alternatively, a pulsed laser can be used) and the detector must be connected to a time-sensitive system, such as an oscilloscope, a multichannel analyzer, or a boxcar integrator [11].

The emission spectra can also be recorded at different times after the excitation pulse has been absorbed. This experimental procedure is called *time-resolved luminescence* and may prove to be of great utility in the understanding of complicated emitting systems. The basic idea of this technique is to record the emission spectrum at a certain *delay time*, t , in respect to the excitation pulse and within a temporal *gate*, Δt , as schematically shown in fig. 2.11. Thus, for different delay times different spectral shapes are obtained.

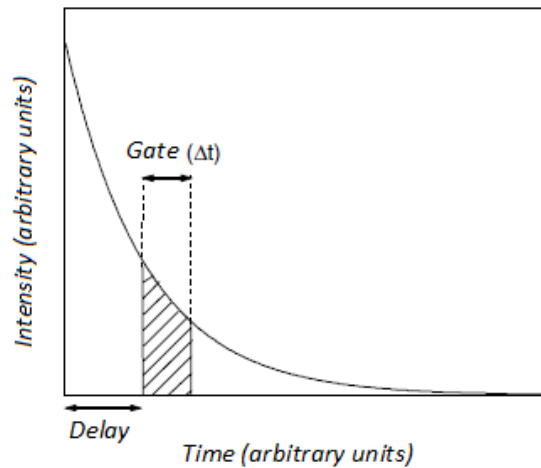


Figure 2.11. Schematic temporal decay of luminescence, having gate of width Δt at a delay time t [11].

2.7.4. Electron Paramagnetic Resonance

The majority of stable molecules are held together by bonds in which electron spins are paired; in this situation there is no electron spin, no electronic magnetic moment, and hence no interaction between the electron spins and an applied magnetic field. On the other hand, some atoms and molecules contain one or more electrons with unpaired spins, and these are the substances which are expected to show *electron spin resonance (e.s.r.)* spectroscopy; since such substances are also paramagnetic, this type of spectroscopy is often referred to as *electron paramagnetic resonance (e.p.r.)* [20].

The energy differences studied in EPR spectroscopy are due predominantly to the interaction of an unpaired electron in the sample with a magnetic field B_0 , produced by a magnet in the laboratory. This effect is called the *Zeeman effect*. Because the electron has a magnetic moment, it acts like a compass or a bar magnet when it is placed in a magnetic field. Since energies are quantized, a single unpaired electron has only two allowed energy states. It has a state of lower energy when the moment of the electron, μ , is aligned with the magnetic field and a higher energy state when μ is aligned against the magnetic field (see fig. 2.12). The two states are designated by the projection of the electron spin, m_s , on the direction of the magnetic field. Because of the electron is a spin $\frac{1}{2}$ particle, the parallel state has $m_s = -1/2$ and the antiparallel state has $m_s = +1/2$. The difference between the energies of these two states, caused by the interaction between the electron spin and the magnetic field, is shown in (2.1).

$$\Delta E = g \mu_B B_0 \Delta m_s = g \mu_B B_0 \quad (2.38)$$

Where g is the g -factor, which is discussed below, μ_B is the Bohr magneton, which is the natural unit of the electron's magnetic moment, and the change in the spin state is $\Delta m_s = \pm 1$.

The energy, $\Delta E = h\nu$, that is required to cause a transition between the two spin states is given by (2.2),

$$\Delta E = h\nu = g \mu_B B_0 \text{ and } \mu_B = g_e \beta / 2 \quad (2.39)$$

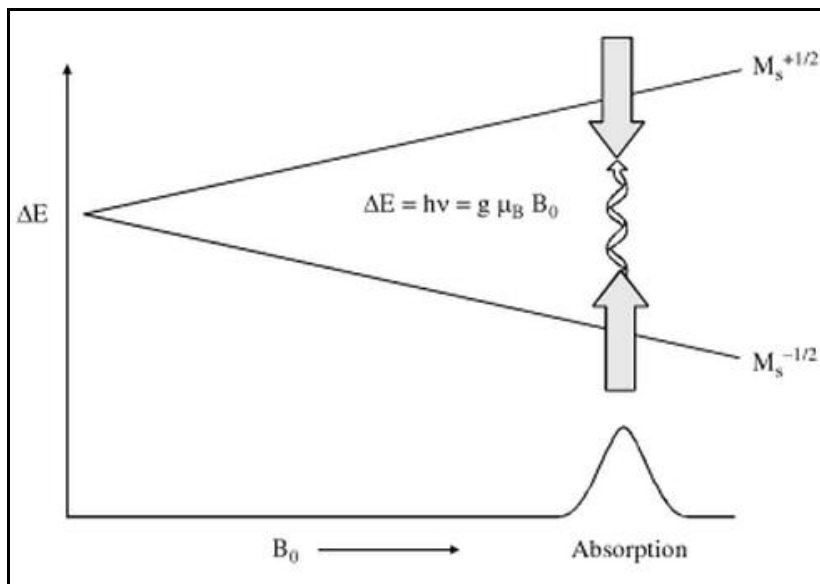


Figure 2.12. Variation of magnetic field resulting in splitting and divergence of energies of the two spin states of an unpaired electron and subsequent absorption of energy by the spin at resonance

Two facts are apparent from (2.1) and (2.2) and its graph in fig. 2.12.

- The two spin states have the same energy in the absence of a magnetic field, so without a magnetic field, there is no energy difference to measure.
- The energies of the spin states diverge linearly as the magnetic field increases and the energy difference depends linearly on the magnetic field.

Because the energy difference between the two spin states can be varied by changing the magnetic field strength, there are two potential approaches to obtain spectra. The magnetic field could be held constant while the frequency of the electromagnetic radiation is scanned, which would be analogous to UV-VIS spectroscopy. Alternatively, the electromagnetic radiation frequency could be held constant while the magnetic field is scanned as shown in fig. 2.12.

Absorption of energy occurs when the magnetic field “tunes” the two spin states such that the energy difference matches the energy of the applied radiation. This field is called the “field for resonance”. Because of difficulties in scanning microwave frequencies and because of the use of a resonant cavity for signal detection, most EPR spectrometers operate at constant microwave frequency and scan the magnetic field.

The field for resonance is not a unique “fingerprint” for identification of a compound because spectra can be acquired at different microwave frequencies. The g-factor is given by

$$g = h\nu / \mu_B B_0 \quad (2.40)$$

It is independent of the microwave frequency, so the g-factor is a better way to characterize signals. Note that high values of g occur at low magnetic fields and vice versa. A list of fields for resonance for a $g = 2$ signal at microwave frequencies commonly available in commercial EPR spectrometers is presented in Table 2.1. Spectrometers are labeled with a letter as shown in the table that is based on the designation that engineers used for microwaves in that frequency range.

Table 2.1 Field for resonance for a $g = 2$ sample at various microwave frequencies

Microwave band	Microwave frequency (GHz)	B_0 (for $g = 2$) (gauss)
L	1	390
S	3	1070
X	9	3380
K	24	8560
Q	35	12,480
W	94	33,600

The g-factor helps to distinguish and identify types of samples. Carbon-centered radicals have g close to the “free electron value,” which is 2.0023. Hetero-atoms shift the g-factor. Metal ions

have very different g-factors. In immobilized samples the anisotropy of g may be observed (i.e. it may depend on the orientation of the molecule with respect to B_0 .)

2.7.4.1. EPR Spectrum and linewidth

When unpaired electrons exist in a substance their spins are aligned at random in the absence of a field. When placed in a magnetic field, however, they will each have a preferred direction and, since the spin quantum number of an electron is $\frac{1}{2}$, each can be thought of as spinning either clockwise or anticlockwise about the field direction, ESR spectroscopy essentially measures the energy required to reverse the spin of an unpaired electron.

The intensity of ESR absorption is proportional to the concentration of the free radical or paramagnetic material present. Thus we have immediately a technique for estimating the amount of free radical present; the method is extraordinarily sensitive, in favorable cases some 10^{-13} mol of free radical being detectable.

The width of an ESR peak depends, on the relaxation time of the spin state under study. Of the two possible relaxation processes, the spin-spin relaxation time of $10^{-6} - 10^{-8}$ s; the spin-lattice relaxation is efficient at room temperature ($\sim 10^{-6}$ s) but becomes progressively less so at reduced temperatures, often becoming several minutes at the temperature of liquid nitrogen. For most samples, then, we could choose 10^{-7} s as a typical relaxation time and, using this in the Heisenberg uncertainty relation, we calculate a frequency uncertainty (line width) of ~ 1 MHz. A shorter relaxation time will increase this width, and 10 MHz is not uncommon. Clearly this is much wider spectral line. Further, a broad line is more difficult to observe and measure than a sharp one and, for this reason; ESR spectrometers nearly always operate in the derivative mode. Fig. 2.13 shows the block diagram of the EPR set up to produce a spectrum.

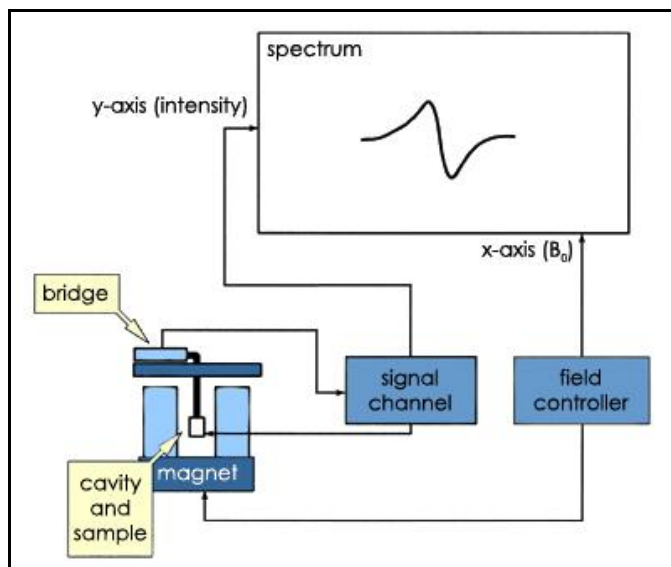


Figure 2.13. Block diagram of a typical EPR spectrometer.

Among the many tools the analyst has available, EPR has some special advantages. For example, one can use several methods to detect the presence of a particular metal, but the EPR g values and hyperfine couplings provide information about the metal species, not just its presence, thereby permitting speciation as well as quantification. EPR is very specific to unpaired electrons, and thus is a very good “needle in the haystack” method. It detects only the species with unpaired electrons, ignoring essentially everything else in the sample matrix.

2.7.5. Positron Annihilation Spectroscopy (PAS)

PAS has demonstrated itself as a powerful tool of micro-structural studies of condensed matter. Atomic-scale details of the microstructure like, e.g., electronic structure and small-sized defects can be investigated by PAS. The main advantages of PAS can be summarized as follows:

- Small-sized defects at low concentration can be detected by PAS which can otherwise be hardly investigated by traditional basic techniques like, e.g., TEM or X-ray diffraction.
- PAS can probe both the bulk properties of mater as well as near-surface regions and layered structures.

- Reliable theoretical calculations of PAS parameters are nowadays feasible in metals and semiconductors. These may substantially simplify unique interpretation of data measured by PAS.
- PAS is a non-destructive technique.

2.7.5.1. Principles of PAS

Positron (e^+) is the antiparticle of electron (e^-). The electromagnetic interaction between electrons and positrons makes possible annihilation of $e^+ - e^-$ pairs in which the total energy of the annihilating pair may be transferred to quanta of the electromagnetic field. Principal channel of this reaction is the two-photon annihilation,



Basic principles which PAS investigations can be summarized as follows:

When positrons are implanted into a condensed medium, they get quickly in thermal equilibrium with their surroundings. Positron wave-function can be localized in the attractive potential of a defect. Being thermalized, positrons interact with their environment and eventually annihilate with electrons of the medium. Measurable parameters of annihilation reaction reflect the structure of the medium. There are two ways how the dependencies of the PAS parameters on the medium structure arise:

- Through the state of the electron participating in the annihilation reaction. This introduces dependence on the local electronic structure of the host at the annihilation site.
- Through the state of the positron itself at the moment of annihilation: the free positron, positron captured at a trap, different states of the Ps atom in the medium. This state is a result of medium-dependent positron interactions prior to annihilation.

The processes which positrons undergo in matter before they annihilate with environmental electrons proceed with characteristic time and length scales. Fig. 2.14 shows various steps before positron annihilation takes place in the material.

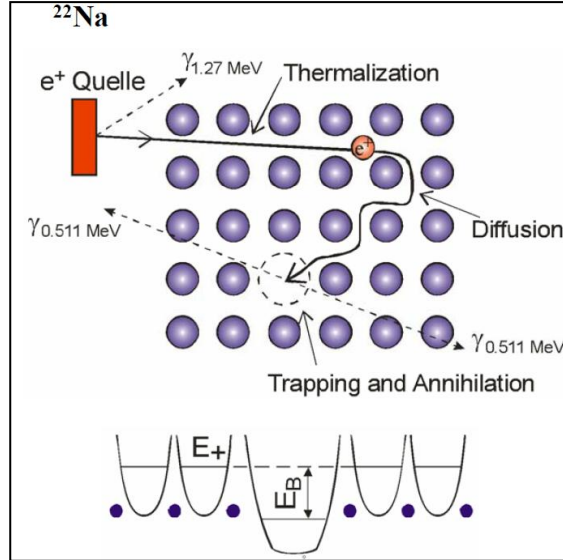


Figure 2.14. Mechanism of PAS

2.7.5.2. Positron Lifetime Spectroscopy

The positron lifetime t is a function of the electron density at the annihilation site. The annihilation rate λ , which is the reciprocal of the positron lifetime t , is given by the overlap of the positron density $n_+(\mathbf{r}) = |\psi^+(\mathbf{r})|^2$ and the electron density $n_-(\mathbf{r})$ [21],

$$\lambda = \frac{1}{\tau} = \pi r_0^2 c \int |\psi^+(r)|^2 n_-(r) \gamma dr$$

Where, r_0 is the classical electron radius, c the speed of light, and \mathbf{r} the position vector. The correlation function $\gamma = \gamma[n_-(r)] = 1 + \Delta n_- / n_-$ describes the increase Δn_- in the electron density due to the Coulomb attraction between a positron and an electron. This effect is called enhancement.

When positrons are trapped in open-volume defects such as vacancies and their agglomerates the positron lifetime increases with respect to the defect-free sample. This is due to the locally reduced electron density of the defect. Thus, a longer lifetime component, which is a measure of the size of the open volume, appears. The strength of this component, i.e. its intensity, is directly related to the defect concentration. In principle, both items of information, i.e. the kind and concentration of the defect under investigation, can be obtained independently by a single measurement. This is the major advantage of positron lifetime spectroscopy compared with angular correlation of annihilation radiation or Doppler-broadening spectroscopy with respect to defect issues.

The timing pulses are used to start and stop the charging of a capacitor in the time-to-amplitude converter (TAC). The stop pulse is coax-cable delayed in order to shift the time spectrum into a linear region of the TAC. The spectrum is stored in a multi-channel analyzer. This experimental arrangement is called “fast-fast coincidence” setup (fig. 2.15).

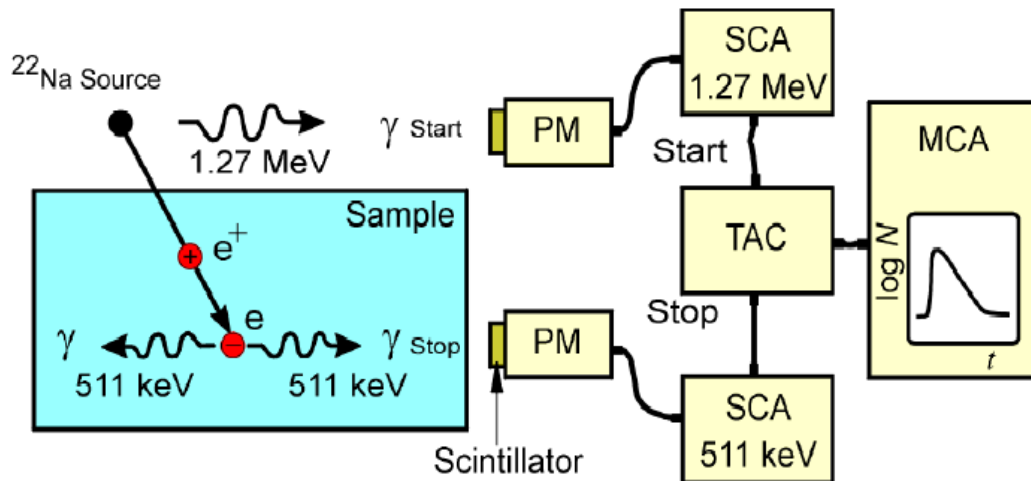


Figure 2.15. Scheme of the positron lifetime experiment in fast-fast coincidence. The lifetime is measured as the time difference between the appearance of the start and stop γ -quanta (PM—photomultiplier, SCA—single-channel analyzer).

2.7.5.3. Momentum Distribution Techniques

Conservation of momentum during the annihilation process is the reason for the fact that the annihilation radiation contains information on the electron momentum distribution at the annihilation site. This can be used for the study of the electron structure in solids and for the investigation of defects. There are two basic techniques studying the momentum distribution: Doppler-broadening spectroscopy and angular correlation of annihilation radiation.

2.7.5.4. Positron annihilation studies on α -Al₂O₃:C

Positron annihilation studies were performed on single crystals of Al₂O₃:C by Muthe et al. [22] in 2009 to understand the nature of defects generated. Results show the presence of aluminium vacancies in crystals annealed in vacuum. On annealing in the presence of graphite, ingress of carbon in these vacancies is indicated by different PAS measurements. A simultaneous enhancement of dosimetry properties has been observed. The study provides evidence that association of carbon with aluminium vacancies helps in creation of effective dosimetry traps. Single crystals of α -Al₂O₃ were subjected to different heat treatments in a composite reducing environment of carbon and vacuum. PAS studies show that the duration of heat treatment and the cooling rate have significant influence on the nature of Al vacancies. Annealing in the presence of graphite results in incorporation of carbon near Al vacancies as well as leads to improved dosimetric properties. The nature of Al vacancies associated with main dosimetric peak (~ 190°C) and low temperature peak (~ 54°C) is different. As recombination in all cases has been attributed to F and F⁺ centres, enhancement of dosimetric properties on annealing in carbon is attributed to changes in Al vacancies acting as dosimetry traps.

2.8. Investigation of defect centers responsible for TL/OSL in $\text{MgAl}_2\text{O}_4:\text{Tb}^{3+}$

Magnesium aluminium oxide spinel (MgAl_2O_4) is used in various technological applications such as light emitting devices including laser, optical, electrical applications and also in radiation environment [23]. Rare-earth-doped MgAl_2O_4 are reported to be long persistent afterglow emission phosphors used in light emitting device and color display [23,24]. Many of its properties viz. density, melting point are intermediate between those of its constituent oxides (MgO and Al_2O_3) [25]. The crystal structure of MgAl_2O_4 is a face-centered cubic lattice of oxygen ions, with a lattice parameter of 8.08 \AA . It has the cubic space group $\text{Fd}\bar{3}\text{m}$. Unit cell is formed with eight molecules, in which there are 64 tetrahedral symmetry sites and 32 octahedral sites. MgAl_2O_4 of natural origin have 8 magnesium ions occupying tetrahedral sites and 16 aluminium ions occupying octahedral sites. However, synthetic MgAl_2O_4 crystal can have up to 30% of cation antisite disorder [26-30].

Synthesis of $\text{MgAl}_2\text{O}_4:\text{Tb}^{3+}$

Combustion synthesis or self propagating high temperature synthesis (SHS) provides an attractive practical alternative to the conventional synthesis for producing advanced materials, such as ceramics, composites etc. The underlying basis of SHS is highly efficient energetic exothermic reaction with the evolution of various gases along with the high intense flame. It volatilizes low boiling point impurities and results in purer products than those produced by the other conventional synthesis. The combustion synthesis of MgAl_2O_4 doped with terbium is described as follows:

Magnesium nitrate, aluminum nitrate, urea and terbium nitrate were used as starting materials. MgAl_2O_4 was prepared in stoichiometric ratio (oxidation to reducing valency) O/F =1. Metal nitrates, urea and desired amount of dopant are dissolved in de-ionized water in a

glass beaker. The beaker was kept inside a furnace which was set at 550 °C. Once the water boiled off, the metal nitrate and urea react and ignite. The energy released from the reaction can produce temperature in excess of 1500 °C. The reaction is self-propagating and is able to sustain this high temperature long enough, from 1 to 5s typically, to form the desired product. The entire combustion process was over in about 5min. Polycrystalline MgAl₂O₄ was prepared by this method. The following section report results of XRD, PL, TL and OSL properties of thus prepared MgAl₂O₄ doped with terbium. Subsequent section illustrates findings of ESR studies carried out to identify centers playing role in TL and OSL.

Results

2.8.1. XRD Studies

Fig. 2.16 shows the XRD pattern of as-prepared MgAl₂O₄ and standard XRD pattern (JCPDS file 75-0905). XRD of MgAl₂O₄ shows various planes of diffraction with miller indices (111), (210), (311), (400), (422), (511), and (440). This result confirms the formation of the crystal phases of MgAl₂O₄ which includes the Al³⁺ ions in octahedral symmetry and Mg²⁺ occupying the tetrahedral symmetry site.

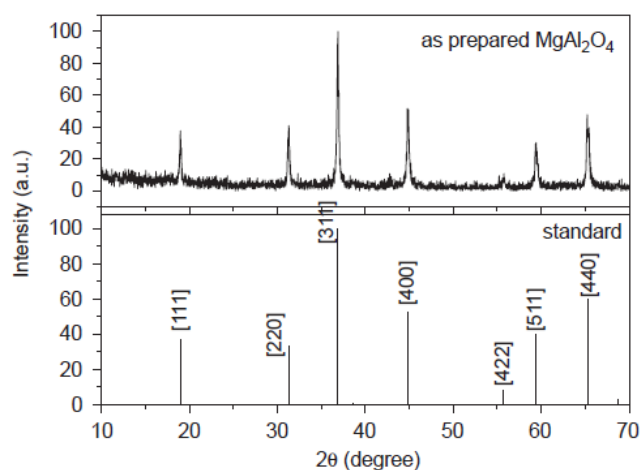


Figure 2.16. XRD of powder MgAl₂O₄(as-prepared) and standard XRD pattern (JCPDS file 75-0905)

2.8.2. Photoluminescence Studies

Fig. 2.17(a) displays the PL excitation and emission spectra of (0.5 mol %) Tb^{3+} doped $MgAl_2O_4$. The emission spectrum consists of several lines at 380, 415, 440, 490, 545, 580 and 620nm corresponding to transitions $^5D_3-^7F_6$, $^5D_3-^7F_5$, $^5D_3-^7F_4$, $^5D_4-^7F_6$, $^5D_4-^7F_5$, $^5D_4-^7F_4$ and $^5D_4-^7F_3$, respectively. Considerable contribution is observed from the higher level emission $^5D_3-^7F_J$, mainly in blue region and the transition from the lower level emissions are $^5D_4-^7F_J$, mainly in the green region. Since the J values involved in the transition are high, the crystal field splits the levels into many sublevels, which give the complicated spectrum. The excitation spectrum (emission wavelength at 545 nm) shows an intense peak at 245nm corresponding to 4f-5d transition and weak peak at 320, 355 and 370nm corresponding to f-f transitions in Tb^{3+} . Fig. 2.17(b) shows that 0.5 mol% concentration of Tb^{3+} gives the maximum PL intensity. Furthermore, the emission intensity of Tb^{3+} varies with annealing temperature. The as prepared samples were annealed at temperature range from 700 to 1100°C for 1h. PL spectrum was recorded for each annealed sample. Fig. 2.17(c) shows that 900°C annealed phosphor gives the maximum PL emission intensity (about 4 times that of as prepared phosphor). Each data point in Fig. 2.17(b) and (c) is the average of five measurements with an uncertainty of ~ 7%. Due to the rapid combustion process, production of defects is inevitable because of the partially incomplete crystallization.

Besides this, the cation disorder in spinel structure is considerable so that there exist a great number of defects, which can serve as electron and/or hole traps. Some of these defects may act as quenching centres for PL. The defects may be reduced drastically and the sample achieves a better diffusion of defects after the heat treatment, resulting in the enhanced PL intensity of Tb^{3+} ions [31].

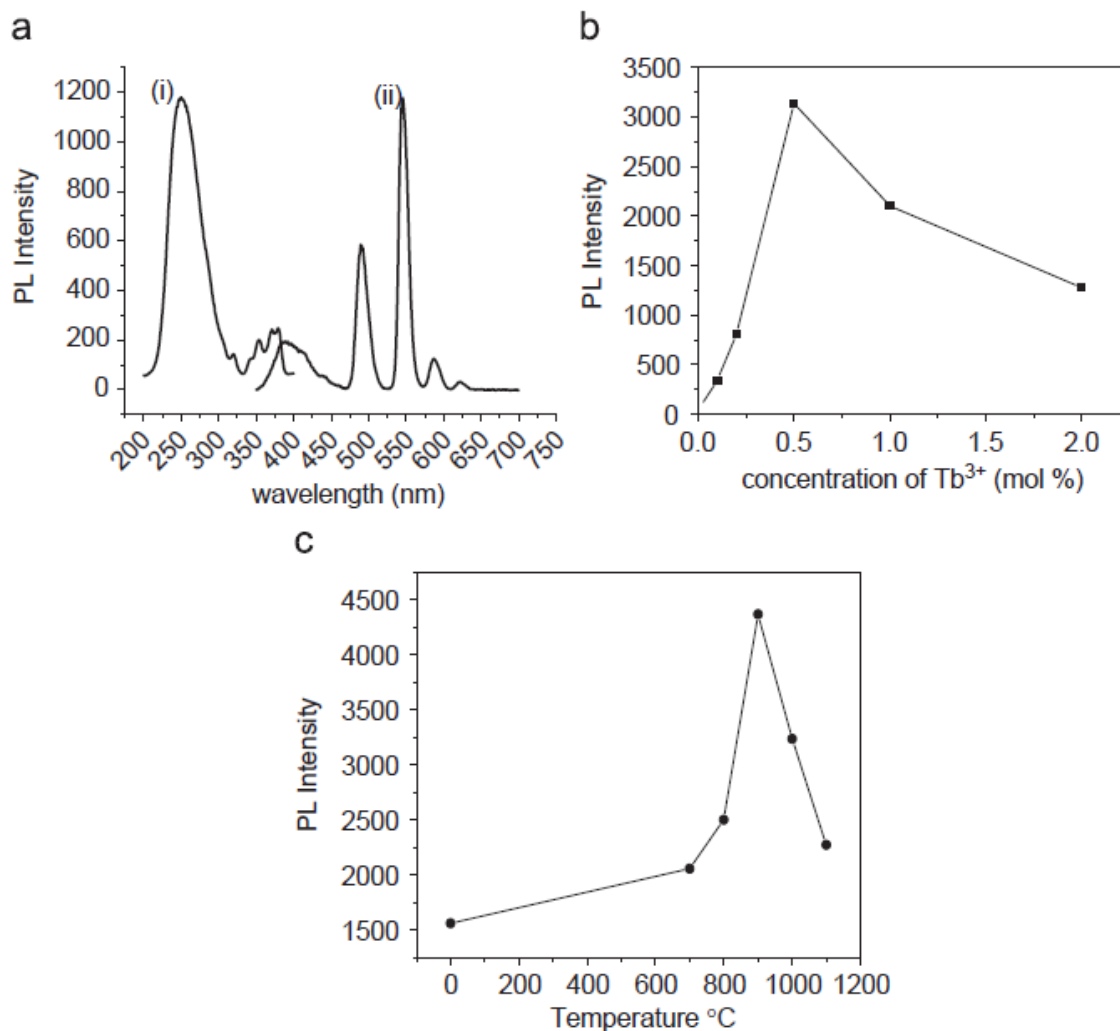


Figure 2.17. (a) PL excitation ($\lambda_{em}=545$ nm) (i) and emission spectrum ($\lambda_{exc}=245$ nm), (ii) of MgAl₂O₄:Tb (0.5 mol%). (b) Variation of PL emission intensity of MgAl₂O₄:Tb³⁺ with Tb³⁺ concentration. (c) Variation of PL intensity of MgAl₂O₄:Tb³⁺ with annealing temperature.

2.8.3. Thermoluminescence Studies

Fig. 2.18 represents the TL glow curve of the sample MgAl₂O₄ doped with Tb³⁺. Three TL peaks at 120, 220 and 340°C were observed. The activation energy (trap depth) of the peaks was measured (E=1.01, 1.03 & 1.25 eV respectively) using thermal cleaning of the peaks and initial rise method [32].

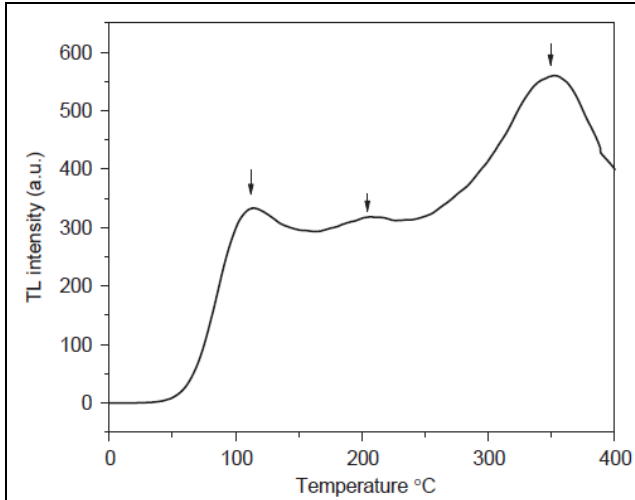


Figure 2.18. TL glow curve of Tb^{3+} doped $MgAl_2O_4$ ($\beta=5^\circ C/s$, test dose= $20Gy$) (TL peaks are indicated by arrow mark).

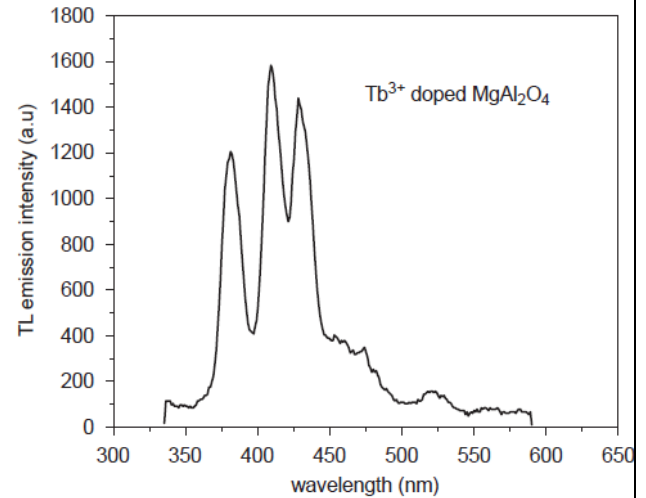


Figure. 2.19. TL emission spectrum of Tb^{3+} doped $MgAl_2O_4$ (dose= $2.5 kGy$).

Fig. 2.19 shows the TL emission spectra of Tb^{3+} doped sample. Tb^{3+} shows the emission at 380, 415, 440 and 545 nm for the TL peaks, which corresponds to the characteristic f–f transitions of Tb^{3+} ion. TL emission and PL results show Tb^{3+} is not playing role in trapping the charge carriers but it acts as a luminescent centre in TL. The difference in TL emission spectrum as compared to the PL emission spectrum is due to the fact that the former is not corrected for the PMT response.

2.8.4. *Optically Stimulated Luminescence Studies*

Continuous wave OSL decay of Tb^{3+} doped $MgAl_2O_4$ is shown in Fig. 2.20(a). OSL emission was recorded after irradiating the sample with gamma-ray dose of 10Gy. The wavelength of stimulation light source was 470nm. Fig. 2.20(b) shows the third order exponential fit of the OSL decay curve. The de-convolution is performed under first order kinetic consideration and the errors of all the three fitted time constants so obtained is less than 2% as shown in the inset of fig. 2.20(b). It consists of three components having decay time $\tau_1 = 1.32s$, $\tau_2 = 4.73s$, $\tau_3 =$

16.16s, photo-ionization cross-sections $\sigma_1 = 4.31 \times 10^{-18}$, $\sigma_2 = 1.2 \times 10^{-18}$, $\sigma_3 = 0.35 \times 10^{-18}$ cm² and the contribution of each component is 36.9%, 20.8% and 42.3%, respectively. The photo-ionization cross-sections were determined from the OSL intensity curve [15].

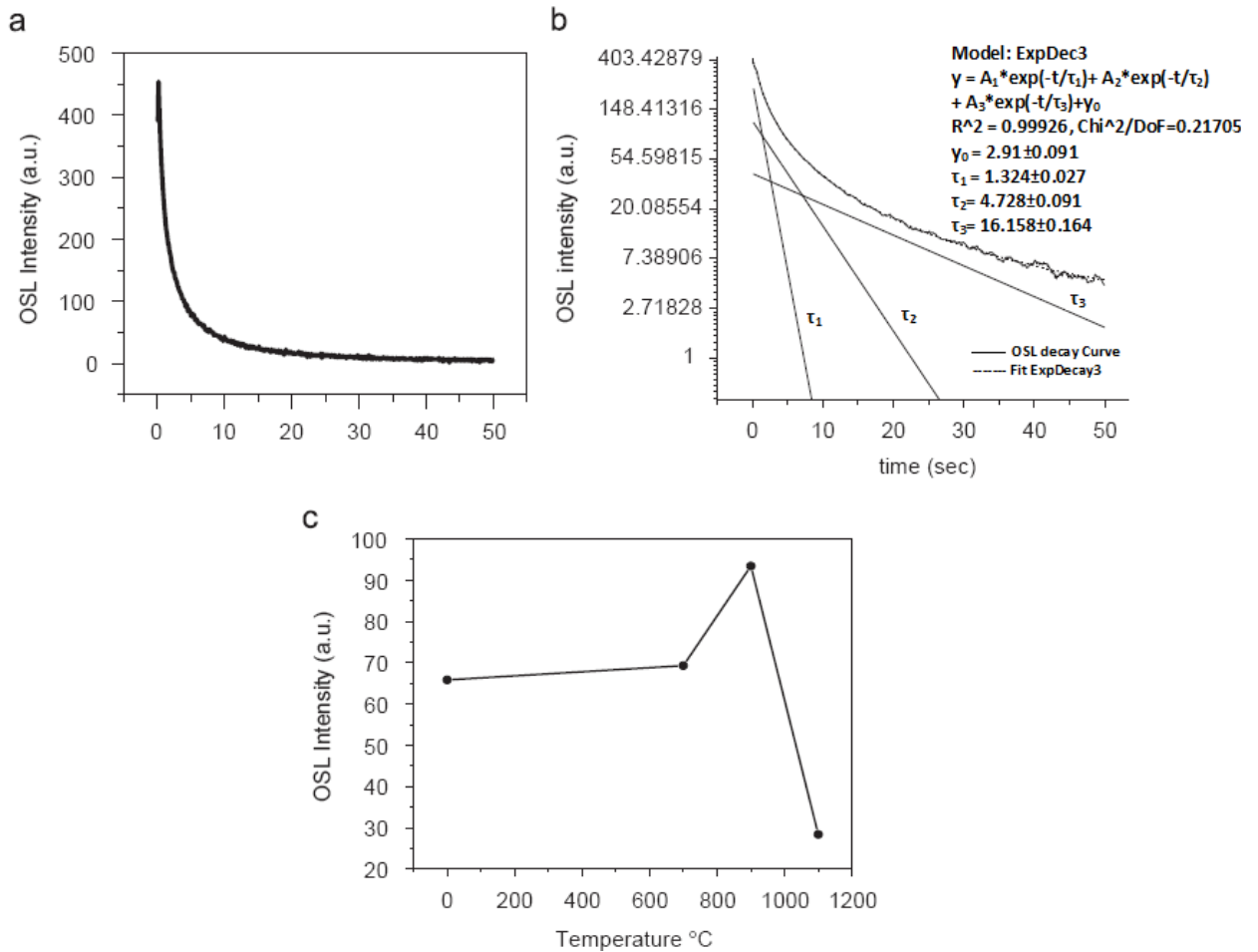


Figure 2.20. (a) CW-OSL curve of MgAl₂O₄:Tb³⁺ (test dose= 10Gy). (b) Exponential fit of OSL decay curve with time constants ($\tau_1=1.32s$, $\tau_2=4.73s$, $\tau_3=16.16s$) fitting parameters are shown in inset data. (c) Variation of OSL intensity with annealing temperature for MgAl₂O₄:Tb³⁺

Fig. 2.20(c) shows the OSL emission intensity of Tb³⁺ doped MgAl₂O₄ measured for samples annealed at different temperatures. The equal amount of annealed samples was exposed to the same gamma dose and the OSL measurements were carried out. Each data point in Fig. 2.20(c) is the average of five readings with uncertainty of $\pm 5\%$. The sample heated to 900°C is 1.5

times sensitive than the as prepared sample. This result is consistent with the PL results where it is shown that the PL intensity of the annealed phosphor is about four times that of as prepared phosphor.

2.8.5. *Electron Spin Resonance Studies*

Fig. 2.21 shows the ESR spectra at room temperature (for the dose of 3kGy) of both undoped and Tb^{3+} -doped $MgAl_2O_4$. The observed spectrum appears to be superposition of at least two distinct centres. This inference is based on thermal-annealing experiments (shown in fig. 2.22(a)). It is possible to identify two centres and these are labeled in Fig. 2.21(a). The ESR line labeled as I is due to a centre characterized by a single broad ESR line with anisotropic g-value 2.011 and 42 gauss linewidth. ESR spectra of the undoped and Tb^{3+} doped $MgAl_2O_4$ exhibit a large linewidth of centre I indicating an unresolved hyperfine structure. Aluminium (^{27}Al) as well as magnesium (^{25}Mg) in $MgAl_2O_4$ has isotopes with nuclear spin 5/2. ^{27}Al is much more abundant (100%) than ^{25}Mg (10.1%) and its nuclear magnetic moment is higher (3.6385) than that of ^{25}Mg (0.8545) [26, 33]. It is therefore, likely that the electronic spin will be interacting with aluminium ions. It is known that the cation disorder and non-stoichiometry of $MgAl_2O_4$ provide a large number of lattice defects, which may serve as trapping centres. In such a case, oxygen vacancies should lead to F^+ centres by trapping electrons after irradiation. On the other hand, hole trapping at aluminium or magnesium vacancies can lead to formation of two types of V centres [26].

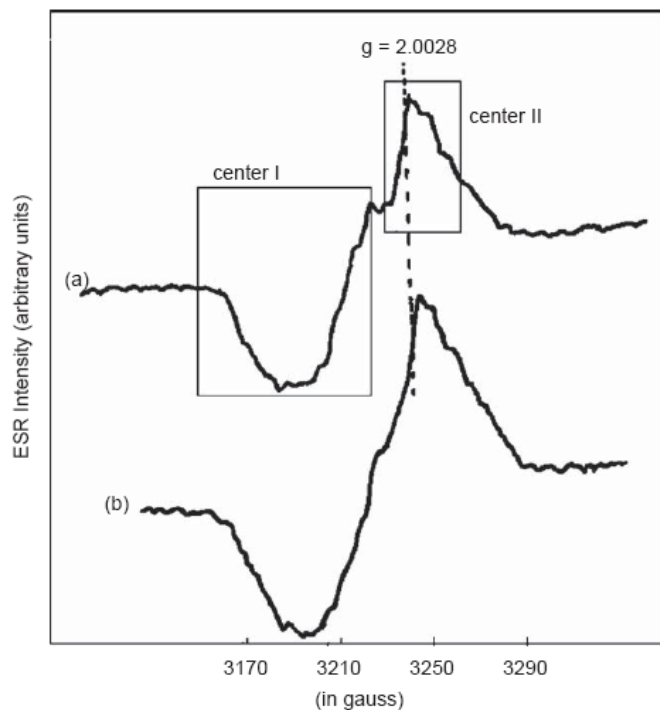


Figure 2.21. ESR spectra measured at room temperature (for dose of 3kGy) (a) undoped (b) Tb^{3+} doped

The observed broad ESR line of centre I and the associated unresolved hyperfine structure indicates that the unpaired electron is delocalized and interacts with nearby aluminium nuclei. Hence centre I is assigned to an O^- centre stabilized by a nearby cation vacancy (a hole trapped in a Al^{3+}/Mg^{2+} ion vacancy). The unpaired electron in this centre resides mainly in an oxygen $2p_\sigma$ atomic orbital [34]. The observed positive g-shift of centre I is also in accordance with the expectations for a V centre. It may be mentioned that a similar centre in neutron irradiated $MgAl_2O_4$ has also been ascribed to a V centre [26, 35]. The stability of centre I was measured using the pulsed thermal-annealing method with the uncertainty of $\pm 2\%$. After heating the sample up to a given temperature, where it is maintained for 3min, it is cooled rapidly down to room temperature for ESR measurements. Fig. 2.22(b) shows the thermal annealing behavior of centre I which decay in two stages. The first stage is in the temperature range 80–140°C and

this stage appears to relate to the TL peak at 120°C. Second stage of decay (150–240°C) is correlated to the 220°C TL peak. Two stage decay of centre I shows that it consists of two types of V centres (hole trapped in Mg^{2+} or Al^{3+} vacancy) decaying at two different temperature ranges. The ESR line labeled as II in fig. 2.21 (a) is due to a centre characterized by a single ESR line with anisotropic g-value 2.0052 and 10 gauss linewidth. One of the most probable centres, which can be formed after irradiation in this phosphor is F^+ centre (an electron trapped at an anion vacancy). Hutchison [36] first observed F centre in neutron irradiated LiF. In LiF, a single broad line (linewidth ~100gauss) with a g-factor 2.008 was observed. X-or gamma-ray irradiation also produces such a centre in other systems like alkali halides. Such centres are characterized by: (1) a small g-shift, which may be positive or negative, (2) a large linewidth (caused due to unresolved hyperfine structure) and (3) saturation properties characteristic of an in-homogeneously broadened ESR line.

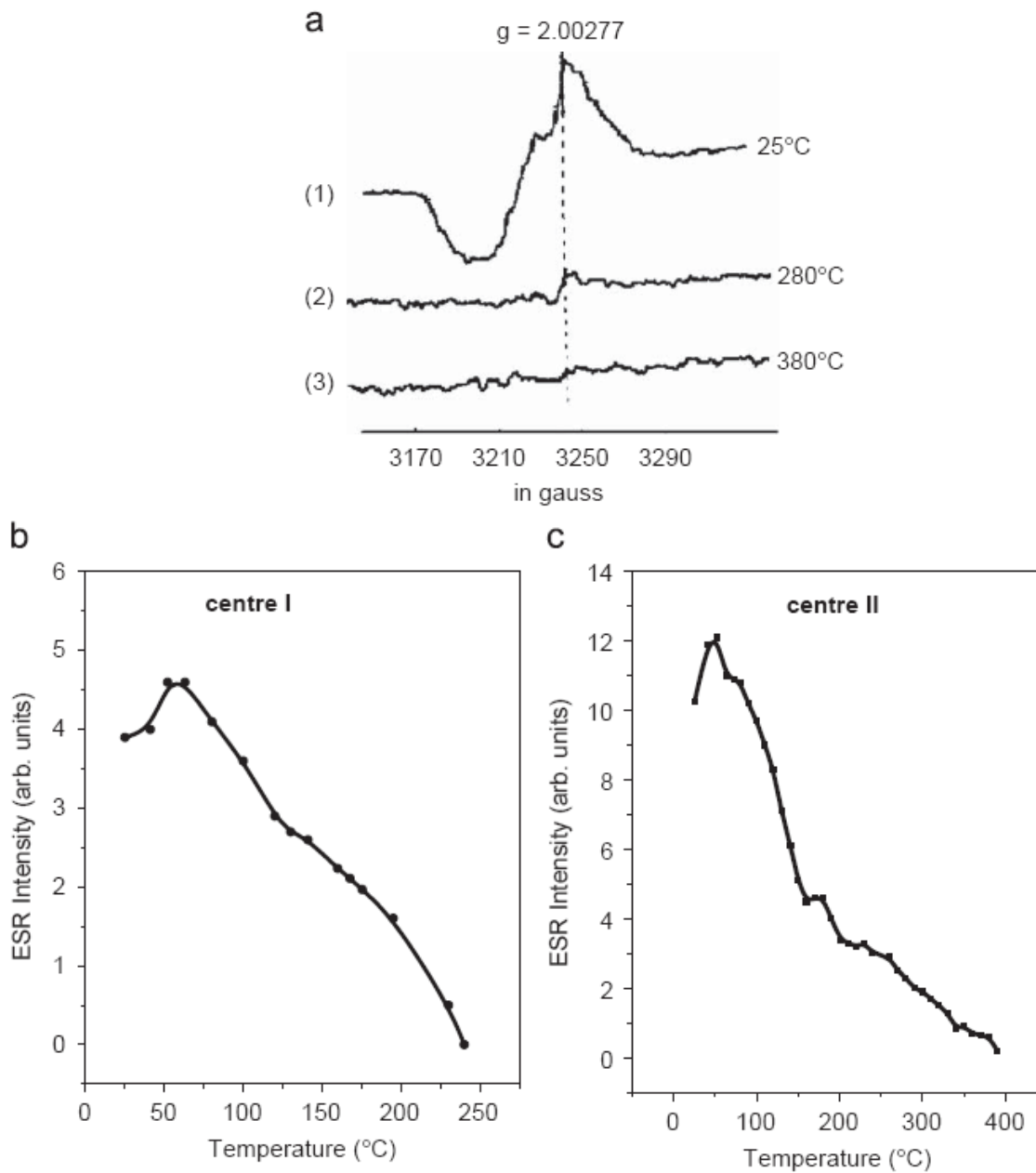


Figure. 2.22. (a) ESR spectra of $MgAl_2O_4$ (Gamma dose = 3kGy), (1) immediately after irradiation (2) and (3) refer to spectra recorded after annealing at 280 and 390°C, respectively. (b) Thermal decay of centre I (V centre) in $MgAl_2O_4$. (c) Thermal decay of centre II (F+ centre) in $MgAl_2O_4$.

Irradiation leads to the trapping of an electron at an anionic vacancy and such trapping is the basis for the formation of F^+ centres. Hyperfine interaction with the nearest neighbor cations is the major contribution to the linewidth. Defect centre II formed in the present system is

characterized by a small g-shift and the line width is reasonably large. The centre also does not exhibit any resolved hyperfine structure. Recently, such a centre was reported in LiAlO_2 phosphor [37]. On the basis of these observations and considerations of the characteristic features of the defect centres likely to be formed in a system such as $\text{MgAl}_2\text{O}_4:\text{Tb}^{3+}$, the centre II is assigned to F^+ centre.

Fig. 2.22(c) shows the thermal-annealing behavior of centre II which decay in three stages with the uncertainty of $\pm 2\%$. The decay temperature range 70–160°C is associated with the low temperature TL peak at 120°C. Second stage of decay 180–240°C is correlated to the 220°C TL peak. The decay of the centre II also occurs in the temperature range 260–380°C and this decay is associated with the high temperature TL peak at 340°C. Hole trap responsible for 340°C TL peak is not identified from the ESR studies. Three stage decay of centre II shows that F^+ centre acts as recombination centre where the hole from the V centre is released and recombines with the electron in F^+ centre. The recombination energy is transferred to nearby Tb^{3+} ion which results in characteristic Tb^{3+} emission (fig. 2.23). PL and TL emission shows that Tb^{3+} is acting as a luminescent centre. The concentration of defect centres increases, when MgAl_2O_4 is doped with Tb^{3+} as seen from the fig. 2.21. Fig. 2.24(a) shows the variation of V centre and F^+ centre concentration with respect to dose. V centre saturates around 5000 Gy whereas F^+ centre intensity increases up to the studied dose of 7000 Gy. ESR dose–response study shows that the defect centres are formed only during irradiation. Fig. 2.24(b) shows the ESR spectra of irradiated $\text{MgAl}_2\text{O}_4:\text{Tb}^{3+}$ after bleaching it with blue light (470nm) for different duration of time. It is seen that ESR intensity of both the V and F^+ centres decreases with the duration of blue light. This result indicates that both the defect centers are playing role in the TL and OSL process.

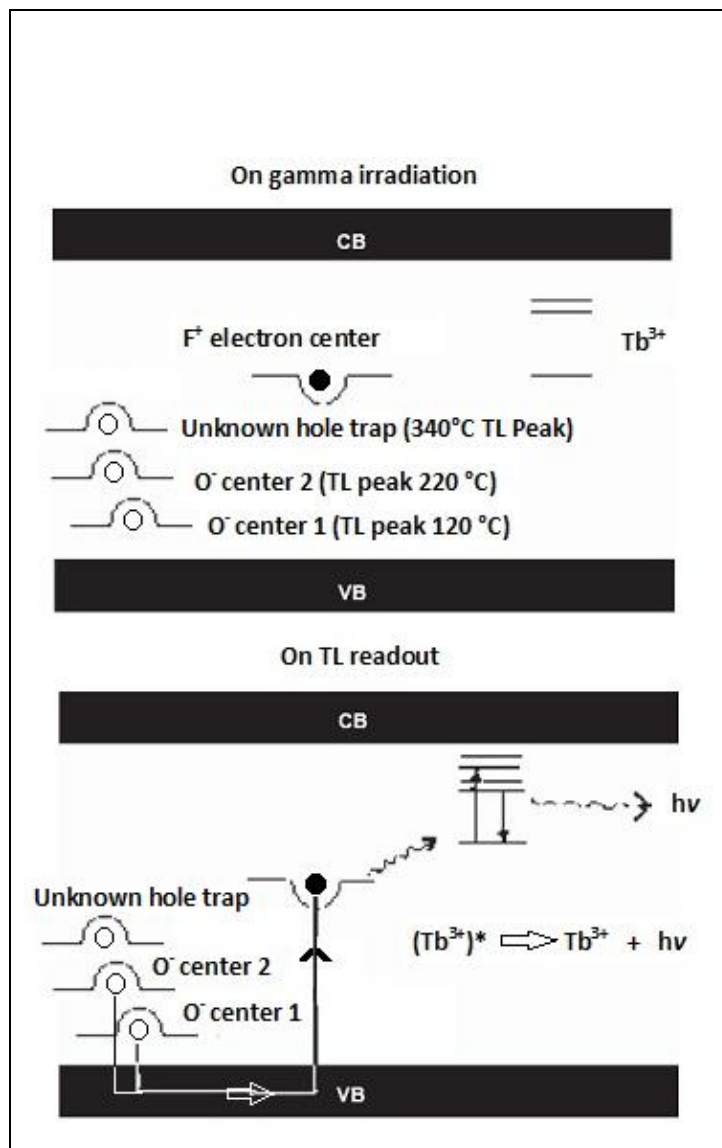


Figure 2.23. Model for 120 and 220°C TL peak in $MgAl_2O_4:Tb^{3+}$.

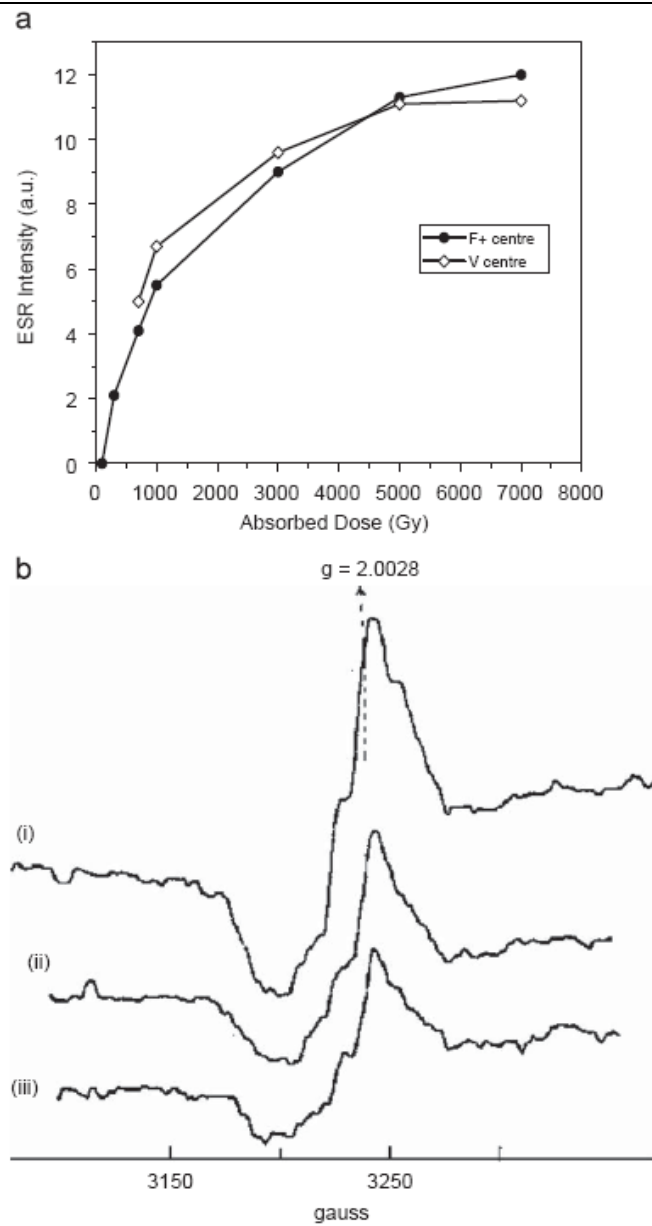


Figure 2.24. (a)Variation of ESR intensity of defect centres (V and F^+ centre) with the absorbed dose. (b)ESR spectrum (i) after irradiation (ii) illuminate their irradiated sample with blue light for 4h (iii) illumination for 6h.

2.9. Summary

This chapter highlights nature and types of defects and their importance as it critically decides luminescence in solids and also for a typical phosphor material to qualify to the status of a bonafide phosphor, it is necessary to understand its defect structure and establish its correlation with the observed sensitivity and also with the variations in process parameters. The characterization of a phosphor with regards to the nature of defects, their concentration and distribution is an integral part of development of synthesis protocol. Therefore, defects and luminescence and other aspects like concentration quenching and thermal quenching in materials is also discussed and the later being illustrated by means of configurational coordinate diagram. The study of defects and ability to generate them in a controlled manner is central to deliver a dosimetric grade material by various pathways one such being the process of diffusion of a dopant into the host lattice and therefore being addressed with a précis on TL and OSL kinetic analysis of phosphor materials; followed by the description of other spectroscopic techniques like Electron Paramagnetic Resonance, Positron Annihilation Spectroscopy, Photoluminescence, Optical Absorption etc. that can probe the role of defects involved and suggest a possible luminescence mechanism. Eventually the chapter highlights the TL, OSL and ESR studies carried on $\text{MgAl}_2\text{O}_4:\text{Tb}^{3+}$ during the course of this research work. $\text{MgAl}_2\text{O}_4:\text{Tb}^{3+}$ phosphor is prepared by combustion synthesis. Three TL peaks are observed at 120, 220 and 340°C. It exhibits OSL when stimulated with 470nm light. The sample thermally treated at 900°C gives maximum PL and OSL emission intensity. Two defect centres, centre I and II are identified in irradiated $\text{MgAl}_2\text{O}_4:\text{Tb}^{3+}$ phosphor and these centres are assigned to V and F^+ centres, respectively. V centre (hole centre) appears to correlate with the 120 and 220°C

TL peaks while F^+ centre which acts as recombination centre is correlated with TL peaks at 120, 220 and 340°C. PL and TL emission results indicate Tb^{3+} acts as luminescent centre.

References:

1. Efthimios Kaxiras, *Atomic and Electronic Structure of Solids*, Cambridge University Press (2003)
2. A. Kelley, G.W. Groves and P. Kidd, *Crystallography and crystal defects*, John Willey & Sons Pvt. Ltd. 285 (2000).
3. G. Blasse and B. C. Grabmaier, *Luminescent Materials*, Springer, Heidelberg (1994).
4. Eduardo G. Yukihara and S. W. S. McKeever, *Optically Stimulated Luminescence: Fundamentals and Applications*, A John Wiley and Sons, Ltd., Publication (2011).
5. B. H. Bransden and C. J. Joachain, *Physics of Atoms and Molecules*, Prentice Hall, Harlow (1983).
6. B. Henderson and G. F. Imbusch, *Optical Spectroscopy of Inorganic Solids*, Clarendon Press, Oxford (1989).
7. B. Di Bartolo, *Optical Interactions in Solids*, John Wiley & Sons, Inc., New York (1968).
8. N. F. Mott and R. W. Gurney, *Electronic Processes in Ionic Crystals*, Clarendon Press, Oxford (1940).
9. M. S. Akselrod, N. Agersnap Larsen, V. H. Whitley, and S.W.S. McKeever, *J. Appl. Phys.*, **84**, 3364 (1998b).
10. E. Daran, R. Legros, A. Munoz-Yague, and L. E. Bausa, *J. Appl. Phys.*, **76**(1), 270 (1994).
11. Jose Solé, Luisa Bausa, Daniel Jaque, *An Introduction to the Optical Spectroscopy of Inorganic Solids*, John Wiley & Sons Ltd, (2005)
12. W. Hoogenstraaten, *Philips Res. Repts.* **13**, 515 (1958).

13. J. C. Inkson, *J. Phys. C: Solid State Phys.*, **14**, 1093 (1981).
14. S. T. Pantelides, *Rev. Mod. Phys.*, **50**, 797 (1978).
15. L. Bøtter-Jensen, S. W. S. McKeever, and A. G. Wintle, *Optically Stimulated Luminescence Dosimetry*, Elsevier, Amsterdam (2003).
16. G. Lucovsky, *Solid State Commun.*, **3**, 299 (1965).
17. H. G. Grimmeiss and L.-A° Ledebø, *J. Phys. C: Solid State Phys.*, **8**, 2615 (1975a).
18. H. G. Grimmeiss and L.-A° Ledebø, *J. Appl. Phys.*, **46**, 2155 (1975b).
19. M. Fox, *Optical Properties of Solids*, Oxford University Press, Oxford (2001).
20. Colin N. Banwell and Elaine M. McCash, *Fundamentals of Molecular Spectroscopy*, Tata McGraw-Hill Education, 4th edition (2006).
21. R. M. Nieminen, M. J. Manninen, *Positrons in solids*. Hautajarvi P. (ed.). Springer-Verlag, Berlin (1979).
22. K. P. Muthe, K. Sudarshan, P. K. Pujari, M.S. Kulkarni, N. S. Rawat, B. C. Bhatt and S K Gupta, *J. Phys. D: Appl. Phys.* **42** 105405 (2009).
23. H. Nakagawa, K. Ebisu, M. Zhang, M. Kitaura, *J. Lumin.* 102–103 590 (2003).
24. D. Jia, W.M. Yen, *J. Lumin.* 101 115 (2003).
25. Pradip Bandyopadhyay, G.P. Summers, *Phys. Rev. B* 31 2422 (1985).
26. A. Ibarra, F.J. Lopez, M. Jimenez de Castro, *Phys. Rev. B* 44 7256 (1991).
27. T.J. Gray, in: A.M. Alper (Ed.), *High temperature oxides*, Academic, New York, (Pt.IV) (1971).
28. U. Schmocker, H.R. Boesch, F. Waldner, *Phys. Lett. A* 40 237 (1972).
29. G.E. Bacon, *Acta Crystallogr.* 5 684 (1952).
30. E. Stoll, P. Fischeer, W. Halg, G. Maier, *J. Phys. (Paris)* 25 447 (1964).

31. J. Shu Fen Wang, Feng Gu, Meng Kai Lu, Xiu Feng Cheng, Wen Guo Zou, Guang Jun Zhou, Shu Mei Wang, Yuan Yuan Zhou, *J. Alloys Compd.* 394 255 (2005).
32. S.W.S. McKeever, *Thermoluminescence of Solids*, Cambridge University Press, Cambridge, (1985).
33. R.C. Weast (Ed.), *Handbook of Chemistry and Physics*, CRC, Cleveland, 1971.
34. J.E. Wertz, P. Auzins, J.H.E. Griffiths, J.W. Orton, *Disc. Faraday Soc.* 28 (1959) 136.
35. V.T. Gritsyna, V.A. Kobayakov, *Zh. Tekh. Fiz.* 55 (1985) 354 [*Sov. Phys. Tech. Phys.* 30 (1985) 206].
36. C.A. Hutchison, *Phys. Rev.* 75 (1949) 1769.
37. Bhushan Dhabekar, E. Alagu Raja, Sanjeev Menon, T.K. Gundu Rao, R.K. Kher, B.C. Bhatt, *Radiat. Meas.* 43 (2008) 291.

Chapter 3

Formulation of Initial Rise method for TL kinetic analysis - Theoretical and Experimental approach

3.1. Introduction

The application of initial rise method, in the case of the general order kinetics of thermoluminescence, has so far been limited to finding the thermal activation energy. However, the order of kinetics and pre-exponential factors could not be evaluated using initial rise method thus one has to resort to other methods of glow curve analysis. In this chapter a novel method has been suggested to calculate the kinetic order and the pre-exponential factor from the Arrhenius plots of the initial rise part of the TL glow curve. The method uses the intercept values on the TL intensity axis of the Arrhenius plots at two or more known doses to evaluate the value of kinetic order.

3.2. Theoretical Formulation

The TL characteristic of any material is labeled by parameters like kinetics obeyed by the TL process, the trap depth E , frequency factor s , etc. Since the pioneering work of Randall and Wilkins [1] and Garlick and Gibson [2] there has been a plethora of published papers dealing with methods by which the trapping parameters (mainly E and s) can be obtained from a TL glow curve. It is known that the glow peak temperature T_m is independent of radiation dose in first order kinetics whereas in second order kinetics, the glow peak temperature T_m decreases with the increase of dose, and the TL glow curves representing second order kinetics are more symmetric than that of the first order TL glow curves.

The initial rise method is the simplest experimental procedure that was first suggested by Garlick and Gibson [2] to obtain the trap depth and is independent of the kinetics involved. In the initial rise part of a TL curve (early rising range of temperatures), i.e. $T \ll T_m$ (where T_m is the temperature at which TL maxima occurs), the rate of change of trapped carrier population is

negligible, hence TL intensity I is strictly proportional to $\exp(-E/kT)$, assuming frequency factor remains same and there is no overlapping of glow peaks, i.e.

$$I(T) = A \cdot \exp\left(-\frac{E}{kT}\right)$$

where A is a constant, $I(T)$ is the TL intensity at any temperature T , when the sample is heated at a linear heating rate of $\beta = dT/dt$, as E is the thermal activation energy and k is Boltzmann's constant. If the plot of $\ln(I)$ vs. $1/T$ is made over this initial rise region ($T \ll T_m$), then a straight line of slope $-E/k$ is obtained from which the activation energy E is easily found. The important requirement in this analysis is that n (the concentration of the trapped carriers at any instant) remains approximately constant. Only upon increase in temperature beyond a critical value, T_c , does this assumption become invalid. However, the initial rise technique can be used only when the glow peak is well defined and clearly separated from the other peaks.

Halprein et al. [3] suggested an improvement to the initial rise method considering general-order kinetics, i.e.

$$I(T) = s' n^b \exp\left(-\frac{E}{kT}\right) \quad (3.1)$$

Where b is the order of kinetics and s' is the pre-exponential factor.

If β is the constant heating rate, n can be calculated as

$$\int_t^\infty I dt = \frac{1}{\beta} \int_T^\infty I dT \quad \text{and if } b \text{ is known a plot of } \ln(I/n_b) \text{ vs. } 1/T \text{ yields a straight line of slope } -E/k.$$

The general order kinetics expression as proposed by May and Partridge [4] is

$$I(t) = -\beta \frac{dn}{dT} = C s' n^b \exp\left(-\frac{E}{kT}\right) \quad (3.2)$$

Where I is expressed in the units of $\text{cm}^{-3}\text{s}^{-1}$ and n in cm^{-3} , C is scaling factor, the quantity s' turns out to have the dimensions $\text{cm}^{-3(b-1)}\text{s}^{-1}$. In order to balance the dimensions in equation (3.1), Rasheedy [5] proposed that s' may be replaced by $s' = s / N^{b-1}$. Here, s is frequency factor (s^{-1}) and N the total concentration of the traps (cm^{-3}). This definition of s' fits well into the first and second order kinetics expressions of Randall and Wilkins [1] and Garlick and Gibson [2] in which $b=1$ and $b = 2$, respectively and the corresponding s' values are equal to s and s / N respectively. Sunta et al. [6] have used the successive interpolation method to find the values of s' corresponding to the range of b values from $b = 1$ to $b = 2$. They arrived at the same expression as above stated expression of Rasheedy. Equation (3.2), thus may be written as

$$I(T) = Cs \frac{n^b}{N^{b-1}} \exp\left(-\frac{E}{kT}\right) \quad (3.3)$$

In the sections to follow formalism of new method is proposed for the determination of TL parameters including kinetic order, pre-exponential factor and frequency factor using the initial rise method for TL equation of general order kinetic over a varying set of doses.

3.2.1. Determining Kinetic Order

In the initial rise part when the condition $n = n_0$ applies, we have from equation (3.2)

$$\ln I(T) = \ln Cs' n_0^b - \frac{E}{kT} \quad (3.4)$$

where n_0 is the initial concentration of trapped electrons.

The first term on the right hand side is the intercept on the $\ln I(T)$ vs. $1/T$ straight line. Call it I_1 .

Thus $I_1 = \ln Cs' n_0^b$

Now if the dose to the sample is increased by a factor X , and the initial rise curve is recorded with the same β value, the intercept becomes $\ln Cs'(Xn_0)^b$. Call it I_2 . It may be seen that

$$I_2 - I_1 = \ln Cs'(Xn_0)^b - \ln Cs'n_0^b$$

$$I_2 - I_1 = \ln(X)^b$$

We thus have

$$b = \frac{I_2 - I_1}{\ln X} \quad (3.5)$$

The intercepts I_1 and I_2 being measurable at two doses differing by a factor of X , the b value may be readily found. Here it is assumed that the traps fill up linearly with dose and the total TL intensity too grows linearly with trap occupancy.

3.2.2. Determining Pre-exponential Factor

Again from the intercept of the $\ln I(T)$ vs. $1/T$ graph of the initial rise part, the intercept I may be expressed as (see equation 3.1)

$$I = \ln Cs'n_0^b = \ln s' + \ln Cn_0^b$$

$$\text{Or } I = \ln s' + \ln Cn_0 + \ln n_0^{b-1}$$

$$\text{Or } s' = \text{Anti log}[I - \ln Cn_0 - (b-1)\ln n_0] \quad (3.6)$$

Having measured the b value from equation (3.4), the value of s' may be found by using the fact that Cn_0 = Total area of the glow peak. One may be able to find the n_0 value from the optical absorption band if such a band could be found for the concerned TL traps. In the present work the input value of n_0 is used to simulate the results.

3.2.3. Determining Frequency Factor

The frequency factor s is a meaningful quantity as opposed to the empirical quantity s' . To find the s value, one may use the equation (3.3) to plot the $\ln I(T)$ vs. $1/T$ graph for the initial rise part. The intercept I , now is given by

$$I = \ln Cs' n_0^b = \ln Csn_0 \left(\frac{n_0}{N} \right)^{b-1}$$

On rearranging the terms it leads to

$$s = \text{Anti log} \left[I - \ln A - (b-1) \ln \left(\frac{n_0}{N} \right) \right] \quad (3.7)$$

This equation too needs the knowledge of area under the TL peak ($Cn_0 = A$). Additionally n_0/N also is required. The latter, may be estimated from the TL intensity vs. dose curve. If one assumes saturating exponential pattern for the TL intensity growth, one has at $n_0/N = 1$, the TL intensity nearly saturated, (Actually at $n_0/N \approx 0.632$ [7]. One may estimate n_0/N at lower doses assuming linear relation.)

However, for first order kinetic TL process equation (3.7) on substituting $b = 1$ reduces to the expression

$$s = \text{Anti log} [I - \ln A] \quad (3.8)$$

Clearly, determining frequency factor s , from equation (3.8) for first order kinetic process is very simple and it requires intercept value of initial rise plot and area under the TL peak, both of which can be experimentally obtained.

Table 3.1. Calculated values of E, b and s for different trap occupancies for input b = 1

Trap occupancy or dose (D)	Intercept (I)	TL Area (Cn ₀)	Dose ratio (X=D/D ₁)	Trap Depth E(eV)	Order of kinetic $b = (I_2 - I_1)/nX$	Frequency factor $s = \text{Anti log} [I - \ln A]$
10 ¹² (D ₁)	55.2 (I ₁)	10 ¹²	1	0.998	-	0.936 x 10 ¹²
10 ¹³	57.5	10 ¹³	10	0.998	1.0	0.936 x 10 ¹²
10 ¹⁵	62.1	10 ¹⁵	10 ³	0.998	1.0	0.936 x 10 ¹²
10 ¹⁷	66.7	10 ¹⁷	10 ⁵	0.998	1.0	0.936 x 10 ¹²

Table 3.2. Calculated values of E , b , s and s' for different trap occupancies for input $b = 1.5$

Trap occupancy (D)	Intercept (I ₁)	TL Area (Cn ₀)	Dose ratio (X)	Trap Depth E(eV)	Order of Kinetic, b	Frequency factor, s^*	Pre-exponential Factor, $s' **$
10 ⁻⁵ (D ₁)	49.5 (I ₁)	10 ¹²	1	0.999	-	0.964 x 10 ¹²	3260
10 ⁻⁴	52.9	10 ¹³	10	0.998	1.497	0.935 x 10 ¹²	3260
10 ⁻²	59.8	10 ¹⁵	10 ³	0.998	1.497	0.932 x 10 ¹²	3307
1	66.7	10 ¹⁷	10 ⁵	0.997	1.495	0.920 x 10 ¹²	3407

* $s = \text{Anti log} \left[I - \ln Cn_0 - (b-1) \ln \left(\frac{n_0}{N} \right) \right]$, ** $s' = \text{Anti log} [I - \ln Cn_0 - (b-1) \ln n_0]$

Table 3.3. Calculated values of E , b , s and s' for different trap occupancies for input $b = 2$

Trap occupancy (D)	Intercept (I ₁)	TL Area (Cn ₀)	Dose ratio (X)	Trap Depth E(eV)	Order of Kinetic, b	Frequency factor, s^*	Pre-exponential Factor, $s' **$
10 ⁻⁵ (D ₁)	43.7 (I ₁)	10 ¹²	1	0.998	-	0.977x10 ¹²	1.044 x 10 ⁻⁵
10 ⁻⁴	48.3	10 ¹³	10	0.998	1.997	0.971x10 ¹²	1.044 x 10 ⁻⁵
10 ⁻²	57.5	10 ¹⁵	10 ³	0.998	1.996	0.953x10 ¹²	1.078 x 10 ⁻⁵
1	66.7	10 ¹⁷	10 ⁵	0.998	1.993	0.909x10 ¹²	1.161 x 10 ⁻⁵

* Expressions for s and s' are same as that used in Table 3.2.

3.3. Numerical Simulations

The initial rise intensities $I(T)$ were computed numerically using the following input parameters in equation (3.3): $E = 1\text{eV}$, $s = 10^{12}\text{s}^{-1}$, $C = 1$, $N = 10^{17}\text{cm}^{-3}$ and $\beta = 2\text{Ks}^{-1}$. Fig. 3.1 shows numerically simulated TL curves for using $b = 1, 1.5$ and 2 . Computations were repeated at various n_0 values. Runge-Kutta second order technique is used. Initial rise $I(T)$ values were calculated until $I(T)$ value reached no more than 5% of the peak intensity as shown in fig. 3.2.

Intercepts of the Arrhenius plots were calculated by fitting the straight line equation to the computed $\ln I(T)$ values at different T.

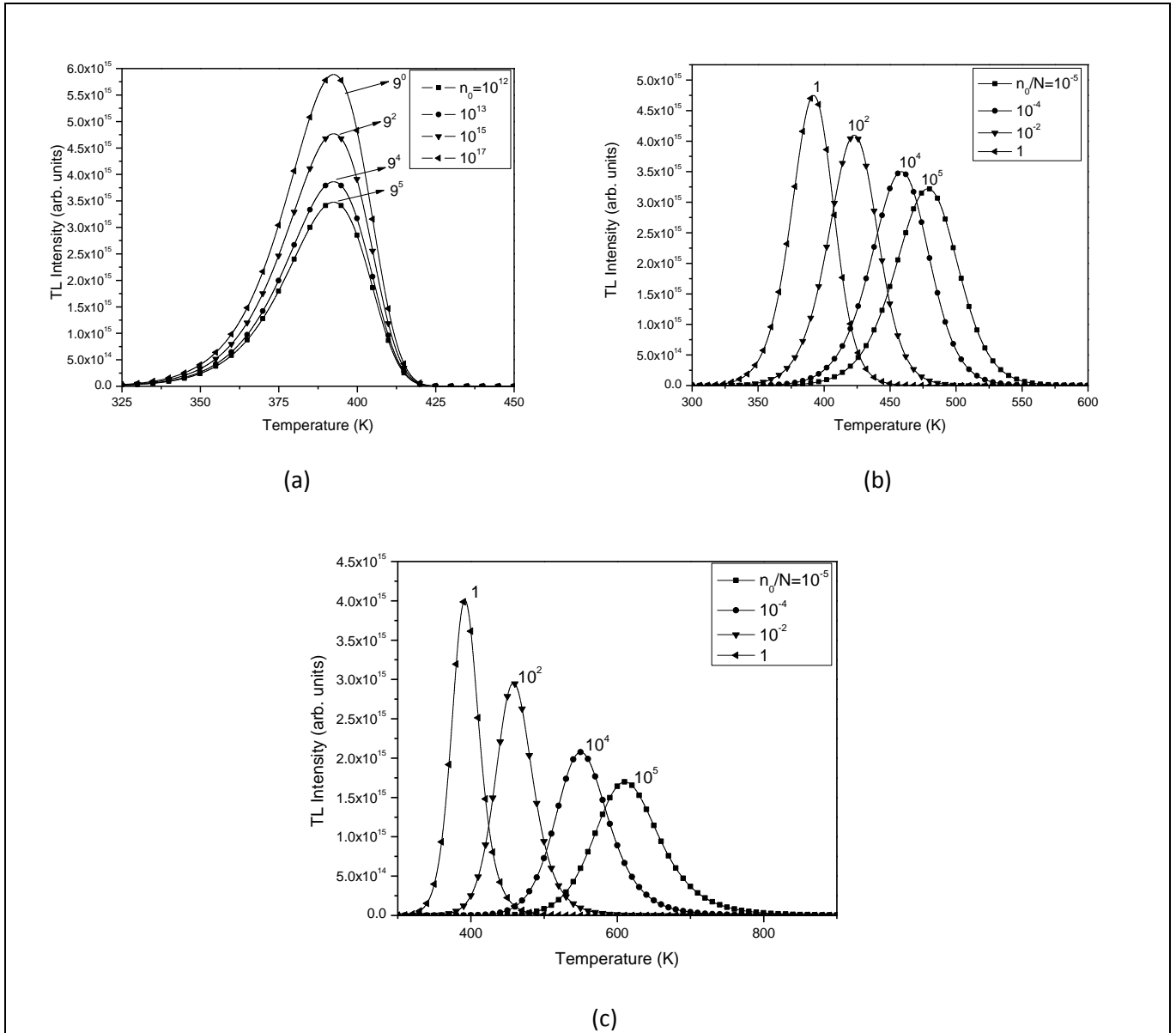


Figure 3.1. Numerically simulated TL curves with input parameters being $E=1eV$, $s=10^{12} s^{-1}$, $N=10^{17} cm^{-3}$, $n_0=10^{12}, \dots, 10^{17}$. The respective curves are multiplied with a factor shown. (a) $b=1$, (b) $b = 1.5$ & (c) $b=2$.

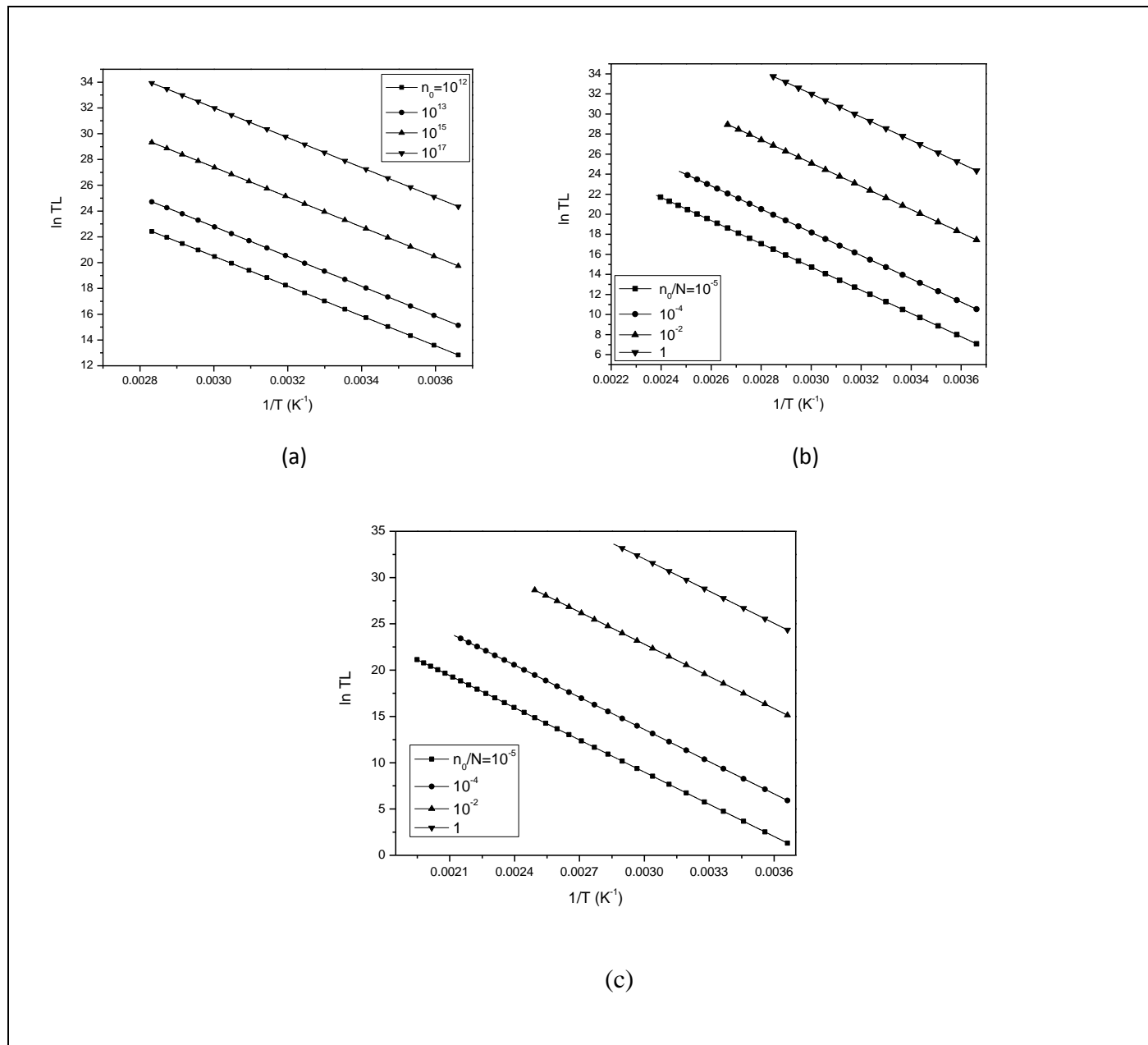


Figure.3. 2. Initial rise plots for curves in fig. 3.1, here the points considered are up to the 5 % of TL peak intensity. (a) $b = 1$, (b) $b = 1.5$ and (c) $b = 2$.

3.4. Experimental Validation

For the experimental validation of this technique it is difficult to find a suitable phosphor that has clean and well resolved TL peaks. However, using the technique of thermal

cleaning we can remove the satellite or embedded peaks, if any, in the TL glow curve of the phosphor material. For the experimental validation of the proposed technique, $\text{CaSO}_4:\text{Dy}$ phosphor samples weighing 5 mg each were taken and exposed to 100, 300 and 500 mGy absorbed dose of $^{90}\text{Sr}/^{90}\text{Y}$ beta source. The analysis of the high temperature TL peak at $\sim 230^\circ\text{C}$ is performed. The samples were given thermal treatment up to 150°C to remove low temperature TL peaks. The TL glow curve peaking at 230°C is recorded at 4 K/s heating rate as shown in fig. 3.3.

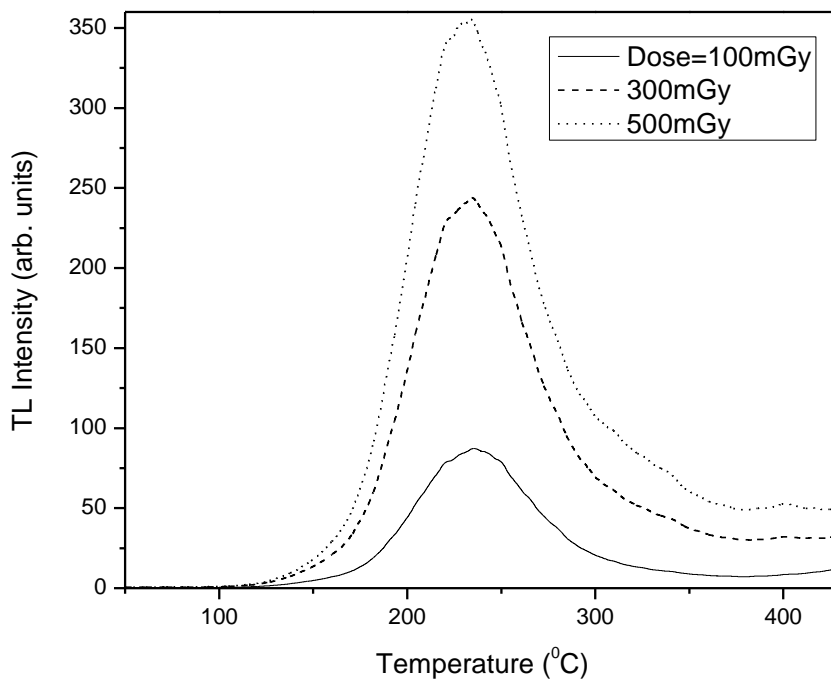


Figure 3.3. 230°C TL glow peak of $\text{CaSO}_4:\text{Dy}$ samples.

Fig. 3.4 shows the initial rise plot of TL glow curves (as shown in fig. 3.3). Table 3.4 shows the analysis of 230°C TL glow peak of $\text{CaSO}_4:\text{Dy}$. The order of kinetics is found to be 1.13 and 1.19. For the sake of simplicity and calculation of frequency factor we have assumed that first

order kinetics is followed by 230°C TL peak of CaSO₄: Dy. The frequency factor at three known doses is of the order 10¹⁰s⁻¹ as shown in Table 3.4. The experimentally calculated TL parameters using the proposed technique (Table 3.4) is found to match with the literature [8].

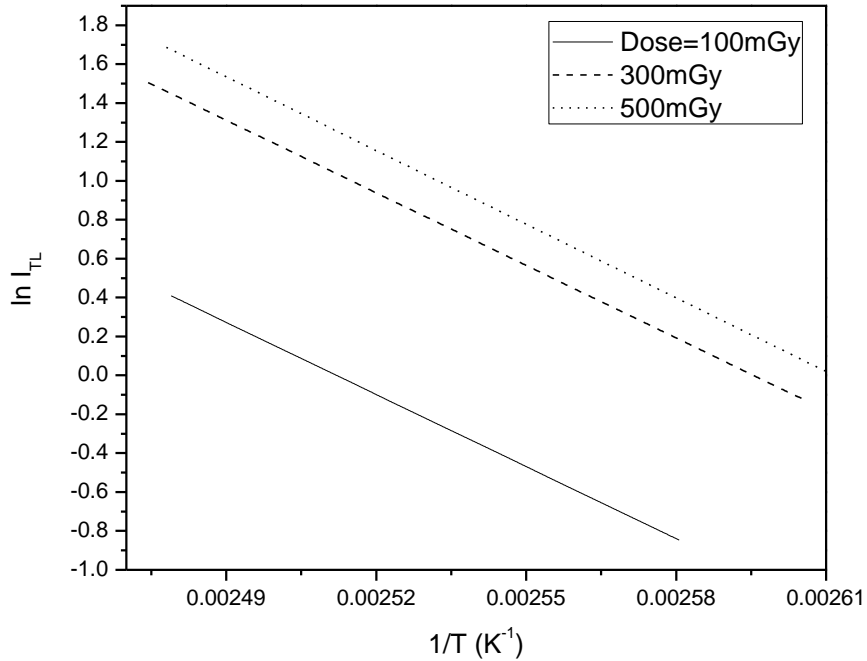


Figure 3.4. Initial rise plots of 230°C TL peak of CaSO₄: Dy.

Table 3.4. Experimentally calculated TL parameters for 230°C TL peak of CaSO₄: Dy

Dose(D) (mGy)	Intercept(Error) (I)	TL area (Cn ₀)	Dose-ratio (X=D/D ₁)	Trap Depth E(eV)	Kinetic order $b = \frac{I_2 - I_1}{\ln X}$	Frequency factor $s = \text{Anti log}[I - \ln A]$
100(D ₁)	31.04(0.21)(I ₁)	2038	1	1.13	-	1.49 x 10 ¹⁰
300	32.28 (0.14)	6190	3	1.14	1.13	1.69 x 10 ¹⁰
500	32.96 (0.14)	9130	5	1.14	1.19	2.26 10 ¹⁰

3.5. Results

The agreement between the values found from simulation and the input values in the case of E , b and s is quite good. The values for these quantities are almost independent of changes in trap occupancy n_0 . On the other hand the value found for s' has strong dependence on b . This is not unexpected, since as discussed in above the dimension of s' are $\text{cm}^{3(b-1)}\text{s}^{-1}$, which indicates that s' would undergo changes as b changes. The values found for s' listed in Table 3.1-3.3 are in agreement with the definition $s' = s/N^{b-1}$, which support the validity of equation (3.6). The experimental values of E , b and s as calculated for 230°C TL peak is in good agreement with the values reported in the literature.

To sum up, the intercepts of the Arrhenius plots of initial rise part of the TL glow peaks, can be used to find b , s or s' . The expressions derived for finding these parameters for a glow peak are general in nature. As may be seen from the results presented in Table 3.1-3.3 these expressions are applicable to the glow peaks of any order of kinetics, irrespective of whether the said peaks are of first, second or general order.

This method being essentially an extension of initial rise method, limitations associated with initial rise apply here as well therefore it is not applicable when TL glow curve consists of several overlapping peaks as often is the case.

3.6. Conclusion

It has been shown that the initial rise method can be used to determine the order of kinetics, pre-exponential factor and frequency factor apart from trap depth E . Using theoretical simulations and finding the trapping parameters from the derived equations we have shown its validity. The essence of this technique lies in the fact that all these parameters can be determined independently i.e. expression for the determination of b and s parameters is

independent of E . Thus the uncertainty and error associated with one parameter does not propagate into the determination of another.

References:

1. J.T. Randall, M.H.F. Wilkins, *Proc. R. Soc. A* **184** 366 (1945).
2. G.F.J. Garlick, A.F. Gibson, *Proc. Phys. Soc.* **60** 574 (1948).
3. A. Halperin, A. Braner, *Phys. Rev.* **117** 408 (1960).
4. C.E. May, J.A. Partridge, *J. Chem. Soc.* **40** 1401 (1964).
5. M.S. Rasheedy, *J. Phys.: Condens. Matter* **5** 633 (1993).
6. C.M. Sunta, B.C. Bhatt, P.S. Page, in: *Proceedings 3rd International Conference on Luminescence and Its Applications, New Delhi*, p. 30 (2008).
7. C.M. Sunta, E.M. Yoshimura, E. Okuno, *Radiat. Meas.* **23** 655 (1994).
8. Numan Salah, P.D. Sahare, S.P. Lochab, Pratik Kumar, *Radiat. Meas.* **41** 40 (2006).

Chapter 4

Characterization and study of temperature dependence of photo-ionization cross section in $\text{Al}_2\text{O}_3:\text{C}$

4.1 Introduction

TL and OSL characterization of Al₂O₃:C material prepared by post growth thermal impurification (PGTI) technique has been carried out and has been investigated for dose dependence of its photo-ionization cross-section. A model has been proposed to explain measured dose dependence of Photo-ionization cross section. Multiple OSL peaks of Al₂O₃:C have been resolved using a recently reported non-linear light modulation based optically stimulated luminescence (NL-OSL) technique for the first time. Thermal assistance energy associated with photo-ionization cross-section of Al₂O₃:C has been determined by simultaneous stimulation with continuous 470nm light and linearly increasing temperature (a process termed as Thermally Assisted (TA)-OSL) as well as under isothermal conditions. Theoretical modeling has also been carried out for the observed TA-OSL. The value of thermal assistance energy (E_A) and temperature independent pre-exponential factor of photo-ionization cross-section were found to be ~ 0.03eV and ~ 4.24 x 10¹⁸cm² respectively. Temperature dependence of cross section showed Arrhenius nature.

4.2. TL and OSL Characterization of developed α-Al₂O₃:C

The dosimetric utility of these samples was ascertained by excitation and emission spectroscopy and through measurement of TL and OSL response. The analysis of the results obtained through characterization of different samples processed using PGTI technique mentioned in chapter 1 is discussed below.

4.2.1. TL Studies

Dosimetric properties of the crystals were studied using TL technique. In order to record the TL response, the samples were irradiated using a calibrated ⁹⁰Sr/⁹⁰Y beta source to an absorbed dose of 0.33Gy and the TL glow curves were recorded at a constant heating rate of

4K/s in an indigenously designed and calibrated programmable reader system [1]. The TL glow curve of some popular phosphors and the processed anion defective α - Al_2O_3 is recorded by normalizing the TL intensity to the sample mass as shown in fig. 4.1. TL measurements were also carried out for TLD-100 and $\text{CaSO}_4:\text{Dy}$. The sensitivity of various phosphors is given in Table 4.1. The dosimetric TL peak height of each phosphor is compared to check the TL sensitivity. The processed Al_2O_3 invariably shows two well-defined, non-overlapping glow peaks at 56 and 190°C as shown in fig. 4.2.

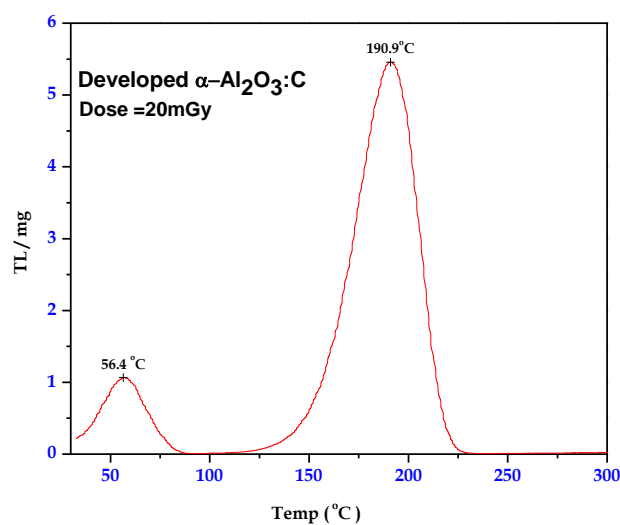


Figure 4.1. TL glow curve of developed α - $\text{Al}_2\text{O}_3:\text{C}$ phosphor for 20mGy dose.

The low temperature peak is attributed to shallow traps and is found to decay within five minutes after irradiation. The TL sensitivity of the processed sample is found to be 41 times higher than TLD-100 and almost 0.5 times to the commercial sample. However, the ratio of low temperature peak to the dosimetric peak of the processed sample is 1:5 as against 1:14 in case of commercial sample. The TL response of the samples was found to depend on the process temperature as shown in Fig. 4.3. The maximum TL response was obtained for the samples processed at 1500°C.

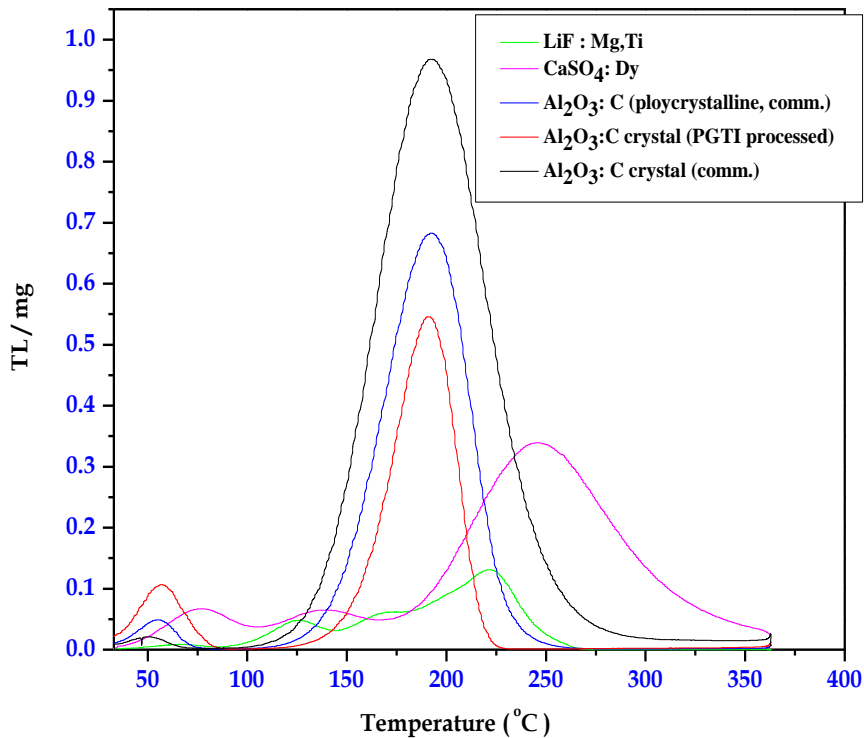


Figure 4.2. TL glow curves of α - $\text{Al}_2\text{O}_3\text{:C}$ and other popular TL phosphors for 12.5mGy absorbed dose

The normalized TL response of the commercial and the processed sample is shown in fig. 4.4. It may be noted that the FWHM of the dosimetry peak of processed sample is approximately 30% less than the commercial sample and no substantial difference in geometrical factor ($\mu_g \approx 0.46$) is observed between them. This indicates the similarity between trap depths and nature of defects in PGTI processed and commercial samples.

Table 4.1 TL Sensitivity Comparison of different phosphors

<i>Phosphors</i>	<i>Sensitivity (area)</i>	<i>Sensitivity (height)</i>
LiF:Mg,Ti	1.00	1.00
CaSO₄:Dy	38.46	25.68
Al₂O₃:C (Polycrystalline Comm.)	37.75	51.82
Al₂O₃:C (Disc, Comm.)	69.34	73.34
Al₂O₃:C (PGTI Developed)	24.97	41.29

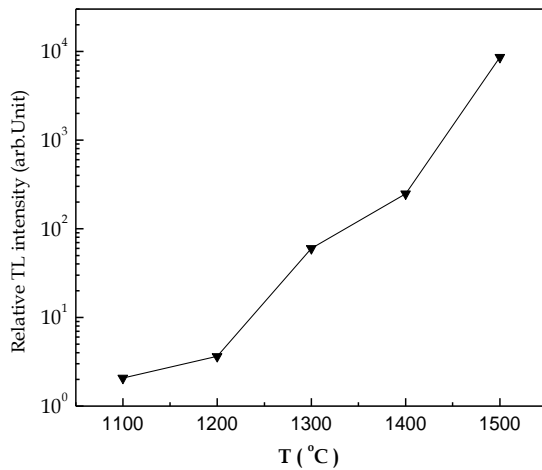


Figure 4.3. Effect of Process Temperature on the TL response of $\alpha\text{-Al}_2\text{O}_3\text{:C}$.

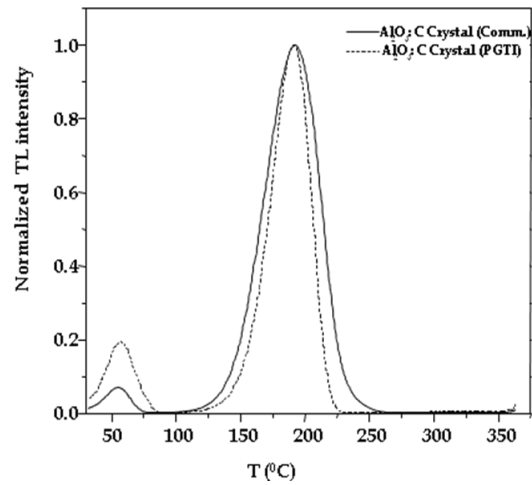


Figure 4.4. Normalized TL response of commercial $\alpha\text{-Al}_2\text{O}_3\text{:C}$ and processed $\alpha\text{-Al}_2\text{O}_3\text{:C}$.

4.2.2. OSL Studies

OSL studies were performed at room temperature for which, the samples were irradiated to an absorbed dose of 12.5mGy. The optical excitation unit consists of a high intensity blue light emitting diode (LED) cluster with $\lambda_p = 470\text{nm}$, $\Delta\lambda = 70\text{nm}$. The light intensity at the sample position was measured to be $100\text{mW}/\text{cm}^2$ for a 350mA dc through LED cluster. The GG-435 and UG-1 optical filters were used to prevent the stimulating radiation from reaching PMT. The luminescence intensity was recorded using a photon counting module interfaced to the computer. All OSL measurements were compared to the $\alpha\text{-Al}_2\text{O}_3\text{:C}$ single crystal (TLD -500 disc, 5mm dia., 1mm thick, produced by Urals Polytechnical Institute, hereafter called as commercial sample). Apart from TL response the processing temperature also critically influences the OSL response of the material in terms of sensitivity as shown in Fig. 4.5. It is seen that, the samples processed at 1500°C (which was maximum attainable temperature for the

furnace used) show excellent OSL response. Fig. 4.6 shows OSL response of the processed samples (at 1500°C) and commercial sample. Fig. 4.7 shows normalized OSL response of these samples.

The OSL response of the commercial samples show two distinct components (fast and slow) originating from two different trap levels having different photo-ionization cross sections as shown in fig.4.7. The photo-ionization cross-section of the fast component of commercial samples is 11 times the slow component. The photo-ionization cross-section of the processed samples is approximately 1.7 times the fast component of the commercial samples. This indicates a faster OSL readout possibility in case of the processed samples.

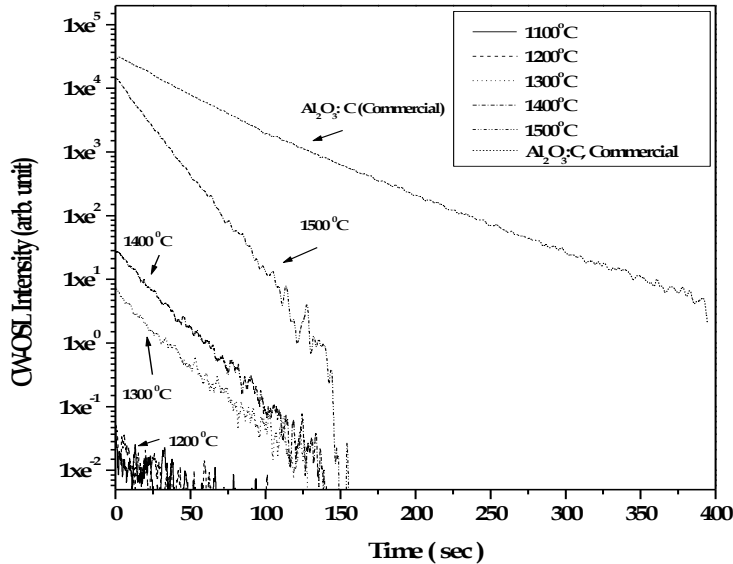


Figure 4.5. Effect of Process Temperature on the OSL response of α -Al₂O₃:C.

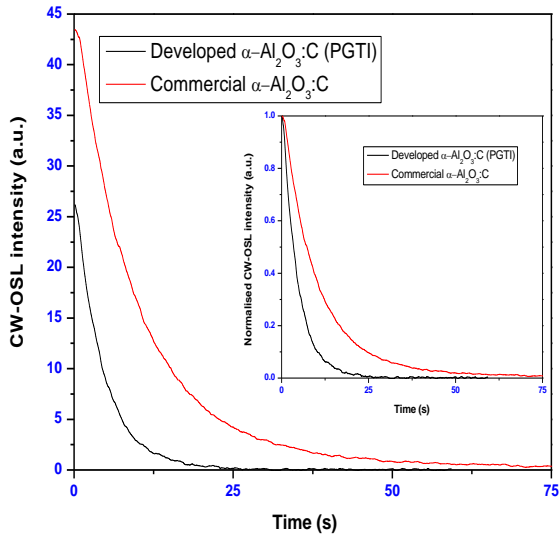


Figure 4.6. CW-OSL response of the Developed and Commercial $\alpha\text{-Al}_2\text{O}_3\text{:C}$ samples irradiated to 10.0 mGy $^{90}\text{Sr}/^{90}\text{Y}$ beta source.

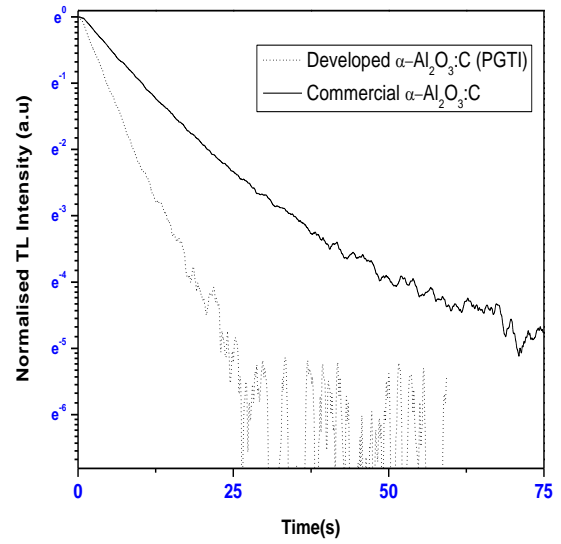


Figure 4.7. Normalized CW-OSL response of the Developed and Commercial $\alpha\text{-Al}_2\text{O}_3\text{:C}$ samples irradiated to 10.0 mGy.

Dose Linearity

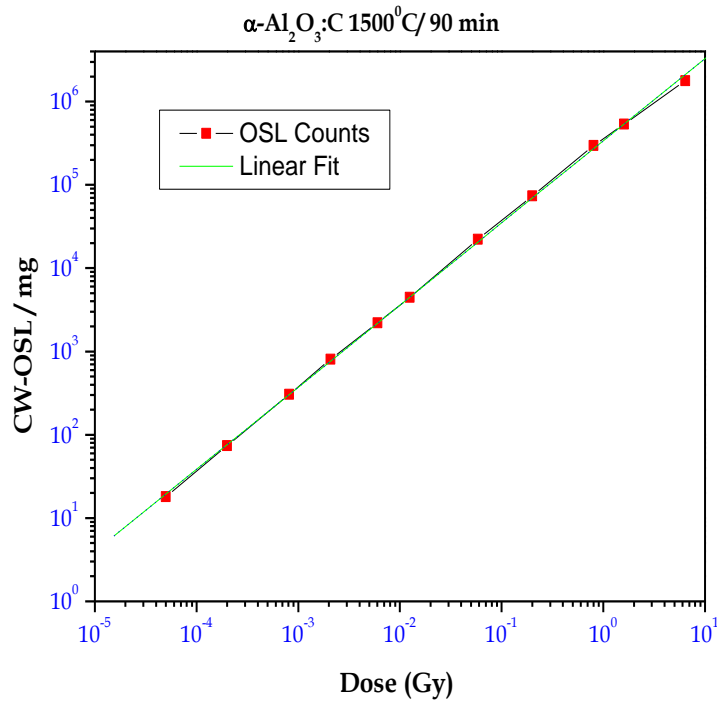


Figure 4.8. CW-OSL response of $\alpha\text{-Al}_2\text{O}_3\text{:C}$ sample for $^{90}\text{Sr}/^{90}\text{Y}$ β dose.

Another prerequisite for a phosphor, in order that it becomes applicable for the dosimetric measurements, is to identify the range of doses over which its response is linear and its detection threshold. Linearity is defined as the ability to reproduce the input characteristics symmetrically and this can be expressed by the equation $y = mx + c$ where y is the output, x the input, m the slope ($m=1$ is linear, $m<1$ is sub-linear and $m>1$ supra-linear) and c the intercept. The linearity is expressed as a percentage of the departure from the linear value, i.e. maximum deviation of the output curve from the best-fit straight line during any calibration cycle.

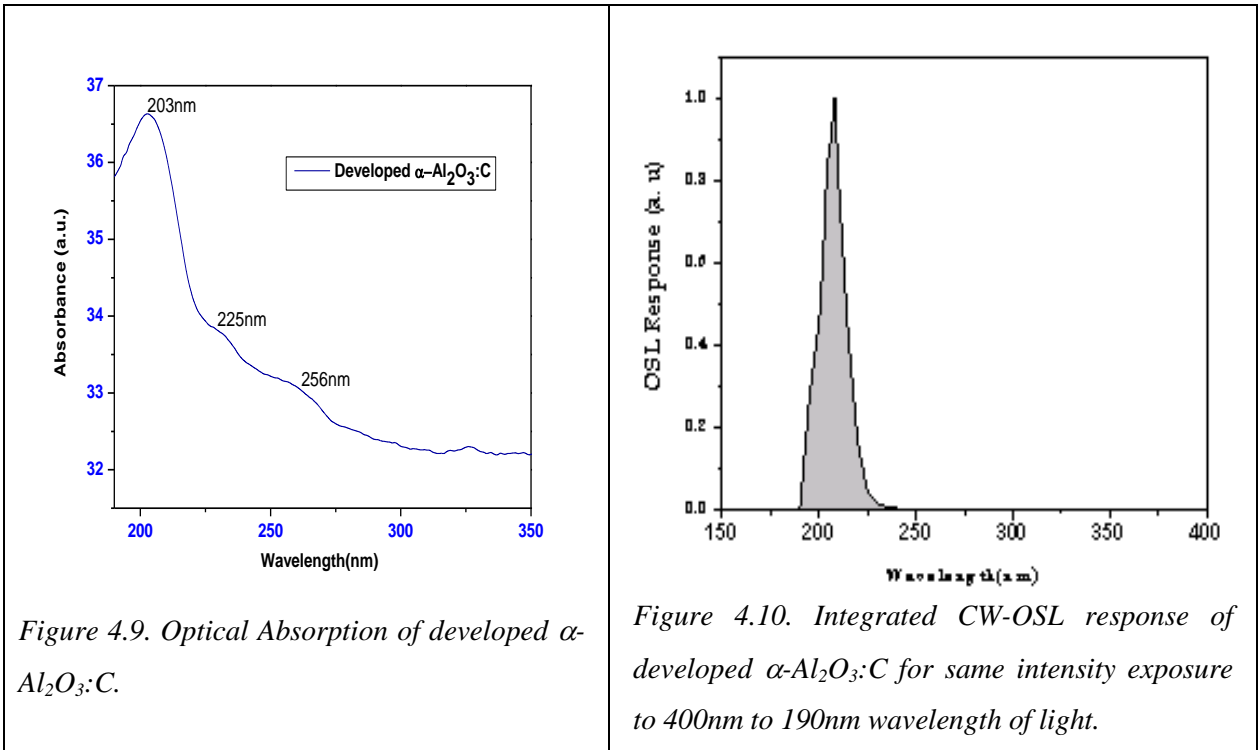
The dose linearity and the detection threshold measurements are carried out on the α - $\text{Al}_2\text{O}_3:\text{C}$ samples. The beta irradiations on the α - $\text{Al}_2\text{O}_3:\text{C}$ samples were carried out using a calibrated $^{90}\text{Sr}/^{90}\text{Y}$ beta source to different absorbed doses. Fig. 4.8 shows the dose vs. CW-OSL response of the processed samples for $^{90}\text{Sr}/^{90}\text{Y}$ beta source. The samples were found to have a linear response up to 1Gy. Minimum measurable dose of $50\mu\text{Gy}$ ($\pm 3\sigma$) could be detected using the PGTI processed $\text{Al}_2\text{O}_3:\text{C}$ samples.

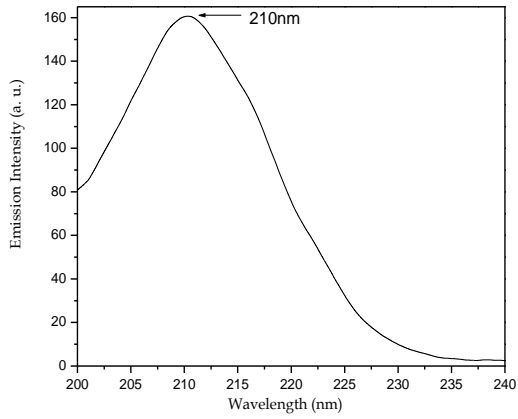
The observed TL /OSL sensitivity in materials is due to a) the generation of defects that traps the electron at meta-stable state and b) the introduction of recombination center. The characterization of some meta-stable charge trap levels can be done by taking TL of the material and measuring associated TL parameters such as trap-depth, frequency factor etc. The other thermally stimulated processes can also be used such as thermally stimulated conductivity (TSC), thermally stimulated exo-electron (TSE) etc. The OSL technique further provides the photo-ionization cross-section associated with trap levels. We have seen in chapter 2 that the photo-ionization cross-section is very complex function that depends on lattice parameters such as refractive index, effective mass of electron, optical threshold of ionization of defects etc. The TL/OSL properties of materials highlight one aspect of defects. But to fully understand the type

of defect other non destructive spectroscopic techniques such as Optical Absorption (OA) and Photoluminescence (PL) are extensively used.

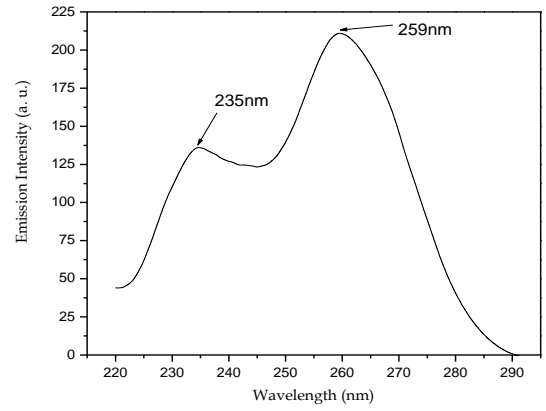
4.2.3. Optical Absorption Studies

Fig. 4.9 shows the optical absorption spectrum of the α -Al₂O₃:C crystals processed at 1500°C for 90 minutes. It shows a peak at 203nm, which implies the formation of F center (i.e. two electrons trapped at an anion vacancy) while the bands at 225nm and 255nm confirm the formation of F⁺ center (single electron trapped at an anion vacancy) in the crystal. These values are in agreement with those reported in the literature. When an irradiated α -Al₂O₃:C single crystal was exposed to UV light of wavelength 203nm and subsequently subjected to readout in the OSL reader, it gives OSL. This confirms that F centers which are already present in an unirradiated α -Al₂O₃:C single crystal, are ionized by UV light (203nm) and electrons thus released to the conduction band are trapped in the OSL active traps. Fig. 4.10 shows the Integrated CW-OSL response of α -Al₂O₃:C for exposure to UV light of 400nm to 190nm.

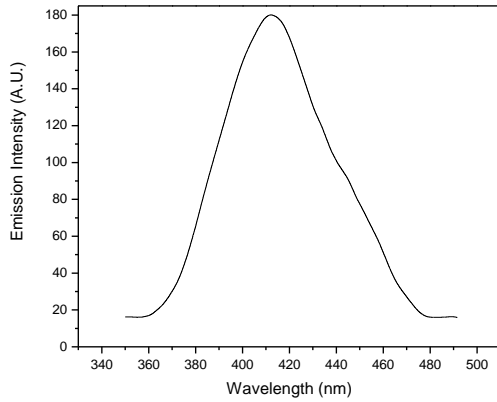




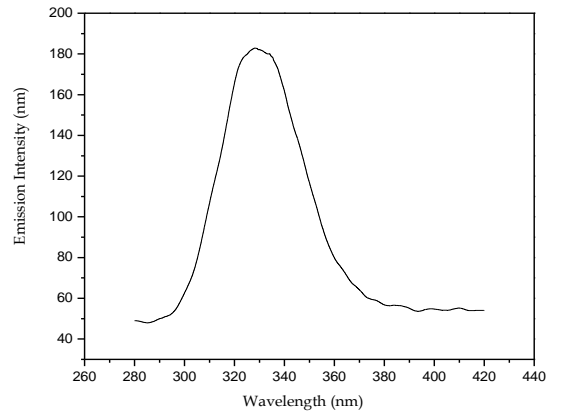
(a) Excitation spectra of F center for 413nm emission



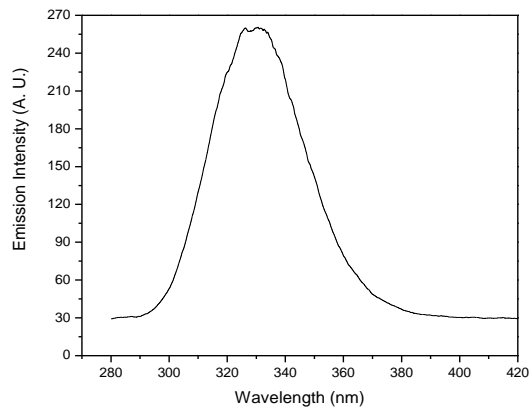
(b) Excitation spectra of F⁺ center for 325nm emission



(c) Emission spectra of F center when excited by 210nm



(d) Emission Spectra of F⁺ center when excited by 235nm



(e) Emission spectra for F⁺ center when excited by 260nm

Figure 4.11.: Photo-Luminescence spectra of F and F⁺ centers in Al₂O₃:C

4.2.4. PL studies

The excitation and emission spectra were recorded on the developed samples using Hitachi F-4500 fluorescence spectrometer to confirm the formation of F and F⁺ centers. Specifications of Hitachi F-4500 fluorescence spectrometer mentions light source of 150 W xenon lamp in a self-deozonating lamp house; Large aperture stigmatic concave diffraction grating, 900 lines/mm, Blazed wavelength: excitation at 300nm and emission at 400nm; wavelength range on both excitation and emission sides being 220 to 730nm, and zero-order light; wavelength accuracy is within ± 2.0 nm. Fig. 4.11 shows PL spectra of F and F⁺ centers for α -Al₂O₃:C.

4.2.5. Conclusion

The α -Al₂O₃:C developed using Post Growth Thermal Impurification (PGTI) technique represents an alternative approach towards the synthesis of ultra-sensitive phosphor which involves heating a α -Al₂O₃ single crystal in the presence of graphite under vacuum of 10⁻⁵Torr to the temperatures around 1500°C. Since the temperatures at which defects are generated are substantially lower than the melting point of α -Al₂O₃ i.e. 2047°C the extent of defect creation can be varied by simply changing the process temperature and time. The samples so produced have absorption peaks at 203, 225 and 255 nm confirming the formation of F and F⁺ centres. PL studies independently established the formation of F and F⁺ centers in the processed material. These samples invariably show two clearly defined peaks in their TL response. The samples have shown the substantial OSL response as well. The comparison of the PL spectra of the samples before and after processing in the presence of graphite indicate important role of carbon diffusion in rendering the samples sensitive towards radiation.

4.3. Dose dependence of photo-ionization cross section in Al₂O₃:C

This section discusses the dose dependence studies of photo-ionization cross section on Single crystals of Al₂O₃:C developed indigenously using vacuum assisted post growth thermal impurification (PGTI) technique which is described in section 1.11.1 of chapter 1. A model is also suggested to explain this observation.

4.3.1. Experimental

Single crystals of Al₂O₃:C developed using vacuum assisted post growth thermal impurification technique were used to study the dose dependence of photo-ionization cross-section in this material. Irradiations were performed using ⁹⁰Sr/⁹⁰Yr beta source and optical stimulation wavelength used was 470nm ($\Delta\lambda=20$ nm). The range of dose delivered to the material is from 20mGy to 85Gy. Beyond this dose the response of the material saturates due to filling of all the traps responsible for OSL in the material.

4.3.2. Results

Nature of CW-OSL curves for various doses is shown in fig. 4.12. It is observed that for lower, intermediate and higher doses the CW-OSL curve follows first, second and third order exponential decay respectively and the mathematical equations to obtain the fit are

$$\text{For Lower doses } (< 1\text{Gy}) \quad I_{CWOSL} = n_{01}\sigma_1\phi\exp(-\sigma_1\phi t)$$

$$\text{Intermediate doses } (1\text{Gy to } 5\text{Gy}) \quad I_{CWOSL} = n_{01}\sigma_1\phi\exp(-\sigma_1\phi t) + n_{02}\sigma_2\phi\exp(-\sigma_2\phi t)$$

$$\text{Higher doses } (>5\text{Gy}) \quad I_{CWOSL} = n_{01}\sigma_1\phi\exp(-\sigma_1\phi t) + n_{02}\sigma_2\phi\exp(-\sigma_2\phi t) + n_{03}\sigma_3\phi\exp(-\sigma_3\phi t)$$

It is observed that photo-ionization cross section increases with increase in dose as evident from Table 4.2 which is graphically represented in fig. 4.13. All slow, intermediated and fast components of photo-ionization cross-section follow the similar trend. Decay time of CW-OSL signal is inversely proportional to cross-section.

Table 4.2. Experimentally determined OSL decay time; and slow, intermediate & fast components of photo-ionization cross-section

Dose(Gy)	OSL decay time (s)			Photo-Ionization Cross-sections (cm ²)		
	Fast (τ_1) (Error)	Intermediate (τ_2) (Error)	Slow (τ_3) (Error)	Fast (σ_1) (x10 ⁻¹⁸)	Intermediate(σ_2) (x10 ⁻¹⁹)	Slow (σ_3) (x10 ⁻²⁰)
0.02	2.72±0.009	-	-	2.33	-	-
0.05	2.65±0.008	-	-	2.38	-	-
0.2	2.54±0.006	-	-	2.49	-	-
1	2.48±0.003	83.9±0.41	-	2.55	0.75	-
5	2.35±0.004	33±0.31	125.0±1.01	2.69	1.92	5.06
10	1.93±0.003	30.2±0.36	103.7±1.16	3.28	2.09	6.1
29.5	1.46±0.005	26.2±0.27	97.0±1.08	4.33	2.41	6.52
85	1.37±0.004	22.8±0.24	87.1±0.90	4.62	2.77	7.26

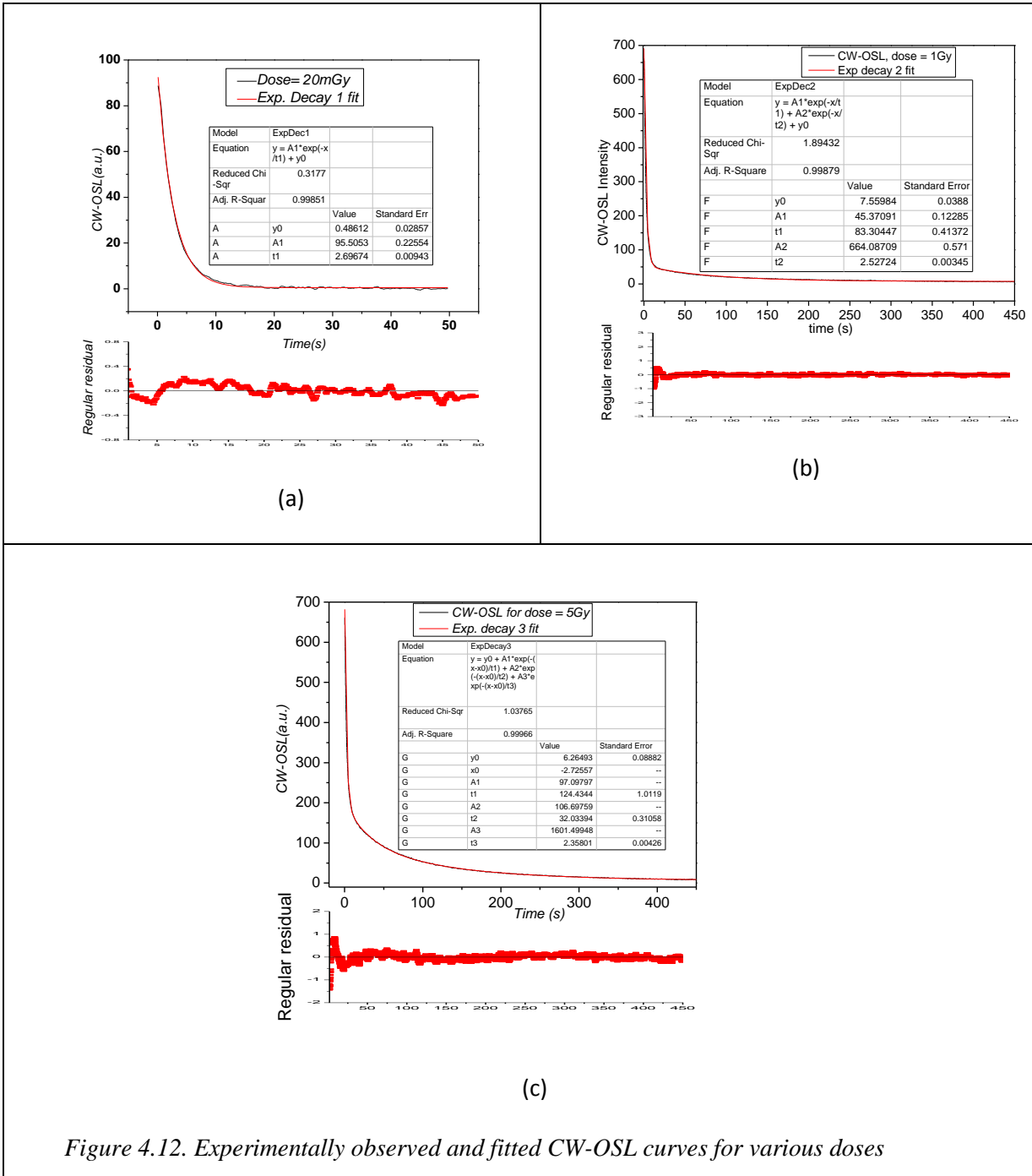


Figure 4.12. Experimentally observed and fitted CW-OSL curves for various doses

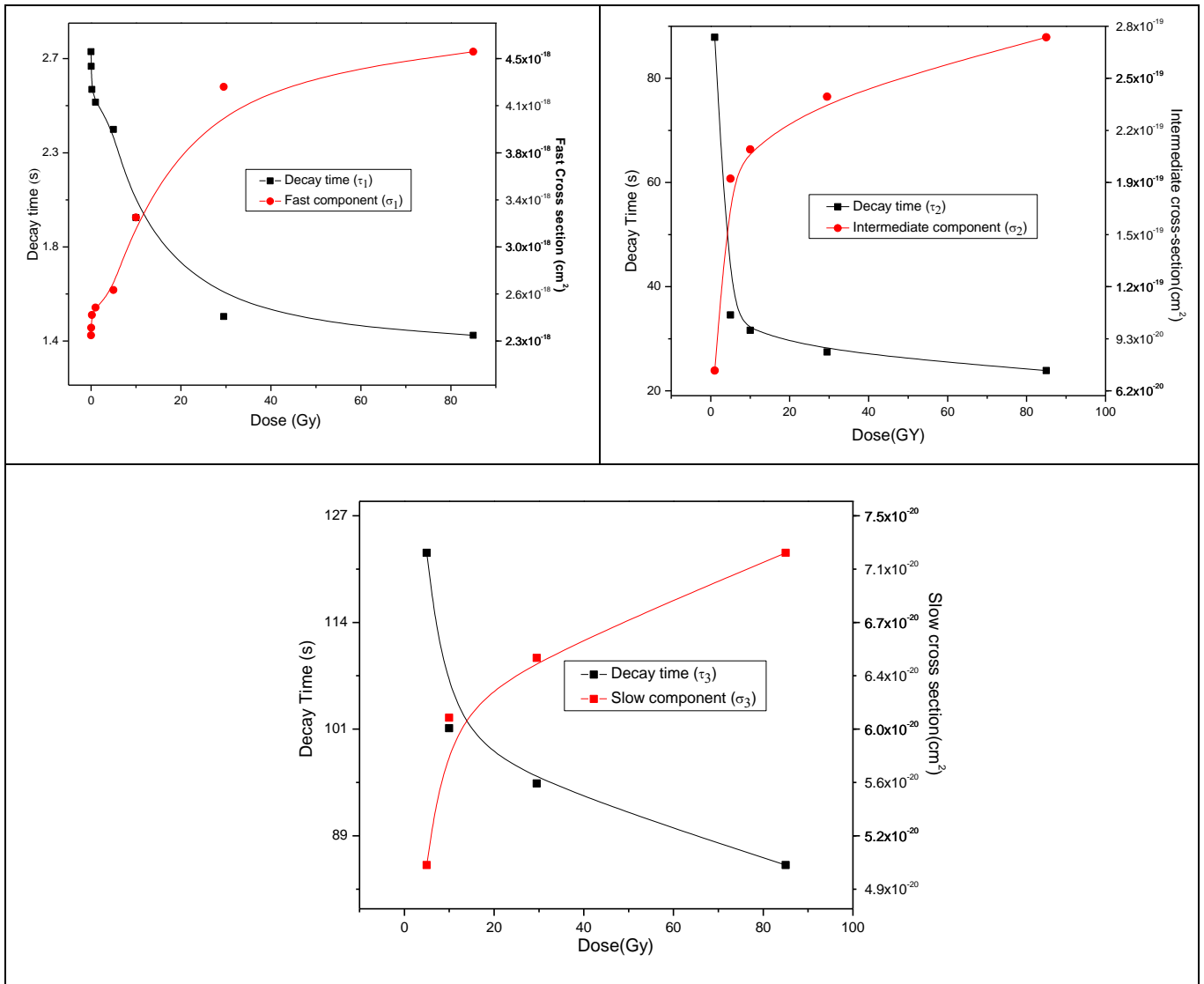


Figure 4.13. CW-OSL decay time and photo-ionization cross section w.r.t. to absorbed dose in $Al_2O_3:C$

4.3.3. Model to explain the dose dependence of photo-ionization cross-section

Since we have three types of OSL traps in terms of photo-ionization cross-section fast (σ_1), intermediate (σ_2) and slow (σ_3) as shown in fig. 4.14. Therefore in this model we assume that the trapping probability T_σ for three traps is such that $T_{\sigma_1} > T_{\sigma_2} > T_{\sigma_3}$. Traps with cross-section σ_1 respond to the lower doses and thus get filled first consequence of which is first order exponential fit for lower doses. For intermediate doses, the occupancy index of traps with photo-ionization cross-section σ_1 is \sim unity, that leads to filling of traps with cross-section σ_2

and therefore 2nd order exponential fit of CWOSL. Similarly, CWOSL decay pattern follows 3rd order exponential fit for higher doses.

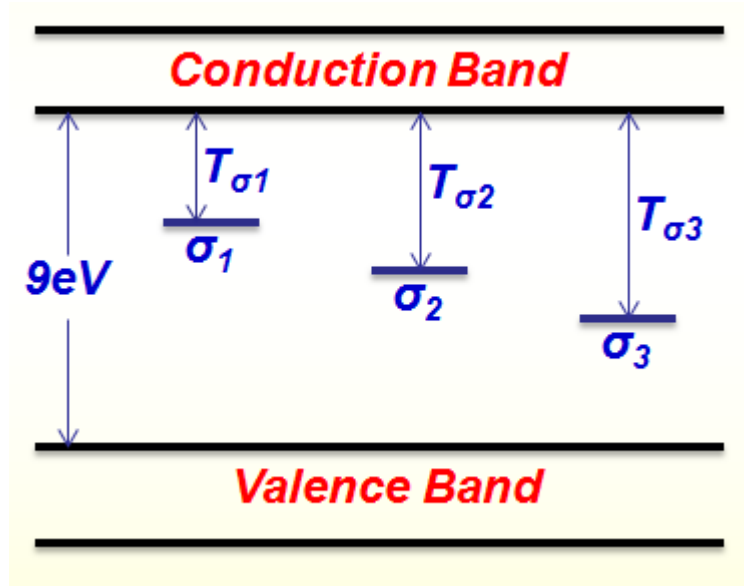


Figure 4.14. Band gap diagram showing components of photo-ionization cross-section in Al₂O₃:C

4.3.4. Model to explanation the increase in σ as a function of dose

When trapped electrons are stimulated by optical means and pumped to conduction band (CB) then it either recombines radiatively with recombination center (RC) to give luminescence signal or is trapped by some competitor trap present in the forbidden band (FB) of lattice which delays the acquisition of OSL on time scale. Now as dose increases the occupancy index of competitor traps increases (reduction in the concentration of unoccupied competitor traps) thereby implying efficient and accelerated recombination of electrons with RC. This is how an increase in photo-ionization cross-section with increase in dose may be explained. It is important to mention that the relative magnitude of three components of cross sections is in the order $\sigma_1 > \sigma_2 > \sigma_3$.

4.4. Investigations on temperature dependence of photo-ionization cross-section in $\text{Al}_2\text{O}_3:\text{C}$

The temperature dependent nature of CW-OSL decay constant can be understood, by investigating the temperature dependence characteristics of photo-ionization cross-section (σ) of OSL trap, as the decay constant is product of former (i.e. σ) and stimulation flux. Spooner [2] has studied the temperature dependent nature of photo-ionization cross-section in quartz by taking elevated temperature isothermal CW-OSL measurements and suggested that the temperature dependence photo-ionization cross-section follows Arrhenius nature. It is suggested that the photo-ionization cross-section consists of basically of two parts - one is temperature independent and the other temperature dependent exponential term. Therefore the value of photo-ionization cross-section measured at room temperature is the value of photo ionization cross-section with thermal assistance of energy from 0 K to room temperature. In this section we present a new method to determine the thermal assistance energy associated with OSL traps, which helps to determine the two distinct terms - temperature independent pre-exponential factor and temperature dependent part of photo-ionization cross-sections. The theoretical formulation of newly suggested method has been verified by numerical simulation and experimental validation using most popular OSL grade dosimeter $\alpha\text{-Al}_2\text{O}_3:\text{C}$ phosphor. The present work also brings out more detailed information about the phenomenon of Thermally Assisted (TA)-OSL in dosimetry traps of grade $\alpha\text{-Al}_2\text{O}_3:\text{C}$, which will be helpful to extend the applicability of $\alpha\text{-Al}_2\text{O}_3:\text{C}$ in radiation dosimetry [2, 3].

4.4.1. Theory of Method

Spooner [2] in 1994 described this temperature dependence of photo-ionization cross-section effect in terms of thermal activation from a ground state to an intermediate excited state, with activation energy E_A , from where optical excitation to the delocalized band takes place (as

shown fig. 4.15). The decay constant of CW-OSL curve was observed to follow Arrhenius law.

This can also be expressed in terms of photo ionization cross-section $\sigma(T, \lambda)$ as

$$\sigma(T, \lambda) = \sigma_o(\lambda) e^{-\frac{E_A}{kT}} \quad (4.1)$$

Where k is the Boltzmann's constant and $\sigma(T, \lambda)$ is the photo ionization at temperature T (K) and stimulation wavelength λ . The $\sigma_o(\lambda)(cm^2)$ is the a pre-exponential photo ionization cross-section which is free from thermal perturbations. However, for optical transitions from deep traps to a parabolic delocalized band it can be expressed [4] as

$$\sigma_o(\lambda) = K \sqrt{E_o} \frac{(h\nu - E_o)^{3/2}}{h\nu(h\nu - \delta E_o)^2} \quad (4.2)$$

Where K is a constant, $h\nu$ is the energy of the stimulation light of wavelength λ , E_o is the optical ionization threshold energy for the trap, and δ is a constant ($\delta = 0.559$ for quartz) [5].

The excitation rate $f(T, \lambda)$ (s^{-1}) of CW-OSL can be expressed in terms of product of photo-ionization cross-section and stimulation intensity $\phi(\lambda)$ (no. of photons/cm²/s), as

$$f(T, \lambda) = \sigma(T, \lambda) \phi(\lambda) \quad (4.3)$$

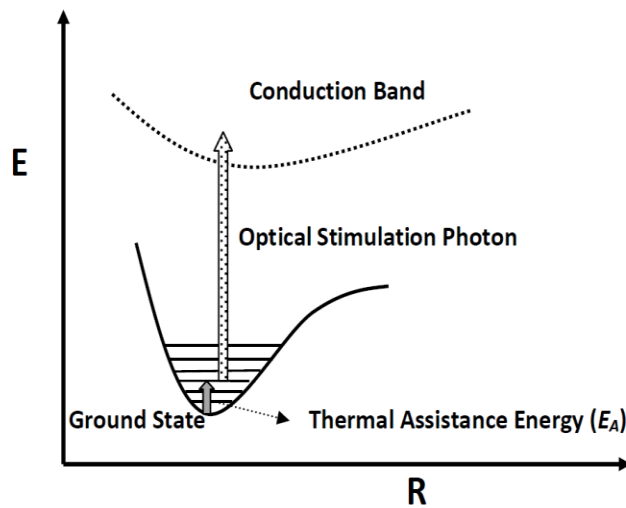


Figure 4.15. Configuration coordinate diagram of trap level and conduction band.

Considering simplified one-trap one recombination center model (OTOR) one can assume quasi-equilibrium condition where the rate of change of electron population in conduction band is negligibly small as compared to the rate of change of concentration of electrons in the OSL traps, i.e.

$$\frac{dn_c}{dt} \ll \frac{dn}{dt}, \frac{dm}{dt} \text{ and } n_c \ll n, m$$

Where n_c and n are the concentration (in m^{-3}) of electrons in conduction band and OSL active traps respectively; m is the concentration of holes in recombination trap levels. Thus, the OSL intensity, I_{OSL} is proportional to rate of depletion of OSL active electron traps, and when proportionality constant is taken as unity then we have,

$$I_{OSL} = -\frac{dn}{dt} \quad (4.4)$$

Under no re-trapping of optically released carriers, i.e. first-order kinetics, the OSL intensity I_{OSL} of equation (4.4) can be re-written as

$$I_{OSL} = \frac{dm}{dt} = -\frac{dn}{dt} = n f(T, \lambda) \quad (4.5)$$

Under a given stimulation wavelength (λ) and for a fixed given temperature (T), the value of photo-ionization cross-section, $\sigma(T, \lambda)$ remains constant for the given trap level. If we keep the stimulation flux constant with respect to time as $\phi(\lambda) = \phi_o(\lambda)$ then equation (4.3) can be rewritten as

$$f(T, \lambda) = f = \sigma(T, \lambda) \phi_o(\lambda) = \phi_o \sigma_o(\lambda) e^{-\frac{E_A}{kT}} = f_o(\lambda) e^{-\frac{E_A}{kT}} \quad (4.6)$$

Incorporating equation (4.6) into equation (4.5), and solving for OSL intensity I_{OSL} we get CW-OSL equation as

$$I_{OSL} = n_o f e^{-f t} = I_o e^{-f t} \quad (4.7)$$

Where, I_o is initial CW-OSL intensity and n_o is the initial concentration (m^{-3}) of trapped charges at time $t = 0$. The plot of equation (4.7) is a well-known exponential decay function with decay constant f ($=1/\tau$). Now consider the more dynamic approach to investigate the temperature dependence nature of this equation (4.7) by incorporating linear increase in temperature (keeping stimulation intensity constant) as

$$T = T_o + \beta t \quad (4.8)$$

Where T is the instantaneous temperature *in* Kelvin, T_o is start temperature in Kelvin. The β is the heating rate (K/s) and t is the time (s). This linearly increasing temperature will modulate the excitation rate $f(T, \lambda)$ with respect to increasing temperature.

4.4.2. Analysis under first-order kinetics ($b=1$)

The assumption of first-order kinetics requires that the re-trapping of optically released charges is negligibly small, and hence the equation (4.5) can be written as

$$I_{TA-OSL} = \frac{dm}{dt} = -\frac{dn}{dt} = n\phi_o\sigma_o(\lambda)e^{-\frac{E_A}{kT}} = n f_o(\lambda)e^{-\frac{E_A}{kT}} \quad (4.9)$$

Simplifying which we obtain

$$I_{TA-OSL} = n_o f_o(\lambda) e^{-\frac{E_A}{kT}} e^{-\frac{f_o}{\beta} \int_{T_o}^T e^{-\frac{E_A}{kT'}} dT'} \quad (4.10)$$

Equation (4.10) gives the TA-OSL intensity under 1st order kinetics. The plot of numerically generated OSL intensity is shown in fig. 4.16 for input parameters being $E_A = 0.241\text{eV}$, $\beta = 2\text{K/s}$ and $\sigma_o(\lambda) = 2 \times 10^{-16}\text{cm}^{-2}$, with CW stimulation intensity $\phi_o = 33\text{mW/cm}^2$ of 470 nm light. Equation (4.10) seems to be similar to that for TL intensity for 1st order kinetic at a given heating rate β (refer equation 4.11) except that the attempt to escape factor (S) also termed as frequency factor in the expression for TL intensity has been replaced by f and thermal trap

depth (E) by thermal assistance energy E_A in TA-OSL equation. The TL intensity equation can be expressed as

$$I_{TL} = n_o S e^{-\frac{E}{kT}} e^{-\frac{S}{\beta} \int_{T_o}^T e^{-\frac{E}{kT}} dT} \quad (4.11)$$

Traditionally OSL is recorded in time domain as luminescence intensity vs time, so the equation (4.11) can be rewritten in time domain as

$$I_{TA-OSL} = n_o f_o(\lambda) e^{-\frac{E_A}{k(T_o + \beta t)}} e^{-\int_0^t \frac{E_A}{k(T_o + \beta t')} dt} \quad (4.12)$$

The condition for temperature at which TA-OSL maximum occurs can be derived from equation (4.11) and is given by

$$\frac{E_A \beta}{k T_M^2} = \phi_o \sigma_o(\lambda) e^{-\frac{E_A}{k T_M}} \quad (4.13)$$

Where T_M is the absolute temperature at which TA-OSL intensity peak occurs. The shift in TA-OSL peak position (time and temperature domain) with heating rate β is shown in fig. 4.17. For given a stimulation intensity, TA-OSL peak temperature T_M increases with heating rate β . But in time scale TA-OSL peak occurs earlier with increase in heating rate. Also TA-OSL peak shift occurs earlier in time domain with increase in stimulation intensity ϕ_o as shown in fig. 4.18. Equations (4.11) and (4.13) are very useful for determining E_A and σ_o . As the initial part of the equation (4.11) can be considered to be dominated by the 1st exponential factor term the log of TA-OSL intensity vs $1/kT$ plot for initial part gives slope as E_A . Subsequently equation (4.15) can be used for determining σ_o as ϕ_o can be measured using photodiode with appropriate correction to its quantum sensitivity for given stimulation wavelength.

4.4.3. Analysis under general-order kinetics ($b \neq 1$)

Considering a more general approach of general- order kinetics the TA-OSL equation is

$${}^b I_{TA-OSL} = -\frac{dn}{dt} = \frac{n^b}{n^{b-1}} \phi_o \sigma_o(\lambda) e^{-\frac{E_A}{kT}} = \frac{n^b}{n^{b-1}} f_o(\lambda) e^{-\frac{E_A}{kT}} \quad (4.14)$$

Where ${}^b I_{TA-OSL}$ is the TA-OSL intensity for given value of ϕ_o and b . Solution of equation (4.14) gives TA-OSL intensity for general-order kinetics with respect to temperature as

$${}^b I_{TA-OSL} = n_o \phi_o \sigma_o(\lambda) e^{-\frac{E_A}{kT}} \left[1 + (b-1) \frac{\phi_o \sigma_o(\lambda)}{\beta} \int_{T_o}^T e^{-\frac{E_A}{kT'}} dT' \right]^{b/1-b} \quad (4.15a)$$

This in time domain can be expressed as

$${}^b I_{TA-OSL} = n_o \phi_o \sigma_o(\lambda) e^{-\frac{E_A}{k(T_o + \beta t)}} \left[1 + (b-1) \phi_o \sigma_o(\lambda) \int_0^t e^{-\frac{E_A}{k(T_o + \beta t')}} dt' \right]^{b/1-b} \quad (4.15b)$$

Equations (4.15a) & (4.15b) represent TA-OSL intensity under constant light stimulation for the general-order kinetics. Fig. 4.16 depicts numerically simulated TA-OSL intensity for various order of kinetics at fixed stimulation intensity. Fig. 4.16 clearly shows the effect of re-trapping (i.e. the order of kinetics) on the TA-OSL intensity curves. It is observed from fig. 4.16 that as the order of kinetics increases the peak intensity decreases and the TA-OSL peak is obtained in a shorter time. The temperature at which maximum in TA-OSL intensity occurs can be obtained as

$$\frac{\beta E_A}{k T_M^2} = b \phi_o \sigma_o(\lambda) e^{-\frac{E_A}{k T_M}} \left[1 + (b-1) \frac{\phi_o \sigma_o(\lambda)}{\beta} \int_{T_o}^{T_M} e^{-\frac{E_A}{k T'}} dT' \right]^{-1} \quad (4.16)$$

Equation (4.16) gives the condition of maxima for TA-OSL intensity. Here also, as the order of kinetics increases the TA-OSL peak will occur at lower temperature. The value of T_M also decreases with increase in value of stimulation intensity ϕ_o (fig. 4.18). Therefore to get the TA-OSL peak in shorter time (or lower temperature) one has to select higher values of heating rate and stimulation flux.

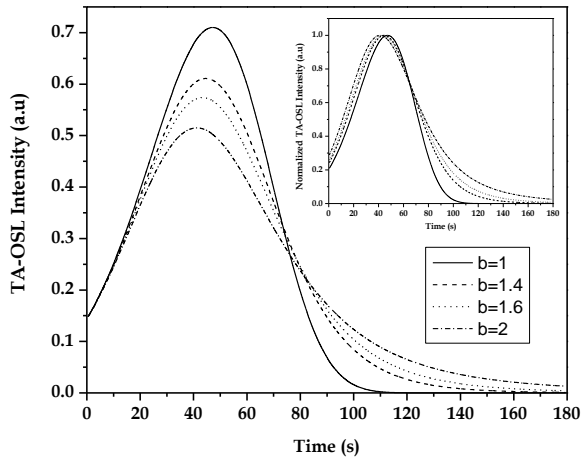


Fig.4.16. Numerically simulated TA-OSL signal vs time for various order of kinetic values with $\beta=2\text{K/s}$, $E_A=0.24\text{eV}$, $\sigma_o(\lambda)= 2 \times 10^{-16}\text{cm}^2$ & $\phi_o=33\text{mW/cm}^2$ at 470nm . The inset shows the corresponding normalized plots.

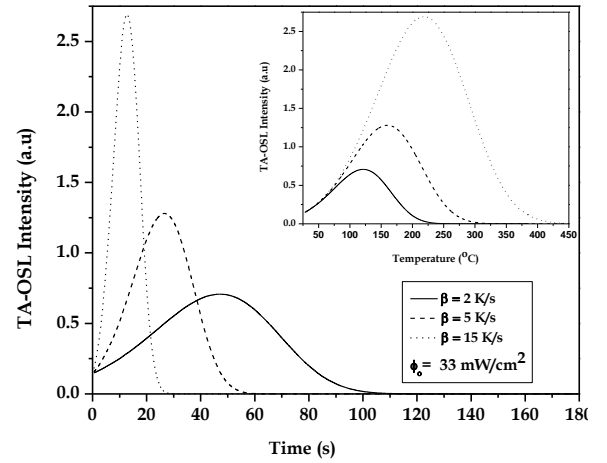


Fig.4.17. Numerically simulated TA-OSL signal vs. time plot for various heating rates β with $\phi_o = 33\text{mW/cm}^2$, $E_A=0.24\text{eV}$, and $\sigma_o(\lambda)= 2 \times 10^{-16}\text{cm}^2$. The inset shows same numerically simulated TA-OSL signal against temperature for various heating rates.

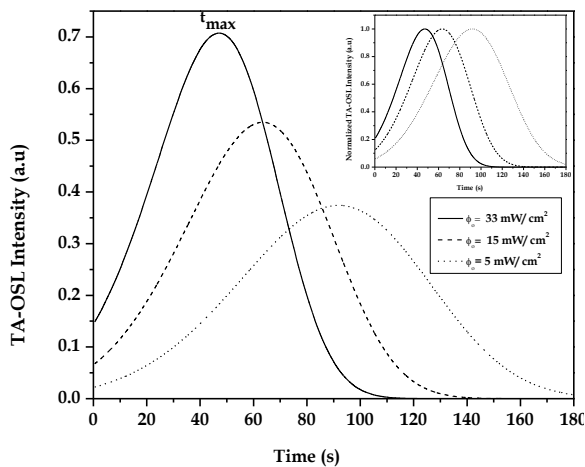


Fig.4.18. Numerically simulated TA-OSL signal vs time plot for various CW stimulation intensity ϕ_o with $\beta=2\text{K/s}$, $E_A=0.24\text{eV}$, $\sigma_o(\lambda)= 2 \times 10^{-16}\text{cm}^2$. The inset shows the normalized plots.

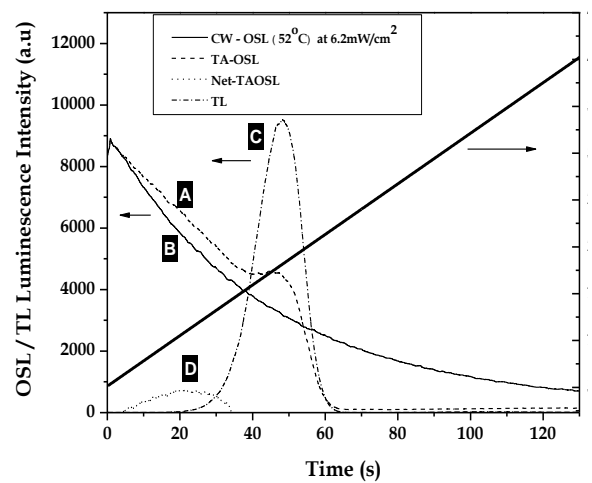


Fig.4.19. (A)TA-OSL signal recorded with CW stimulation and linear heating of 3K/s (B) CW-OSL recorded at 52°C with $\phi_o = 6.2\text{mW/cm}^2$ (C) TL recorded for 60mGy dose (D) Subtraction of curves $D= A- B - \zeta C$ is resultant net TA-OSL.

4.4.4. Materials and Method

Dosimetry grade single crystals of α -Al₂O₃:C (5mm dia. and 0.9 mm thick, Urals Polytechnique Institute, Russia.) were irradiated using a calibrated 5mCi, ⁹⁰Sr/⁹⁰Y beta source. TA-OSL was recorded at RT in integrated TL and OSL Reader System [6] consisting of a high intensity blue LED ($\lambda_p = 470\text{nm}$, $\Delta\lambda = 20\text{nm}$) cluster as a stimulating light source, transistor based high current LED driving circuit to drive LEDs. Before irradiation, the samples were optically bleached for 10 min. at $\sim 400^\circ\text{C}$ using 470 nm LED light source at power $\sim 100\text{mW}/\text{cm}^2$ with GG-435 optical filter across it to cut off UV components in the blue LED spectrum. This bleaching removes hard to bleach OSL components which may interfere with TA-OSL measurements [7]. UG-1 filter is used across PMT to cut-off stimulating light.

4.4.5. Results

4.4.5.1. Generation of Thermally Assisted (TA)-OSL signal

The dosimetry TL peak in α -Al₂O₃: C is reported to occur at 182°C along with low temperature peak at 54°C [8]. To investigate temperature dependent TA-OSL signal we irradiated α -Al₂O₃: C dosimeter to a dose of 60mGy. Apart from this to avoid interference due to the low temperature (54°C) TL peak during the TA-OSL measurements, all TL and OSL measurements were carried out at temperature $\geq 54^\circ\text{C}$. Since the photo-ionization cross-section of OSL traps in α -Al₂O₃:C sample is sufficiently large to give CW-OSL signal even at stimulation intensity $< 10\text{mW}/\text{cm}^2$ and as most of the OSL in α -Al₂O₃: C is contributed by the traps responsible for the dosimetry TL peak, the weak stimulation intensity ($6.2\text{mW}/\text{cm}^2$) has been used along with linear heating of 3K/s to record TA-OSL measurements. All measurements have been recorded after the post irradiation period of 5min., as this allows phosphorescence due to low temperature TL peak at 54°C to decay considerably. Fig. 4.19, curve (A) shows the TA-OSL signal which consists of CW-OSL with thermal assisted

component and TL remaining signal from 182°C peak recorded for the samples after absorbed dose of 60mGy. In order to separately find the presence of TA-OSL component from curve (A), we have to separate OSL and TL contribution from curve (A). To do this, the sample has been given elevated temperature optical bleaching of 10 min. at $\sim 100\text{mW/cm}^2$ followed by 60mGy irradiation. The CW-OSL thus recorded at temperature 54°C with same stimulation intensity (i.e. 6.2mW/cm^2) is shown in Fig. 4.19 curve (B). In the similar way TL has been recorded at heating rate of 3K/s (in absence of stimulated light) for same absorbed dose as shown in fig. 4.19 curve (C). The net increase in TA-OSL signal curve (D) as compared to CW-OSL and TL is given by $D = A - B - \zeta C$ as shown in fig. 4.19, curve (D). The constant ζ is the scaling factor which takes care of reduction in TL glow curve area due to simultaneous application of optical and thermal stimulation during TA-OSL readout. It can be seen from fig. 4.19, that area of the 182°C TL glow peak recorded in the absence of optical stimulation (fig. 4.19, curve (C)), is larger compared to TL part visible in TA-OSL, curve (A). The TA-OSL signal increases with increasing temperature as predicted by 1st exponential term in equation (4.15b). However, at the relatively longer time the 2nd exponential term dominates and represents the decreasing part of TA-OSL curve. As result a well-defined TA-OSL peak occurs in time as well as temperature domain as depicted from TA-OSL curve shown in fig. 4.19 (Curve (D)). Fig. 4.20 (a) shows the TA-OSL signal recorded for different in CW stimulation intensities. Since in $\alpha\text{-Al}_2\text{O}_3\text{:C}$ it is found that dominant OSL is coming from the defects responsible for the 182°C TL peak, therefore with the increase CW optical stimulation intensity, the TA-OSL signal increases with consequent decrease in TL component. The shift in TA-OSL signal in time domain has been observed as predicted theoretically; experimental results are shown in fig. 4.20 (b) for various stimulation intensities for an adsorbed dose of 60

mGy and a heating rate of 3K/s. As expected from equation (4.15), the TA-OSL peak was found to shift to higher temperature which is shown in figs. 4.21(a) and (b).

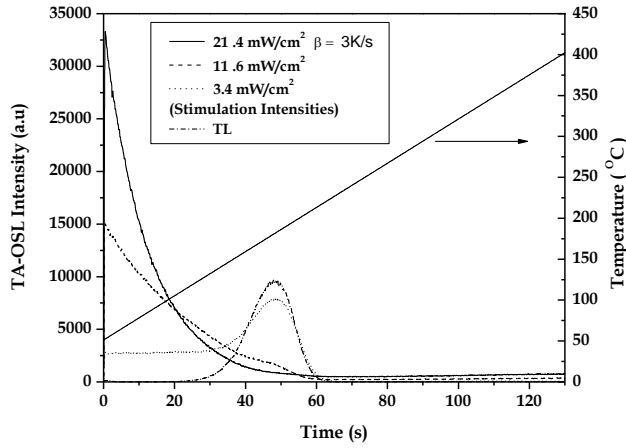


Fig. 4.20(a). TA-OSL curve for various CW stimulation intensities and fixed heating rate of 3K/s.

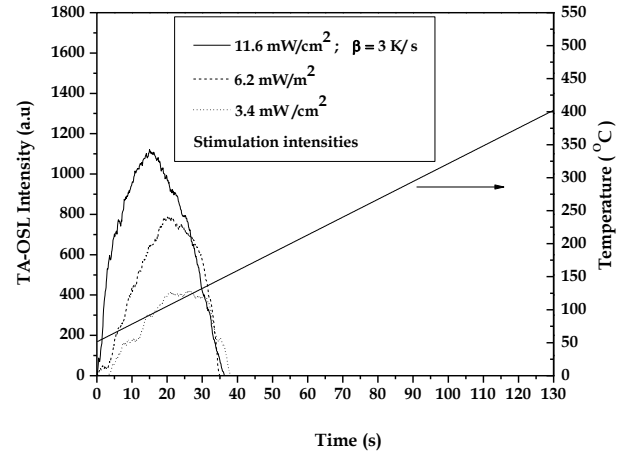


Fig. 4.20(b). Net TA-OSL curve for various CW stimulation intensities and fixed heating rate of 3K/s for 60mGy absorbed dose.

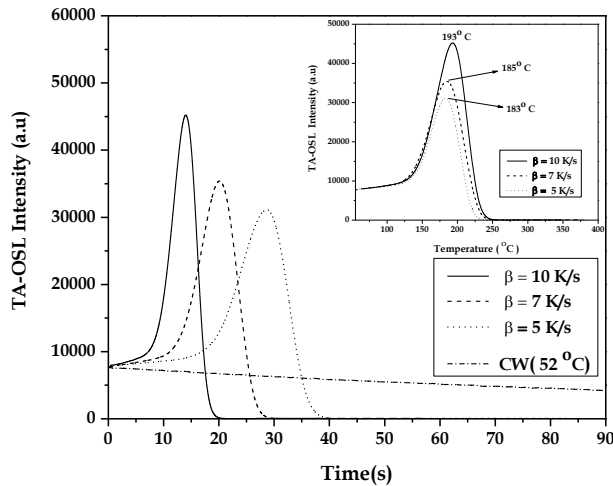


Fig. 4.21(a). TA-OSL curve for various heating rate under CW stimulation intensity of 3.7mW/cm² at 470nm. Inset gives corresponding curves in temperature domain.

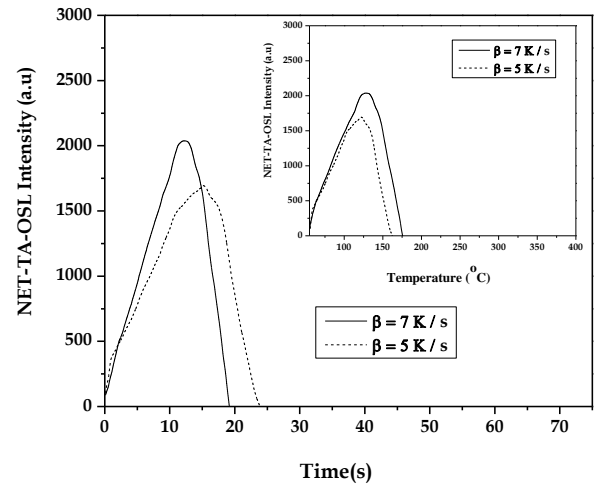


Fig. 4.21(b). Net-TA-OSL curve for heating rates 7K/s and 5K/s under CW stimulation intensity of 3.7mW/cm² at 470nm. The inset gives the corresponding curves in the temperature domain.

4.4.5.2. Measurements of thermally assisted energy and pre-exponential factor in $\alpha\text{-Al}_2\text{O}_3\text{:C}$

The measurement of thermal assistance energy (E_A) and the pre-exponential photo-ionization cross-section $\sigma_o(\lambda)$ can be done in two steps. First, the determination of E_A using equation (4.15a). Since the initial rise part of TA-OSL is governed by 1st exponentially increasing part of equation (4.15a) and under weak stimulation product of $n_o f_o$ can be assumed to remain nearly constant. Therefore the under the weak stimulation assumption the equation (4.15a) can be expressed as

$$I_{TA-OSL} = B e^{-\frac{E_A}{k T}} \quad (4.17)$$

Where B is a constant and the plot of $\ln(\text{Integrated } I(T)_{TA-OSL})$ vs $1/kT$ gives linear plot with slope as thermal assistance energy (E_A). The figs. 4.21 (a) shows the CW-OSL recorded at a constant temperature of 52°C for weak stimulation. The comparison of TA-OSL with CW-OSL (at 52°C) in fig. 4.21(a) clearly shows the increasing intensity of TA-OSL signal with increase in heating rate. Since for temperature $< 100^\circ\text{C}$, TL signal from main dosimetry TL peak in $\alpha\text{-Al}_2\text{O}_3\text{:C}$ does not interfere with TA-OSL signal, the rise in TA-OSL signal in initial part is purely due to exponentially increasing parts as given in equation (4.17). The plot of natural logarithm of integrated TA-OSL vs $1/kT$ for a heating rate of 7 K/s has been shown in fig. 4.22 from 68°C to 100°C. The TA-OSL signal data above 100°C has been not considered due to, expected thermal quenching of luminescence signal in $\alpha\text{-Al}_2\text{O}_3\text{:C}$ [9] and partial interference of TL signal generated due to dosimetry 182°C TL peak. The slope of line $\ln(I_{TA-OSL})$ vs. $1/kT$ as shown in fig. 4.22 is found to be $E_A \approx 0.03$ eV. With increase in heating rate the shift (in time and temperature domain) occurs in TA-OSL peak as well as in dosimetry TL peak as shown in the inset to the fig. 4.21(a). The value of $\sigma(300\text{K}, 470\text{nm})$ has been determined for $\alpha\text{-Al}_2\text{O}_3\text{:C}$ sample by varying the stimulation power and recording value of excitation rate at

different stimulation power (flux ϕ ($\lambda=470\text{nm}$)) as shown in fig. 4.23. The slope of this line gives value of σ (300K, 470nm) and is found to be $\sim 1.33 \times 10^{-18} \text{cm}^2$. Since the value of thermal assistance energy E_A has been already estimated using fig. 4.22 and equation (4.17). Now incorporating the above determined values of E_A and σ (300K, 470nm) in equation (4.1), we get the value of pre-exponential factor as $\sigma_0 \sim 4.24 \times 10^{-18} \text{cm}^2$. Therefore equation (4.1) can be rewritten as

$$\sigma(T, 470\text{nm}) = 4.24 \times 10^{-18} e^{-\frac{0.030}{kT}} \quad (4.18)$$

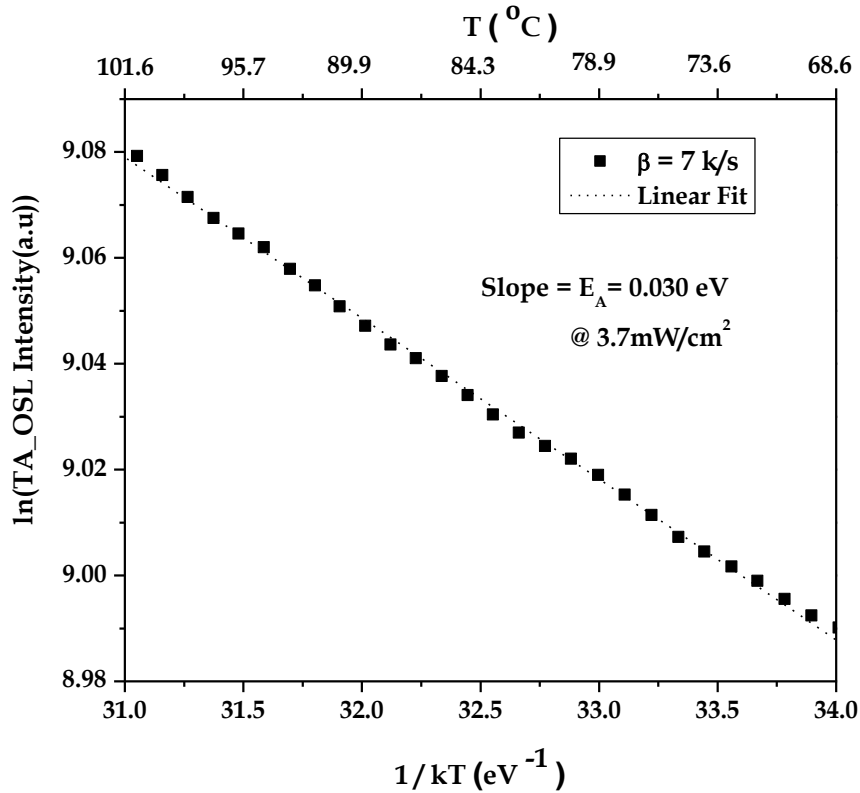


Fig.4.22. Log of TA-OSL vs. $1/kT$ gives slope as thermal assistance energy of OSL trap E_A for heating rate $\beta = 7\text{K/s}$ and CW stimulation of 3.7mW/cm^2 for absorbed dose of 60mGy .

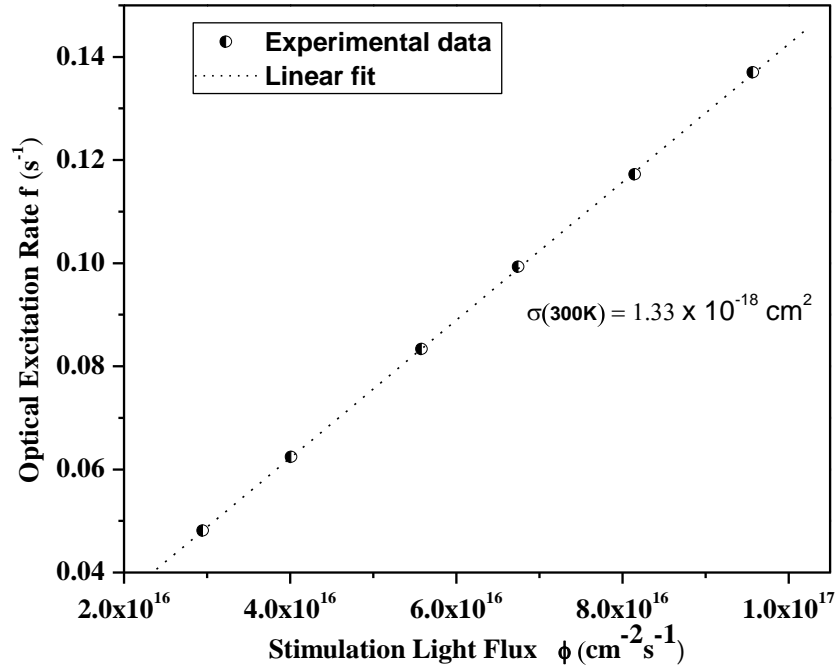


Fig.4.23. Optical excitation vs stimulation flux at room temperature for 470nm of light slope of above line gives the value of photo-ionization cross-section at room temperature.

In order to determine the value of pre-exponential factor must be varied independently for this we have taken the CW-OSL at different elevated temperatures for the irradiated $\alpha\text{-Al}_2\text{O}_3$: C phosphor at stimulation power of $52\text{mW}/\text{cm}^2$ as shown in fig. 4.24(a). The value of CW-OSL decay constant is found to increase with increase in temperature of CW-OSL measurements from 23°C to 150°C . The inset to fig. 4.24(a) clearly shows increase in the value of photo-ionization cross-section associated with main OSL dosimetry trap in $\alpha\text{-Al}_2\text{O}_3$: C phosphor. The thermal assistance energy responsible for this increase in value of photo ionization cross section can be determined independently using the following equation with incorporation of equation (4.1)

$$f(T, \lambda) = \phi_o(\lambda) \sigma(T, \lambda) = \phi_o(\lambda) \sigma_o(\lambda) e^{-\frac{E_A}{kT}} = f_o e^{-\frac{E_A}{kT}} \quad (4.19)$$

The natural logarithm of excitation at different temperature i.e. $\ln(f(T, \lambda))$ v.s $1/kT$ will give slope as thermal assistance energy (E_A) associated with OSL traps and intercept will give the value of pre-exponential factor (σ_o). The fig. 4.24 (b) shows the graph of $\ln(f)$ vs. $1/kT$ and the thermal assistance energy associated with OSL traps is determined as $E_A \sim 0.039$ eV and pre-exponential factor $\sigma_o \sim 6.36 \times 10^{-18} \text{cm}^2$. The numerically simulated TA-OSL signal for $\alpha\text{-Al}_2\text{O}_3\text{: C}$ using $E_A \sim 0.03\text{eV}$ and $\sigma_o \sim 4.24 \times 10^{-18} \text{cm}^2$ under various stimulation intensities of 470nm light with 3 K/s heating rate has been shown in fig. 4.25(a). For this simulation TL parameters have been taken for 1st order kinetics with $E=1.1\text{eV}$ and frequency factor $S = 2.5 \times 10^{13} \text{s}^{-1}$ (using initial rise method). The results curves of fig. 4.25(a) are in closely resembling the similar experimental measured curves shown in fig.4.20(a). In the similar way the effect of different heating rates on numerically computed TA-OSL using experimentally determined values of E_A and σ_o has been shown in fig. 4.25(b). The resultant curves of fig. 4.25(b) are in good agreement with experimentally measured TA-OSL curves shown fig. 4.20(b) under similar conditions. The comparison of the net TA-OSL signal numerically generated using experimentally determined values of TL and OSL parameters as shown in fig. 4.26, curve (D) for 12mW/cm^2 optical stimulation with corresponding TA-OSL signal measured experimentally are in good agreement (fig. 4.19). These results show the validity in assumption of considering Arrhenius nature of temperature dependence of photo-ionization cross-section in dosimetry OSL traps of $\alpha\text{-Al}_2\text{O}_3\text{: C}$.

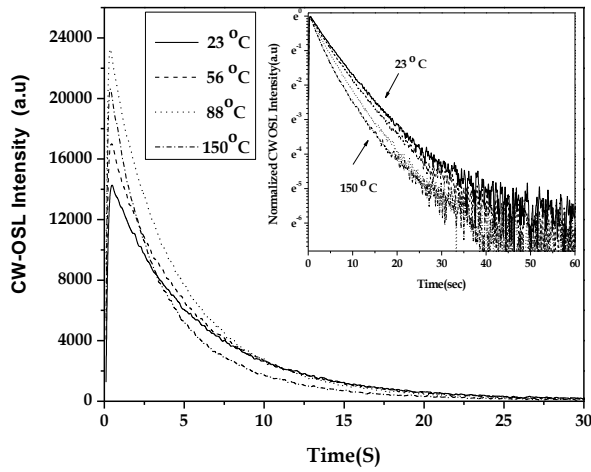


Fig. 4.24(a). The CW-OSL response at various elevated temperature for 60mGy absorbed dose. Inset shows the normalized CW-OSL curves.

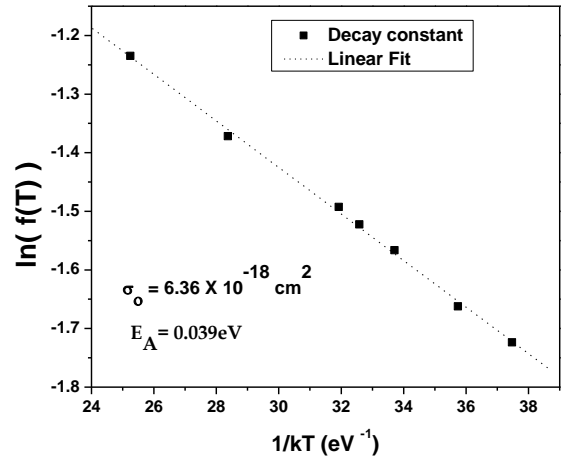


Fig. 4.24(b). Variation of excitation rate for 52mW/cm² with 1/kT gives slope as E_A and intercept value gives σ_o.

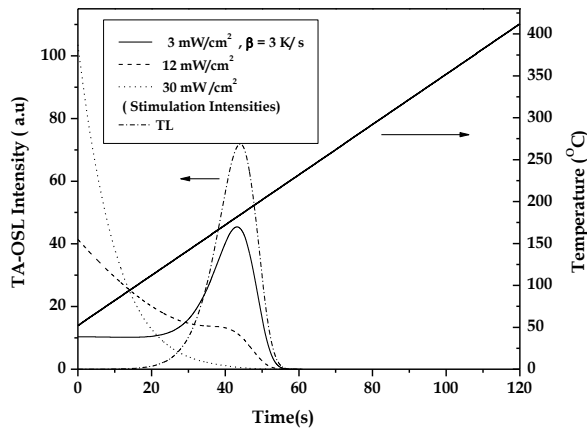


Fig. 4.25(a). Numerically simulated TA-OSL curve for various CW stimulation intensities and fixed heating rate of $\beta = 3 \text{ K/s}$ with $E_A = 0.03\text{eV}$, $\sigma_o = 4.24 \times 10^{-18}\text{cm}^2$, $E = 1.1\text{eV}$ and $S = 2.5 \times 10^{11}\text{s}^{-1}$.

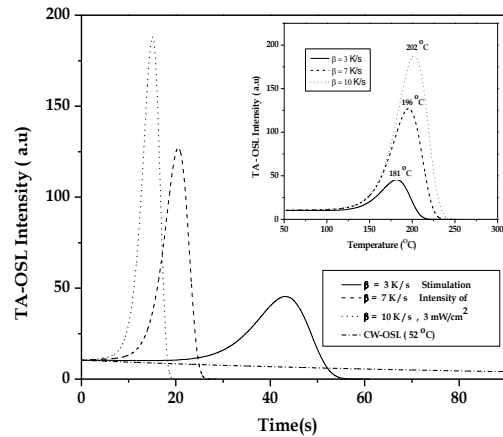


Fig. 4.25(b). Numerically simulated TA-OSL curve for various heating rates and fixed CW intensity 3mW/cm² & experimentally determined value of $E_A = 0.03\text{eV}$, $\sigma_o = 4.24 \times 10^{-18}\text{cm}^2$, $E = 1.1\text{eV}$ and $S = 2.5 \times 10^{11}\text{s}^{-1}$. Inset figure shows the temperature domain plot of TA-OSL signal.

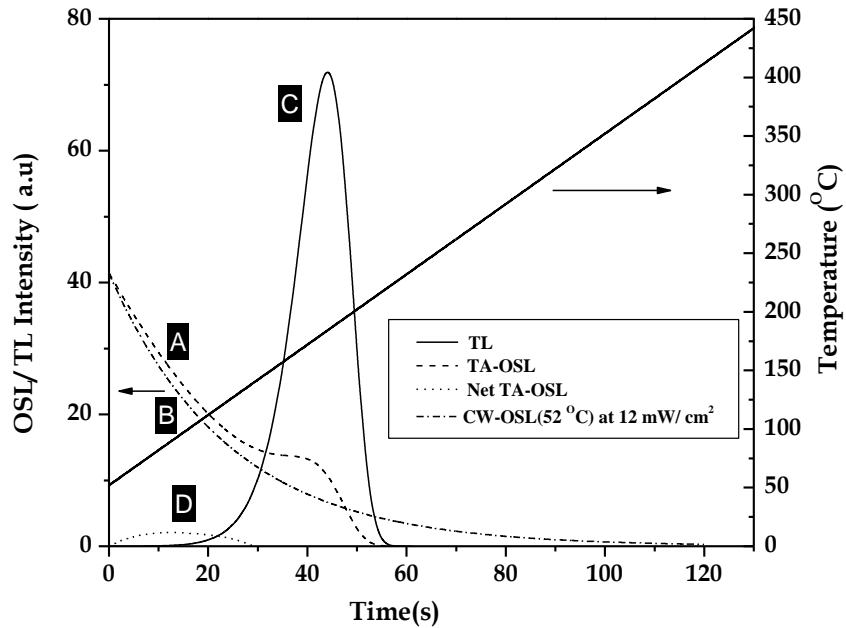


Fig.4.26. Using experimentally determined value $E_A=0.03\text{eV}$, $\sigma_o = 4.24 \times 10^{-18}\text{cm}^2$, $E=1.1\text{eV}$ and $S=2.5 \times 10^{11}\text{s}^{-1}$ numerical simulated curves for $\alpha\text{-Al}_2\text{O}_3\text{:C}$. Curve (A) is TA-OSL signal recorded with CW stimulation and $\beta=3\text{K/s}$. Curve (B) is the CW-OSL recorded at 52°C with 12mW/cm^2 stimulation light. Curve (C) is a TL glow curve. Curve (D) is the subtraction of curves, i.e. $D=A-B-\zeta C$, is net TA-OSL.

4.4.7. Conclusion

This work highlights the Arrhenius nature of temperature dependence of photo-ionization cross-section of OSL dosimetry traps in $\alpha\text{-Al}_2\text{O}_3\text{:C}$. The theoretical formulation for determining thermal assistance energy has been very helpful in explaining the thermal assistance nature of OSL dosimetry traps in $\alpha\text{-Al}_2\text{O}_3\text{:C}$. The thermal assistance energy associated with dosimetry OSL trap in $\alpha\text{-Al}_2\text{O}_3\text{:C}$ has been measured using two different methods and found to agree within experimental limitations. The simulation of numerically generated TA-OSL signal using experimentally determined values of thermally assistance energy and pre-experimental factor of $\alpha\text{-Al}_2\text{O}_3\text{:C}$ is in good agreement with experimentally recorded TA-OSL signal.

4.5. Non-Linear Light Modulation Studies on α -Al₂O₃: C

While applying OSL, the traditional way of stimulating phosphor is continuous wave (CW)-OSL mode, where the stimulation intensity is held constant with respect to time and decay of OSL signal is recorded. The decay constant of such CW-OSL curve under 1st order of kinetics contains direct information about photo-ionization cross-section of traps participating in OSL phenomenon. The other OSL technique is the Linearly Modulated (LM)-OSL, in which the intensity of stimulation at sample increased linearly with respect to time. This leads to multiple OSL components in LM-OSL curve corresponding to different photo-ionization cross-sections of the different traps participating in LM-OSL phenomenon. The LM-OSL method provides very useful information about different active OSL traps along with order of kinetics [10]. The advantage of LM-OSL is obvious over CW-OSL, as the latter gives non-exponential complex decay function under very closely spaced active OSL traps having different values of photo-ionization cross-section as well as for the traps obeying non-first order of kinetics. Therefore LM-OSL technique is generally used for probing information about active OSL traps, having very close value of photo-ionization cross-sections. Mishra et al. [11] have theoretically formulated more generalized approach to Non-Linear-OSL phenomenon. Also, recently, Bos and Wallinga [12] presented a mathematical description of OSL signal under linearly, hyperbolically, exponentially and reciprocally increasing, stimulation intensity for an one-trap one recombination-center model assuming charge transfer by 1st order kinetics. In the present work, by using non-linearly modulated (particularly for parabolic profiles) OSL, we have established that NL-OSL technique provides better signal to noise ratio compared to LM-OSL technique. The extended dose linearity associated with traps having relatively larger photo ionization cross-section in α -Al₂O₃:C phosphor has also been demonstrated using NL-OSL technique.

4.5.1. Theory of NL-OSL

Using one trap one recombination center model and considering first-order kinetics, the relation for the non-linear stimulation modulation OSL (NL-OSL) intensity is given by

$$I_{NL-OSL} = n_0 \sigma \gamma' t^l e^{-\left(\frac{\sigma \gamma'}{l+1}\right) t^{l+1}} \quad (4.20)$$

Where γ' is a constant related to stimulation flux by the relation

$$\phi(\lambda) = \phi(\lambda, t, l) = \gamma' t^l \quad (4.21)$$

and ' l ' is the parameter that can take values in the range $0 < l < \infty$ (like 0.1, 0.5, 1, 2, ..., etc).

The value of l will determine the power of light modulation in the time domain, for example, $l=1$ will produce linear light modulation (LM) and $l=2$ will lead to parabolic, non-linear light modulation. This parameter γ' is related to stimulation flux rate at any instant of time by the relation

$$\gamma = \frac{d\phi}{dt} = \gamma' l t^{l-1} \quad (4.22)$$

Thus l can be termed as Time Base Power (TBP) of light modulation (Mishra et al., 2008). We can express the stimulation excitation rate (f) by the relation

$$f = \sigma(\lambda) \gamma' t^l \quad (4.23)$$

The time required to reach the maximum value of I_{NL-OSL} intensity can be obtained by applying condition of maximum intensity, which gives

$${}^l_1 t_{\max} = [1/\sigma \gamma']^{\frac{1}{l+1}} \quad (4.24)$$

Where ${}^l_1 t_{\max}$ is the time required to reach peak intensity in NL-OSL curve for TBP being ' l ' for first-order kinetics.

Considering general- order kinetics and solving NL-OSL equation, we get the NL-OSL

intensity for given values of l and b as

$${}^l I_{NL-OSL} = \sigma \gamma' n_0 t^l \left[1 + (b-1) \frac{\sigma \gamma' t^{l+1}}{l+1} \right]^{b/(1-b)} \quad (4.25)$$

Equation (4.25) represents OSL intensity under non-linear light modulation for the general-order kinetics (i.e. $b > 0$ and $b \neq 1$). The time required to reach the maximum ${}^l t_{\max}$ can be obtained by taking the time derivative of equation (4.25) and equating it to zero, we get

$${}^l t_{\max} = \left[\frac{l(l+1)}{\sigma \gamma' (b+l)} \right]^{\frac{1}{l+1}} \quad (4.26)$$

Increase in the order of kinetics will decrease the value of ${}^l t_{\max}$ i.e. the OSL peak will appear in a shorter time, for both LM- and NL – OSL processes. It is found that the value of ${}^l I_{NL-OSL-\max}$ decreases with an increase in the order of kinetics for a given value of ' l '. On the other hand, for a given value of the order of kinetics ${}^l I_{NL-OSL-\max}$ is found to increase with increase in ' l '. This is expected in order to conserve the total area under all NL-OSL curves for same value of n_0 (dose). Apart from this an increase in the order of kinetics results in a stretching of the LM-OSL curve in the time domain into a long tail [10].

4.5.2. Specific advantages of NL-OSL over LM-OSL technique

The LM-OSL technique offers valuable information about different OSL active traps in terms of different peaks corresponding to these traps. However, in LM –OSL one has to record data for longer time with slowly but linearly increasing intensity in order to avoid overlapping of LM-OSL peaks having very close values of photo-ionization cross-section. This long time of OSL recording also gives considerable amount of noise as PMT dark counts due to scattering of stimulating light from sample holder, LED light leakage to PMT due to inadequate optical

filtration for the stimulated light. This results in degradation of overall signal to noise ratio. The overall noise in the recorded OSL signal can be expressed as follows

$$\text{Noise in OSL } (N_{OSL}) = N_{PMT} + N_{sc} + N_e \quad (4.27)$$

Where, N_{PMT} : Noise due to PMT dark count,

N_{sc} : Noise generated due to scattering of stimulation light from sample / sample holder and inadequate optical filter action which does not fully cut off stimulation wavelength.

N_e : Noise contributed due to electronics hardware / circuit used for stimulation as well as detection of PMT output signals at amplifier and pre-amplifier.

The noise due to dark count in PMT (N_{PMT}) can be reduced by properly controlling the bias voltage, providing adequate cooling to PMT, shielding against external magnetic field by μ -shielding material [13]. The major noise component in OSL reader systems is the noise originated due to leakage of stimulation light (N_{sc}). It has dependence on many factors; most important among these is selection in the set of cut-off optical filters. For example, most of OSL readers used to study the OSL from α - Al_2O_3 : C, contain the combination of optical filters across blue LED and PMT, e.g., GG-435 + UG-1 or GG-420 + Hoya (U)-340. Since both these combinations of filters have partially overlapping transmission band across 400-440 nm, the incident blue (470nm) light after leakage through the filter combination system, scattering from sample / sample holder reaches PMT photocathode. Apart from this both UG-1 and Hoya U-340 optical filters have considerable transmission in red (>690nm) range, which transmits the low intensity red components of blue LEDs and contributes to unwanted background signal. However, due to low quantum efficiency of bi-alkali photocathode PMT in the red region the noise due to this wavelength range is less important as compared to the noise contribution due to blue overlapping wavelength range. The contribution of these noise signals increases with increase in the value of stimulation intensity and reflectivity of sample/sample holder. The

contribution of this noise can be reduced substantially by reducing the reflectivity of sample holder and statistically stabilizing the stimulation intensity, so that the large part of this noise signal can be subtracted as constant background. Therefore, in brief, the noise generated due to scattering of stimulation light N_{sc} can be reduced if the total integrated stimulation flux incident on sample during readout is reduced without compromising on total OSL signal. In the more traditional method using CW-OSL, it is not possible to achieve lower total integral flux without compromising on total OSL signal as the total integral flux required to take out complete OSL signal is fixed for the given dose for the given material . The proposed NL-OSL technique (particularly for the parabolic light stimulation profiles) has this possible advantage. For this, let us consider a set of stimulation parameters such that LM-stimulation and NL-stimulation intensities approaching the same maximum value (ϕ_0) at the same time (t_0), as this assumption will help in direct comparison of background signals. To compare integrated area under the LM- and NL- light stimulation curves i.e. the integrated area under the LM stimulation curve (A_{LM}) and NL-stimulation curve (A_{NL}) can be expressed as the ratio of the two integrated areas, and given by relation

$$\frac{A_{LM}}{A_{NL}} = \frac{l+1}{2} \quad (4.28)$$

From equation (4.28) one could infer that the ratio of integrated light flux of the LM stimulation to NL stimulation depends linearly on TPB i.e. the value of l . Therefore, for $l=2$, we get $A_{LM}/A_{NL}=1.5$, and for $l=3$, it is 2. One could infer from equation (4.28) that for integration of background signals for the same time duration, and for the same final value of stimulation intensity (ϕ_0), the background signal for the NL-OSL mode will be lesser than that for the LM-OSL mode.

Since the background signal measured by stimulation of the un-irradiated OSL sensitive phosphor is mainly contributed by leakage of stimulated flux and scattered stimulation light, and PMT dark current, equation (4.28) can be helpful in knowing the rough estimate of the ratio of background signals. However, experimentally determined background signals and integrated NL- and LM-OSL signals for the same radiation dose, will only be helpful in determination of signal-to-noise ratio in the two cases. The aim of this investigation is to present results in α -Al₂O₃: C for obtaining better signal to noise ratio for NL- OSL stimulation as compared to LM-OSL case.

4.5.3. Materials and method

The dosimetry grade single crystals of α -Al₂O₃: C (TLD 500; 5 mm dia, 0.8 mm thick) were irradiated using a calibrated ⁹⁰Sr/⁹⁰Y beta source to an absorbed dose of 40 mGy and used for recording NL-OSL and LM-OSL signals. The NL-OSL was recorded at room temperature for the irradiated samples in a laboratory developed OSL measurement set-up [6] consisting of a high intensity blue light emitting diode ($\lambda_p = 470$ nm, $\Delta\lambda = 20$ nm) cluster as a stimulating light source. The samples were optically bleached with ~ 100 mW/cm² by 470 nm light for 10 min, before the irradiation. The light intensity at the sample position was measured using Si photodiode (OSD-5).

4.5.4. Results

4.5.4.1. Experimental Generation of NL Stimulation Profiles

Fig. 4.27 reflects the dynamic sub-linearity of ≈ 12.9 % for optical stimulation intensity in the range of 0-100 mW/cm² for $l = 1$. This non- linearity in LED light output intensity occurs due to loss of the luminescence emission efficiency of LED pn-junction by heat generated with high forward bias current (≈ 500 mA @ 5.6V). The sufficient cooling to LED by heat sink, and forced air cooling, considerably reduces this problem. The linear current ramp to LED has been

given and stimulation power at sample position has been determined using photodiode as shown in fig.4.28. As the LED current ramp generated linearly with respect to time the light intensity profile generated by LEDs suffers sub-linearity of $\approx 7.1\%$ in time domain for the same time interval (fig.4.28). An appropriate real time optical feedback signal using photodiode in LED driver hardware and suitable software corrected forward biased LED current remarkably compensates for LEDs light output non-linearity, thereby helping in achieving nearly linear optical intensity vs. time profiles. The various stimulation profiles are generated by NL-OSL reader system are measured using photodiode at sample position as shown in fig.4.32 with termination of the all NL-OSL profiles with different values of l for the same time interval and for the same stimulation final intensity.

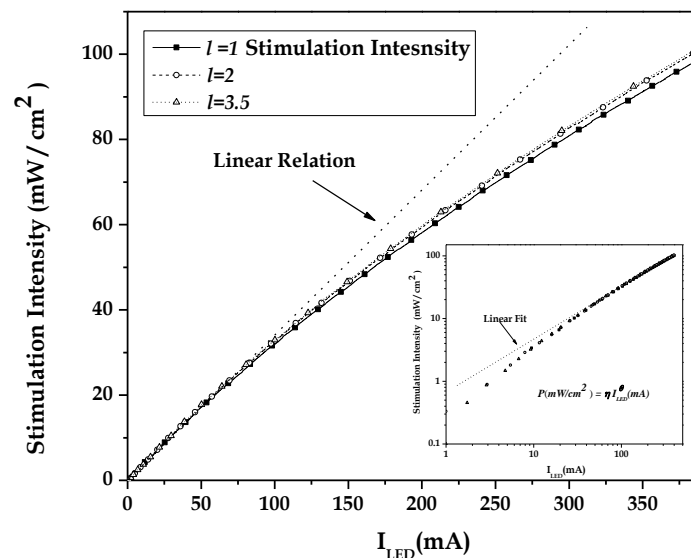


Figure 4.27. Variation of stimulation power at sample position with linear increase in LED forward bias current for various values of TBP(l).

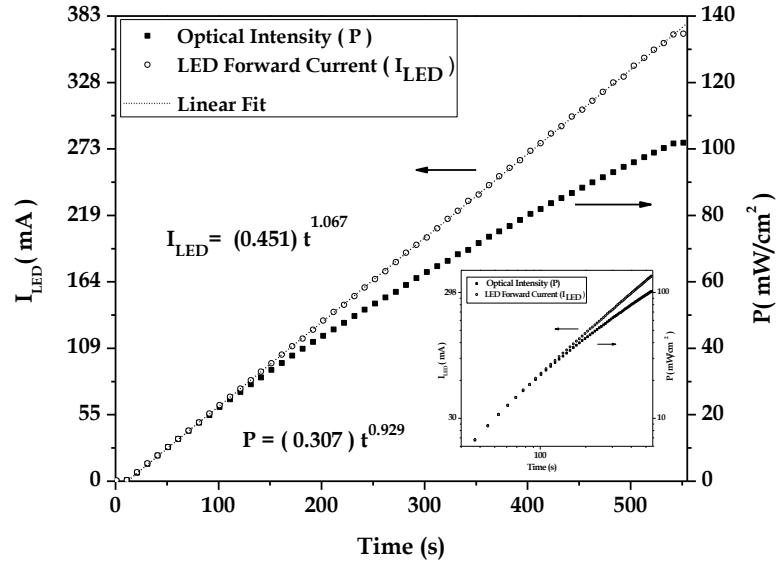


Figure 4.28. Comparison of linear LED forward bias current I_{LED} profile with optical stimulation intensity (P) recorded at sample position by the photo diode. Inset figure shows both plots in log scale.

4.5.4.2. Measurements of background scattering signal during NL - Stimulation Profiles

The comparison of signal-to-noise ratio (S/N) in all NL stimulation cases is required in order to measure scattering counts during the NL-OSL stimulation, with an un-irradiated OSL sample. This scattering contributes to the background signal, which is termed as N_{sc} . The relation of this background counts with stimulation intensity (P) has been shown in Fig.4.29. The background counts due to scattering of stimulation light can be expressed as

$$N_{sc} = \kappa P^m \quad (4.29)$$

Where N_{sc} is signal due to leakage of scattered light from the filter assembly that is detected by PMT. It corresponds to current/charge generated in PMT due to photons falling on the photocathode.

' κ ' is a constant which depends on reflectivity, geometrical considerations, solid angle cone seen by photocathode from sample position, the focusing of stimulation light on sample position and the set of cutoff filters used across PMT & LED based stimulation assembly.

Therefore, this factor varies with sample to sample and optical surface quality of OSL sample under readout.

' P ' is the optical stimulation intensity expressed in mW/cm^2 .

' m ' is dimensionless constant which measures the degree of linearity of N_{sc} for given range of optical stimulation intensity (P). The values of κ and m have been determined for the present OSL reader system as 9.1 and 0.98, respectively and also shown in fig. 4.29. Since the present value of m (≈ 0.98) shows that the N_{sc} is directly proportional to optical stimulation power, as expected, any reduction in optical stimulation power will directly lead to reduction in noise contributed due to this stimulation light scattering. The experimentally recorded value of N_{sc} for various values of TBP (for fixed value of final stimulation intensity) with single crystal α - $\text{Al}_2\text{O}_3:\text{C}$ has been shown in fig. 4.30. The net integral counts in fig. 4.30 due to the scattering stimulation noise N_{sc} has been extracted from total background noise by subtraction of PMT and electronic noise for same period but in the absence of any stimulation.

In order to measure signal to noise ratios of these experimental NL- stimulation profiles the ratio of integral area under LM - stimulation (A_{LM}) with respect to integral area of NL - stimulation (A_{NL}) have been taken for various values of TBP(I) as given in equation 4.28. The fig.4.31 shows plot of experimentally measured values of ratio (A_{LM}/A_{NL}) vs TBP. Since the LED power to current profile is sub-linear there is deviation from theoretical set values of TBP observed as shown in fig.4.31. The theoretical value of TBP is the value of TBP set for the forward current profile of LED driver circuit. However, as predicted from equation (4.28) the measure of signal to noise ratio (A_{LM}/A_{NL}) has been found to improve remarkably with increase in value of TBP.

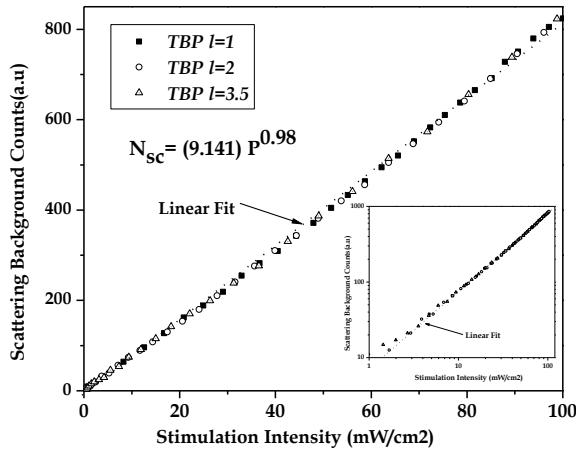


Figure 4.29. Background count due to Stimulation light detected by PMT with sample stimulated for $l=1$ for fixed final intensity and fix time. Inset figure shows both plots in log scale.

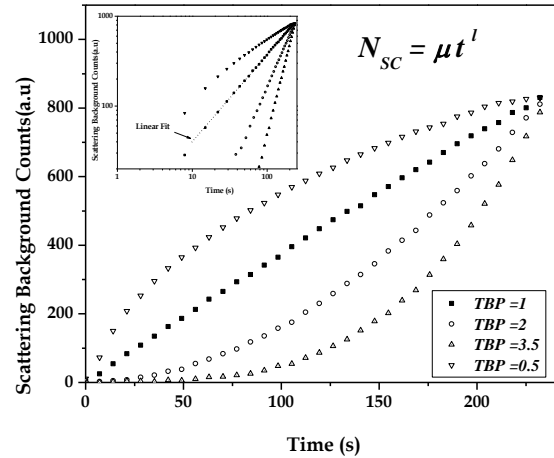


Figure 4.30. Variation of scattering background signal recorded in PMT for various values of “ l ”, for fixed final intensity and fix time. Inset figure shows both plots in log scale.

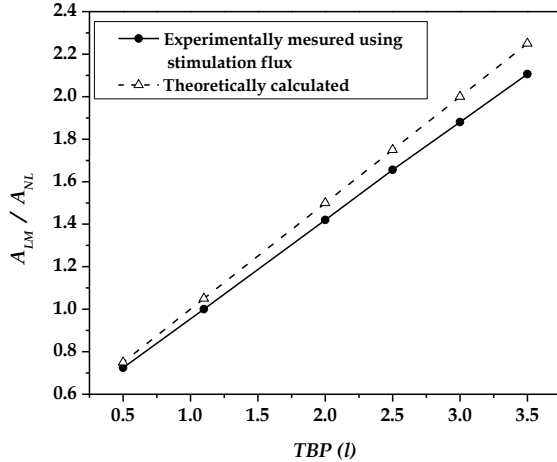


Figure 4.31. Theoretical and experimental signal to noise ratio A_{LM} / A_{NL} with various value of “ l ”, for fixed final intensity and fixed time.

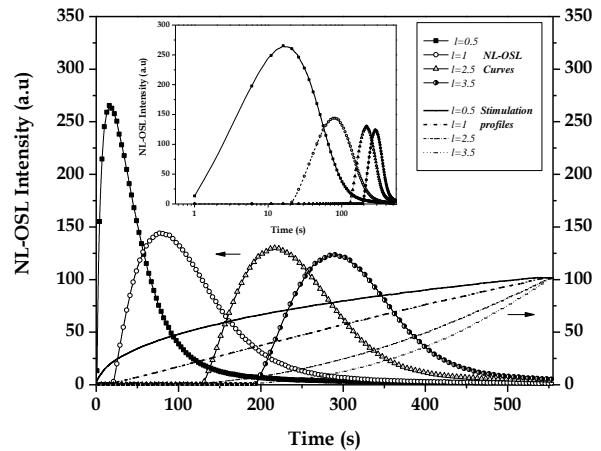


Figure 4.32. NL-OSL curves recorded for various value of “ l ”, for fixed final intensity and fixed time. Inset figure shows NL-OSL plots in log scale for time axis.

4.5.4.3. *Measurements of NL-OSL of α -Al₂O₃:C*

The NL-OSL readout of on single crystals of α -Al₂O₃:C along with corresponding stimulation profiles has been recorded for various TBP with fixed final stimulation intensity (ϕ_0) of 100 mW /cm² (for fixed time $t_0=550$ s) as shown fig.4.32. The shift in NL-OSL peak position towards higher time with increase in value of TBP can be seen clearly along with decrease in peak intensity. The value of TBP < 1 has resulted in OSL response almost similar to CW-OSL except the rising part of this NL-OSL. Since all the readouts are carried out at the same fixed absorbed dose of 40 mGy, the area under all NL-OSL curves are same after subtracting their corresponding background signal which were recorded for sample that was optically erased before irradiation. However, with increased value TBP, the total integral stimulation light intensity flux reduces for same absorbed dose, which results in better signal to noise ratio. Thus, it is possible to achieve lower detection threshold with same dosimeter by using NL stimulation. This is the basic advantage of NL-OSL for TBP >1. Apart from this, NL-OSL is expected to give more useful results for the very closely overlapping OSL peaks originating from very closely lying values of photo-ionization cross-sections. The plot of signal to noise ratio v/s time recorded for TBP =2.5, has been shown for various doses in fig.4.33; the inset graph shows normalized S/N ratios. It can be seen that peak position of S/N plot, in time domain, does not vary with dose. Therefore, the time corresponding to S/N peak position can be taken as the optimum time to record OSL signal with highest signal to noise ratio for all practical measurements. The high signal to noise ratio can be attributed to NL-OSL signal predominance primarily due to optical stimulation of charge from the traps having largest photo ionization cross-section. Biswas et al. [14] in 2009 have reported that the decay of α -Al₂O₃:C OSL can be described by a sum of three exponentials , termed as fast , medium and slow components. The shape of the OSL decay of α -Al₂O₃:C is reported to be dose dependent. It is

reported that the growth of these components with radiation dose is different such that the fast component grows linearly up to 300Gy and the medium and slow components saturate at about 20Gy. Therefore, for dosimetric application, it will be preferable to integrate area upto or below the time interval corresponding to occurrence of S/N peak. The dose linearity thus recorded is shown in fig.4.34, which was found to be linear from 100μGy to 100Gy. This choice of integrating NL-OSL up to the time corresponding to occurrence of peak in S/N vs time plot, also gives the option of multiple readout as only part of the OSL signal is depleted during such NL-OSL measurements. This is shown in fig. 4.35. The curve in fig. 4.35 can be fitted by 2nd order exponential and expressed as

$$NL-OSL(N) = A_0 + A_1 e^{-\lambda_1 N} + A_2 e^{-\lambda_2 N} \quad (4.30)$$

where NL-OSL (N) is the integrated NL-OSL signal corresponding to the occurrence of NL-OSL peaks in the Nth readout; A₀, A₁, A₂, λ₁ and λ₂ are the constants to be determined experimentally. The inset to fig.4.35 shows the corresponding results as pi graph. It can be seen that the 1st NL-OSL readout gives ~30 %, while 2nd and 3rd readouts give ~ 20% and ~13 %, respectively, of the total OSL signal.

4.5.4.4. Limitations of NL-OSL technique

Few of the limitations of NL-OSL technique being a) it is time taking technique for resolving closely lying embedded OSL peaks, b) hardware design and requirement is not easy and stringent as there is high current requirement at the end of the non linear light modulation profile, c) thus the components may not have such wide and dynamic linearity to handle high current requirements d) to perform segregation of peaks time and stimulation profile varies drastically from sample to sample and thus for unknown OSL phosphor lots of trial and error needs to be carried out to attain the desired segregation and resolution of closely lying OSL peaks e) not suitable for routine applications.

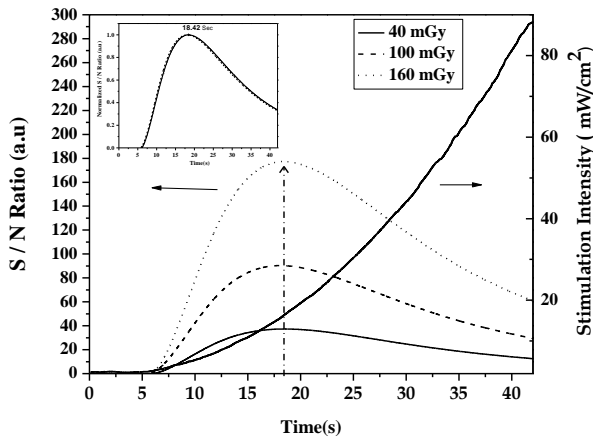


Figure 4.33. Signal to noise ratio curve of NL-OSL recorded for different for various absorbed doses for fixed final intensity and fixed time at $TBP(l)=2.5$. Inset graph shows the normalized signal to noise ratio curves.

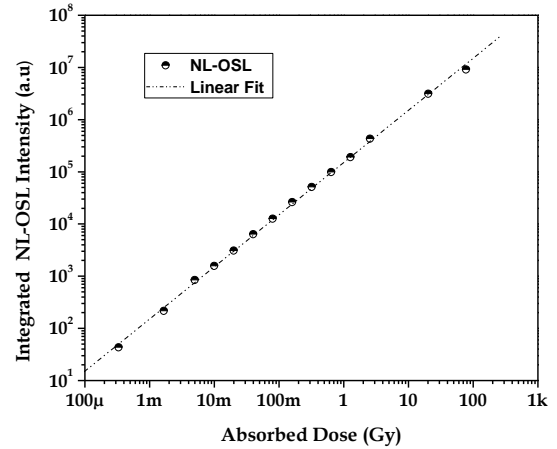


Figure 4.34. NL-OSL readout up to the peak of signal to noise ratio v/s absorbed dose absorbed dose for fixed final intensity

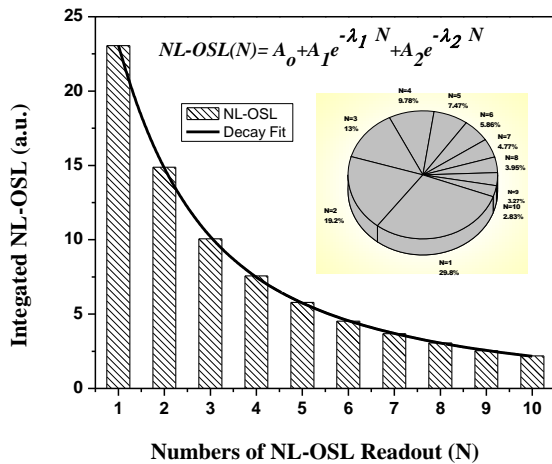


Figure 4.35. Multiple NL-OSL readout for 20mGy absorbed dose at $TBP(l) = 2.5$. Inset figure shows the pi graph indicating the fraction of OSL signal extracted in successive readouts.

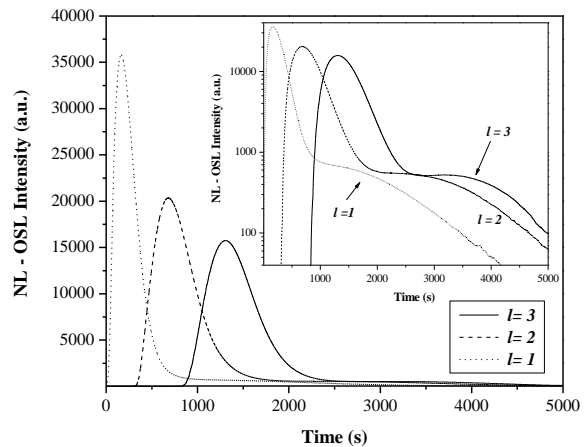


Figure 4.36. Separation of multiple OSL components in $Al_2O_3:C$ using NL-OSL readout for 400mGy absorbed dose for fixed same time and same fixed final intensity.

4.5.5. Conclusion

The NL-OSL technique provides relatively high signal to noise ratio, thereby has inherent potential of improving the minimum detection dose threshold of α -Al₂O₃:C phosphor. The option of multiple readouts, along with good dynamic dose linearity of OSL active traps having largest photo-ionization cross-section, make NL-OSL technique a potential choice for routine dosimetry application for re-estimation/confirmation of the measured radiation dose as well as for accident dosimetry using α -Al₂O₃:C. Thus by using this technique, the dynamic dose linearity of α -Al₂O₃:C has been extended to up to the studied dose of 100Gy; and yields useful results for the very closely overlapping OSL peaks originating from very closely lying values of photo-ionization cross-sections.

References

1. A. Seethapathy, M. S. Kulkarni, G. Nilashree, & S. Kannan, *Proc. 20th annual conference on medical physics*, Bhopal, India.(1999).
2. N. A. Spooner, *Radiat. Meas.* **23**, 593 (1994).
3. A. Chruścińska, *Radiat. Meas.* **45**, 991 (2010).
4. H. G. Grimmeiss and L-Å. Ledebø, *J. Phys. C: Solid State Phys.* **8**, 2615 (1975).
5. C.S. Alexander, M. F. Morris, S. W. S. Mckeever, *Radiat. Meas.* **27**, 153 (1997).
6. M. S. Kulkarni, D. R. Mishra, D. N. Sharma, *Nul. Ins., Method in Phys. B.* **262**, 384 (2007).
7. Nancy K. Umisedo, Elisabeth M. Yoshimura, Patricia B.R. Gasparian, E.G. Yukihara, *Radiat. Meas.* **45**, 151 (2010).
8. D.R. Mishra, M.S. Kulkarni, K.P. Muthe, C. Thinaharan, M. Roy, S.K. Kulshreshtha, S. Kannan, B.C. Bhatt, S.K. Gupta, D.N. Sharma, *Radiat. Meas.* **42**, 170 (2007).

9. M. S. Akselrod, N. Agersnap Larsen, V. Whitley, S. W. S. McKeever, *J Appl. Phy.* **84**, 3364 (1998).
10. G. Kitis and V. Pagonis, *Radiat. Meas.* **43**, 737 (2008).
11. D.R. Mishra, M.S. Kulkarni, N.S. Rawat, K.P. Muthe, S.K. Gupta, B.C. Bhatt, D.N. Sharma, *Radiat. Meas.*, **43** 1177 (2008).
12. A. J. J. Bos and J. Wallinga, *Physical Rev. B* **79**, 195118 (2009).
13. J. A. Baicker, *IEEE Trans Nucl. Sci.* NS-7 74 (1960).
14. R.H. Biswas, M.K. Murari, A.K. Singhvi, *Radiat. Meas.* **44**, 543 (2009).

Chapter 5

Application of $\text{Al}_2\text{O}_3:\text{C}$ for OSL based neutron dosimetry

5.1 Introduction

This chapter begins with introduction of neutrons, its broad classification in terms of energy, interaction of neutron with matter and certain techniques for the detection of neutrons in general. Subsequently the investigations of defects in α - Al_2O_3 single crystals irradiated to various thermal neutron fluence in the range of 10^{15} to 10^{18} n/cm² in the CIRUS reactor is highlighted. It is found that thermal neutron irradiation introduces considerable oxygen vacancies in the irradiated samples, which is confirmed by the presence of F (203 nm) and F⁺ (225 and 255 nm) bands in their optical absorption (OA) spectra. Later part of this chapter highlights the studies that demonstrates the use of $\text{Al}_2\text{O}_3\text{:C}$ for OSL based neutron dosimetry. For these studies indigenously developed $\text{Al}_2\text{O}_3\text{:C}$ using melt processing of polycrystalline alumina in graphite ambience (the preparation of which is mentioned in Chapter 1) is extensively used. The neutron response of detectors prepared using $\text{Al}_2\text{O}_3\text{:C}$ phosphor mixed with neutron converters was studied in mono-energetic neutron fields. The detector pellets were arranged in two different pairs: $\text{Al}_2\text{O}_3\text{:C} + {}^6\text{LiF}/\text{Al}_2\text{O}_3\text{:C} + {}^7\text{LiF}$ and $\text{Al}_2\text{O}_3\text{:C} + \text{high density polyethylene}/\text{Al}_2\text{O}_3\text{:C} + \text{Teflon}$, for neutron dosimetry using albedo and recoil proton techniques. The results pertaining to Hp(10) response of the $\text{Al}_2\text{O}_3\text{:C} + {}^{6,7}\text{LiF}$ dosimeters with increasing neutron energy and response of the $\text{Al}_2\text{O}_3\text{:C} + \text{high-density polyethylene}$ $\text{Al}_2\text{O}_3\text{:C} + \text{Teflon}$ dosimeters are also presented.

5.2. Neutrons

The neutron is a subatomic hadron particle which has the symbol n or n⁰, no net electric charge and a mass (1.0086 amu) slightly larger than that of a proton. With the exception of hydrogen, nuclei of atoms consist of protons and neutrons, which are therefore collectively

referred to as nucleons. Free neutrons are produced in nuclear fission and fusion. Dedicated neutron sources like research reactors and spallation sources produce free neutrons for use in irradiation and in neutron scattering experiments.

5.2.1. Classification of Neutrons

It is convenient to classify neutrons according to their energies. At the low end of the scale, neutrons can be in approximate thermal equilibrium with their surroundings. Their energies are then distributed according to the Maxwell–Boltzmann formula. The energy of a thermal neutron is sometimes given as 0.025 eV, which is the most probable energy in the distribution at room temperature (20°C). The average energy of thermal neutrons at room temperature is 0.038 eV. Thermal-neutron distributions do not necessarily have to correspond to room temperature. “Cold” neutrons, with lower “temperatures,” are produced at some facilities, while others generate neutrons with energy distributions characteristic of temperatures considerably above 20°C. Thermal neutrons gain and lose only small amounts of energy through elastic scattering in matter. They diffuse about until captured by atomic nuclei. Neutrons of higher energies, up to about 0.01 MeV or 0.1 MeV (the convention is not precise), are known variously as “slow,” “intermediate,” or “resonance” neutrons. “Fast” neutrons are those in the next-higher-energy classification, up to about 10 MeV or 20 MeV. “Relativistic” neutrons have still higher energies.

5.2.2. Interaction of neutrons with Matter

Like photons, neutrons are uncharged and hence can travel appreciable distances in matter without interacting. Under conditions of “good geometry” a narrow beam of mono-energetic neutrons is also attenuated exponentially by matter. The interaction of neutrons with electrons, (which is electromagnetic in nature) is negligible. In passing through matter a neutron can

collide with an atomic nucleus, which can scatter it elastically or inelastically. When the scattering is inelastic, the nucleus absorbs some energy internally and is left in an excited state. The neutron can also be captured, or absorbed, by a nucleus, leading to a reaction, such as (n, p), (n, 2n), (n, α), or (n, γ). The reaction changes the atomic mass number and/or atomic number of the struck nucleus.

Typically, a fast neutron loses energy in matter by a series of (mostly) elastic scattering events. This slowing-down process is called neutron moderation. As neutron energy decreases, scattering continues, but the probability of capture by a nucleus generally increases. Neutron eventually after thermalization moves randomly by elastic scattering until absorbed by a nucleus. Cross sections for the interactions of neutrons with atomic nuclei vary widely and usually are complicated functions of neutron energy. Since, the hydrogen nucleus (a proton) has no excited states, only elastic scattering and neutron capture are possible. The capture cross section for hydrogen is comparatively small, reaching a value of only 0.33 barn (1 barn = 10^{-24} cm²) at thermal energies, where it is largest. Thermal neutron capture is an important interaction in hydrogenous materials. The nucleus possesses discrete excited states, which can enhance or depress the elastic and inelastic scattering cross sections at certain values of the neutron energy.

Elastic Scattering: Elastic scattering is the most important process for slowing down neutrons; the contribution by inelastic scattering is usually small in comparison. We treat elastic scattering here. The maximum energy that a neutron of mass M and kinetic energy E_n can transfer to a nucleus of mass m in a single (head-on) elastic collision is given by

$$Q_{\max} = \frac{4mME_n}{(M + m)^2} \quad (5.1)$$

Setting $M = 1$, we can calculate the maximum fraction of a neutron's energy that can be lost in a collision with nuclei of different atomic-mass numbers m . Some results are shown in Table 5.1 for nuclei that span the periodic system. For ordinary hydrogen, because the proton and neutron masses are equal, the neutron can lose all of its kinetic energy in a head-on, billiard-ball-like collision. As the nuclear mass increases, one can see how the efficiency of a material per collision for moderating neutrons grows progressively worse. As a rule of thumb, the average energy lost per collision is approximately one-half the maximum.

Table 5.1 Maximum Fraction of Energy Lost, Q_{\max}/E_n (refer Eq. 5.1), by neutron in Single Elastic Collision with Various Nuclei

Nucleus	Q_{\max}/E_n
1_1H	1.000
2_1H	0.889
4_2He	0.640
9_2Be	0.360
${}^{12}_6C$	0.284
${}^{16}_8O$	0.221
${}^{56}_{26}Fe$	0.069
${}^{118}_{50}Sn$	0.033
${}^{238}_{92}U$	0.017

An interesting consequence of the equality of the masses in neutron–proton scattering is that the particles separate at right angles after collision, when the collision is non-relativistic. The elastic scattering of neutrons plays an important role in neutron energy measurements. Under suitable conditions the recoil energies of nuclei in a proportional-counter gas under neutron bombardment can be measured. The nuclear recoil energy and angle are directly related to the neutron energy. When a neutron of energy E_n strikes a proton, which recoils with energy Q at an angle θ with respect to the incident neutron direction, then the conservation of energy and

momentum requires that $Q = E_n \cos^2\theta$. Thus, if Q and θ can be measured individually for a number of incident neutrons, one obtains the incident neutron spectrum directly. This equation governs the working of proton-recoil neutron spectrometer. More often, only the energies of the recoil nuclei in the gas (e.g., ^3He , ^4He , or 1H and ^{12}C from CH_4) are determined, and the neutron energy spectrum must be unfolded from its statistical relationship to the recoil-energy spectra. The unfolding is further complicated by the fact that the recoil tracks do not always lie wholly within the chamber gas (wall effects).

5.2.3. Neutron detection

Neutrons are detected indirectly by observing the protons knocked loose by them or by nuclear reactions induced by them. For example, the alpha particles are easily detected in the following reactions shown in Table 5.2.

Table 5.2 Main isotopes used as neutron converters in luminescence detectors and corresponding natural abundance, thermal neutron cross-section and products [1, 2]

Isotope	Natural abundance	σ^* (barns)	Products
^6Li	7.4%	940	^3H (2.75 MeV) + ^4He (2.05 MeV)
^{10}B	19.8%	3840	^7Li (1.0 MeV) + ^4He (1.8 MeV) ^7Li (0.83 MeV) + ^4He (1.47 MeV) + γ (0.48MeV)
^{157}Gd	15.7%	255000	^{158}Gd + γ s + conversion e^- + X-rays (29–182 keV)
^{155}Gd	14.8%	60900	^{156}Gd + γ s + conversion e^- + X-rays (39–199 keV)

*Cross-section for capture of thermal neutrons.

Slow neutrons are measured by a proportional counter, which is filled with BF_3 gas. The products, ^7Li and alpha particle ionize the gas in the proportional counter and the signals are detected.

Fission reactions induced by neutrons can also serve for neutron detection.

Neutron activation analysis (NAA): Activation samples may be placed in a neutron field to characterize the energy spectrum and neutron fluence. Activation reactions having different

energy thresholds can be used including $^{56}\text{Fe}(n,p)^{56}\text{Mn}$, $^{27}\text{Al}(n,\alpha)^{24}\text{Na}$, $^{93}\text{Nb}(n,2n)^{92\text{m}}\text{Nb}$, & $^{28}\text{Si}(n,p)^{28}\text{Al}$.

Fast neutrons: Neutrons whose kinetic energy is above about 1 keV are generally classified as fast neutrons. They give large portions of their kinetic energy to the protons. Energetic protons ionize, and they are detected as such.

5.2.4. Health hazards and Need for neutron dosimetry

In health physics neutron is considered a fourth radiation hazard. Sometimes more severe hazard of neutron radiation is neutron activation, the ability of neutron radiation to induce radioactivity in most substances it encounters, including the body tissues of the workers. This occurs through the capture of neutrons by atomic nuclei, which are transformed to another nuclide, frequently a radionuclide. This process accounts for much of the radioactive material released by the detonation of a nuclear weapon. It is also a problem in nuclear fission and nuclear fusion installations, as it gradually renders the equipment radioactive; eventually the hardware must be replaced and disposed of as low-level radioactive waste. Compared to conventional ionizing radiation based on photons or charged particles, neutrons are repeatedly moderated and slowed by light nuclei like hydrogen. As tissue is mostly hydrogenous due to water content therefore neutron interacts with human tissue and causes biological damage. As neutrons that strike the hydrogen nucleus (proton, or deuteron) impart energy to that nucleus, they in turn will break from their chemical bonds and travel a short distance, before stopping. Those protons and deuterons are high linear energy transfer particles, and are in turn stopped by ionization of the material through which they travel. Consequently, in living tissue, neutrons have a relatively high relative biological effectiveness, and are roughly ten times more effective at causing cancers or LD-50 compared to photon or beta

radiation of equivalent radiation exposure. Further, because of the magnitude of the cross section, the efficiency of energy transfer, and the abundance of hydrogen in soft tissue, neutron–proton (n–p) scattering is usually the dominating mechanism whereby fast neutrons deliver dose to tissue. Over 85% of the “first-collision” dose in soft tissue (composed of H, C, O, and N) arises from n–p scattering for neutron energies below 10 MeV. Captures of neutron by proton and deuterium lead to the formation of deuterium and tritium respectively. The cross sections are small, and many neutrons decay if not captured.

Nuclear reactors are the most copious sources of neutrons. The energy spectrum of neutrons from the fission of ^{235}U extends from a few keV to more than 10 MeV. The average energy is about 2MeV. Research reactors often have ports through which neutron beams emerge into experimental areas outside the main reactor shielding. These neutrons are usually degraded in energy, having passed through parts of the reactor core and coolant as well as structural materials.

Therefore, personnel dosimetry and dose tracking requirements at nuclear facilities has become increasingly more rigorous. Unfortunately, due to the inherent difficulty of neutron dosimetry, few direct-reading neutron dosimeters exist that are not cost-prohibitive. Typically, a neutron dosimeter consists of the reusable and durable albedo dosimeter (which measures body–reflected neutrons) in conjunction with a TLD badge containing chips for mixed gamma/neutron exposures. Albedo dosimetry requires knowledge of the neutron energy spectrum of concern, which changes even in the area surrounding a human body due to scattering.

5.3. Studies on neutron irradiated pure α -Al₂O₃ single crystals

Irradiation of single crystal Al₂O₃ in the reactor (i.e. fast and thermal neutrons and gamma radiation) produces many color centers in the pure Al₂O₃ single crystal. Levy and Dienes [3] in 1955 have shown for the first time that the reactor irradiation of α -Al₂O₃ causes the growth of an optical absorption (OA) band at about 203 nm (F centers) and 230 & 255 nm (F⁺ centers) which is hard to generate by X-ray and gamma ray irradiation. These bands occur when oxygen atoms are displaced from the lattice causing the formation of F (oxygen vacancy with two trapped electrons) and F⁺ (oxygen vacancy with one trapped electron) centers in Al₂O₃. The oxygen vacancies can be introduced into α -Al₂O₃ by a variety of methods such as additive and subtractive coloration [4] and induction of defects by ionizing radiation (Levy, 1961). Various studies have been performed on the neutron irradiated alumina and its effect on the formation of F and F⁺ centers over the past four decades [4-6]. The most dominating and important luminescence centers generated in crystalline α -Al₂O₃ by above methods are the electron traps: F and F⁺ centers with observed optical absorption (OA) peaks at 203 nm, 225 & 255 nm corresponding to optical transition ¹S→¹P, 1A→2A & 1A→1B respectively. This OA in F and F⁺ gives rise to subsequent emission ³P→¹S (420 nm, $\tau \sim 35$ ms) and 1B→1A (330 nm, $\tau_R < 7$ ns) [23]. In order to obtain an appropriate F center concentration and F- aggregate centers. Atobe et al., [7] have used the loop of low temperature irradiation facility with circulating helium gas (-250°C). The F and F⁺ centers in Al₂O₃:C are also found to play a decisive role in rendering it sensitive towards ionizing radiation [8]. The thermoluminescence (TL) mechanism of neutron irradiated Al₂O₃ crystals has been reported by Saliquir et al. [9]. The F- type center related TL emission bands near 340, 430, 530 nm have been related to the atomic displacement

defects in the neutron-irradiated Al_2O_3 crystals. The details of the defects, their production mechanism, and dependence on the neutron energy are some of the important topics need to be investigated for better understanding TL and optically stimulated luminescence (OSL) phenomenon in thermal neutron irradiated $\alpha\text{-Al}_2\text{O}_3$ crystals. The sections to follow discuss the study of the F and F^+ centers in $\alpha\text{-Al}_2\text{O}_3$ crystals upon irradiation to thermal neutrons up to 10^{18} n/cm^2 and its implications on TL and OSL response.

5.3.1. Experimental

In our experiments, commercially available plain single crystals $\alpha\text{-Al}_2\text{O}_3$ (thickness ~ 0.4 mm, 1100 plane obtained from M/s Crystal Growth, Russia) were cut to 10 mm x 10 mm size. The samples were irradiated in CIRUS reactor for various thermal neutron fluences in the range 10^{14} n/cm^2 to 10^{18} n/cm^2 (including associated fast neutrons and gamma rays). At thermal neutron fluence of 10^{17} n/cm^2 the associated fast neutron fluence and gamma dose values were 7.12×10^{14} n/cm^2 and 47.5 kGy respectively, whereas for the fluence of 10^{18} n/cm^2 the corresponding values were 7.12×10^{15} n/cm^2 and 475 kGy. Therefore, reactor irradiation of samples implies irradiation with thermal and fast neutrons and gamma radiation. The reactor neutron irradiated samples were studied using the OA, photoluminescence (PL), continuous wave OSL (CW-OSL) and TL techniques. The absorption spectrum was recorded on a UV-VIS scanning spectrophotometer (UV-2101PC, SHIMADZU) and the TL and CW-OSL responses were recorded using the in-house developed TL-OSL reader system (10).

PL studies were performed over the wavelength range of 200-600 nm at the room temperature by employing an Edinburg fluorescence spectrometer (Model FLP920). The xenon flash lamp was used for excitation. TL emission measurements were carried out using an in-house developed high resolution TL emission set-up consisting of a compact Sciencetech 9030

monochromator directly mounted on a TL drawer assembly at an optimized focal distance. The heater temperature was adjusted based on the TL peak being studied and the wavelength resolved TL emission curve is recorded during the thermal stimulation. The dosimetric properties of the crystals were studied using CW-OSL technique. The TL and CW-OSL were also recorded on the crystals by irradiating them to an absorbed dose of 0.1 Gy using a calibrated ^{60}Co gamma source. The TL measurements were compared with the $\alpha\text{-Al}_2\text{O}_3\text{:C}$ single crystal (TLD -500 disc, 5 mm diameter, 1 mm thick).

5.3.2. *Results*

5.3.2.1. *Optical absorption studies*

The OA spectra recorded on single crystal $\alpha\text{-Al}_2\text{O}_3$ irradiated to various reactor neutron fluences in the range of 10^{14} to 10^{18} n/cm^2 show the growth of F (OA bands at ≈ 203 nm) and F^+ (OA bands at ≈ 230 and 255 nm) center absorption bands with the increase in the neutron fluence (fig. 5.1). The induction of F and F^+ absorption bands is attributed to the presence of associated fast neutrons in the beam, as the high fluence of thermal neutrons (having average energy of 0.025 eV) may not be able to induce significant defects in alumina. This is because the constituent atoms of the host material (alumina) do not have thermal neutron capture cross-section and fast neutrons from reactor can generate oxygen vacancies through inelastic collisions. However, the growth of both F and F^+ bands is not significant for the reactor neutron fluence less than 10^{17} n/cm^2 . The individual OA peaks of F and F^+ centers for the $\alpha\text{-Al}_2\text{O}_3$ crystal irradiated to 10^{18} n/cm^2 fluence of reactor neutrons is resolved and shown in fig. 5.2. It may be noted that the appearance of the band at 230 nm in the background of 203 nm peak implies that the concentration of F^+ centers is in excess of 10^{15} cm^{-3} [8]. The ratio of the F^+/F band intensity is much smaller in $\alpha\text{-Al}_2\text{O}_3$ samples irradiated with reactor neutron fluence \leq

10^{17} n/cm² than that observed in α -Al₂O₃:C (TLD-500) single crystals (reported to be ~12) [11]. However, the ratio increases considerably for neutron fluence of 10^{18} n/cm², indicating increase in the concentration of defects in the material. The increase in F⁺ center concentration could be due to the formation of large concentration of charge compensators in the neutron irradiated α -Al₂O₃ samples; such charge compensators are expected to favor formation of F⁺ band. The intensity of OA band of an optical transition is related to the concentration of absorbing centers N , index of refraction n , and oscillator strength f by the well known Smakula formula [12]

$$Nf = 8.21 \times 10^{15} \text{ cm}^{-3} \frac{n}{(n^2 + 2)^2} \int \alpha(E) dE \quad (5.2)$$

Where α is the decadic absorption coefficient in cm⁻¹ and E is energy in eV. The F/F⁺ concentration ratio of α -Al₂O₃ samples irradiated to thermal neutron fluence of 10^{18} n/cm² is 0.68, whereas ratios of F₂₀₃/F₂₃₀⁺ and F₂₀₃/F₂₅₅⁺ are found to be 2.28 and 0.97 respectively.

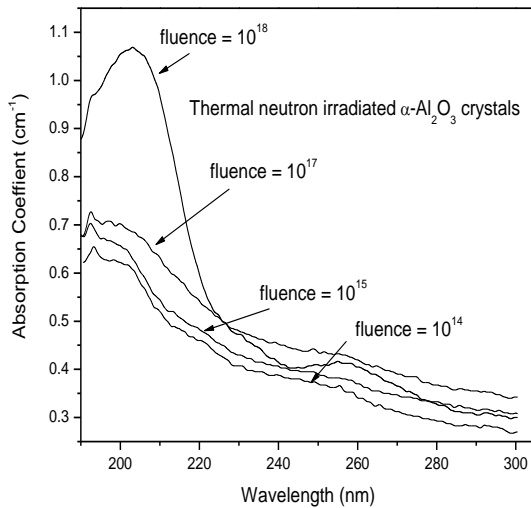


Figure 5.1. OA spectra of irradiated α -Al₂O₃ crystals for various thermal neutron fluence.

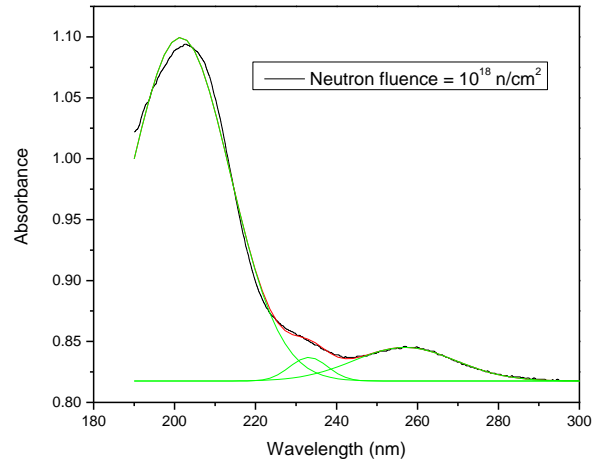


Figure 5.2. OA spectra of Al₂O₃ crystals irradiated to thermal neutron fluence of 10^{18} n/cm² with a Gaussian fit.

5.3.2.2. PL studies

Emission and excitation spectra of F and F^+ centers in $\alpha\text{-Al}_2\text{O}_3$ single crystal irradiated to thermal neutron fluence of 10^{18} n/cm^2 are shown in fig. 5.3. The F center emission is recorded by excitation using 204 nm wavelength which corresponds to the excitation energy of F center. It is interesting to note that, on excitation with 204 nm, F^+ emission band at 330 nm is observed in addition to the F center emission band at 410 nm. Also, the F^+ emission band is quite pronounced compared to the F center band indicating the formation of excess F^+ centers by thermal neutron irradiation of Al_2O_3 single crystals. This is in agreement with the ratio of F/F^+ (0.68) calculated using Smakula formula. Thus, the PL and OA studies independently establish the abundance of F^+ center in the thermal neutron irradiated Al_2O_3 single crystals. Fig. 5.4 shows emission spectra of F^+ centers obtained by excitation with 228 and 258 nm.

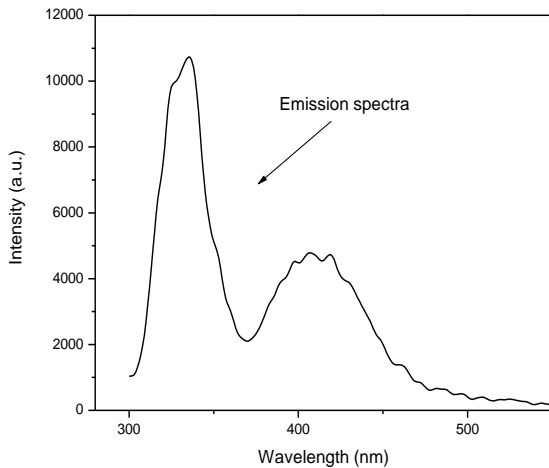


Figure 5.3. Emission spectra of F center in $\alpha\text{-Al}_2\text{O}_3$ crystals irradiated to thermal neutron fluence of 10^{18} n/cm^2 on excitation with 204 nm.

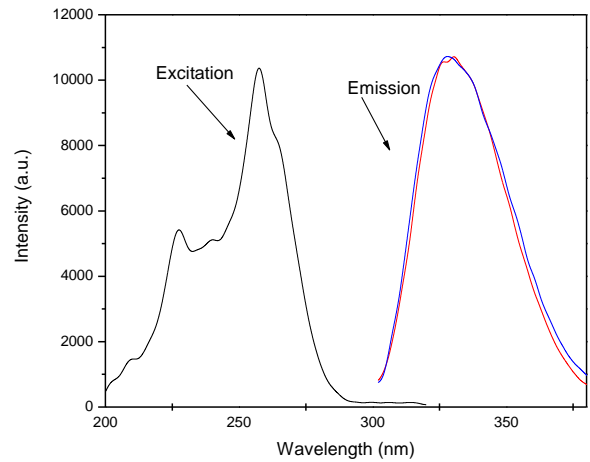


Figure 5.4. Excitation and emission spectra for F^+ centers in $\alpha\text{-Al}_2\text{O}_3$ crystals irradiated to thermal neutron fluence of 10^{18} n/cm^2 .

5.3.2.3. TL studies

Fig. 5.5 shows the TL emission spectrum recorded at 473 K of the α -Al₂O₃ single crystal irradiated to 10¹⁸ n/cm² of reactor neutrons. The TL emission bands near 340 and 410 nm were observed in neutron irradiated α -Al₂O₃. These bands correspond to F⁺ and F emissions respectively, in the TL process. Further, 410 nm emission has been attributed to the atomic displacement defects as F-type centers caused by neutron irradiation [7, 9]. Fig. 5.6 shows the TL glow curves recorded on the α -Al₂O₃ crystals irradiated to reactor neutron fluence in the range 10¹⁴-10¹⁸ n/cm². The TL readout of the samples show complex and overlapping glow curve structure with three prominent glow peaks at 160, 248 and 340 °C for 2 K/s heating rate. The TL intensity for α -Al₂O₃ crystals was found to increase with increase in reactor neutron fluence as shown in inset of fig. 5.6. The induction of intense TL in the crystal is due to associated fast neutron fluence in the beam. The results presented in fig. 5.7 indicate that gamma irradiated as well as neutron irradiated samples induce TL in the α -Al₂O₃ crystals. However, the TL intensity induced by crystals irradiated to reactor neutrons of 10¹⁷ n/cm² is about 250 times higher than the samples irradiated to gamma dose of 47.5 kGy (the associated gamma dose in the neutron irradiated sample). As thermal neutrons cannot induce significant TL in alumina as the constituent atoms of the host material do not have thermal neutron cross-section. However, fast neutrons can induce significant defects in alumina through inelastic collisions. Therefore the intense TL in the neutron irradiated samples is predominantly due to the effect of fast neutrons. The TL peak of TLD-500 single crystal irradiated to a ⁶⁰Co gamma dose of 0.1 Gy was observed to occur at ~ 190°C for a heating rate 2 K/s. It is evident that the defects formed due to neutron irradiation of α -Al₂O₃ crystals are different than those formed in α -Al₂O₃:C crystals prepared using Czochralski method [8].

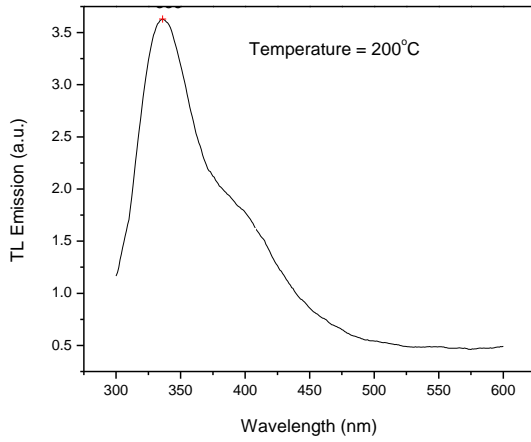


Figure 5.5. TL emission spectrum of the $\alpha\text{-Al}_2\text{O}_3$ crystals irradiated to thermal neutron fluence of 10^{18} n/cm^2

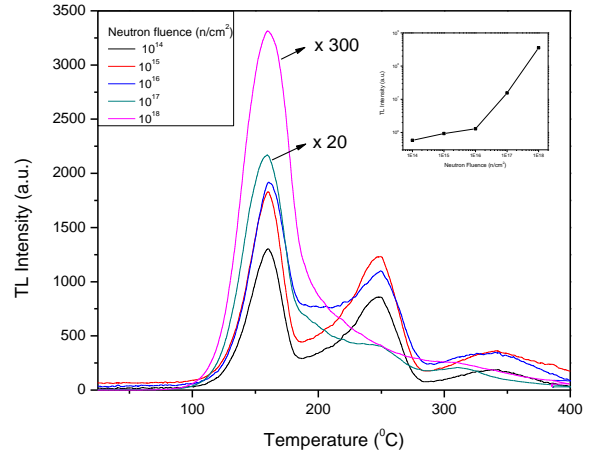


Figure 5.6. TL glow curves recorded on $\alpha\text{-Al}_2\text{O}_3$ crystals irradiated to reactor neutron fluence in the range 10^{14} - 10^{18} n/cm^2 . The inset figure shows the TL intensity vs. reactor neutron fluence for $\alpha\text{-Al}_2\text{O}_3$ crystals.

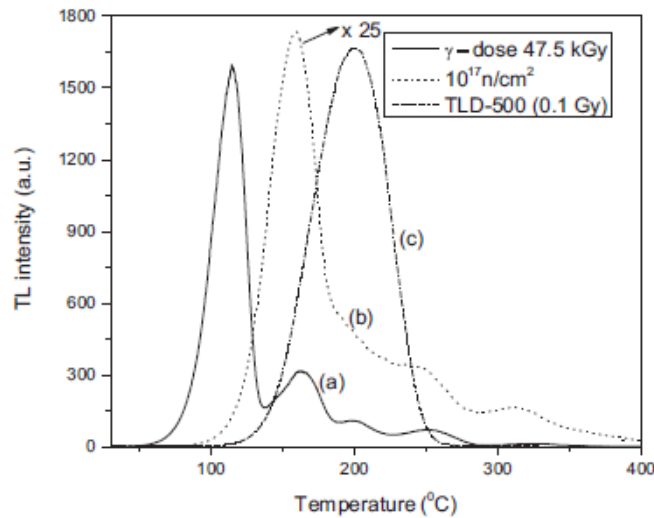


Figure 5.7. Comparison of TL glow curves of $\alpha\text{-Al}_2\text{O}_3$ single crystals after (a) irradiation to thermal neutron fluence of 10^{17} n/cm^2 and (b) gamma dose of 47.5 kGy. For direct comparison of intensities of the glow curves (a) and (b), the intensities should be multiplied by the factor given against the curves. (c) TL glow curve of $\alpha\text{-Al}_2\text{O}_3\text{: C}$ (TLD-500) is given for comparison of TL peak position only.

5.3.2.4. CW-OSL studies

The CW-OSL of the α -Al₂O₃ single crystals irradiated to thermal neutron fluence in the range 10^{14} n/cm² to 10^{18} n/cm² using blue light stimulation (470nm) is shown in fig. 5.8. The light intensity at the sample position was recorded to be 40 mW/cm². The CW-OSL response of neutron irradiated α -Al₂O₃ crystals increases with increase in thermal neutron fluence. The OSL response is found to be maximum for α -Al₂O₃ crystals irradiated to thermal neutron fluence of 10^{18} n/cm² (fig. 5.8). The normalized CW-OSL intensity curves are shown in fig. 5.9 from which it is evident that the photo-ionization cross-section increases with increase in thermal neutron fluence in the irradiated α -Al₂O₃ crystals. For the thermal neutron fluence of 10^{18} n/cm², the fast and slow components of photo-ionization cross-section are found to be 8.1×10^{-18} and 1.2×10^{-18} cm² respectively.

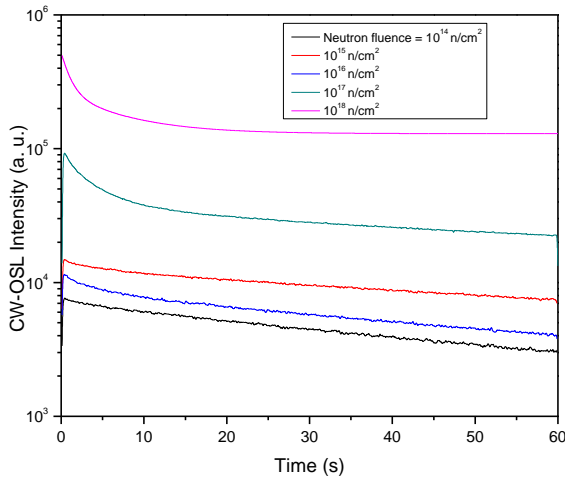


Figure 5.8. CW-OSL response of α -Al₂O₃ crystals for various thermal neutron fluence.

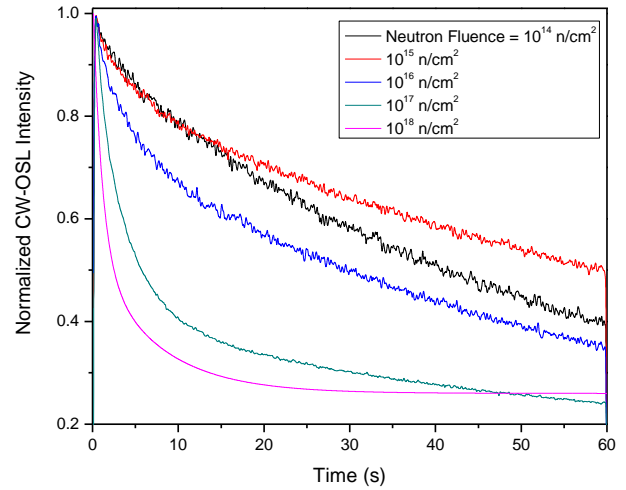


Figure 5.9. Normalised OSL response of α -Al₂O₃ crystals for various thermal neutron fluence.

5.3.3. *Conclusion*

The neutron irradiation of α -Al₂O₃ single crystals generate F and F⁺ centers. The concentration of the F and F⁺ centers increases with increase in the fluence of reactor neutrons and are responsible for the observed TL and OSL in the α -Al₂O₃ crystals. The α -Al₂O₃ crystals irradiated to reactor neutron fluence $< 10^{17}$ n/cm² show weak TL and OSL response. TL intensity induced by crystals irradiated to reactor neutrons of 10^{17} n/cm² is about 250 times higher than the samples irradiated to gamma dose of 47.5 kGy (the associated gamma with neutron fluence of 10^{17} n/cm²). Thermal neutrons cannot induce significant TL in alumina. However, fast neutrons can induce significant defects in alumina through inelastic collisions. The intense TL and OSL is attributed to the induction of F and F⁺ centers generated predominantly due to the effect of fast neutron component in the reactor irradiated α -Al₂O₃ single crystals. However, the OSL active defect centers in α -Al₂O₃:C are different than those induced in neutron irradiated α -Al₂O₃.

5.4. Development of Neutron-Sensitive OSL Detectors

Al_2O_3 has a small cross-section for neutron interaction, resulting in practically zero neutron sensitivity. For example, the neutron sensitivity of $\text{Al}_2\text{O}_3:\text{C}$ at 14 MeV neutrons is ~20% of the neutron sensitivity of $^7\text{LiF}:\text{Mg,Ti}$, which is commonly used as a neutron-insensitive TLD [13]. The lack of neutron sensitivity of $\text{Al}_2\text{O}_3:\text{C}$, combined with the fact that this is the most important OSL material used in personal dosimetry, has been pointed out as one of the major disadvantages of the OSL technique when compared with the TL technique for personal dosimetry [14]. Clearly, however, this is a problem of the material, not the OSL technique per se.

Understanding the intricacies involved in neutron dosimetry is crucial to implement α - $\text{Al}_2\text{O}_3:\text{C}$ material for OSL-based personnel neutron monitoring, as most information on neutron sensitivity is known from measured TL characteristics of Al_2O_3 . The thermal neutron sensitivity of a TL/OSL material is defined as its response against the neutron fluence as compared to that for a fixed dose of ^{137}Cs gamma rays and expressed in equivalent mGy per 10^{10} ncm^{-2} or in mGy cm^2 . The thermal neutron TL sensitivity of Al_2O_3 is reported to be $3 \times 10^{10} \text{ mGy cm}^2$ to $4 \times 10^{10} \text{ mGy cm}^2$, which is lower than that of TLD-700 and comparable to that of $\text{CaSO}_4:\text{Dy}$ ($3.32 \times 10^{10} \text{ mGy cm}^2$) and BeO ($2 \times 10^{10} \text{ mGy cm}^2$). The neutron TL response in terms of absorbed dose relative to radiation from a ^{137}Cs source of $\text{Al}_2\text{O}_3:\text{C}$ is reported to be about one tenth of that of TLD-700 for neutron energies from 0.3 MeV to 6 MeV (i.e. in the range 0.000 to 0.011) and increases to 0.047 for 14 MeV neutrons.

Among the luminescent detectors, albedo dosimeters based on TL detectors are the commonly used neutron personnel dosimeters for a variety of neutron fields [15, 16] including high-energy accelerators [17]. At workplaces in the nuclear fuel cycle, the neutron fields span

energies from thermal to 20 MeV. Therefore it is necessary to investigate the neutron response of the dosimetry materials in this energy range using well-characterized neutron beams.

In following sections, detector pairs prepared using α -Al₂O₃:C OSL phosphor powder mixed with neutron- sensitive and neutron-insensitive converters, were irradiated in monoenergetic neutron fields with energies in the range from 24 keV to 14.8 MeV and in the field of a bare ²⁵²Cf radionuclide source and their neutron response was determined. α -Al₂O₃:C as synthesized in the Bhabha Atomic Research Centre by melting polycrystalline alumina in graphite ambience under high vacuum [18] and commercially available material obtained from Landauer Inc., USA, were used. ⁶LiF and high-density polyethylene (HDPE) neutron converters were selected [19, 20] and the albedo and proton radiator techniques were used for this study. The neutron sensitivity of the α -Al₂O₃:C + ⁶LiF detector is based on the ⁶Li(n, α)T reaction which has its highest cross section for thermal neutrons.

In the case of high-energy neutron fields, TL dosimetry usually relies on the detection of the so-called albedo neutrons, which are neutrons moderated inside the body of the person wearing the dosimeter and backscattered. In the TL albedo dosimetry technique, detectors of different types (e.g. containing ⁶Li which is sensitive to thermal neutrons and ⁷Li which is nearly insensitive to thermal neutrons) are used for personnel monitoring to discriminate the neutron and photon contributions to the dose. A similar technique has been adopted in the current study to discriminate the neutron and photon contributions. The neutron response is obtained by subtracting the reading of the α -Al₂O₃:C + ⁷LiF detector from the reading of the α -Al₂O₃:C + ⁶LiF detector. Albedo dosimeters are mainly sensitive to low energy neutrons and their personal dose equivalent response changes drastically with neutron energy, making the

application of field-dependent correction factors necessary at workplaces. A flatter response at higher energies is expected using the recoil proton technique.

As α -Al₂O₃:C is highly sensitive to photon radiation and the expected neutron response is small, a subtraction of the photon response needs to be as accurate as possible. Therefore, a mixture of α -Al₂O₃:C with poly tetra fluoro ethylene (PTFE or Teflon) having a similar absorption for photons, but containing no hydrogen is used. The neutron response is determined by subtracting the response of α -Al₂O₃:C + Teflon detectors from the response of α -Al₂O₃:C + HDPE detectors.

5.4.1. Sample preparation

The α -Al₂O₃:C phosphor material (grain size 20 μ m to 100 μ m) was mixed uniformly with different neutron converters. Cold-pressed detector discs 5 mm in diameter and 0.5 mm in thickness were prepared using the powder mixture of α -Al₂O₃:C and one of the following materials: LiF enriched with ⁶Li (~ 99% enriched) in 1:1 weight ratio, ⁷LiF (~ 99% enriched) in 1:1 weight ratio, high density polyethylene (grain size 53 μ m to 75 μ m) in 1:0.5 weight ratio and Teflon powder (grain size ~ 35 μ m) in 1:0.5 weight ratio. The detector discs were arranged in pairs: type (i) α -Al₂O₃:C + ⁶LiF and α -Al₂O₃:C + ⁷LiF, type (ii) α -Al₂O₃:C + HDPE and α -Al₂O₃:C + Teflon. For the purpose of comparison, equivalent discs were prepared using commercially available α -Al₂O₃:C phosphor (grain size 20 μ m to 90 μ m) from Landauer Inc., USA, and the four different additives (as indicated above), types (iii) and (iv). All detector discs were optically bleached using blue light (470 nm) for 60 minutes before each irradiation.

5.4.2. Irradiations

The different samples were irradiated using quasi-monoenergetic reference neutron fields with energies of 24 keV, 144 keV, 1.2 MeV, 6.0 MeV and 14.8 MeV, produced with ion

accelerators [21], a field of a bare ^{252}Cf radionuclide neutron source [22], and a field of a ^{137}Cs photon source. Table 5.3 gives the list of mono-energetic neutron beams available at PTB, Germany. In the present study, all irradiations were carried out with Physikalisch-Technische Bundesanstalt (PTB), the national metrology institute of Germany (figures 5.10 & 5.11).

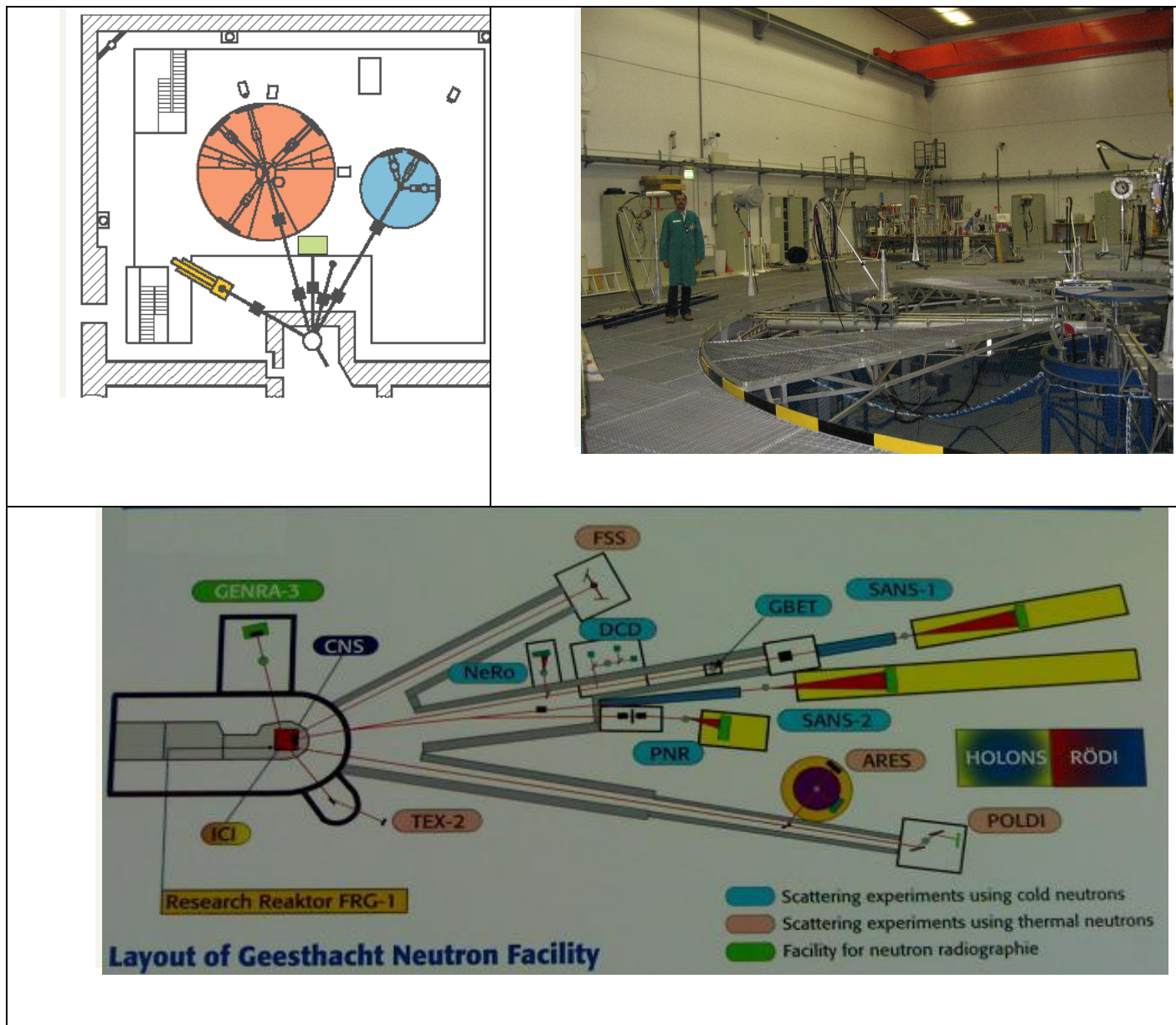


Figure 5.10. Facilities at PTB Germany and layout of neutron facility

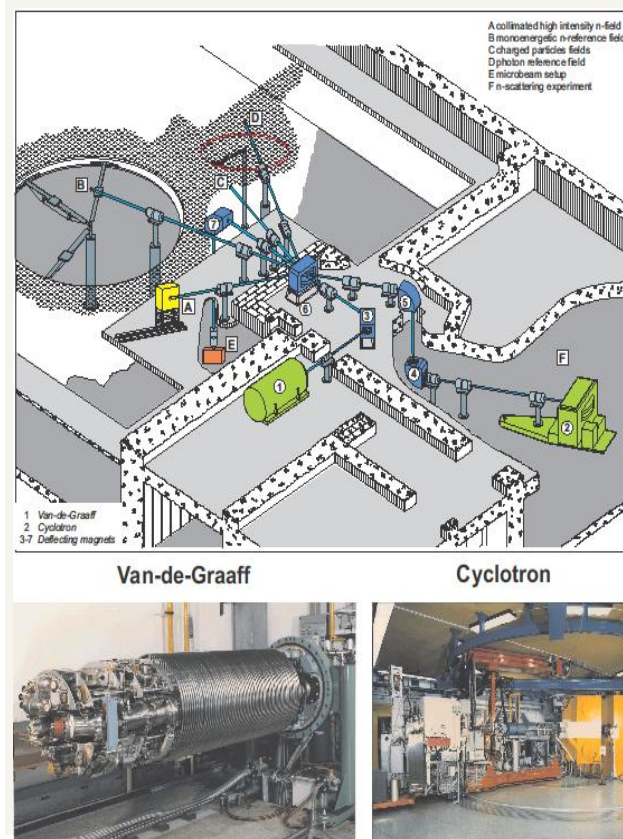


Figure 5.11 Experimental Hall

The detector discs were assembled in a light-tight holder with dimensions of 9.5 cm x 9.5 cm, made of aluminium, 0.5 mm in thickness, in front, and a Trovidur plastic sheet, 1 mm in thickness, on the backside. The four detector pairs, types (i) to (iv), were irradiated together with another pair of $\alpha\text{-Al}_2\text{O}_3\text{:C} + {}^6\text{LiF}$ and $\alpha\text{-Al}_2\text{O}_3\text{:C} + {}^7\text{LiF}$ detectors which were covered on the top of the aluminium plate with a 1 mm thick cadmium plate (area: 11 mm x 22 mm) in order to reduce the direct thermal neutron response during irradiation (type (v) = type (i) covered with cadmium). Thus, in total, five different types (see Table 5.4) were irradiated simultaneously; of each type, four samples were used in order to obtain better statistics. In the present study, all irradiations were carried out on the detector holder mounted on an ISO water

slab phantom, having outer dimensions of 30 cm x 30 cm x 15 cm, walls made of PMMA (front wall: 2.5 mm thick, other walls: 10 mm thick), filled with water [23]. The detector holders' front side (aluminium plate) was facing the source. In the case of the accelerator-based fields and the ^{252}Cf field, the phantom surface was positioned at a distance of 50 cm from the target and 58 cm from the source, respectively. Additional free-in-air irradiations were performed in the neutron fields at the same distances in order to investigate the contributions due to backscatter from the phantom. Irradiations with a ^{137}Cs photon source were performed for calibration purposes at a distance of 69 cm free-in-air, too.

Table 5.3: Accelerator produced mono-energetic neutrons at PTB, Germany

Reaction	$\langle E \rangle$ MeV	ΔE MeV	Φ (1m dist.) $\text{cm}^{-2} \text{s}^{-1}$	$H^*(10)$ (1m dist.) mSv/h
$^7\text{Li}(p,n)^7\text{Be}$	0.024	0.001	5.00×10^1	0.0035
$^7\text{Li}(p,n)^7\text{Be}$	0.144	0.012	5.52×10^1	0.02
$^7\text{Li}(p,n)^7\text{Be}$	0.250	0.012	2.62×10^1	0.015
$^7\text{Li}(p,n)^7\text{Be}$	0.565	0.010	8.42×10^1	0.08
$\text{T}(p,n)^3\text{He}$	1.2	0.098	4.26×10^2	0.53
$\text{T}(p,n)^3\text{He}$	2.5	0.104	1.61×10^3	2.28
$\text{D}(d,n)^3\text{He}$	5.0	0.18	4.56×10^2	0.68
$\text{D}(d,n)^3\text{He}$	8.0	0.1	9.86×10^3	15.22
$\text{T}(d,n)^4\text{He}$	14.8	0.9	8.51×10^2	1.70
$\text{T}(d,n)^4\text{He}$	19.0	0.25	2.61×10^2	0.57

*All values are given for a beam current of $1 \mu\text{A}$

Table 5.4 Types of detector used in the study

Combination of $\alpha\text{-Al}_2\text{O}_3\text{:C}$ neutron converter Grain size	Grain size of powder (μm)	Ratio of $\alpha\text{-Al}_2\text{O}_3\text{:C}$ to neutron converter
$\alpha\text{-Al}_2\text{O}_3\text{:C(Landauer)}+{}^6\text{LiF}/\alpha\text{-Al}_2\text{O}_3\text{:C(Landauer)}+{}^7\text{LiF}$	20-90 both	1:1 both
$\alpha\text{-Al}_2\text{O}_3\text{:C(BARC)}+{}^6\text{LiF}/\alpha\text{-Al}_2\text{O}_3\text{:C(BARC)}+{}^7\text{LiF}$	20-100;20-100	1:1 both
$\alpha\text{-Al}_2\text{O}_3\text{:C(BARC)}+\text{HDPE}/\alpha\text{-Al}_2\text{O}_3\text{:C(BARC)}+\text{Teflon}$	20-100;53-75;20-100;35	1:0.5 both
$\alpha\text{-Al}_2\text{O}_3\text{:C(Landauer)}+\text{HDPE}/\alpha\text{-Al}_2\text{O}_3\text{:C(Landauer)}+\text{Teflon}$	20-90;53-75;20-90;35	1:0.5 both
$\alpha\text{-Al}_2\text{O}_3\text{:C(Landauer)}+{}^6\text{LiF}/\alpha\text{-Al}_2\text{O}_3\text{:C(Landauer)}+{}^7\text{LiF}$ with Cd	20-90;20-90	1:1 both

* This type is the same as type (i), except that these detectors were placed behind a shielding made of 1 mm cadmium

The relatively short distances selected for the neutron irradiation provide a low contribution of wall scattered neutrons. In the case of the accelerator fields - which are produced in a large low-scatter hall - the fluence contribution of scattered neutrons at the measuring position (50 cm) is in the order of 1% to 2% [21]. The accelerator fields also contain photons which contribute a few percent to personal dose equivalent and which can change, depending on beam and target conditions. The contribution of scattered neutrons is higher for the source facility. The sources are mounted in the PTB bunker room having inside dimensions of 7 m x 7 m x 6.5 m and walls 1 m in thickness made of reinforced concrete. The fluence contribution of scattered neutrons at the measuring position (58 cm) is 10.9%. In addition, the ${}^{252}\text{Cf}$ neutron field contains photons which contribute 3.7% to the personal dose equivalent [22].

The neutron fluence at the accelerator was determined using hydrogen-filled proportional counters and recoil proton telescopes and was monitored during the irradiation by Precision Long Counters [21, 24]. The fluence of direct neutrons was converted into personal

dose equivalent $H_p(10)$ using fluence-to-personal dose equivalent conversion coefficients for normal incidence as given by ICRU [25]. In the case of the ^{252}Cf source, the reference values of $H_p(10)$ were calculated from the source strength for a reference distance of 58 cm, including direct and scattered contributions of neutrons. The $H_p(10)$ values for the irradiations performed varied from 0.2 mSv to 100 mSv in the case of the ^{252}Cf neutron source, were fixed to 2 mSv in the case of the ^{137}Cs photon source and varied at the accelerator: Irradiations with high values of $H_p(10)$ were applied in fields with neutron energy above 1 MeV (about 8 mSv, 50 mSv and 70 mSv in cases of irradiations with 1.2 MeV, 6 MeV and 14.8 MeV neutrons, respectively) and low personal dose equivalent values were applied at neutron energies below 1 MeV (about 1.4 mSv and 0.1 mSv in the case of irradiations with 144 keV and 24 keV neutrons, respectively). The reasons for the high dose values at high neutron energies were the expected decrease of the albedo response and also the expected low response of the dosimeters containing proton converters at these energies.

5.4.3. OSL measurements

$\alpha\text{-Al}_2\text{O}_3\text{:C}$ powder mixed with various neutron converters and pressed into pellets were investigated using the continuous wave (CW-) OSL method. The Risø TL/OSL-DA-15 reader available at the PTB was used for this purpose. CW-OSL readouts were carried out using blue (470 nm) light stimulation and a Hoya 340 filter in front of the photomultiplier tube. The stimulation light intensity at the sample position was $\sim 25 \text{ mW/cm}^2$. The CW-OSL intensity was recorded on the samples for 40 seconds with a 66.67 ms acquisition time (600 channels).

5.4.4. Data analysis

In dosimetry applications, it is generally the case that the OSL area and initial OSL intensity are proportional in the linear dose range for gamma irradiation [26]. Also, the shape of

the OSL curves is dependent on the LET of the radiation and dose [26-28]. In the case of neutron irradiated samples, it was observed that the OSL curve decays faster as compared to the once observed for gamma irradiated samples. However, for dose evaluation, the initial CW-OSL signal integrated over the first second (15 channels) is used to obtain the signal ‘S’ as in this region S/N ratio is better when compared with the analysis done by taking total area into consideration. The average of the last fifty channels in the OSL curve is subtracted as background from each channel.

First, the CW-OSL signal of all detectors exposed to the ^{137}Cs photon source with a 2 mGy dose was measured and the signal was called reference signal “ S_R ”. This reference signal is used to account for variations in detector mass or intrinsic sensitivity. For any radiation quality, the individual calibration factor for a detector is $N_i = 2\text{mSv}/S_{R,i}$ and the measured personal dose equivalent, $H_p(10)_{\text{meas}}$, is then yielded by

$$H_p(10)_{\text{meas}} = N_i S$$

The neutron-sensitive detectors $\alpha\text{-Al}_2\text{O}_3\text{:C}+^6\text{LiF}$ indicate both the neutron and the photon component, $H_p(10)_{\text{meas},n+\gamma}$ and the neutron component, $H_p(10)_{\text{meas},n}$ is determined by subtracting the photon component indicated by the $\alpha\text{-Al}_2\text{O}_3\text{:C}+^7\text{LiF}$ discs, $H_p(10)_{\text{meas},\gamma}$

$$H_p(10)_{\text{meas},n} = H_p(10)_{\text{meas},n+\gamma} - H_p(10)_{\text{meas},\gamma}$$

In the same way, the neutron component of the $\alpha\text{-Al}_2\text{O}_3\text{:C}+\text{HDPE}$ is determined by subtracting the photon component indicated by the $\alpha\text{-Al}_2\text{O}_3\text{:C}+\text{Teflon}$ discs. The assigned standard uncertainty of the personal dose equivalent values and responses are based on the standard deviation of the mean of four readings and the standard uncertainty of the reference dose (usually in the order of 5%). Finally, the neutron response, R_n , is obtained by dividing the

measured neutron personal dose equivalent, $H_p(10)_{\text{meas},n}$ by the reference value of the neutron personal dose equivalent, $H_p(10)_n$:

$$R_n = H_p(10)_{\text{meas},n} / H_p(10)_n.$$

5.4.5. Results

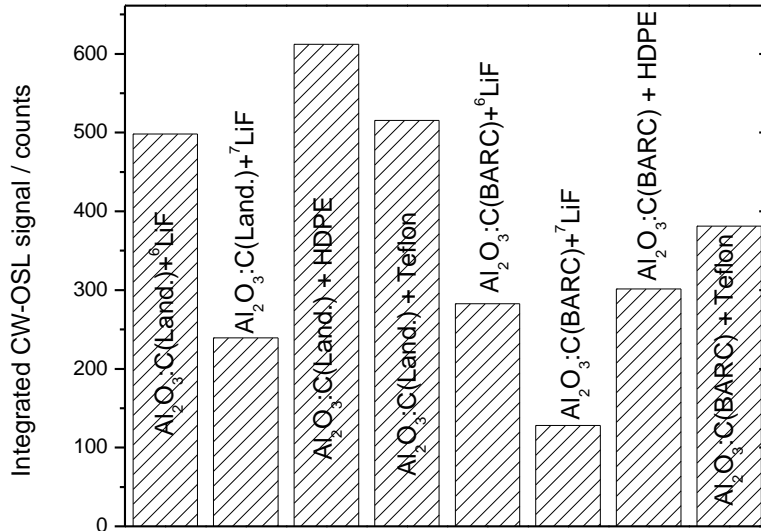


Figure 5.12. Integrated CW-OSL signal (first 15 channels) of $\alpha\text{-Al}_2\text{O}_3:\text{C}$ mixed with ${}^6\text{LiF}$, ${}^7\text{LiF}$, HDPE and Teflon after irradiation to 2 mSv ${}^{137}\text{Cs}$ calibration dose.

The photon readings of $\alpha\text{-Al}_2\text{O}_3:\text{C}$ (both BARC made and commercially available Landauer samples) mixed with various neutron converters and irradiated to a 2 mSv ${}^{137}\text{Cs}$ calibration dose are shown in fig. 5.12. Different OSL readings are due to the varying coloration / brightness of the neutron converter materials which are added to the $\alpha\text{-Al}_2\text{O}_3:\text{C}$ material. For example, the ${}^7\text{LiF}$ powder is more greyish than the ${}^6\text{LiF}$ powder and mixtures with ${}^7\text{LiF}$ show signals a factor of about two lower than mixtures with ${}^6\text{LiF}$. In addition, the

photon sensitivity of the α - $\text{Al}_2\text{O}_3:\text{C}$ material produced at BARC is about a factor of two smaller than that of the Landauer material, however, similar trends are seen in the OSL response of α - $\text{Al}_2\text{O}_3:\text{C}$ (Landauer) and α - $\text{Al}_2\text{O}_3:\text{C}$ (BARC) materials.

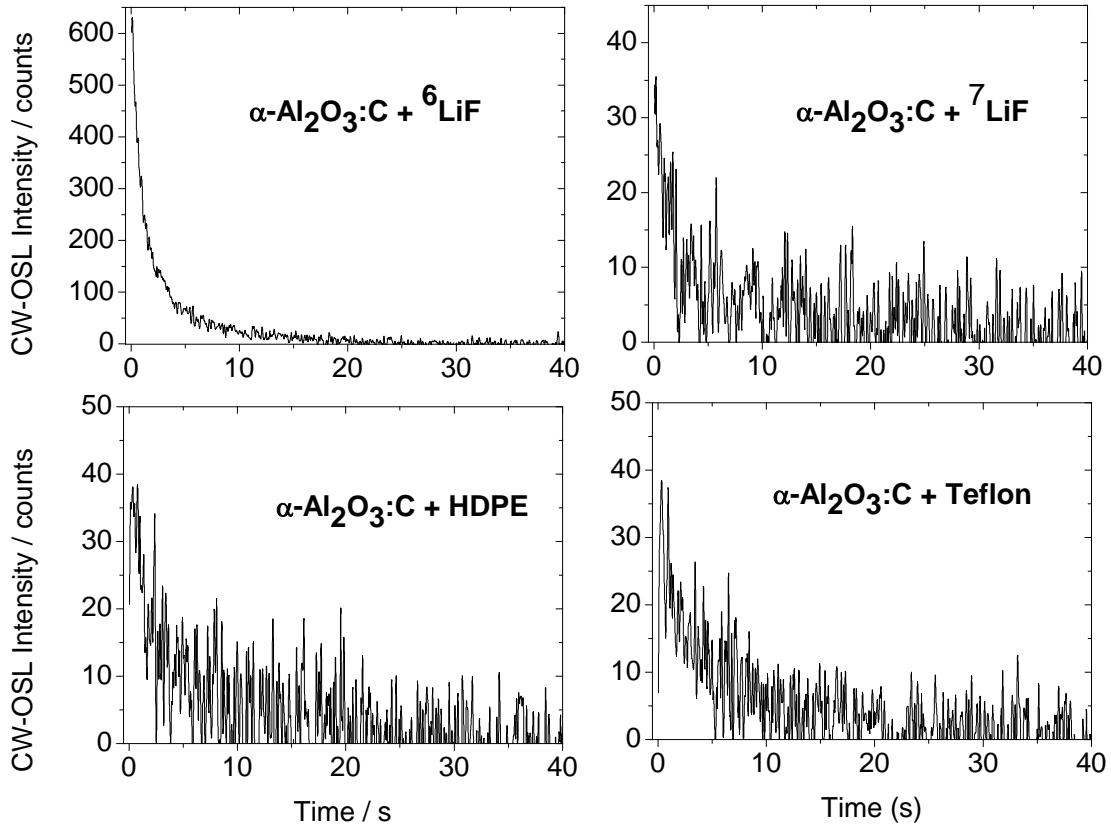


Figure 5.13. CW-OSL signal recorded on α - $\text{Al}_2\text{O}_3:\text{C}$ mixed with ^6LiF , ^7LiF , HDPE and Teflon and irradiated on an ISO water slab phantom to 24 keV neutrons with $H_p(10) = 98 \mu\text{Sv}$.

Fig. 5.13 shows the typical CW-OSL signal recorded from the α - $\text{Al}_2\text{O}_3:\text{C}$ detectors (mixed with different additives: ^6LiF , ^7LiF , HDPE and Teflon) and irradiated on an ISO water slab phantom to 24 keV neutrons with $H_p(10) = 98 \mu\text{Sv}$. It can be seen that the α - $\text{Al}_2\text{O}_3:\text{C} + ^6\text{LiF}$ detector shows a higher CW-OSL signal than all other discs. The higher CW-OSL signal of α - $\text{Al}_2\text{O}_3:\text{C} + ^6\text{LiF}$ is due to charged particles produced by the $^6\text{Li}(n,\alpha)\text{T}$ reaction, induced by the

incident 24 keV neutrons as well as by neutrons which are moderated in the phantom and backscattered.

Table 5.5 shows the results of the different chips of α -Al₂O₃:C mixed with ⁶LiF/⁷LiF, and HDPE/Teflon, and the neutron response, R_n , of detector pairs after irradiations with a ²⁵²Cf source with $H_p(10) = 10$ mSv. For all mixtures, a photon dose equivalent of about 0.6 mSv is indicated (corresponding to about 6% photon dose contamination), which is slightly higher than the value of 3.7% photon contribution to personal dose equivalent as given by Kluge [22]. The 3.7% was given for free-in-air irradiation. The photon dose equivalent on the phantom is higher due to secondary photons produced in the phantom. This may explain the 6% photon dose.

Table 5.5: Dose reading due to neutron- and photon-sensitive discs, $H_p(10)_{meas,n+\gamma}$ dose reading due to photon-sensitive discs, $H_p(10)_{meas,\gamma}$ resulting neutron dose reading, $H_p(10)_{meas,n}$ and neutron response, R_n , of irradiations with a ²⁵²Cf source, with a neutron personal dose equivalent of $H_p(10) = 10$ mSv.

Combination of α -Al ₂ O ₃ :C + neutron converter	$H_p(10)_{meas,n+\gamma}$ / mSv	$H_p(10)_{meas,\gamma}$ / mSv	$H_p(10)_{meas,n}$ / mSv	Neutron response, R_n
α -Al ₂ O ₃ :C(Landauer)+ ⁶ LiF / α -Al ₂ O ₃ :C(Landauer)+ ⁷ LiF with Cd shielding	2.105 ± 0.079	0.624 ± 0.044	1.481 ± 0.091	0.148 ± 0.009
α -Al ₂ O ₃ :C(Landauer)+ ⁶ LiF / α -Al ₂ O ₃ :C(Landauer)+ ⁷ LiF	2.354 ± 0.128	0.666 ± 0.060	1.688 ± 0.141	0.169 ± 0.014
α -Al ₂ O ₃ :C(BARC)+ ⁶ LiF / α -Al ₂ O ₃ :C(BARC)+ ⁷ LiF	2.642 ± 0.163	0.522 ± 0.094	2.120 ± 0.188	0.212 ± 0.018
α -Al ₂ O ₃ :C(BARC)+HDPE / α -Al ₂ O ₃ :C(BARC)+ Teflon	0.783 ± 0.035	0.664 ± 0.033	0.119 ± 0.048	0.012 ± 0.005
α -Al ₂ O ₃ :C(Landauer)+HDPE / α -Al ₂ O ₃ :C(Landauer)+ Teflon	0.670 ± 0.019	0.599 ± 0.011	0.071 ± 0.022	0.007 ± 0.002

From table 5.5 it is clear that the disc pair $\alpha\text{-Al}_2\text{O}_3\text{:C}+{}^6\text{LiF}$ / $\alpha\text{-Al}_2\text{O}_3\text{:C}+{}^7\text{LiF}$ yields the maximum neutron response. The cadmium cover in front of the dosimeters reduces the neutron response by about 10%. This is only a quite small reduction as the cadmium mainly absorbs the thermal neutrons, however, in a ${}^{252}\text{Cf}$ radiation field only few thermal neutrons are available. The neutron responses of the $\alpha\text{-Al}_2\text{O}_3\text{:C}+{}^{6,7}\text{LiF}$ detectors and the $\alpha\text{-Al}_2\text{O}_3\text{:C}+\text{HDPE/Teflon}$ detectors are found to be slightly higher for BARC material than those found for Landauer material. The value of 0.169 ± 0.014 for the Landauer $\alpha\text{-Al}_2\text{O}_3\text{:C}+{}^{6,7}\text{LiF}$ detectors is very close to the value (0.17 ± 0.03) reported by Mittani et al. [20] for a similar mixture and cold pressed pellets. The neutron response of the present configuration of the $\alpha\text{-Al}_2\text{O}_3\text{:C} + \text{HDPE/Teflon}$ is in the order of $\sim 1\%$, which is very low and needs to be improved in order to become useful for personal dosimeter applications.

The neutron indication, $H_p(10)_{\text{meas,n}}$ of $\alpha\text{-Al}_2\text{O}_3\text{:C}$ mixed with ${}^{6,7}\text{LiF}$ and irradiated with ${}^{252}\text{Cf}$ neutron is shown in fig. 5.14 as a function of the reference personal dose equivalent $H_p(10)$ (linearity). The indication increases nearly linearly from 0.2 mSv to 100 mSv. Fig. 5.15 shows the neutron indication, $H_p(10)_{\text{meas,n}}$ of $\alpha\text{-Al}_2\text{O}_3\text{:C}$ mixed with HDPE/Teflon, again as a function of neutron personal dose equivalent after irradiations with a ${}^{252}\text{Cf}$ source. The neutron indication is considerably lower than that shown in fig. 5.14. This indicates that the technique using HDPE as converter material is less effective due to low cross-sections and/or low ranges of charged particles which need to be detected within the sensitive $\alpha\text{-Al}_2\text{O}_3\text{:C}$ material. This is also the result of recent calculations which predict OSL neutron indications for similar mixtures with neutron converters [29]. Thus, the values are presented on a linear instead of logarithmic scale. Starting from higher doses (about 1 mSv) and within the uncertainties, the indications increase also linearly with dose equivalent.

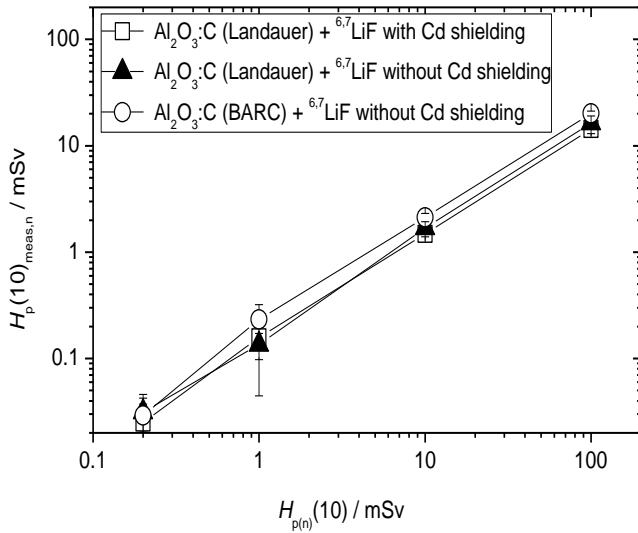


Figure 5.14. OSL neutron dose indication, $H_p(10)_{meas,n}$ of $\alpha\text{-Al}_2\text{O}_3\text{:C}$ mixed with ${}^{6,7}\text{LiF}$ and irradiated on an ISO water slab phantom with ${}^{252}\text{Cf}$ neutrons as a function of the reference personal dose equivalent $H_p(10)_n$. The lines show linear fits to the data.

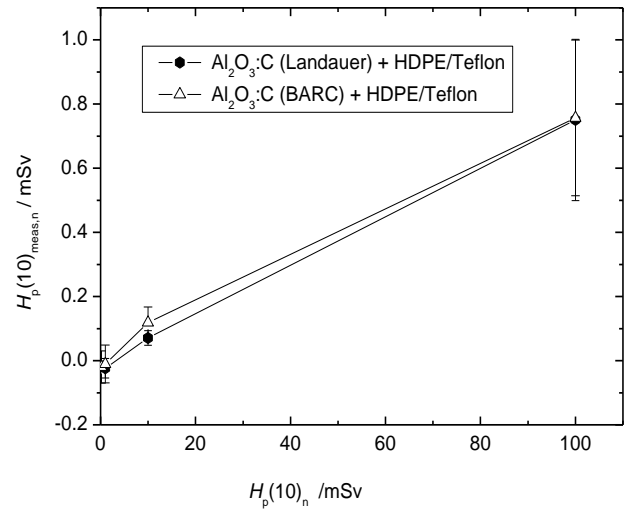


Figure 5.15. OSL neutron dose indication, $H_p(10)_{meas,n}$ of $\alpha\text{-Al}_2\text{O}_3\text{:C}$ mixed with HDPE/Teflon and irradiated on an ISO water slab phantom with ${}^{252}\text{Cf}$ neutrons as a function of the reference personal dose equivalent $H_p(10)_n$. The lines show linear fits to the data.

The $H_p(10)$ neutron response, $H_p(10)_{meas,n} / H_p(10)_n$, of the $\alpha\text{-Al}_2\text{O}_3\text{:C}+{}^{6,7}\text{LiF}$ dosimeters irradiated on an ISO water slab phantom for various monoenergetic neutron energies is shown in fig. 5.16. The trend in the neutron response is similar to the personal dose equivalent response of TLD-albedo dosimeters [15]. The response decreases roughly by a factor of 300 as the neutron energy increases to 14.8 MeV. The $H_p(10)$ response values indicated by the $\alpha\text{-Al}_2\text{O}_3\text{:C}+{}^{6,7}\text{LiF}$ dosimeter for free-in-air irradiations with various monoenergetic neutron energies were below 0.02, showing that the dosimeters have no significant response when irradiated free-in-air. Thus, the radiation scattered back from the phantom produces the main part of the indicated dose values.

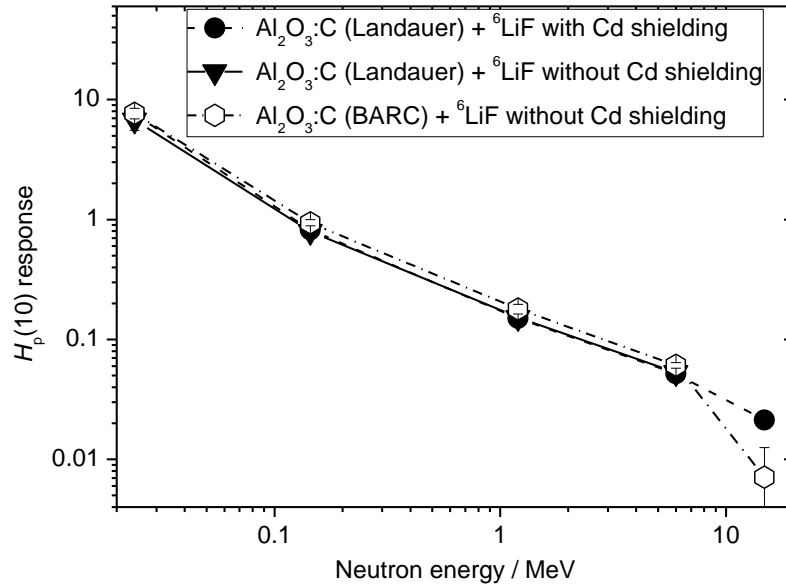


Figure 5.16. $H_p(10)$ response ($= H_p(10)_{meas,n} / H_p(10)$) of the α -Al₂O₃:C+^{6,7}LiF dosimeters irradiated on an ISO water slab phantom for various monoenergetic neutron energies.

The $H_p(10)$ response of dosimeter pairs consisting of α -Al₂O₃:C + HDPE /Teflon are shown for on-phantom and free-in-air irradiations in fig. 5.17 and fig. 5.18, respectively. The α -Al₂O₃:C + HDPE/Teflon dosimeters show no neutron response below 1 MeV; however, the responses at higher energies up to 14.8 MeV are small but significant (in the order of 1% to 2%). This behaviour is different from that of the ^{6,7}LiF detectors, see fig. 5.16, whose response decreases with rising neutron energy. In addition, the response does not change drastically for on-phantom and free-in-air irradiations showing that the high-energy neutrons produce a signal directly in the HDPE. Due to this advantage in comparison to the ^{6,7}LiF detectors, it is expected that this dosimeter response could be further increased by reducing the grain size of both α -Al₂O₃:C and HDPE and by mixing them in an optimised proportion [29] (potentially to about 5% or even larger). The optimised dosimeter pair consisting of α -Al₂O₃:C + HDPE / α -Al₂O₃:C

+ PTFE OSL dosimeters could then be used as a potential dosimeter for monitoring neutrons in high-energy neutron fields. In fields with lower energy neutrons, the albedo technique is still better suited because of the higher neutron response for low-energy neutrons.

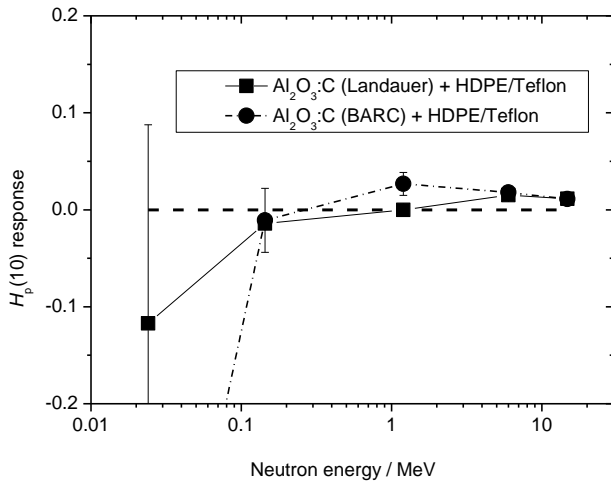


Figure 5.17. Comparison of the $H_p(10)$ response ($H_p(10)_{meas,n} / H_p(10)$) as a function of neutron energy of commercially available (Landauer) and BARC developed $\alpha\text{-Al}_2\text{O}_3\text{:C}$ material mixed with HDPE/Teflon in a 1:0.5 weight ratio irradiated on an ISO water slab phantom.

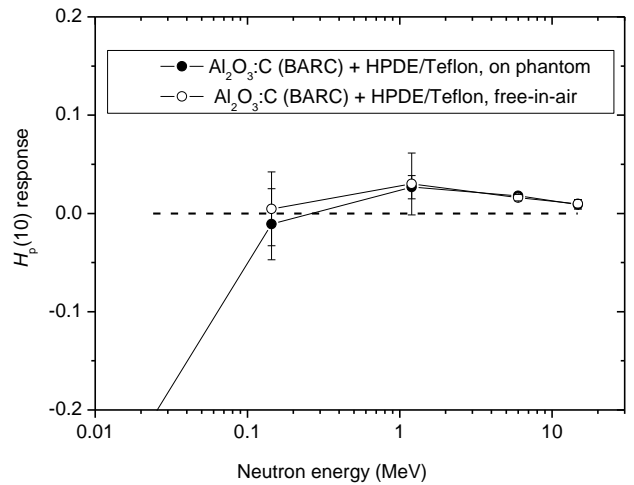


Figure 5.18. Comparison of the $H_p(10)$ response ($= H_p(10)_{meas,n} / H_p(10)$) as a function of neutron energy of commercial $\alpha\text{-Al}_2\text{O}_3\text{:C}$ material mixed with HDPE/Teflon in a 1:0.5 weight proportion for free-in-air and on-phantom irradiation.

5.4.6. Conclusion

$\alpha\text{-Al}_2\text{O}_3\text{:C} + {}^6\text{LiF}$ / $\alpha\text{-Al}_2\text{O}_3\text{:C} + {}^7\text{LiF}$ and $\alpha\text{-Al}_2\text{O}_3\text{:C} + \text{HPDE}$ / $\alpha\text{-Al}_2\text{O}_3\text{:C} + \text{Teflon}$ OSL dosimeters were developed and used for neutron dose measurements using albedo and proton radiator techniques. The OSL signal of the $\alpha\text{-Al}_2\text{O}_3\text{:C} + {}^{6,7}\text{LiF}$ dosimeters showed a linear response in terms of personal dose equivalent, $H_p(10)$, in the range from 0.2 mSv to 100 mSv using a ${}^{252}\text{Cf}$ neutron source. The OSL neutron response in terms of personal dose equivalent, $H_p(10)$, of these dosimeters was found to decrease by about a factor of 300 (from

about 7 to 0.025) with the neutron energy increasing from about 0.024 MeV up to 14.8 MeV which is typical for an albedo dosimeter [16]. Thus, it is possible to develop α -Al₂O₃:C + ^{6,7}LiF OSL dosimeters for personnel monitoring based on the albedo technique and to use field-dependent calibration factors in a way similar to that known from TLD albedo dosimeters. The OSL response of the α -Al₂O₃:C + HDPE/Teflon dosimeters was found to be negligible below 1 MeV and slightly higher and almost constant (0.01 to 0.02) above 1 MeV neutron energy. The use of α -Al₂O₃:C + HPDE / α -Al₂O₃:C + Teflon OSL dosimeters for personnel monitoring may be possible in high-energy neutron fields with low photon contribution, but further efforts are required.

References:

1. G. F. Knoll. *Radiation Detection and Measurements*, (2000) John Wiley & Sons, Inc.
2. C. W. E. Van Eijk. *Radiat. Prot. Dosim.*, **110**, 5 (2004).
3. P. W. Levy and G. J. Dienes, Report of Bristol conference on Defects in crystalline Solids, July 1954. (The Physical Society, London 1955) 256 (1955).
4. K. H. Lee, J. H. Crawford Jr. *Appl. Phys. Lett.* **33** (4), 273 (1978).
5. J. J. Antal and A. N. Goland. *Physical Review* **112**, 103 (1958).
6. Evans, B.D., Stapelbroek, M., 1978. Optical properties of F⁺ center in Crystalline Al₂O₃. *Phys. Rev. B* 18, 7089-7098.
7. Atobe, K., Nishimoto, N. and Nakagawa, M., 1985. Irradiation induced aggregate centers in single crystal Al₂O₃. *Phys. Stat. Sol. (a)* 89, 155-162.
8. Akselrod, M.S., Kortov, V.S., Kravetsky, D.J., Gotlib, V.I., 1990. Highly sensitive thermoluminescent anion-defective α -Al₂O₃:C. *Radiat. Prot. Dosim.* 33, 119-122.

9. Saliquir R.M., Kobayashi T., Awata T., Atobe K. 2010. Radiation Effects and Defects in Solids 165 (2010) 290.
10. Kulkarni, M.S., Mishra, D.R., Sharma, D.N., 2007. A versatile integrated system for thermoluminescence and optically stimulated luminescence measurements Nucl. Instr. and Meth. in Phys. Res. B 262, 348–356.
11. D. R. Mishra, M. S. Kulkarni, K. P. Muthe, C. Thinaharan, M. Roy, S. K. Kulshreshtha, S. Kannan, B .C. Bhatt, S. K. Gupta, D. N. Sharma. *Radia. Meas.* **42**,170 (2007)
12. Smakula, A., 1930. Photoelectric effect and decoloration and excitation of alkali halides. *Zeitschrift fuer Physik* 59, 603-14.
13. G.A.Klemic, N.Azziz and S.A.Marino. *Radiat. Prot. Dosim.* 65 (1996) 221.
14. S.W.S. McKeever, M. Moscovitch. *Radiat. Prot. Dosim.* 104 (2003) 263.
15. E. Piesch and B. Burgkhardt. Albedo neutron dosimetry. *Radiat. Prot. Dosim.* 10 (1985) 175.
16. J.A.B.Gibson. *Radiat. Prot. Dosim.* 23 (1988) 109.
17. T. Haninger and G. Fehrenbacher. *Radiat. Prot. Dosim.* 125 (2007) 361.
18. K.P.Muthe, M.S.Kulkarni, N.S.Rawat, D.R.Mishra, B.C.Bhatt, Ajay Singh and S.K. Gupta. *J. Lumin.* 128 (2008) 445.
19. E.G.Yukihara, J.C.Mittani, F.Vanhavere, M.S.Akselrod. *Radiat. Meas.* 43 (2008) 309.
20. J.C.R.Mittani, A.A.R. da Silva, F.Vanhavere, M.S.Akselrod, E.G.Yukihara. *Nucl. Instrum. Methods Phys. Res. B* 260 (2007) 663.
21. R. Nolte, M. S. Allie, R. Böttger, F. D. Brooks, A. Buffler, V. Dangendorf, H. Friedrich, S. Guldbakke, H. Klein, J. P. Meulders, D. Schlegel, H. Schuhmacher and F. D. Smit. *Radiat. Prot. Dosim.* 110 (2004) 97.

22. H. Kluge. Irradiation facility with radioactive reference neutron sources: basic principles, (1998), *Report PTB-N-34 (Braunschweig: Physikalisch-Technische Bundesanstalt)*, ISBN 3-89701-192-1.
23. ISO, *International Organization for Standardization*, (1998). Reference neutron radiations – Part 3: Calibration of area and personal dosimeters and the determination of their response as a function of neutron energy and angle of incidence. ISO 8529-3.
24. N. J. Roberts, D. J. Thomas, V. Lacoste, R. Böttger, S. Loeb. *Radiat. Meas.* 45 (2010), 1151.
25. International Commission on Radiation and Measurements, 1998. *ICRU Report 57* “Conversion coefficients for use in radiological protection against external radiation”. Bethesda, Maryland, USA.
26. E. G. Yukihara, V. H. Whitley, S. W. S. McKeever, A. E. Akselrod, and M.S. Akselrod, *Radiat. Meas.* 38 (2004) 317.
27. H. Yasuda, I. Kobayashi, H. Morishima, *J. Nucl. Sci. Technol.* 39 (2002) 211.
28. E. G. Yukihara, R. Gaza, S. W. S. McKeever, and C. G. Soares, *Radiat. Meas.* **38**, 59 (2004).
29. M. Luszik-Bhadra, *Radiat. Meas.*, to be published.

Chapter 6

TL and OSL Investigations on Lithium Borate Single Crystals

6.1. Introduction

Lithium borate ($\text{Li}_2\text{B}_4\text{O}_7$), abbreviated as LBO, has been considered to be one of the promising scintillators for the neutron detection due to large thermal neutron capture cross-sections of Li and B. On the other hand it has a low efficiency for unwanted gamma-ray background detection because of low effective atomic number (Z_{eff}) and low material density. An important advantage of this crystal is its transparency up to 160 nm (7.8 eV), which is remarkable even among other borates. The large band gap ($E_g \sim 9$ eV) of these crystals provide a large transparent window energy range for dopants and hence the luminescent spectra have the signs of atomic or ionic emission spectra of the relevant dopant atoms.

LBO is potential host lattice studied for applications in the thermoluminescence (TL) dosimetry as well. Due to its tissue equivalent effective atomic number an energy independent response has attracted several investigations aimed towards improvements in its sensitivity which involved the use of dopants [1-8]. Lithium borate doped with Mn was the first material to be reported for the TL dosimetry [2]. Due to its low TL sensitivity and an emission in the 600 nm region, far from the good response region of most of photomultipliers, several transition metals and rare-earth elements have been tried as alternative dopants to manganese, in order to produce a blue-emitting phosphor. But initially only silver doped $\text{Li}_2\text{B}_4\text{O}_7$ (emission at 290 nm) resulted in comparable thermoluminescence efficiency [7]. Rare earth doping improves linearity, but not sensitivity [8]. Copper doped LBO as a TL phosphor was suggested for radiation dosimetry by Takenaga et al. [3]. Its TL sensitivity is reported to be 20 times higher than that of $\text{Li}_2\text{B}_4\text{O}_7:\text{Mn}$ produced by Schulman et al. [2]. So far copper doped LBO has been found to be the most successful phosphor. Recently it was reported that co-dopants such as In, Ag and Ag + P help in further enhancing TL sensitivity of the LBO:Cu phosphor, as well as in

making its response to photons nearly tissue equivalent [4,9]. The LBO:Cu phosphor is widely studied for its TL dosimetric properties and also is used (in the form of sintered pellets) in commercially available Panasonic TL dosimeters. Different methods of preparation of this phosphor result in rather different TL characteristics, including TL glow curve, sensitivity, dose linearity, etc. [10–14]. Table 1.2 in Chapter 1 gives a brief review and highlights TL characteristics of $\text{Li}_2\text{B}_4\text{O}_7$ based phosphors prepared using different methods. However, until now in most of the studies TL properties of sintered polycrystalline and glassy phosphor have been reported. In addition, LBO single crystal can also be made suitable for neutron and mixed field dosimetry applications by increasing concentrations of ^{10}B and ^6Li in the $\text{Li}_2\text{B}_4\text{O}_7$ material [15]. Recently luminescence and TL properties of doped LBO single crystals have been reported [16-19].

It is reported that single crystals show higher TL intensity, thermal stability and low hygroscopicity as compared with polycrystalline materials [14, 20, 21]. Shahare et al. [22] also showed that crystalline LBO:Cu has good TL sensitivity compared with glassy LBO. Although doped LBO polycrystalline materials are used in dosimeters and also available commercially but single crystals are more advantageous due to the absence of grain boundaries, which makes them high transparent to visible light and very effective for the collection of emitted light from the inner parts of the sample. Also, the resistance to humidity due to its stoichiometric composition and easy handling compared with powder samples make the LBO single crystal ideal for scintillation and thermoluminescence dosimetry (TLD) applications when doped with an efficient activator.

This prompted us for investigating properties of LBO single crystals. The studies carried out and illustrated in this chapter is on TL of LBO: Cu and OSL characterization of LBO: Cu, Ag

single crystals grown using Czochralski method. These crystals were studied using photoluminescence, X-ray diffraction (XRD), time resolved fluorescence and thermoluminescence (TL) techniques. The TL sensitivity of the grown single crystal is found to be 3.3 times that of a conventional TL phosphor, TLD-100. The $\text{Li}_2\text{B}_4\text{O}_7:\text{Cu}$ crystals showed a linear TL dose response in the range from 1 mGy to 1 kGy. Also, $\text{Li}_2\text{B}_4\text{O}_7:\text{Cu, Ag}$ crystals were characterized and studied using TL, OSL and PL techniques. The computerized glow curve deconvolution (CGCD) reveals nearly first order kinetic for all three TL peaks with trap depths for peaks 1, 2 and 3 being 0.77, 1.25 and 1.34 eV respectively and corresponding frequency factor being 1.6×10^9 , 1.3×10^{13} and $6.8 \times 10^{11} \text{ s}^{-1}$. Continuous wave optically stimulated luminescence (CW-OSL) studies of $\text{Li}_2\text{B}_4\text{O}_7:\text{Cu, Ag}$ is first time studied and reported in the literature. The qualitative correlation between TL peaks and CW-OSL response is established. It was observed that emission between Ag^+ states lies in the excitation region of Cu^+ states and it should increase the overall light yield by an energy transfer mechanism.

6.2. Investigations on LBO:Cu Single Crystals

In this section we investigate single crystals of $\text{Li}_2\text{B}_4\text{O}_7$ doped with Cu (0.5 wt%) grown by the Czochralski method. The as-grown crystals have been investigated for radiation dosimetric applications using transmission, photoluminescence and thermoluminescence measurements. The TL kinetic analysis of the main dosimetric peak in LBO:Cu has been reported to follow a non-first-order kinetics [4, 19, 23]. However, in the present studies, we observed that the as-grown single crystals of LBO:Cu obey first order kinetics. The strong evidence to support this observation is that no shift in the TL peak with dose in a wide dynamic range is observed [24]. Hunda et al. [21] also support first order kinetics for the main dosimetric peak of LBO:Cu

single crystals. The TL sensitivity of the LBO:Cu single crystal has been compared with those of some of the popular TL phosphors like TLD- 100, TLD-500 and TLD-900. A detailed analysis of TL parameters of the as-grown crystals is reported.

6.2.1. Experimental

6.2.1.1. Crystal growth

Single crystals of $\text{Li}_2\text{B}_4\text{O}_7$ and $\text{Li}_2\text{B}_4\text{O}_7:\text{Cu}$ phase were grown using the Czochralski method. An automatic diameter controlled crystal puller (Oxypuller, Cyberstar) was used for the growth. Commercially available $\text{Li}_2\text{B}_4\text{O}_7$ polycrystalline powder material (99.99+% pure, Aldrich make) was used as a starting charge for the growth. For Cu doping, high purity CuO (0.5 wt%) was mixed in the starting $\text{Li}_2\text{B}_4\text{O}_7$ polycrystalline charge. The temperature of the charge contained in a platinum crucible of 40mm diameter was raised to a few degrees above its melting point (917°C) to commence the growth. The application of a pull rate of 0.2 mm/h, a rotation rate of 10 rpm and a high longitudinal thermal gradient of about 100°C/cm enabled the growth of clear core-free transparent crystals, 20mm in diameter and of various lengths. Crystals grown at higher rates showed fogginess. Discs of size 20 mm diameter and 2 mm thickness were cut from the grown crystals and optically polished on both sides for transmission and PL measurements. Crystal sample plates of $3 \times 3 \text{ mm}^2$ were cut from the polished discs for TL studies.

Powder X-ray diffraction (XRD) patterns for the grown crystals were recorded using Cu-K α radiation on a diffractometer (Rigaku, Model Dmax-2200). The optical transmission measurements were carried out in the 200–2500nm range with a 0.1 nm resolution, on a JASCO UV–vis–NIR spectrophotometer (Model V670).

6.2.1.2. Photoluminescence measurement

Photoluminescence studies were performed over the wave-length range 200–600 nm at room temperature by employing an Edinburg fluorescence spectrometer (Model FLP920). The excitation wavelength of 230 nm, at which the xenon lamp intensity maximizes, was selected for the measurements. A xenon flash lamp operating at a repetition rate of 60 Hz was employed for recording the temporal behavior of luminescence decay.

6.2.1.3. Thermoluminescence measurement

All the Cu doped $\text{Li}_2\text{B}_4\text{O}_7$ crystals were given an annealing treatment at 300°C for 30 min. It has been found that these are the optimum conditions to erase the residual TL signal and restore the original TL sensitivity of the TL dosimeters. The LBO:Cu single crystals were studied for their TL response in the absorbed dose range 10–1 kGy. The samples were irradiated using a calibrated $^{90}\text{Sr}/^{90}\text{Y}$ beta source of activity 5mCi. The TL glow curves were recorded for a constant heating rate (4 K/s) using a programmable TL reader [25].

TL emission measurements were also carried out using a high resolution TL emission set-up. The TL emission measurement set-up consists of a TL reader with a compact Sciencetech 9030 monochromator directly mounted on a TL drawer assembly at an optimized focal distance. The TL reader consists of a light tight drawer assembly in which the phosphor sample is placed and heated upto 500°C with different heating profiles using a programmable linear temperature controller. The luminescence emitted is focused on to the input slit of the monochromator kept at 2f focal distance from the lens to optimize light collection as well as focusing of light into the input slit of the monochromator. A photomultiplier tube (Hamamatsu R928) is used to measure the emitted light. The heater temperature is adjusted based on the TL peak and the wavelength resolved TL emission curve is recorded during the thermal stimulation.

6.2.3. Results

The colorless clear transparent LBO crystals (both pure and Cu doped) with no segregated phase were obtained by the Czochralski growth method. A photograph of the grown LBO:Cu crystal ingot and a polished section of the crystal are shown in fig.6.1. The XRD pattern (shown in fig. 6.2) of the LBO:Cu single crystal was found to match with the JCPDS-84-2191 data implying the growth of only the $\text{Li}_2\text{B}_4\text{O}_7$ phase. A UV-vis transmission spectrum is shown in fig.6.3. The LBO:Cu crystals showed absorption around 240 nm and lower cutoff wavelength around 200nm. The absorption at 240 nm is due to the $3d^{10} \rightarrow 3d^9 4s$ absorption transition, while an onset of absorption at 200 nm might be due to the $3d^{10} \rightarrow 3d^9 4p$ transition of Cu^+ centers. Thus doping of Cu^+ ions in the crystal was confirmed by UV-vis transmission. Copper doped LBO crystals showed about 90 % transmission in the range 200-2000 nm indicating a good optical quality of the grown crystals.

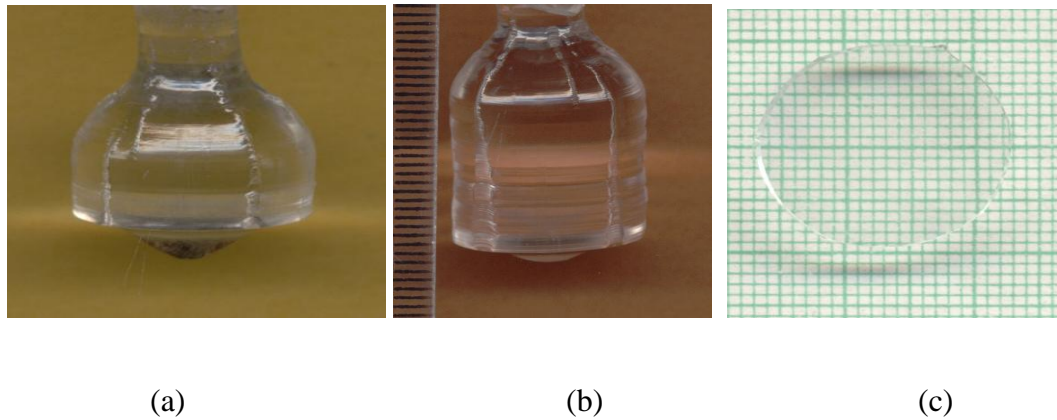


Figure 6.1. Czochralski grown single crystals of (a) LBO:Cu, (b) LBO:Cu,Ag and (c) a polished section.

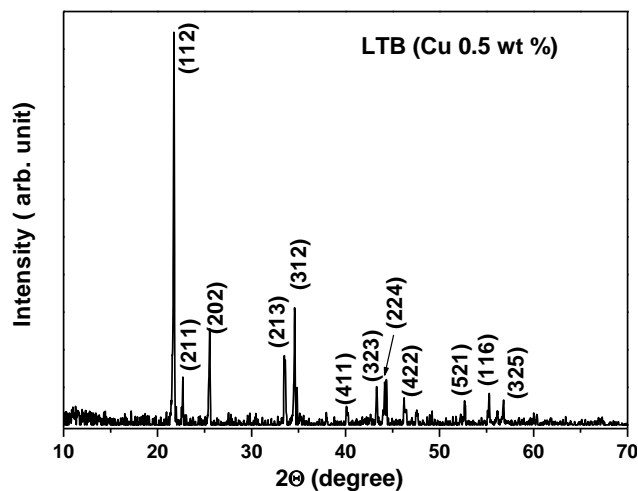


Figure 6.2. The XRD pattern recorded for a powdered sample made using $\text{Li}_2\text{B}_4\text{O}_7:\text{Cu}$ single crystal.

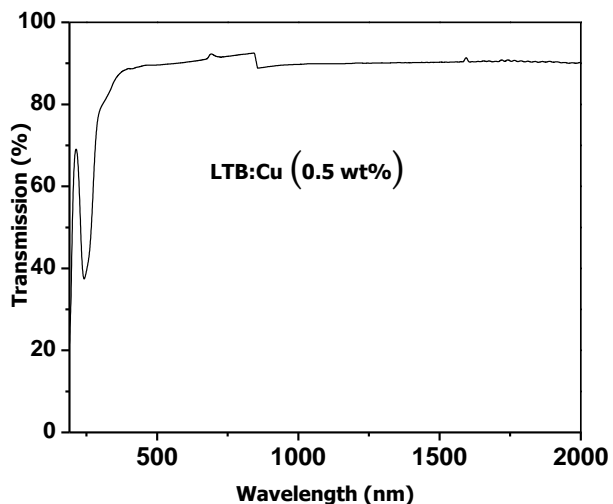


Figure 6.3. Transmission spectrum recorded for a polished plate of a $\text{Li}_2\text{B}_4\text{O}_7:\text{Cu}$ single crystal.

6.2.3.1. PL Studies

Emission and excitation spectra of Cu doped LBO single crystal are shown in fig. 6.4. The presence of an intense emission at 360 nm, which is a characteristic emission of Cu^+ ions suggests the presence of Cu^+ emission centers in the crystal [26,27]. The time resolved fluorescence as shown in fig. 6.5 revealed a single exponential decay of the emission with a decay time of 24.18 μs . The emission peak position and a long decay time permit to ascribe this emission to parity and spin forbidden $3d^9 4s \rightarrow 3d^{10}$ transition from the triplet state of Cu^+ ions. These absorption and emission characteristics indicate the presence of Cu^+ ions as emitting species in the Cu-doped LBO crystals. This is also supported by Cu^+ emission in $\text{NaCl}:\text{Cu}$ single crystal [26] and $\text{LiF}:\text{Mg,Cu,P}$ [27].

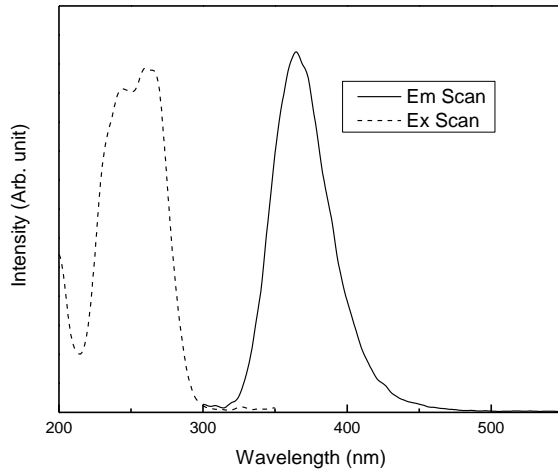


Figure 6.4. Excitation and emission spectra of a Cu-doped LBO crystal.

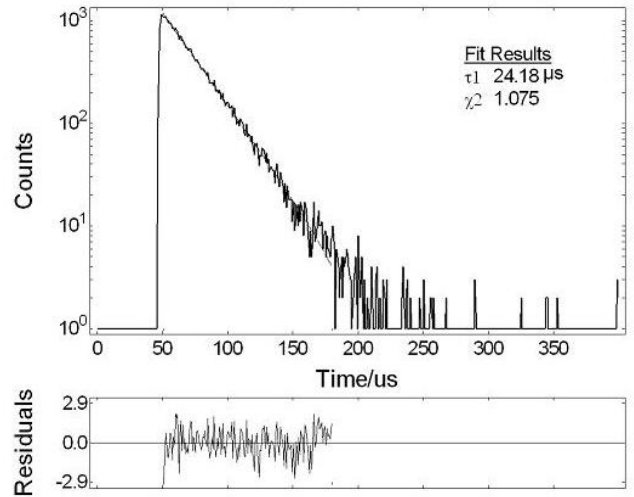


Figure 6.5. Luminescence decay curve and difference between the fitted and measured data of a Cu-doped LBO crystal.

6.2.3.2. TL Analysis

TL Glow curves for various absorbed doses using a $^{90}\text{Sr}/^{90}\text{Y}$ beta source are shown in fig.6.6. These are composed of 2 well defined and well separated TL peaks with a low temperature peak (peak-1) at 402 K and high a temperature peak (peak-2, the main dosimetric peak) at around 513 K. It is observed that the low temperature TL peak fades completely when stored at room temperature in dark for 24h and while peak-2 remains the same. Moreover, these peaks did not shift with a dose in the range 0.1–150 Gy.

6.2.3.2a. TL emission

Fig. 6.7 shows the TL emission spectrum of a $\text{Li}_2\text{B}_4\text{O}_7:\text{Cu}$ single crystal recorded at 483 K. The TL emission band is peaked at 352 nm. This emission is attributed to the Cu^+ emission due to the transition $3d^{10} \rightarrow 3d^9 4s$ [22].

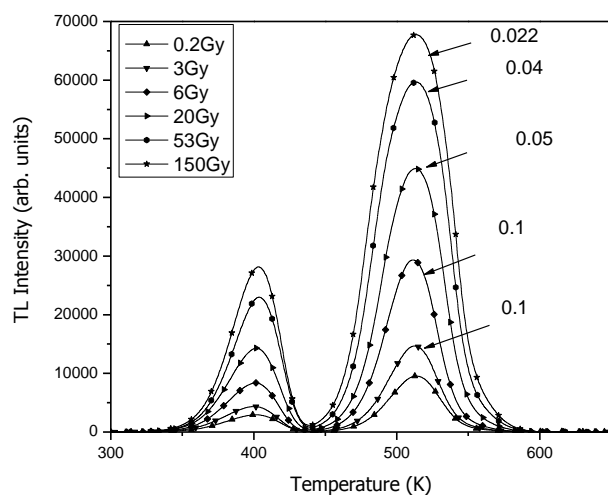


Figure 6.6. TL Glow curves obtained at 4 K/s for various absorbed doses using $^{90}\text{Sr}/^{90}\text{Y}$ beta source. The respective TL curves are multiplied with a factor shown against each glow curve for a direct comparison of the TL peak intensities. The first peak is at 402 K and the second peak at 513 K.

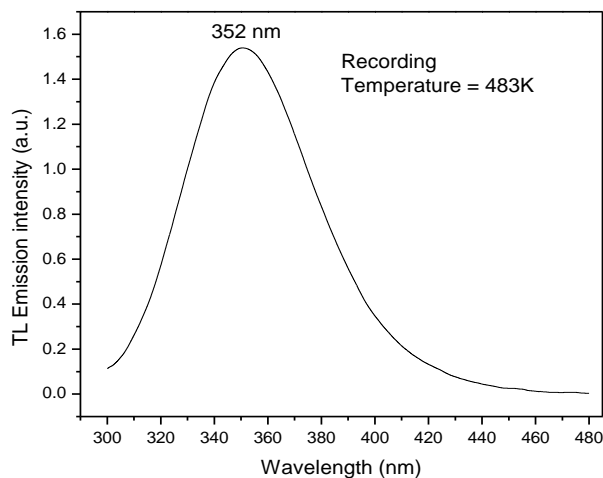


Figure 6.7. TL emission spectrum of a $\text{Li}_2\text{B}_4\text{O}_7:\text{Cu}$ single crystal recorded under isothermal decay condition at 483 K.

6.2.3.2b. TL Kinetic and trap depth Analysis

For kinetic and trap depth analysis TL glow curves were recorded at a heating rate of 1K/s. For this samples were exposed to a low dose (100 mGy) as peak characterization studies are recommended at low doses for the generalized glow peaks [24]. Fig. 6.8a and b shows the normalized TL glow curves for peak-1 and peak-2 of LBO:Cu for the heating rate of 1 K/s. TL peak-2 is obtained by thermal cleaning of peak-1 for its kinetic and trap depth analysis. It is evident from fig.6.6 that there is no shift in low as well as high temperature TL peaks with dose in the range 0.2–150 Gy, suggesting that the as-grown LBO:Cu single crystals obey first order kinetics [24]. On the basis of computer modeling Hunda et al. [21] also mentioned first order

kinetics for the high temperature peak of LBO:Cu at 228°C. Prokic [4] (sintered LBO:Cu, In pellets) and Huy et al. [19] (LBO:Cu single crystals using Bridgeman technique) reported non-first order kinetics for the LBO:Cu phosphors whereas Manam and Sharma [23] (polycrystalline LBO:Cu powder) have reported second order kinetics for the main TL peak at 175°C. Presumably, the method of preparation affects the kinetics in the LBO:Cu system.

To overcome the geometrical reproducibility and the contact problem of the sample with the heating planchett that apparently alters kinetics the method suggested by Chen [28] was followed according to which

$$\mu = \frac{\delta}{\omega} = \frac{T_2 - T_M}{T_2 - T_1} ,$$

Where, T_M is the peak temperature at the maximum; T_1 and T_2 are, respectively, the temperatures on either side of T_M , corresponding to half intensity; $\tau = T_M - T_1$ is the half-width at the low temperature side of the peak; $\delta = T_2 - T_M$ is the half-width toward the fall-off side of the glow peak; $\omega = T_2 - T_1$ is the total half-width; and $\mu = \delta/\omega$ is the so-called geometrical shape or symmetry factor.

Apart from Chen's method the method proposed by Balarin [29], which gives the kinetic order as a function of the parameter $\gamma = \delta/\tau$ was also used to evaluate kinetic order. For peak-1 both the methods predict first order kinetics and for peak-2 Chen's method gives order of kinetic as 1.27 and Balarin's method gives 1.25. Martini et al. [14] reported a value of 1.25 for kinetic order of the 206°C TL peak in the LBO:Cu single crystals. Table 6.1 gives the kinetic analysis of peak-1 and peak-2 using the methods proposed by Chen and Balarin. To determine the energy depth of local trapping levels, two methods, namely Chen's method and variable

heating methods were used. TL glow curves were recorded at heating rates of 1 and 2 K/s and are shown in fig. 6.9(a).

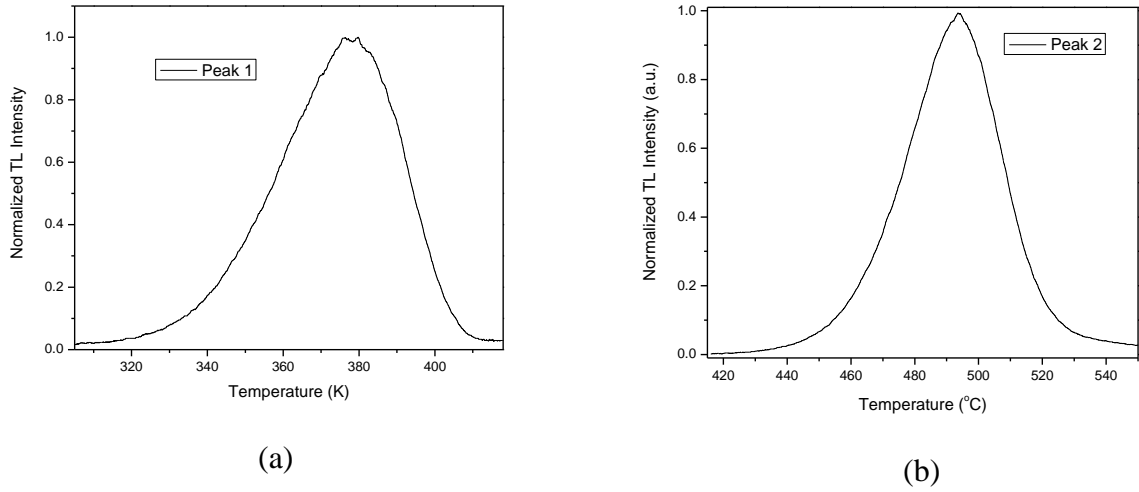


Figure 6.8. Normalized TL glow peaks of LBO: Cu for an absorbed dose of 100mGy recorded at heating rate of 1K/s. (a) Peak 1 is low temperature peak and (b) Peak 2 is high temperature or dosimetric peak.

Table 6.1. Kinetic analysis of TL peaks 1 and 2 shown in Figure 6.8

Peak	T_1 (K)	T_2 (K)	T_M (K)	δ	τ	Chen's Method		Balarin's Method	
						$\mu_g = \frac{T_2 - T_M}{T_2 - T_1}$	Kinetic order (b)	$\gamma = \delta/\tau$	Kinetic order (b)
Peak-1	356.2	394.4	37.1	16.3	21.9	0.426	1	0.744	1
Peak2	475.4	509.2	493.9	15.3	18.5	0.452	1.27	0.827	1.25

(i) Chen's Method

The method derived by Chen [30] was employed for evaluating trap depth 'E'. This method is useful for a broad range of energies ranging between 0.1 eV and 2.0 eV, and for values of the pre-exponential factors between 10^5 s^{-1} and 10^{23} s^{-1} . Furthermore, Chen's method does not

make use of any iterative procedures and does not require knowledge of the kinetic order, which is found by using the symmetry factor μ from the peak shape. The equations can be summed up as

$$E_{\alpha} = c_{\alpha} \left(\frac{kT_M^2}{\alpha} \right) - b_{\alpha} (2kT_M)$$

Where T_M is peak temperature at maxima, k the Boltzmann's constant ($k = 8.617 \times 10^{-5}$ eV/K) and α is τ , δ , or ω . The values of c_{α} and b_{α} are summarized as below:

$$\begin{aligned} c_{\tau} &= 1.510 + 3.0(\mu - 0.42) & b_{\tau} &= 1.58 + 4.2(\mu - 0.42) \\ c_{\delta} &= 0.976 + 7.3(\mu - 0.42) & b_{\delta} &= 0 \\ c_{\omega} &= 2.52 + 10.2(\mu - 0.42) & b_{\omega} &= 1, \end{aligned}$$

With μ being 0.42 for first-order, and 0.52 for second-order TL glow peaks. Using parameters given in Table 6.1, we obtain the value of E in eV for peak-1 as $E_{\tau} = 0.76$, $E_{\delta} = 0.77$, $E_{\omega} = 0.77$, mean value = 0.765 eV. Similarly, the analysis for peak-2 yields $E_{\tau} = 1.68$, $E_{\delta} = 1.67$, $E_{\omega} = 1.69$, giving the mean value of the activation energy as 1.69 eV.

(ii) Variable Heating rate method for evaluation of Trap depth and Frequency factor

Assuming first order kinetics as described above, the TL parameters were determined using a variable heating rate method on single crystals of LBO:Cu. Expression for trap depths E is,

$$E = k \frac{T_{m1}T_{m2}}{T_{m1} - T_{m2}} \ln \left[\frac{\beta_1 \left(\frac{T_{m2}}{T_{m1}} \right)^2}{\beta_2} \right] \quad (6.1)$$

where β_1 and β_2 are heating rates (in K/s) corresponding to the peak temperatures T_{m1} and T_{m2} (in K) respectively. For evaluating frequency factor S , from condition of TL maxima we obtain

$$S = \frac{\beta E}{kT_m^2} \exp \left(\frac{E}{kT_m} \right) \quad (6.2)$$

The mean-life τ (in s) of TL traps for peak 1 and peak 2 at a given temperature T is given by,

$$\tau = S^{-1} \exp\left(\frac{E}{kT}\right) \quad (6.3)$$

The TL parameters of the LBO:Cu single crystals are shown in Table 6.2. The activation energies determined using this method are found to be 0.81 eV and 1.70 eV for peaks-1 and peak-2, respectively which are in good agreement with the values evaluated using Chen's method.

Table 6.2. TL parameters for LBO: Cu using the variable heating rate method.

Heating rate β (K/s)	Peak 1 (K)	Peak 2 (K)	Trap Depth E (eV)		Frequency factor S (s ⁻¹)		Mean life τ (s)
			Peak 1	Peak 2	Peak 1	Peak 2	
1.0	377.2±0.3	493.8±0.3	0.81±0.05	1.70±0.07	5.2×10 ⁹	1.7×10 ¹⁶	9.5 ×10 ³
2.0	387.1±0.3	502.1±0.3					1.9×10 ¹²

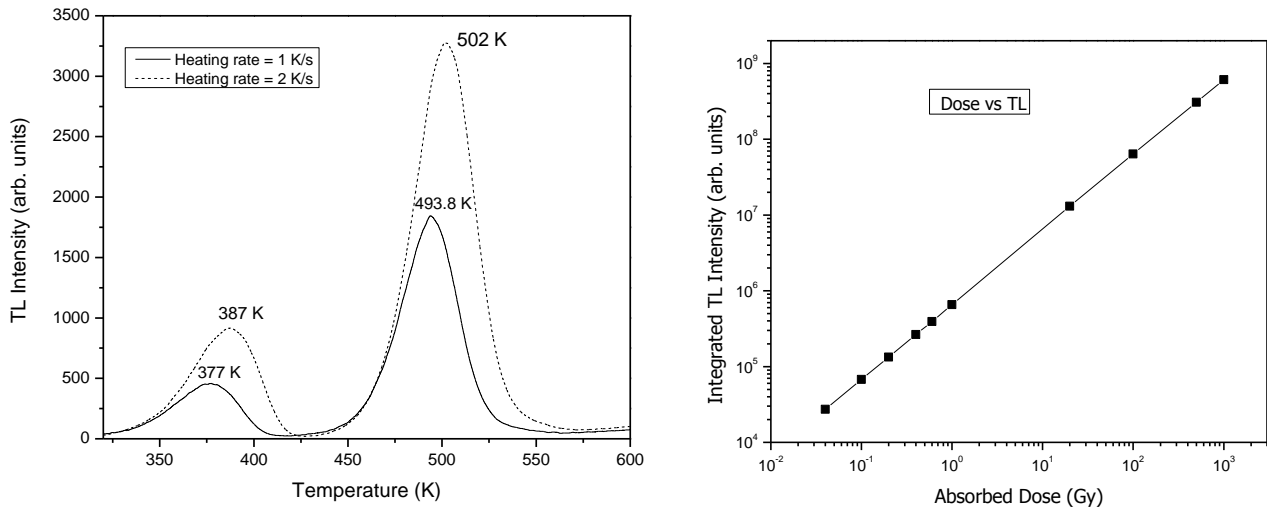


Figure 6.9. a) TL glow curves of LBO:Cu at different heating rates for an absorbed dose of 100 mGy. b) Dose vs. TL response of the high temperature TL peak (Peak 2) of LBO: Cu single crystals.

6.2.3.3. Dose response and Minimum Detectable Dose (MDD)

The dose vs. TL response of LBO:Cu single crystals is shown in fig. 6.9(b). It is found to be linear in the dose range of 1 mGy to 10^3 Gy. The minimum detectable dose (MDD) in LBO:Cu is estimated to be about 100 μ Gy. Martini et al. [14] reported a linear dose-response in the dose range of 2×10^{-4} to 20 Gy. It is also reported that the TL sensitivity of LBO:Cu crystals is higher than the powder. Furetta et al. [1] estimated the MDD to be 20 μ Gy for the sintered pellets. During experimental determination of MDD, a combination of high TL sensitivity of the related dosimeter material, and the type of TLD reader used, are the essential factors. According to the observations of Srivastava and Supe [20], doping with Cu induces linear dose response behavior in various TL materials, up to 10^3 Gy. TL sensitivity of the LBO:Cu single crystals has been compared with those of some of the popular TL phosphors like TLD-100, TLD-500 and TLD-900. For this standard materials were taken in the form of single crystal except TLD 900 (which was in the powder form). Table 6.3 gives sensitivity comparison of as grown LBO: Cu single crystals with various commercially available TL phosphors. Here, entire area under the TL glow curve is taken into consideration.

Table 6.3. Sensitivity comparison of LBO:Cu with other commercially available TL phosphors.

TL material	Sensitivity
LBO: Cu	3.3
Undoped LBO	< 0.3
TLD 500	52
TLD 100	1
CaSO ₄ : Dy	34
LBO: Cu, In	5.9

6.2.3.4. Effect of co-doping Indium in LBO: Cu Single crystals

The doping of Cu (0.25 wt.%) and Indium (0.25 wt.%) in LBO is found to enhance the TL sensitivity of LBO: Cu,In by a factor of 1.8 when compared to LBO:Cu as evident from Fig. 6.10. The TL glow curve for LBO: Cu,In single crystals has TL peaks at 135, 182 and 235°C and that for LBO: Cu is at 130 and 235°C. The trap depths for 135 and 235°C TL peak in LBO:Cu, In are found to be similar to the corresponding peaks for LBO: Cu and is attributed to the presence of copper ions in the single crystals of LBO. The low temperature peak in both LBO:Cu and LBO: Cu,In is found to fade completely within 24 hours. The high temperature TL peaks in LBO:Cu and LBO:Cu,In are found to be very stable and exhibits negligible fading when stored at room temperature for a period of one month.

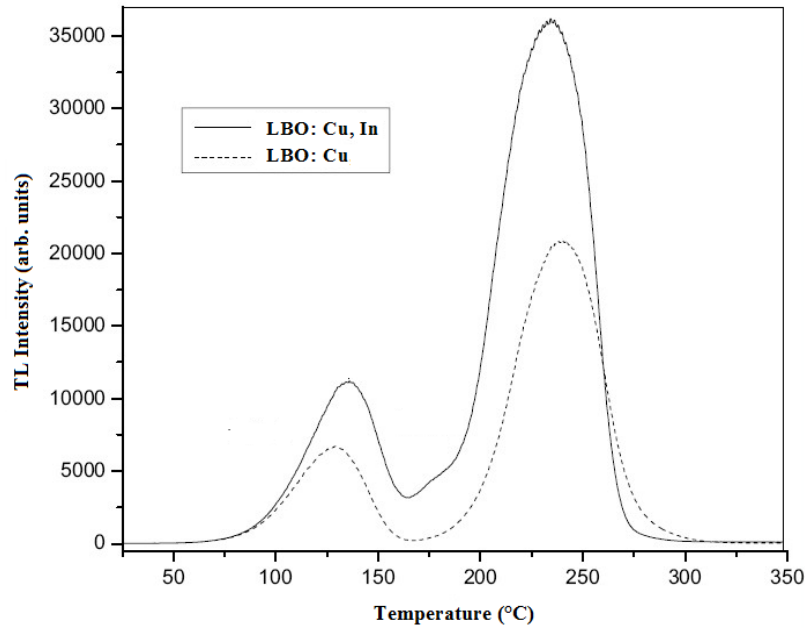


Figure 6.10: TL glow curve for LBO: Cu and LBO: Cu, In recorded at a heating rate of 3.5 K/s for an absorbed dose of 1Gy (from $^{90}\text{Sr}/^{90}\text{Y}$ beta source)

6.2.4. Conclusion

Highly transparent and clear single crystals of the $\text{Li}_2\text{B}_4\text{O}_7:\text{Cu}$ have been grown using Czochralski method. A UV–vis transmission spectrum confirms the doping of Cu^+ ions in the crystal. Intense emission at 360 nm and single exponential decay (24.18 μs) strongly point to one type of Cu^+ ions as the emitting species. The TL emission in LBO:Cu is also due to the energy levels of Cu^+ state. Its TL sensitivity was found to be 0.33 and 0.06 times that of TLD-100 and TLD-500 respectively. Doping with Cu enhances TL sensitivity and linear dose-response in the material. The material is found to have linear dose-response in the range of 1 mGy to 1 kGy. The LBO:Cu (0.5 wt.%) crystal has a main dosimetric TL peak at about 513 K and a low temperature TL peak at about 402 K for a heating rate of 4 K/s. Low temperature TL peak fades completely when stored at room temperature in dark for 24 hrs. Moreover, these peaks did not shift with a dose in the range from 0.1 Gy to 150 Gy. It is therefore concluded that the TL peaks obey first order kinetics. However, using Chen's method and Balarin's method the order of kinetics was found to be 1 and 1.25 for low and high temperature peaks respectively. The activation energy of low and high temperature peaks, using variable heating rate method is evaluated to be 0.82 eV and 1.7 eV respectively. The results of Chen's method is in very good agreement with trap depths evaluated using variable heating rate method assuming the first order kinetic. Co-doping of indium with copper in LBO enhances its TL sensitivity by 1.8 to that of LBO: Cu. The LBO:Cu and LBO: Cu, In phosphors have potential for their use in various radiation dosimetric applications, particularly in the medical dosimetry due to its tissue equivalence.

6.3. Investigations on LBO:Cu, Ag single crystals

Although doped LBO has been found to be very useful TL material its OSL properties have not been reported for radiation dosimetry applications so far. The $\text{Li}_2\text{B}_4\text{O}_7:\text{Cu}$ is reported to be sensitive to light. The direct sunlight causes considerable fading of TL signal in LBO: Cu material [3, 31]. It is reported that Cu-doped LBO has the most intense emission for UV excitation [32]. This disadvantage of fading of TL signal in sunlight could be exploited as an advantage to use doped LBO for radiation dosimetry using optically stimulated luminescence (OSL) technique. The OSL readout technique offers major advantage of avoidance of thermal quenching associated with TL phosphors apart from numerous other advantages [33] which are very important from dosimetry point of view. However, no significant OSL signal could be recorded on the LBO:Cu single crystals grown by Czochralski technique [34] using 470 nm blue light stimulation. However, the doubly doped LBO single crystals with Cu and Ag did show considerable OSL signal for blue light stimulation as compared to its TL signal. The sections to follow discuss the OSL and TL properties of the grown single crystal LBO doped with 0.5 wt % Cu and Ag using Czochralski technique.

6.3.1. *Experimental*

a) Crystal Growth

Single crystals of $\text{Li}_2\text{B}_4\text{O}_7$ doubly doped with Cu and Ag were grown by the Czochralski method. Commercially available $\text{Li}_2\text{B}_4\text{O}_7$ polycrystalline powder material (99.99+ % pure, Aldrich make) was used as a starting charge for the growth. For doping, high purity CuO and Ag_2O (0.25 wt % each) were mixed in the starting $\text{Li}_2\text{B}_4\text{O}_7$ polycrystalline charge for the preparation and growth of LBO: Cu, Ag single crystal. Other growth conditions and parameters are similar to the one described in section 6.2.1.1 of this chapter.

b) PL Measurements

For optical measurements, grown crystals were cut perpendicular to the growth direction and polished to a mirror finish. Description of measurement set up is in section 6.2.1.2

c) TL and OSL measurements

The $\text{Li}_2\text{B}_4\text{O}_7:\text{Cu,Ag}$ crystals were given an annealing treatment at 300°C for 30 min. to erase the residual signal and restore the original TL sensitivity of the material. The samples were irradiated using a calibrated $^{90}\text{Sr}/^{90}\text{Y}$ beta source for taking TL and OSL measurements. The TL glow curves were recorded using a programmable TL reader [25] and the CW-OSL measurements were recorded using the in-house OSL reader system [35]. The description of optical excitation unit for the purpose of OSL measurements is mentioned elsewhere in section 4.2.2 of chapter 4.

6.3.2. Results

6.3.2.1. Photo-luminescence studies

Photographs of the grown – pure and Cu and Ag doped single crystals of LBO are shown in fig.6.1. The PL studies on the clear and transparent LBO:Cu, Ag crystals were carried out using UV-VIS transmission spectrum as shown in fig. 6.11. Emission band having a peak at 370 nm and excitation band with a maximum at about 250 nm were ascribed to parity and spin-forbidden $3d^9 4s \leftrightarrow 3d^{10}$ transitions from the triplet state of Cu^+ due to a large Stokes shift of $\sim 10,000 \text{ cm}^{-1}$ and a long decay time of $\sim 24 \mu\text{s}$. The crystal doped with Ag has shown an emission band around 267 nm and excitation band around 210 nm having a decay time of 10 μs . The nature of the luminescence in this region is due to $4d^9 5s \leftrightarrow 4d^{10}$ transition of Ag^+ ion. The emission band of Ag^+ overlaps with the excitation region of Cu^+ states as shown in fig. 6.11c. Hence, in case of co-doping of Ag^+ in LBO: Cu, the emission at 370 nm (due to Cu^+)

dominates over transitions in Ag^+ due to energy transfer from Ag^+ ion to Cu^+ ion. The role of Ag as sensitizer and Cu as activator in LBO:Cu, Ag has also been explained by Patra et. al. [36]. The co doping of Ag in LBO: Cu results in increase in overall emission.

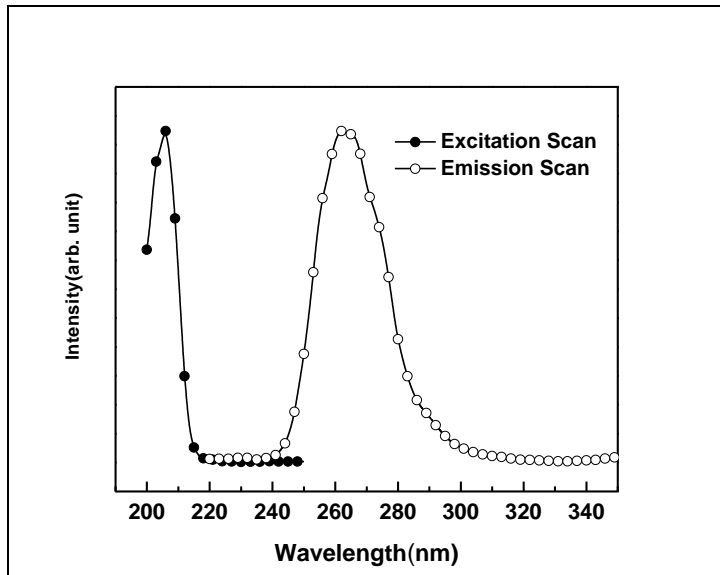


Figure 6.11a. Excitation and emission spectra for Ag in LBO:Cu,Ag

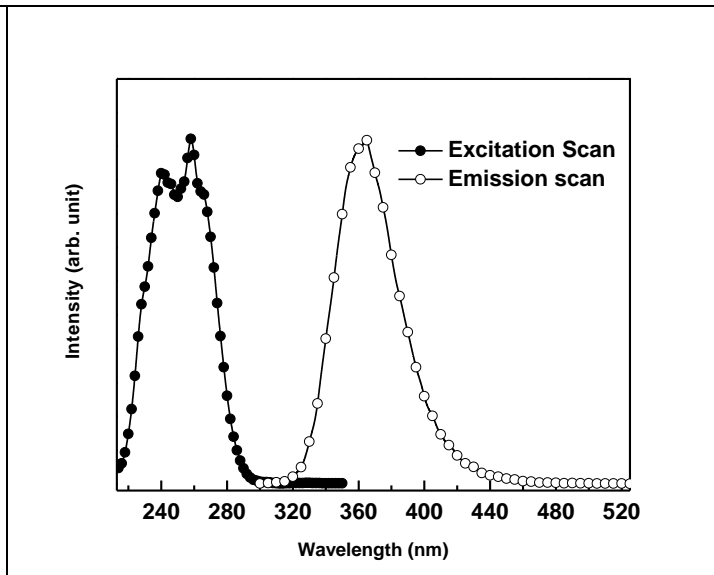


Figure 6.11b. Excitation and emission spectra for Cu in LBO:Cu,Ag

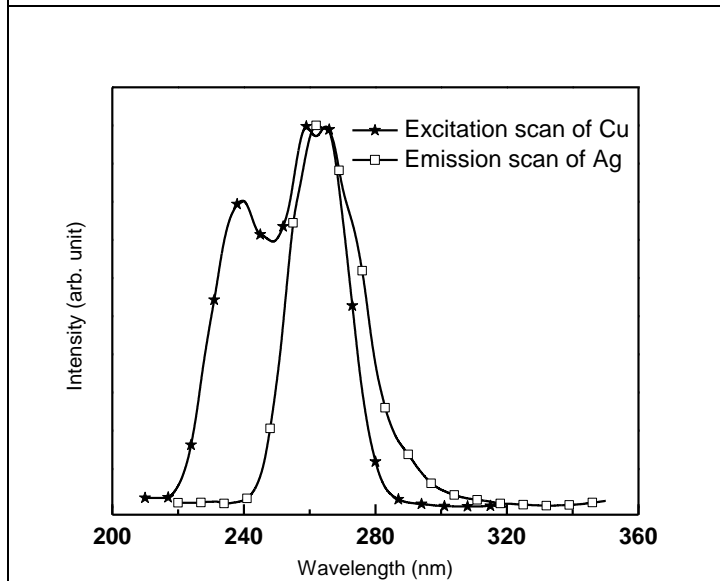


Figure 6.11c. Excitation spectrum for Cu and emission spectrum for Ag in LBO:Cu,Ag

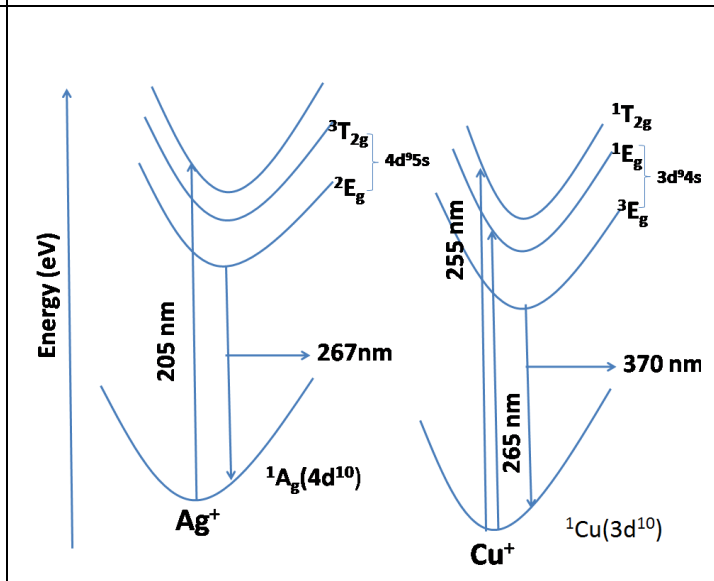


Figure 6.11d. Electronic levels and suggested transitions in LBO:Cu,Ag crystals

6.3.2.2. TL Analysis

a) TL analysis-CCD Analysis

Fig. 6.12 shows the TL recorded on the $\text{Li}_2\text{B}_4\text{O}_7\text{:Cu, Ag}$ crystals for a 300 mGy $^{90}\text{Sr}/^{90}\text{Y}$ beta dose for 1 K/s heating rate. Three glow peaks at $\sim 375, 441$ and 516 K are observed in the $\text{Li}_2\text{B}_4\text{O}_7\text{:Cu, Ag}$ single crystals. For kinetic analysis the experimentally obtained TL glow curve was fitted with Computerized Curve Deconvolution (CCD) procedure (fig. 6.12).

The TL glow-curve was deconvoluted using the following general-order kinetic equation as formulated by Kitis [37]

$$I(T) = I_m b^{b/(b-1)} \exp\left(\frac{E}{kT} \frac{T-T_m}{T_m}\right) \left[Z_m + (b-1)(1-\Delta) \left(\frac{T}{T_m}\right)^2 \exp\left(\frac{E}{kT} \frac{T-T_m}{T_m}\right) \right]^{b/(1-b)}$$

Where $Z_m = 1 + (b-1) \Delta_m$, $\Delta = 2kT/E$ and $\Delta_m = 2kT_m/E$, E (eV) is the activation energy; I_m and T_m are the peak maximum intensity and temperature, respectively; b is the kinetic order and k (eV/K) is the Boltzmann constant.

The frequency factor, S is estimated using the condition of maximum for a general order TL peak given by

$$\frac{\beta E}{kT_m^2} = S \exp\left(-\frac{E}{kT_m}\right) \left[1 + (b-1) \left(\frac{2kT_m}{E}\right) \right]$$

Here heating rate is 1.03 K/s. The kinetic parameters for all the three peaks in LBO: Cu, Ag is shown in Table 6.4.

Table 6.4. Kinetic analysis of TL Peaks 1, 2 and 3 for LBO: Cu, Ag

Peak	Peak Temperature, T_m (K)	Trap Depth, E (eV)	Frequency factor, S (s^{-1})	Kinetic order (b)	Mean life (s) $\tau = S^{-1} \exp(E/kT)$
Peak 1	375.2	0.77	1.6×10^9	1.07	6.13×10^3
Peak 2	440.8	1.25	1.3×10^{13}	1.09	6.39×10^7
Peak 3	515.7	1.34	6.8×10^{11}	1.07	4.08×10^{10}

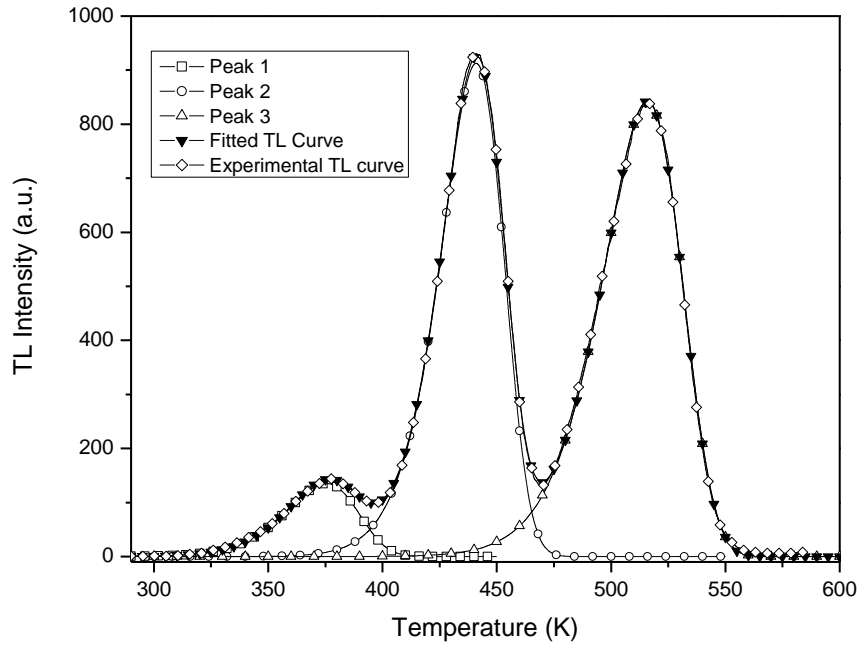


Figure 6.12. TL glow curve of LBO: Cu, Ag obtained at a heating rate of 1 K/s, analyzed into its three individual glow peaks deconvoluted using Computerized Curve Deconvolution (CCD) procedure for general order kinetics.

b) TL Kinetic Analysis of Peak 3

Further analysis of most stable TL glow peak (i.e. TL peak 3 at ~ 516 K) was carried out using the method proposed by Chen and Balarin [28,29].

To overcome the geometrical reproducibility and the contact problem of the sample with the heating planchet that apparently alters the results on the order of kinetics, the method suggested by Chen [20] was followed according to which

$$\mu = \frac{\delta}{\omega} = \frac{T_2 - T_M}{T_2 - T_1} ,$$

Where, T_M is the peak temperature at the maximum; T_1 and T_2 are, respectively, the temperatures on either side of T_M , corresponding to half intensity; $\tau = T_M - T_1$ is the half-width at the low temperature side of the peak; $\delta = T_2 - T_M$ is the half-width toward the fall-off side of the glow peak; $\omega = T_2 - T_1$ is the total half-width; $\mu = \delta/\omega$ is the so-called geometrical shape or symmetry factor.

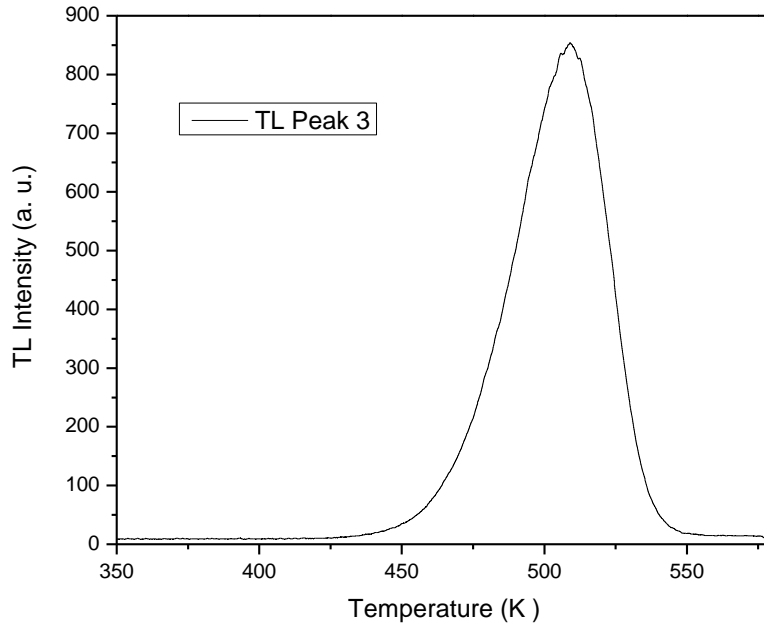


Figure 6.13. Experimentally obtained TL peak 3 for LBO:Cu, Ag for an absorbed dose of 300 mGy recorded at a heating rate of 1 K/s

Apart from Chen's method the method proposed by Balarin [29] which gives the kinetic order as a function of the parameter $\gamma = \delta/\tau$ was also used to evaluate kinetic order. Fig. 6.13 gives experimentally obtained TL glow peak 3 for LBO: Cu, Ag. The TL peak 3 is obtained by thermal cleaning of peak 1 and 2. For the purpose of thermal cleaning the phosphor is exposed to low absorbed dose i.e. 300 mGy as peak characterization studies are recommended at low doses for the generalized glow peaks [24]. Thereafter, the phosphor is heated linearly at a rate of 1 K/s from room temperature to a temperature where maxima of TL peak 2 occurs i.e. 441 K and then the temperature was clamped for about 30s. This ensures cleaning of TL peaks 1 and 2. Now the TL is recorded employing the same heating rate of 1K/s to obtain clean TL peak 3. Table 6.5 gives the kinetic analysis of thus obtained peak 3 using the methods proposed by Chen and Balarin. TL peak 3 obeys first order kinetics.

Table 6.5. Kinetic analysis of Peak 3 shown in fig. 6.13.

Peak	E(eV)	T ₁ (K)	T ₂ (K)	T _M (K)	δ	τ	Chen's Method		Balarin's Method	
							$\mu_g = \frac{T_2 - T_M}{T_2 - T_1}$	Kinetic order (b)	$\gamma = \delta/\tau$	Kinetic order (b)
3	1.34	486.5	527.9	509	18.9	22.5	0.45	1	0.84	1

c) Trap depth analysis of Peak 3

The method proposed by Chen [30] was used for the evaluation of trap depth 'E' of peak-3. The advantage of using this method is that it is applicable for a broad range of energy and frequency factor ranging between 0.1 eV to 2.0 eV, and 10^5 s^{-1} to 10^{23} s^{-1} respectively. Further Chen's method is independent of the kinetic order of a TL peak. The Chen's equation δ , τ or ω for evaluating trap depth is summarized as,

$$E_{\alpha} = c_{\alpha} \left(\frac{kT_M^2}{\alpha} \right) - b_{\alpha} (2kT_M)$$

where, α is δ , τ or ω . The values of c_{α} and b_{α} are summarized as below:

$$c_{\tau} = 1.510 + 3.0(\mu - 0.42) \qquad b_{\tau} = 1.58 + 4.2(\mu - 0.42)$$

$$c_{\delta} = 0.976 + 7.3(\mu - 0.42) \qquad b_{\delta} = 0$$

$$c_{\omega} = 2.52 + 10.2 (\mu - 0.42) \qquad b_{\omega} = 1,$$

with $\mu = 0.42$ for the case of first-order TL glow peaks, and $\mu = 0.52$ for the case of second order peaks.

Using parameters given in Table 6.5, we obtain the value of E for Peak 3 as

$$E_{\tau} = 1.33, E_{\delta} = 1.29, E_{\omega} = 1.33$$

Since Peak 3 obeys nearly first order kinetic thus the condition of maxima can be used for evaluation of frequency factor as below

$$\frac{\beta E}{kT_M^2} = S \exp\left(-\frac{E}{kT}\right)$$

Which gives frequency factor $S = 4.58 \times 10^{11} \text{ s}^{-1}$

6.3.2.3. OSL Studies

6.3.2.3a. CW-OSL of LBO: Cu, Ag and qualitative correlation with TL peaks

The CW-OSL measurements of single crystals of LBO: Cu, Ag were carried out using blue LED stimulation ($\lambda \approx 470 \text{ nm}$, $\Delta\lambda \approx 20 \text{ nm}$) and power $\sim 50 \text{ mW/cm}^2$. Fig. 6.14 shows CW-OSL intensity curves for an absorbed dose of 1.38 Gy from $\text{Sr}^{90}/\text{Y}^{90}$ beta source. The decay curves (a), (b) and (c) in fig. 6.14 correspond to the CW-OSL signal from TL peaks 1, 2, 3 (all three peaks contributing); 2, 3 (Peak 1 annealed); and 3 (Peaks 1 and 2 annealed) respectively. For obtaining curves (b) and (c) in fig. 6.14, the crystal was delivered an absorbed dose of 1.38 Gy each time and were given thermal annealing treatment independently up to 378 K, 440 K at a

heating rate of 1 K/s and subsequently CW-OSL measurements were carried out for 200s. All the curves are fitted with third order exponential fit. Thus, OSL curves (a), (b) and (c) in fig. 6.14 could be fitted with three photo-ionization cross sections using the equation:

$$I_{OSL} = I_1 e^{-\sigma_1 \phi t} + I_2 e^{-\sigma_2 \phi t} + I_3 e^{-\sigma_3 \phi t} \quad (2)$$

Where Φ is stimulating photon intensity (photons/cm²/s) and I_1, I_2 and I_3 are the initial intensities of exponentially decaying components with photo-ionization cross sections σ_1, σ_2 and σ_3 respectively.

Table 6.6 gives fitted parameters for CW-OSL curves (a), (b) and (c).

The ratio of area under the CW-OSL curves (a), (b) and (c) in fig. 6.14 is 1: 0.75: 0.60

Fig. 6.15 (a) and (b) gives absolute and normalized CW-OSL curves (normalized w.r.t. maxima of corresponding CWOSL curve). The curves follow varying decay patterns which may be attributed to the interference of shallow traps (TL traps corresponding to TL peaks 1 and 2) as the occupancy index of traps is different for the three cases.

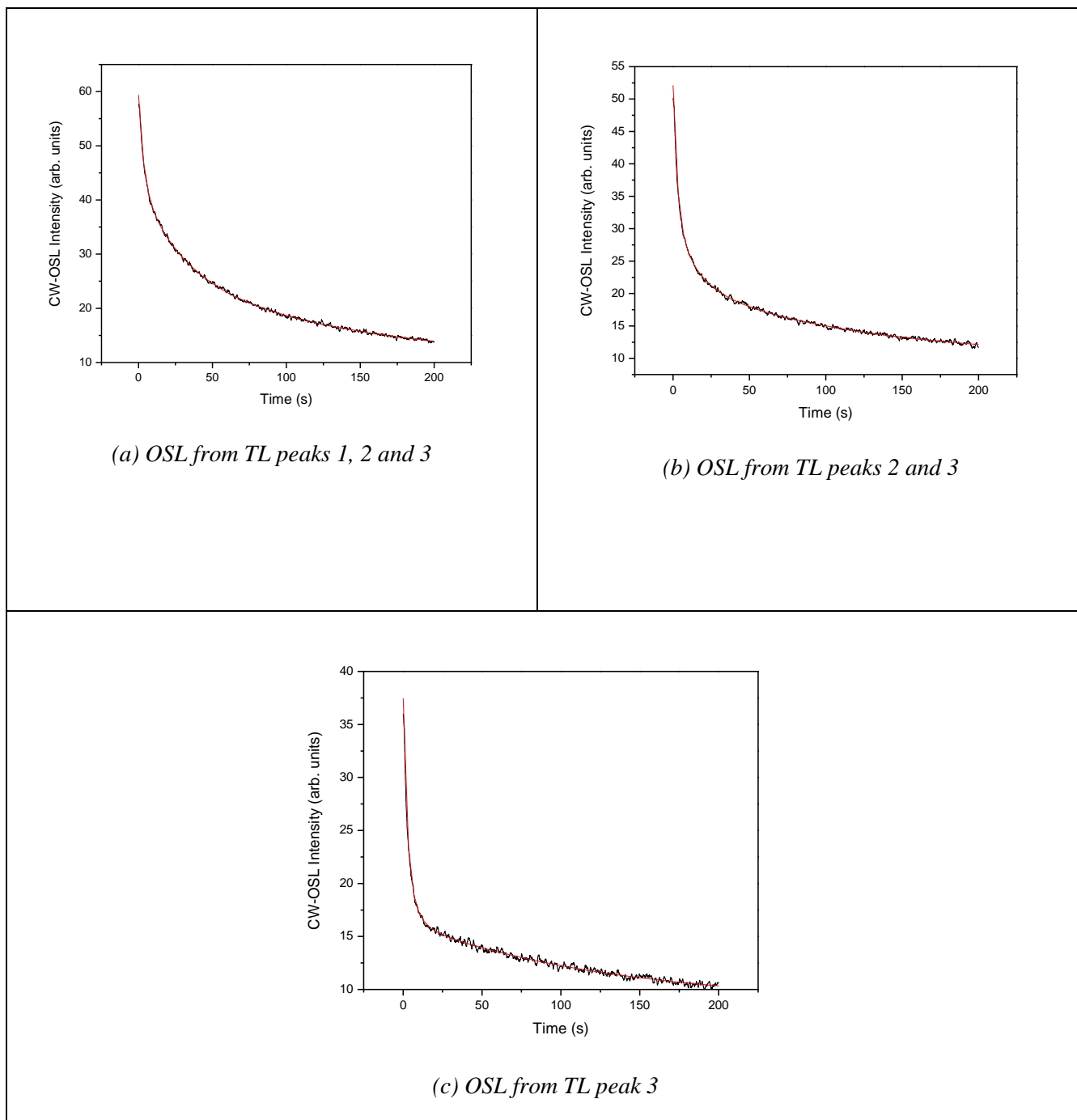


Figure 6.14. CW-OSL curves of LBO: Cu, Ag for an absorbed dose of 1.38 Gy from Sr^{90}/Y^{90} beta source for different cases. All the three are fitted with third order exponential decay.

Table 6.6. CW-OSL parameters of LBO: Cu, Ag for different cases (refer Figure 6.14)

Different cases	Nature of CW-OSL curve	Photo-ionization cross section (cm ²)		
		σ_1	σ_2	σ_3
CW-OSL from TL peaks 1, 2 & 3	3 rd order exponential decay	2.5×10^{-18}	3×10^{-19}	5.9×10^{-20}
CW-OSL from TL peaks 1 & 2	3 rd order exponential decay	3×10^{-18}	6.1×10^{-19}	7.4×10^{-20}
CW-OSL from TL peak 3	3 rd order exponential decay	3.4×10^{-18}	1.3×10^{-18}	6.6×10^{-20}

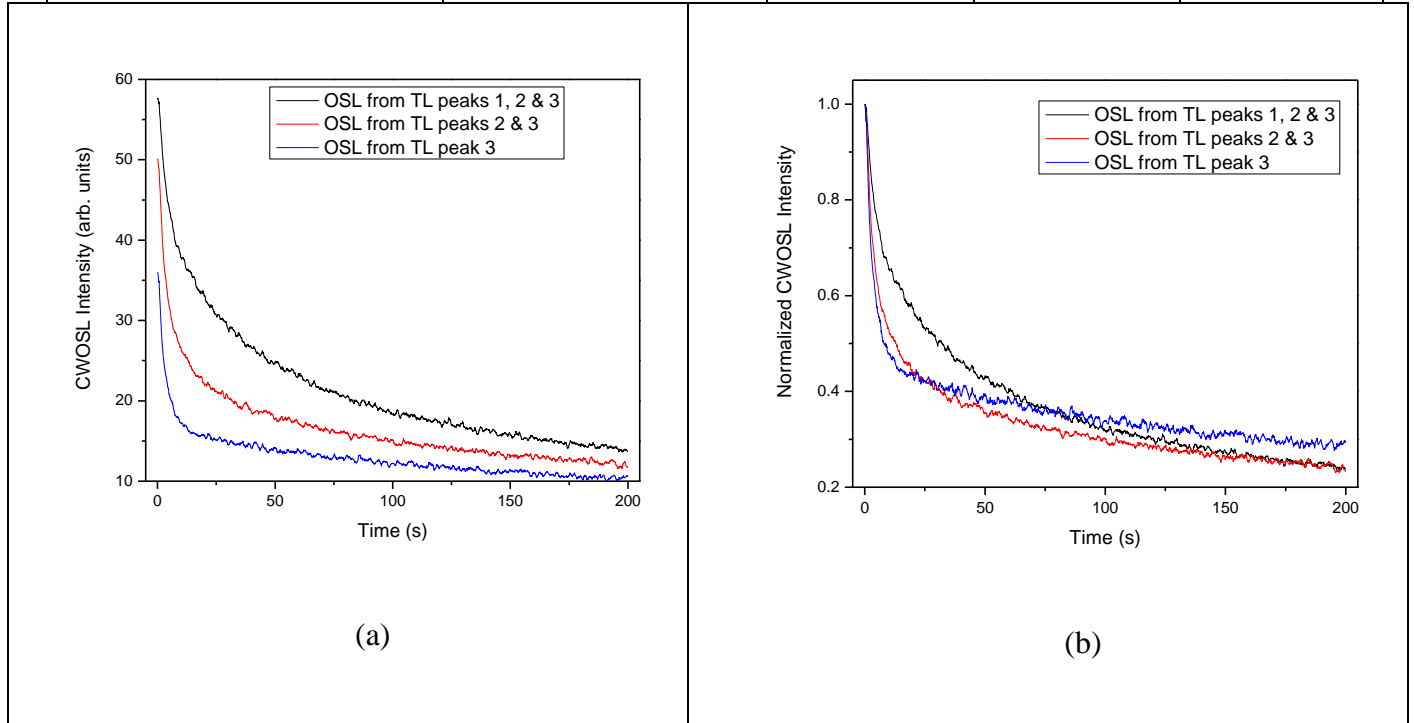


Figure 6.15. CW-OSL curves for different cases (a) Absolute scale and (b) Normalized w.r.t. maxima of corresponding curve

6.3.2.3b. Analysis of faster component of CW- OSL signal

The dosimetric signal of interest is the faster component of OSL signal, i.e. the signal that can be extracted in minimum time on stimulation with light of appropriate frequency. This signal in case of LBO:Cu, Ag is the one that corresponds to cross-section σ_1 in Table 6.6 which is of the

order $\sim 10^{-18} \text{ cm}^2$. From the normalized CW-OSL curves in fig. 6.15b it is evident that the steepest of the three curves is the one in which TL peaks 1 and 2 are annealed i.e. the CW-OSL curve due to TL peak 3 alone. This suggests that TL peak 3 is responsible for fast component of OSL signal. As far as stability of this component is concerned it is expected to be most stable owing to the fact that its origin is TL peak 3 which itself is very stable and doesn't show any fading. Moreover, the contribution of this fast component is about 60% of total OSL area which is considerable and lowest detectable limit based on this fast component is $\sim 16 \text{ mSv}$.

6.3.2.3c. Optimization of CW-OSL stimulation time

The photoionization cross-section for LBO: Cu, Ag is found to be relatively smaller than other OSL grade phosphors like Al_2O_3 : C. Thus it requires high stimulation power and takes longer time to depopulate the OSL traps substantially. Thus there is a need to optimize the stimulation time the duration for which CW-OSL measurements should be carried out for a given stimulation power. This optimization of duration for which CW-OSL stimulation should be performed was conducted by studying the integrated CW-OSL signal as a function of stimulation time in the range varying from 100 to 2000 seconds, using blue LED stimulation peaked at 470nm and power at sample position being 70 mW/cm^2 . After each OSL measurement, the residual TL signal was measured for LBO:Cu, Ag single crystals by performing readout up to 600 K with 1 K/s. Fig. 6.16 shows the integrated OSL signal as a function of illumination time, as well as integrated Residual TL (R-TL), which originates from all the three TL peaks after CW-OSL readout for varying time. It is obvious the OSL signal increases with the illumination time, approaching a saturation level after 2000 s of stimulation. The corresponding residual TL signal exhibits a decreasing pattern as the stimulation (bleaching) time increases. The optimized OSL readout time can be considered as 400 s.

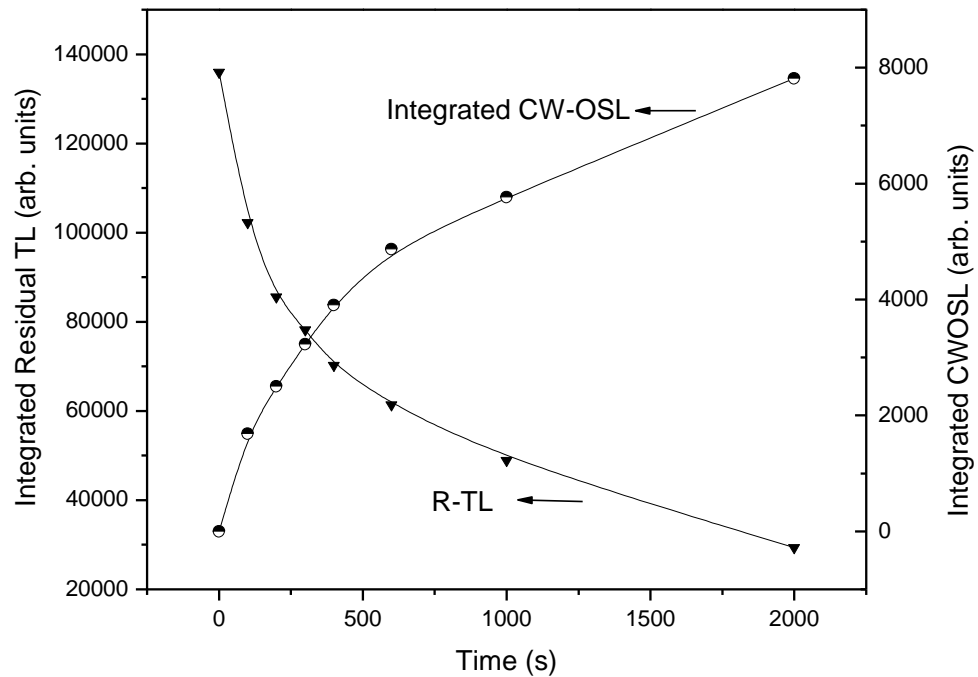


Figure 6.16. Integrated CW-OSL signal for various illumination times and the subsequent residual TL(R-TL) signal (obtained after CW-OSL readout) by readout up to 320 °C with 1 °C/s, as a function of illumination time.

6.3.2.4. OSL readout time versus Residual TL

From figures 6.16 and 6.17, it is evident that residual TL signal diminishes with OSL readout time. Bleaching of three TL peaks takes place (fig. 6.17) due to stimulation with blue (470 nm) light. However, the extent of participation of all the three different types of traps corresponding to three TL peaks is different, as peak 1 and peak 2 are reduced significantly but the TL peak 3 still remains and is not diminished significantly. This may be attributed due to the interference of TL peaks 1 and 2 that traps the charge carriers de-trapped from TL peak 3 while optical stimulation. Its area after bleaching of 2000 s at 70 mW/cm² is around 30% of its initial unbleached area.

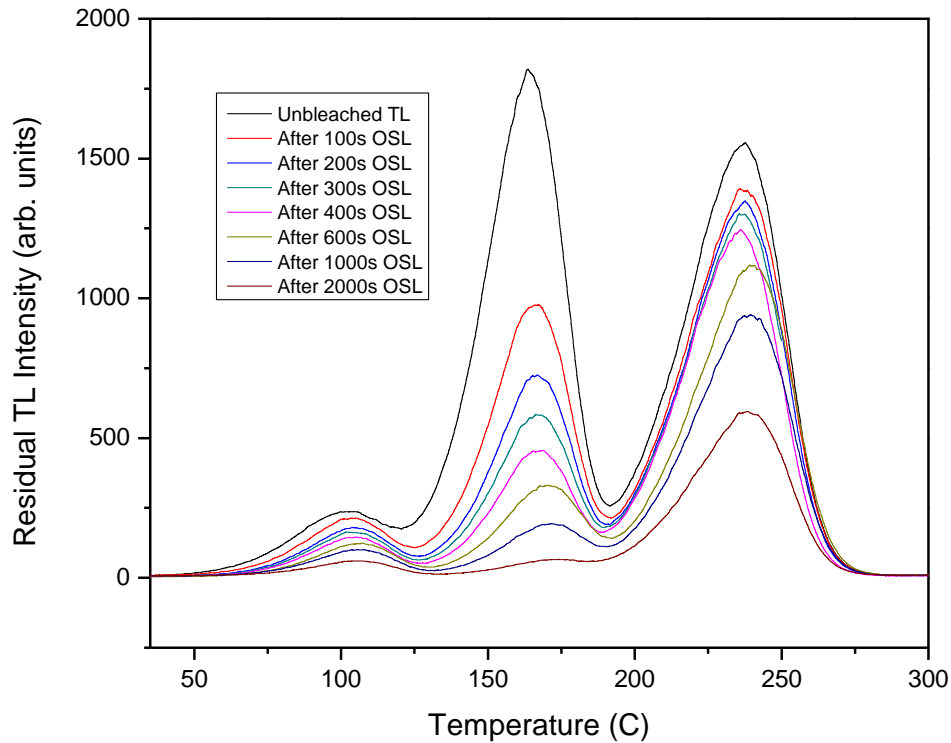


Figure 6.17. Residual TL glow curves obtained after blue light stimulation ranging from 0 to 2000 s.

6.3.2.5. Minimum Detectable Dose (MDD)

The MDD of LBO: Cu, Ag for an absorbed dose of 1.38 Gy in CW-OSL (integrated for a period of 2000 s at 70 mW/cm²) domain is found to be 10mSv. Although in TL domain it is 0.1 mSv. The large difference may be attributed to the fact that photo-ionization cross section of OSL active traps of LBO: Cu,Ag for blue light stimulation is very low and thus traps are not significantly depleted amounting to feeble signal. Also, the shallow TL traps delays the exhibition of OSL signal in time scale and apparently reduces its photo-ionization cross section. However, MDD can be improved further by performing elevated temperature OSL readouts in which the role of shallow traps will be suppressed.

6.3.2.6. LM-OSL Studies

Fig. 6.18 shows a typical LM-OSL curve for LBO: Cu, Ag that was delivered an absorbed dose of 2.2 Gy using $^{90}\text{Sr}/^{90}\text{Y}$ beta source. The stimulation profile was modulated linearly from 0 to 50 mW/cm² power at sample position in 1450 s. The very broad nature of LMOSL curve shows that it consists of embedded peaks which are also evident from CW-OSL curves and its deconvolution. Further for LM-OSL curve, the geometrical factor μ_g which is simply the ratio δ/ω is ~ 0.8 , comparing this value with the standard values given in literature by Kitis et al. [38,39] confirms multiple peak and LM-OSL curve is a convolution of more than one LM-OSL peaks.

6.3.2.7. Elevated temperature OSL Studies on LBO: Cu, Ag Single Crystals

LBO: Cu, Ag as such has poor photo-ionization cross section to exhibit OSL at room temperatures (RT). However preliminary investigations on this material have shown that OSL measurements when carried out at 80°C the CW-OSL response increases by a factor of ~ 2.5 . The photo-ionization cross section apparently increases and thus the OSL readout time can be minimized when temperature is elevated up to 80°C. Further the temperature is not increased beyond 80°C due to the fact that the material starts giving TL response. Prior to perform elevated temperature CW-OSL studies the crystals were annealed at 100°C for 10 minutes so the low temperature TL peak after thermal cleaning does not interfere while taking elevated temperature OSL measurements. The phosphor shows significant increase in OSL yield at elevated temperatures by a factor of two or more when compared with OSL yield at RT as evident from fig. 6.19.

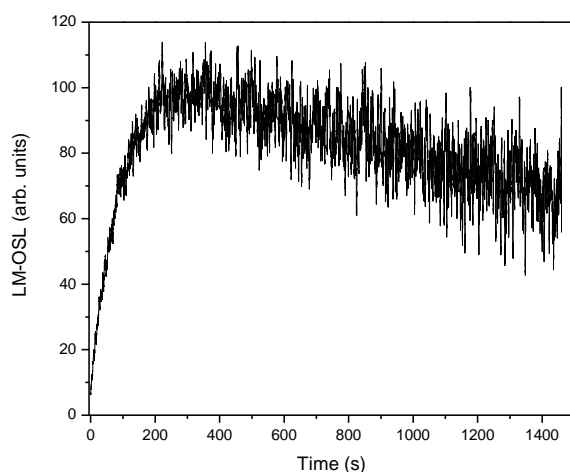


Figure 6.18. LM-OSL curve for LBO: Cu, Ag for an absorbed dose of 2.2 Gy using $^{90}\text{Sr}/^{90}\text{Y}$ beta source.

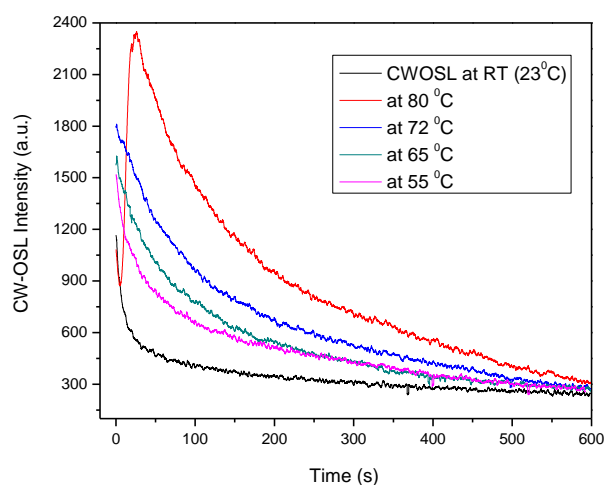


Figure 6.19. CW-OSL response of LBO: Cu, Ag at various elevated temperatures.

6.3.3. Conclusion

All the TL peaks in LBO: Cu, Ag follow first-order kinetics. Emission band having a peak at 370 nm and excitation band with a maximum at about 250 nm are attributed to parity and spin-forbidden $3d^9 4s \rightarrow 3d^{10}$ transitions from the triplet state of Cu^{1+} due to a large Stokes shift of $\sim 10,000 \text{ cm}^{-1}$ and a long decay time of $\sim 24 \mu\text{s}$. The crystal doped with Ag showed an emission band around 267 nm and excitation band around 210 nm with a decay time of 10 μs . The nature of the luminescence in this region is due to the transition of Ag^+ ions at the $4d^9 5S \rightarrow 4d^{10}$. The emission of Ag^+ states lies in the excitation region of Cu^+ states, therefore in case of co-doping of Ag + Cu, the emission at 370 nm in Cu states dominates over that due to transitions in Ag states. Hence doping of Ag plays a role of sensitizer when co-doped with Cu and increases overall emission. LBO is a relatively stable chemical compound and doped LBO is found to have increased TL sensitivity. OSL studies on LBO:Cu, Ag are reported for the first time. The Minimum detectable dose using CW-OSL method is found to be 10 mSv at room temperature.

TL and CW-OSL correlation study suggests that TL peak 3 is responsible for faster OSL component using which the lowest detectable dose is evaluated to be 16 mSv. However, the interference of shallow traps that delays the occurrence of OSL signal in time domain can be suppressed and minimized at elevated temperatures thereby improving MDD and sensitivity of LBO:Cu, Ag that needs to be explored and is a scope of future study. Preliminary investigations have shown that OSL yield increases at elevated temperature up to 80°C. LBO:Cu, Ag crystal can be used as a potential phosphor for remote optical fiber based real time OSL dosimetry for medical physics applications and neutron monitoring.

References:

1. C. Furetta, M. Prokic, R. Salamon, V. Prokic, G. Kitis, *Nucl. Instrum. Methods Phys. Res. Sect. A* 456 (2001) 411.
2. J.H. Schulman, R.D. Kirk E.J. West. Luminescence dosimetry (1967) CONF- 650637, US At. Energy Comm. Symp. Ser. 8, p. 113.
3. M. Takenaga, O. Yamamoto, T. Yamashita, *Nucl. Instrum. Methods* 175 (1980) 77.
4. M. Prokic. *Radiat. Measur.* 33 (2001) 393.
5. N. Can, T. Karali, P. D. Townsend, F. Yildiz. *J. Phys D: Appl. Phys.* 39 (2006) 2038.
6. B. T. Huy, V.X.Quang, H.T.B.Chau. *J. Lumin.* 128 (2008) 1601.
7. J.J. Thompson, Zeimer, L. Paul, *Health Phys.* 25 (1973) 435.
8. B. M. Rzycki, S. P. Morato, *Nucl. Instrum. Methods* 175 (1980) 62.
9. X. Zheng, Ye, T. Qiang, Z.C.hun Xiang, *Sci. China-Phys. Mech. Astron.* 50 (2007) 311.
10. L. Botter-Jensen, P. Christensen, *Acta Radiol. Suppl.* 313 (1972) 247.
11. B.F. Wall, C.M.H. Driscoll, J.C. Strong, E.S. Fisher, *Phys. Med. Biol.* 27 (1982) 1023.

12. A.S. Pradhan, R.C. Bhatt, K.G. Vohra, *Radiochem. Radioanal. Lett.* 53 (1982) 103.
13. S.W.S. McKeever, in: *Thermoluminescence of Solids*, Cambridge University Press, 1985
14. M. Martini, F. Meinardi, L. Kovacs, K. Polgar, *Radiat. Prot. Dosim.* 65 (1996) 343.
15. Ya V. Burak, B.V. Padlyak, V.M. Shevel., *Radiat. Eff. Defects Solids* 157 (2002) 1101.
16. M. Ignatovych, V. Holovey, A. Watterich, T. Vidoczy, P. Baranyai, A. Kelemen, O. Chuiko, *Radiat. Meas.* 38 (2004) 567.
17. Ya V. Burak, O.T. Adamiv, O.T. Antonyak, S.Z. Malynych, M.S. Pidzyrailo, I.M. Teslyuk, *Ukr. J. Phys.* 50 (2005) 1153.
18. K.S. Park, J.K. Ahn, D.J. Kim, H.K. Kim, Y.H. Hawang, D.S. Kim, M.H. Park, Y. Park, J. Yoon, J.Y. Leem, *J. Cryst. Growth* 249 (2003) 483.
19. B.T. Huy, B.M. Ly, V.X. Quang, H.K. Hanh, D.P.T. Tien, V. Hao, T. Ngoc, *J. Phys: Conf. Ser.* 187 (012039) (2009) 1.
20. J.K. Srivastava, S.J. Supe, *J. Phys. D* 22 (1989) 1537.
21. B.M. Hunda, T.V. Hunda, P.P. Puga, A.M. Solomon, V.M. Holovey, G.D. Puga, *J. Optoelectron. Adv. Mater.* 1 (1999) 49.
22. D.I. Shahare, B.T. Deshmukh, S.V. Moharil, S.M. Dhopte, P.L. Muthal, V.K. Kondawar., *Phys. Status Solidi A* 141 (1994) 329.
23. J. Manam, S.K. Sharma, *Radiat. Phys. Chem.* 72 (2005) 423.
24. C.M. Sunta, W.E.F. Ayta, J.F.D. Chubaci, S. Watanabe, *J. Phys. D* 34 (2001) 2690.
25. P. Ratna, P. Chaudhury, G. Nilshree, D.N. Sharma, *J. Med. Phys.* 31 (2006) 200.
26. H. Nanto, T. Usuda, K. Murayama, S. Nakamura, K. Inabe, N. Takeuchi, *Radiat. Prot. Dosim.* 47 (1993) 293.
27. R.R. Patil, S.V. Moharil, *J. Phys. Condens: Matter* 7 (1995) 9925.

28. R. Chen, *J. Appl. Phys.* 40 (1969) 570.
29. M. Balarin, *Phys. Status Solidi A* 54 (1979) K137.
30. R. Chen, *J. Electrochem. Soc.* 116 (1969) 1254.
31. A.R. Lakshmanan, Bhuwan Chandra, R.C. Bhatt, *Radiat. Prot. Dosim.* 1 (1981) 191.
32. N. Senguttuvan, M. Ishii, M. Shimoyama, M. Kobayashi, N. Tsutsui, M. Nikl, M. Dusek, H.M. Shimizu, T. Oku, T. Adachi, K. Sakai, J. Suzuki, *Nucl. Instrum. Methods Phys. Res. A* 486 (2002) 264.
33. S.W.S. McKeever, M. Moscovitch, *Radiat. Prot. Dosim.* 104 (2003) 263.
34. Babita Tiwari, N.S. Rawat, D.G. Desai, S.G. Singh, M. Tyagi, P. Ratna, S.C. Gadkari, M.S. Kulkarni, *J. Lumin.* 130 (2010) 2076.
35. M.S. Kulkarni, D.R. Mishra, D.N. Sharma., *Nucl. Instrum. Method. Phys. Research B* 262 (2007) 348.
36. G.D. Patra, Mohit Tyagi, D.G. Desai, Babita Tiwari, Shashwati Sen, S.C. Gadkari, *J. Lumin.* 132 (2012) 1101.
37. G. Kittis, J.M. Gomez-Ros, J.W.M. Tuyn., *J. Phy. D: Appl. Phys.* 31 (1999) 2636.
38. G. Kitis, V. Pagonis, *Radiat. Meas.* 43 (2008) 737.
39. G. Kitis, C. Furetta, V. Pagonis, *Mod. Phys. Lett.* 23 (2009) 3191.

Chapter 7. Conclusions

7.1. Summary of the work

The present study has explored $\text{Al}_2\text{O}_3:\text{C}$ (polycrystalline as well as single crystals) and $\text{Li}_2\text{B}_4\text{O}_7$ (single crystals) along with their attributes that render them suitable for their application in dosimetry. Although these materials are being developed for their application in OSL domain, their characterization in terms of defects responsible for OSL signal and stability of this signal with time can only be ascertained through TL-OSL correlation studies. Therefore in this research work TL is used as a complimentary technique for an in-depth characterization of the developed OSL material. Photo-ionization cross-section being the key parameter to judge the dosimetric viability of an OSL phosphor, in this work, its dependence on dose and temperature in case of $\text{Al}_2\text{O}_3:\text{C}$ has been extensively investigated. In addition certain novel experimental techniques which have been specifically devised for TL and OSL characterization of a phosphor have been presented and they constitute an important ingredient of this research work.

First chapter of this thesis has presented an introduction of Luminescence phenomenon that includes the details specific to Thermally Stimulated Luminescence and Optically Stimulated Luminescence. Subsequently an overview of popular phosphor materials used in radiation dosimetry is presented with emphasis on $\alpha\text{-Al}_2\text{O}_3:\text{C}$ and $\text{Li}_2\text{B}_4\text{O}_7$. $\alpha\text{-Al}_2\text{O}_3:\text{C}$ developed using different approaches was presented. This chapter also illustrated as to how in case of Al_2O_3 , the introduction of right kind of defects remarkably improved its sensitivity towards radiation and highlighted the necessity and utility of defect engineering i.e. creation of thermally as well as temporally stable defects in a controlled manner while functionalizing it. We have also seen how the defects produced due to dopants can decisively improve sensitivity

of a material system. Thus the dosimetric performance of a material critically depends on defect concentration, its nature and distribution throughout the host lattice.

The **second chapter** has dealt with the techniques that are often used for characterization of such defects and also includes a brief on their classification scheme. In the end of this chapter TL, OSL, PL and ESR investigations on $\text{MgAl}_2\text{O}_4:\text{Tb}^{3+}$ phosphor prepared by combustion synthesis was presented that highlights three TL peaks are at 120, 220 and 340°C in the material and also exhibits OSL when stimulated with 470 nm light. The sample thermally treated at 900°C gives maximum PL and OSL emission intensity. Two defect centres, centre I and II are identified in irradiated $\text{MgAl}_2\text{O}_4:\text{Tb}^{3+}$ phosphor and these centres are assigned to V and F^+ centres, respectively. V centre (hole centre) appears to correlate with the 120 and 220°C TL peaks while F^+ centre which acts as recombination centre is correlated with TL peaks at 120, 220 and 340°C. PL and TL emission results indicate Tb^{3+} acts as luminescent centre.

Apart from material characterization the major contribution and highlight of the present research work is the formulation of novel technique using initial rise method to determine kinetic order and frequency factor in lucid manner with minimum scope of error propagation associated with evaluation of parameters and is elaborated in **chapter three**. It has been shown that the initial rise method can be used to determine the order of kinetics, pre-exponential factor and frequency factor apart from trap depth E . Using theoretical simulations and finding the trapping parameters from the derived equations we have shown its validity. Using this method the experimental values of E , b and s as calculated for 230°C TL peak of $\text{CaSO}_4:\text{Dy}$ is in good agreement with the values reported in the literature. The essence of this technique lies in the fact that all these parameters can be determined independently i.e. expression for the

determination of b and s parameters is independent of E . Thus the uncertainty and error associated with one parameter does not propagate into the determination of another. However, all the limitations associated with initial rise method are applicable here too.

In **fourth chapter** the α -Al₂O₃:C developed using PGTI technique was characterized for its dosimetric performance and also investigated for dose dependence of its photo-ionization cross-sections participating in OSL process. The model was proposed to explain this observation which involves multiple traps in terms of cross-section that offers competition for trapping charge carriers. This has successfully explained an increase in photo-ionization cross-section with increase in dose along with the nature of CW-OSL decay curves which are found to be first, second and third exponential fit at lower, intermediate and higher doses respectively. This chapter also discusses the theoretical formulation for determining thermal assistance energy which is very helpful in explaining the thermal assistance nature of OSL dosimetry traps in α -Al₂O₃: C. The thermal assistance energy associated with dosimetry OSL trap in α -Al₂O₃: C has been measured using two different methods and found to agree within experimental limitations. The reported work highlights the effects of Arrhenius nature observed in temperature dependence of photo-ionization cross-section of OSL dosimetry traps in α -Al₂O₃: C. Preliminary investigations on commercially available α -Al₂O₃:C using non linear modulation of light i.e. NL-OSL technique has also been reported that offers several advantages like high signal to noise ratio, inherent potential of improving the minimum detection dose threshold, extended dynamic dose linearity of α -Al₂O₃:C up to 100Gy with an added advantage of multiple readouts.

Chapter five has taken an account into the application of Al₂O₃: C prepared using melt processing of polycrystalline alumina for neutron dosimetry. Using this phosphor attempt was

made to bring about the detection of neutrons by mixing the same with High Density Polyethylene (HDPE), Poly tetra fluoro ethylene (PTFE), ${}^{6,7}\text{LiF}$. The results indicate that it is possible to develop $\alpha\text{-Al}_2\text{O}_3\text{:C}$ based neutron dosimeters for personnel monitoring based on the albedo technique and it may be possible to use $\alpha\text{-Al}_2\text{O}_3\text{:C+HDPE}/\alpha\text{-Al}_2\text{O}_3\text{:C} + \text{Teflon}$ OSL dosimeters for personnel monitoring may be possible in high-energy neutron fields with low photon contribution, but further efforts are required. This chapter has also highlighted the studies of the F and F^+ centers in single crystals of $\alpha\text{-Al}_2\text{O}_3$ upon irradiation to thermal neutrons up to 10^{18} n/cm^2 and its implications on TL and OSL response. It was observed that the concentration of the F and F^+ centers increased with increase in thermal neutron fluence and is responsible for the observed TL and OSL in the material. On excitation with 204nm, F^+ emission band at 330nm is observed in addition to the F center emission band at 410nm. For $\alpha\text{-Al}_2\text{O}_3$ samples irradiated with neutron fluence $> 10^{16} \text{ n/cm}^2$, the intensity of F^+ emission band is prominent compared to the F center emission band for pure $\alpha\text{-Al}_2\text{O}_3$ single crystals as compared to the corresponding $\alpha\text{-Al}_2\text{O}_3\text{:C}$ TLD-500 single crystals. The $\alpha\text{-Al}_2\text{O}_3$ crystals irradiated to thermal neutron fluence $< 10^{17} \text{ n/cm}^2$ showed weak TL and OSL response. The TL glow curve of the thermal neutron irradiated to $\alpha\text{-Al}_2\text{O}_3$ is different from the TL glow curve structure of the TLD-500 single crystal, which shows dosimetric glow peak at $\sim 190^\circ\text{C}$. The TL and OSL emission is due to the F centers in neutron irradiated to $\alpha\text{-Al}_2\text{O}_3$ as is the case in to $\alpha\text{-Al}_2\text{O}_3\text{:C}$. However, the OSL active defect centers in $\text{Al}_2\text{O}_3\text{:C}$ are different than those induced in neutron irradiated $\alpha\text{-Al}_2\text{O}_3$.

Novel findings of the investigations carried out on LBO:Cu and LBO:Cu,Ag single crystals grown using Czochralski method have been listed out in **chapter six** with their potential applications. Doping with Cu enhances TL sensitivity and linear dose-response in the

LBO material. The material is found to have linear dose-response in the range of 1 mGy to 1kGy with main dosimetric TL peak at about 513 K and a low temperature TL peak at about 402 K for a heating rate of 4 K/s. Low temperature TL peak fades completely when stored at room temperature in dark for 24 hours. Moreover, these peaks did not shift with a dose in the range from 0.1 Gy to 150 Gy. It is therefore concluded that the TL peaks obey first order kinetics. A UV-vis transmission spectrum confirms the doping of Cu^+ ions in the crystal. Intense emission at 360nm and single exponential decay (24.18 μs) strongly point to one type of Cu^+ ions as the emitting species in LBO: Cu. The TL emission in LBO:Cu is also due to the energy levels of Cu^+ state.

Eventually the chapter highlighted studies on LBO: Cu, Ag single crystals too. The TL peaks in LBO: Cu, Ag follow first-order kinetics. Emission band having a peak at 370 nm and excitation band with a maximum at about 250 nm are attributed to parity and spin-forbidden $3d^9 4s \rightarrow 3d^{10}$ transitions from the triplet state of Cu^{1+} due to a large Stokes shift of $\sim 10,000 \text{ cm}^{-1}$ and a long decay time of $\sim 24 \mu\text{s}$. The crystal doped with Ag showed an emission band around 267 nm and excitation band around 210 nm with a decay time of 10 μs . The nature of the luminescence in this region is due to the transition of Ag^+ ions at the $4d^9 5s \rightarrow 4d^{10}$. The emission of Ag^+ states lies in the excitation region of Cu^+ states, therefore in case of co-doping of Ag with Cu the emission at 370 nm in Cu states dominates over that due to transitions in Ag states. Hence doping of Ag plays a role of sensitizer when co-doped with Cu and increases overall emission. OSL studies on LBO:Cu, Ag are reported for the first time. TL and CW-OSL correlation study suggests that TL peak 3 is responsible for faster OSL component. However, the interference of shallow traps that delays the occurrence of OSL signal in time domain can be suppressed and minimized at elevated temperatures thereby improving MDD and sensitivity

of LBO:Cu, Ag that needs to be explored and is a scope of future study. LBO:Cu, Ag crystal can be used as a potential phosphor for remote optical fiber based real time OSL dosimetry for medical physics applications and neutron monitoring.

7.2. Challenges and scope of future studies

This research work highlights materials for dosimetric applications and has extensively discussed the $\text{Al}_2\text{O}_3:\text{C}$ and processes to realize its synthesis. Although sensitivity of $\text{Al}_2\text{O}_3:\text{C}$ is very high but the lacunae associated with this material is its insensitivity to neutron due to negligible thermal neutron absorption cross-section by its constituent elements. To overcome this, efforts have been made which involves addition of neutron converters like ^{10}B , ^6Li , ^{157}Gd etc. However, this converter, besides disturbing the tissue equivalence also limit the range of secondary charged particles (alpha, tritium, proton etc.) due to self absorption and in effect restricts its sensitivity towards neutron.

This limitation can be addressed by taking another approach that involves choosing a host lattice e.g. Lithium Borate ($\text{Li}_2\text{B}_4\text{O}_7$) whose constituent elements themselves have high enough absorption cross-section for neutrons as a result of which the secondary charged particles so generated will be able to deposit their entire energy inside the host lattice resulting into enhanced efficiency of detection, thereby leading to an improved sensitivity. $\text{Li}_2\text{B}_4\text{O}_7$ doped with Cu and co-doped with Ag will be investigated for its neutron response and ability to discriminate in mixed field.

$\text{Al}_2\text{O}_3:\text{C}$ prepared using melt processing of alumina can also be studied using techniques of positron annihilation spectroscopy, raman scattering and fourier transform infrared spectroscopy for detailed investigation of defects and its correlation with observed OSL in the

material. Energy compensation filters for flattening energy response of $\text{Al}_2\text{O}_3:\text{C}$ based OSL detector along with its angular response for gamma radiation is also a scope of future study.

A variety of other materials have been investigated for various OSL applications in the literature. It is often the case that one of the main problems observed with these materials is fading of the OSL signal. This highlights one of the disadvantages of the OSL technique, the fact that the OSL technique simultaneously releases charges from multiple trapping centers, some that are thermally stable and some that are not. Consequently the OSL signal may fade over different time scales, depending on the depth of the multiple traps contributing to the OSL process. Although pre-heating can be used to empty shallow traps associated with unstable OSL components, this is not always practical for commercial applications. Even when shallow traps are emptied prior to the OSL readout it may still be necessary to perform the OSL at elevated temperatures to eliminate or minimize the influence of shallow traps as competitors.

In summary, there is still a scarcity of OSL materials with demonstrated properties suited to dosimetry applications. Progress on the development of OSL materials with engineered properties has been slow and most research has focused on the OSL characterization of existing materials. For some applications (e.g., retrospective dosimetry) this is the only possible approach. However, the development of synthetic materials with optimal characteristics, such as was the case with $\text{Al}_2\text{O}_3:\text{C}$, will require a more focused effort and one in which material synthesis and characterization of luminescence and physical properties are carried out hand-in-hand.